



University of Ioannina
School of Sciences
Department of Physics

EXOTIC LEPTON FLAVOUR VIOLATING PROCESSES IN THE FIELD OF NUCLEUS

PHD THESIS

Dimitrios K. Papoulias
Physicist

Ioannina, 2016



University of Ioannina
School of Sciences
Department of Physics

**EXOTIC LEPTON FLAVOUR
VIOLATING PROCESSES
IN THE FIELD OF NUCLEUS**

PHD THESIS

Dimitrios K. Papoulias
Physicist

Ioannina, 2016



Πανεπιστήμιο Ιωαννίνων
Σχολή Θετικών Επιστημών
Τμήμα Φυσικής

ΕΞΩΤΙΚΕΣ ΑΝΤΙΔΡΑΣΕΙΣ
ΠΑΡΑΒΙΑΣΗΣ
ΛΕΠΤΟΝΙΚΗΣ ΓΕΥΣΗΣ
ΣΤΟ ΠΕΔΙΟ ΤΟΥ ΠΥΡΗΝΑ

ΔΙΔΑΚΤΟΡΙΚΗ ΔΙΑΤΡΙΒΗ

Δημήτριος Κ. Παπούλιας
Φυσικός

Ιωάννινα, 2016

“I have done a terrible thing, I have postulated a particle that cannot be detected”

Wolfgang Pauli, 1930

Three-member Advisory Committee

- Theocharis Kosmas, Professor, Department of Physics, University of Ioannina (Thesis Supervisor)
- Georgios Leontaris, Professor, Department of Physics, University of Ioannina
- José W.F. Valle, Professor, Instituto de Física Corpuscular–C.S.I.C., University of Valencia, Spain

Seven-member Assessment Committee

- Theocharis Kosmas, Professor, Department of Physics, University of Ioannina (Thesis Supervisor)
- Georgios Leontaris, Professor, Department of Physics, University of Ioannina
- José W.F. Valle, Professor, Instituto de Física Corpuscular–C.S.I.C., University of Valencia, Spain
- Leandros Perivolaropoulos, Professor, Department of Physics, University of Ioannina
- Rosa Vlastou-Zanni, School of Applied Mathematics and Physics, National Technical University of Athens
- Dionysios Bonatsos, Director of Research, Institute for Nuclear and Particle Physics, National Centre of Scientific Research “Demokritos”
- Georgios Stavropoulos, Senior Researcher, Institute for Nuclear and Particle Physics, National Centre of Scientific Research “Demokritos”

ΠΡΑΚΤΙΚΟ
ΔΗΜΟΣΙΑΣ ΠΑΡΟΥΣΙΑΣΗΣ ΕΞΕΤΑΣΗΣ ΚΑΙ ΑΞΙΟΛΟΓΗΣΗΣ ΔΙΔΑΚΤΟΡΙΚΗΣ ΔΙΑΤΡΙΒΗΣ

Σήμερα, Τρίτη 9 Φεβρουαρίου 2016, ώρα 10:30, στην αίθουσα Σεμιναρίων του Τμήματος Φυσικής (Αναγνωστήριο, κτίριο Φ2, 3ος όροφος) στη Πανεπιστημιούπολη, πραγματοποιήθηκε η διαδικασία της δημόσιας παρουσίασης, εξέτασης και αξιολόγησης, ενώπιον της Επταμελούς Εξεταστικής Επιτροπής, της Διδακτορικής Διατριβής που εκπόνησε ο υποψήφιος κ. **Δημήτριος Παπούλιας** στα πλαίσια του Προγράμματος Μεταπτυχιακών Σπουδών «Φυσικής» του Τμήματος Φυσικής Παν/μίου Ιωαννίνων.

Την 7-μελή Εξεταστική Επιτροπή, που όρισε με σχετική απόφασή της η Γενική Συνέλευση Ειδικής Σύνοψης του Τμήματος Φυσικής (κατά τη Συνεδρίασή της υπ' αριθμ. 460/18-01-2016), αποτελούν τα ακόλουθα μέλη:

- 1) Θεοχάρης Κοσμάς, Καθηγητής Τμ. Φυσικής, Παν/μίου Ιωαννίνων (Επιβλέπων)
- 2) Γεώργιος Λεοντάρης, Καθηγητής Τμ. Φυσικής, Παν/μίου Ιωαννίνων
- 3) Jose W.F. Valle, Καθηγητής Τμ. Φυσικής, Πανεπιστημίου Valencia, Ισπανίας
- 4) Λέανδρος Περιβολαρόπουλος, Καθηγητής Τμ. Φυσικής, Παν/μίου Ιωαννίνων
- 5) Ρόζα Βλαστού-Ζάννη, Καθηγήτρια, ΣΕΜΦΕ, Ε.Μ.Π, Αθήνα
- 6) Διονύσιος Μπονάτσος, Διευθυντής Ερευνών, Ι.Π.Σ.Φ., Ε.Κ.Ε.Φ.Ε. Δημόκριτος, Αθήνα
- 7) Γεώργιος Σταυρόπουλος, Κύριος Ερευνητής, Ι.Π.Σ.Φ., Ε.Κ.Ε.Φ.Ε. Δημόκριτος, Αθήνα

Ο υποψήφιος παρουσίασε και υποστήριξε δημόσια ενώπιον των μελών της Εξεταστικής Επιτροπής και του ακροατηρίου την εκπονηθείσα διδακτορική διατριβή με τίτλο: "**Εξωτικές Αντιδράσεις Παραβίασης Λεπτονικής Γεύσης-στο Πεδίο του-Πυρήνα**".

Μετά την ολοκλήρωση της δημόσιας προφορικής διαδικασίας, αποχώρησαν το ακροατήριο και ο υποψήφιος και παρέμειναν μόνο τα μέλη της Εξεταστικής Επιτροπής, τα οποία μετά από συζήτηση κατέληξαν στα ακόλουθα συμπεράσματα:

Το θέμα της διατριβής απαιτεί εμβάθυνση σε ευρύ φάσμα φυσικής στοιχειωδών σωματιδίων, πυρηνικής δομής και φυσικής νετρίνων. Ο υποψήφιος έδειξε ότι μελέτησε σε βάθος και κατανόησε πλήρως τις σχετικές έννοιες, ενώ παράλληλα κάλυψε την σχετική βιβλιογραφία με υψηλό βαθμό πληρότητας, τόσο όσον αφορά θεμελιώδεις παλαιότερες εργασίες, αλλά και πρόσφατες ενδιαφέρουσες εξελίξεις.

Η ολοκλήρωση της διατριβής απαιτήσε την χρήση υπολογιστικών κωδίκων οι οποίοι αποτελούν τα πλέον σύγχρονα εργαλεία διεθνώς, καθώς και την ανάπτυξη νέων κωδίκων, στην οποία ο υποψήφιος επέδειξε ιδιαίτερη πρωτοβουλία

Τα αποτελέσματα της διατριβής είναι εξαιρετικά επίκαιρα, όπως μαρτυρεί η δημοσίευση τριών εργασιών στο κορυφαίο περιοδικό Physics Letters B, ενώ παράλληλα έχουν ιδιαίτερη βαρύτητα, όπως μαρτυρεί η δημοσίευση δύο εκτενών εργασιών στα περιοδικά Physical Review D και Advances in High Energy Physics

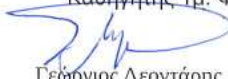
Η παρουσίαση της διατριβής από τον υποψήφιο και η επιτυχής αντιμετώπιση των υποβληθεισών ερωτήσεων κατέδειξε βαθιά κατανόηση των εννοιών και της βιβλιογραφίας από τον υποψήφιο, καθώς και πλήρη γνώση των τεχνικών που χρησιμοποίησε.

Με βάση τα παραπάνω η Επταμελής Εξεταστική Επιτροπή εγκρίνει ομόφωνα την εργασία και εισηγείται ανεπιφύλακτα την απονομή Διδακτορικού Διπλώματος στον κ. **Δημήτριο Παπούλια** με βαθμό **Άριστα**

Τα μέλη της Εξεταστικής Επιτροπής



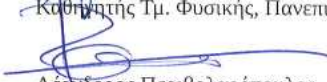
Θεοχάρης Κοσμάς, Επιβλέπων Καθηγητής
Καθηγητής Τμ. Φυσικής, Παν/μίου Ιωαννίνων



Γεώργιος Λεοντέρης,
Καθηγητής Τμ. Φυσικής, Παν/μίου Ιωαννίνων



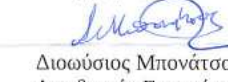
Jose W.F. Valle,
Καθηγητής Τμ. Φυσικής, Πανεπιστημίου Valencia, Ισπανίας



Λεάνδρος Περιβολαρόπουλος,
Καθηγητής Τμ. Φυσικής, Παν/μίου Ιωαννίνων



Ρόζα Βλαστού-Ζάνη,
Καθηγήτρια, ΣΕΜΦΕ, Ε.Μ.Π, Αθήνα



Διούσιος Μπονάτσος,
Διευθυντής Ερευνών, Ι.Π.Σ.Φ., Ε.Κ.Ε.Φ.Ε. Δημόκριτος, Αθήνα



Γεώργιος Σταυρόπουλος,
Κύριος Ερευνητής, Ι.Π.Σ.Φ., Ε.Κ.Ε.Φ.Ε. Δημόκριτος, Αθήνα

Contents

Acknowledgments	xi
1 Introduction	3
1.1 The subject of the present research and motivation	3
1.2 Overview of the Thesis	5
2 The Standard Model and beyond	7
2.1 Introduction	7
2.2 Standard electroweak model	7
2.2.1 Gauge bosons	8
2.2.2 Matter fields	9
2.2.3 Neutral-current neutrino-lepton interactions	11
2.2.4 Charged-current neutrino-lepton interactions	12
2.2.5 Mass generation	13
2.3 Effective low-energy CC and NC Lagrangians	17
2.4 Standard and non-standard neutrino-electron interactions	19
2.4.1 SM neutrino-electron cross sections	19
2.4.2 Non-standard neutrino-electron cross sections	21
2.5 Standard and non standard neutrino-nucleon interactions	22
2.5.1 Neutrino-nucleon cross sections	22
2.5.2 NSI neutrino-nucleon cross sections	23
2.5.3 NSI nucleon form factors	25
3 Description of the Nuclear Structure	27
3.1 Introduction	27
3.2 The nuclear Hamiltonian	27
3.3 The Woods-Saxon potential	29
3.4 Theoretical description of the nuclear ground state	31
3.4.1 The nuclear BCS wavefunction	31

3.4.2	BCS quasi-particles	33
3.4.3	Two-body interactions	35
3.4.4	The BCS nuclear Hamiltonian	37
3.4.5	BCS equations	40
3.4.6	The gap equation	42
3.4.7	Pairing interaction in the Bonn C-D potential	44
3.5	Quasi-particle random phase approximation (QRPA)	48
3.5.1	The proton-proton and neutron-neutron QRPA	51
3.6	Evaluation of the nuclear form factors	52
3.6.1	Nuclear Structure calculations	52
3.6.2	Other methods for obtaining the nuclear form factors	53
4	Neutrino-nucleus processes within the SM	59
4.1	Introduction	59
4.2	The role of neutrino-nucleus processes	59
4.3	The Donnelly-Walecka method	61
4.3.1	Multipole operators	63
4.3.2	Coherent and incoherent neutrino-nucleus cross sections	66
4.4	Derivation of coherent neutrino-nucleus cross section	69
4.5	Results and discussion	73
4.5.1	Integrated coherent neutrino-nucleus cross sections	73
4.5.2	Supernova neutrino simulations	75
4.5.3	Laboratory neutrino simulations	77
4.5.4	Simulated neutrino signals	78
4.5.5	Differential and total event rates	79
4.6	Conclusions	82
5	Exotic neutrino-nucleus processes	85
5.1	Introduction	85
5.2	The role of neutrino NSI interactions in nuclear physics	85
5.3	Neutrino non-standard interactions	88
5.4	Description of the formalism	89
5.4.1	Non-standard neutrino-nucleus reaction cross sections	90
5.5	Results and discussion	93
5.5.1	Integrated coherent neutrino-nucleus NSI cross sections	93
5.5.2	NSI of Supernova neutrinos	95
5.5.3	New stringent limits on $\epsilon_{\mu e}^{fV}$ from $\mu^- \rightarrow e^-$ conversion	99
5.5.4	NSI of neutrinos from spallation neutron sources	101
5.6	NSI in SUSY theories	102
5.7	Conclusions	104

6	Electromagnetic neutrino properties in NSI theories	107
6.1	Introduction	107
6.1.1	Dirac neutrinos	107
6.1.2	Charge-radius	110
6.2	Majorana neutrino magnetic moment	112
6.2.1	Effective neutrino magnetic moments	113
6.3	Tensorial non-standard neutrino interactions	116
6.4	Description of the formalism	117
6.4.1	Non-standard neutrino-nucleus reaction cross sections . . .	118
6.4.2	NSI neutrino transition magnetic moments	119
6.5	Results and discussion	120
6.5.1	Tensorial NSI couplings from SNS experiments	120
6.5.2	NSI neutrino-nucleus events at the TEXONO experiment .	122
6.5.3	Neutrino milli-charge	124
6.6	Conclusions	127
7	Sensitivities to electromagnetic neutrino parameters	129
7.1	Introduction	129
7.2	The role of effective neutrino electromagnetic parameters	130
7.2.1	Standard model prediction	132
7.2.2	Electromagnetic neutrino-nucleus cross sections	133
7.3	Neutrinos from the spallation sources	135
7.3.1	Numerical results	136
7.3.2	Standard Model precision tests at SNS	136
7.3.3	EM neutrino interactions at SNS	138
7.3.4	Sensitivity to the neutrino charge-radius	140
7.4	Neutrinos from reactors	142
7.4.1	Signal cross sections	142
7.4.2	Statistical analysis	146
7.5	Conclusions	153
8	Sterile neutrinos from neutrino-nucleus scattering	155
8.1	Introduction	155
8.2	Neutrino oscillations in vacuum	155
8.2.1	Two neutrino flavour oscillation probabilities	157
8.2.2	Three neutrino flavour oscillation probabilities	159
8.3	Impact of a light sterile neutrino to neutrino-nucleus scattering . .	161
8.4	Numerical results	162
8.4.1	Impact of sterile neutrinos on beta-decay and on neutrino-less double beta-decay	167
8.5	Conclusions	168

9	Summary of Thesis and outlook	169
9.1	Summary and conclusions	169
9.2	Future perspectives	171
A		173
A.1	Notation and conventions	173
A.2	Trace identities	174
A.3	Mandelstam variables	175
B		177
B.1	Nuclear matrix elements of the hadronic current	177
B.2	Compact expressions of the reduced transition matrix elements . .	180
B.3	Nucleon form factors	181
C		183
C.1	Clebsch-Gordan coefficients	183
C.2	3-j symbols	184
C.3	6-j symbols	184
C.4	9-j symbols	185
C.5	Racah W-coefficients	185
C.6	The Wigner-Eckart theorem	186
C.7	Products of coupled tensor operators	186
D		187
D.1	Woods-Saxon wavefunctions	187
D.2	Harmonic Oscillator wavefunctions	188
D.3	Quasi-boson approximation (QBA)	190
D.4	Coefficients entering the quasi-particle representation of pp - nn QRPA	193
D.5	The correlation matrix	194
E		199
E.1	Supernova distributions	199
E.1.1	Fermi-Dirac distribution	199
E.1.2	Power-law distribution	201
F		203
F.1	Nuclear charge density distribution	203
F.1.1	Fourier-Bessel analysis	203
F.1.2	Other models describing the charge distribution	204

Acknowledgments

First and foremost, I wish to express my sincerest appreciation to my Supervisor Professor Theocharis S. Kosmas, Department of Physics, University of Ioannina, for his precious guidance, enthusiasm and continuous support during our collaboration. I feel fortunate for being one of his students and for having so generously been offered such a high level education on theoretical nuclear physics. To me, he has been more than a teacher having his door always opened and answering the infinite number of questions I asked for. His insightful comments, constructive criticism and challenging suggestions during our endless discussions on neutrino physics, have served as a constant motivation for improvement, setting a remarkable foundation for my scientific career.

I feel deeply grateful to the other two members of my Advisory Committee: Professor G.K. Leontaris, Department of Physics, University of Ioannina, deserves a special thanks for his general involvement during the course of my PhD Thesis and the critical reading of the final manuscript. I owe gratitude to Professor J.W.F. Valle, Instituto de Física Corpuscular–C.S.I.C., University of Valencia, Spain, for his kind invitation to work with his prestigious AHEP-group in Valencia and for financial support. My cooperation with Prof. Valle, helped me to gain special knowledge from the particle physics point of view and especially on phenomenological models describing Majorana neutrinos.

I would like to thank the members of the Evaluation Committee of this Thesis: Professor L. Perivolaropoulos, Department of Physics, University of Ioannina, Professor R. Vlastou-Zanni, School of Applied Mathematics and Physics, National Technical University of Athens, Director of Research D. Bonatsos, Institute for Nuclear and Particle Physics, National Centre of Scientific Research “Demokritos” and Senior Researcher G. Stavropoulos, Institute for Nuclear and Particle Physics, National Centre of Scientific Research “Demokritos”, for their willingness to participate in the official defence and their useful remarks that contributed maximally towards improving the final version of my Thesis. At this point, I should particularly acknowledge fruitful discussions on Mathematica with

Professor L. Perivolaropoulos.

During my stay in Valencia, I was given the opportunity to collaborate closely with Dr. M.A. Tórtola (AHEP-group, IFIC-CSIC) and Professor O.G. Miranda, Department of Physics, Centre for Research and Advanced Studies of the National Polytechnic Institute, Mexico. I warmly thank them both, for sharing with me their expertise and brilliant ideas on neutrino physics.

I am also indebted to Emeritus Professor J.D. Vergados, Department of Physics, University of Ioannina, for stimulating discussions and for his inspirational suggestions on the potential next steps I may follow towards extending the present research. It is a pleasure to thank the Research Assistant Professor A. Hatzikoutelis Physics Department, University of Tennessee at Knoxville, USA, for providing me various clarifications related to experimental neutrino physics issues.

I would like to give special thanks to my colleague and good friend Dr. P.G. Giannaka with whom we shared the same office during our PhD studies. I will always remember our long-lasting discussions on nuclear physics, the exchange of ideas and advices, as well as the great mutual encouragement and respect that made pleasant the daily routine in the place of work. Moreover, the considerable technical assistance, especially in the first years of my PhD studies, provided by Dr. T. Smponias and Dr. O.T. Kosmas is highly appreciated.

A great thanks goes to all members forming the AHEP-group at IFIC-CSIC for their hospitality and kindness that made me feel, even from the first day, as an official “*AHEPiano*”. I really enjoyed the time I spent with you, especially in the *cafetería Vallenciana* and your interest in the etymology of Greek words.

I would have never been able to write these lines if I hadn't the limitless support (financial and psychological) and encouragement of my family: Kostas, Toula, Vasia and Amerso, for whom I express my love from the bottom of my heart. Thank you for always standing beside me.

With no doubt, my lady Emi is my hidden power and the person that lies behind this Thesis. After the stressful days at work, her understanding and tolerance were expressed with a big smile and an open hug, that gave me the strength to go on till the end. Thank you so much for being so patient with me, for always supporting my choices and for never saying no. I will make it up to you, the time I have stolen from you.

This PhD Thesis was partly supported by the programme:
“*Prometeu per a grups d'investigació d' Excel·lència de la Conselleria d' Educació, Cultura i Esport, CPI-14-289*” (GVPROMETEOII2014-084).

Abstract

The main objective of the present Thesis is to explore the exotic neutral-current (NC) neutrino processes, predicted by theories beyond the Standard Model (SM) of the electroweak interactions to take place in the field of nucleons and nuclei. The subject of neutrino non-standard interactions (NSI) plays a leading role in recent studies of lepton flavour violating (LFV) processes, now that the three oscillation in propagation paradigm is put in rather solid grounds. In particular, we concentrate on the vector NSI of neutrino scattering off nuclear systems, detectors of ongoing and designed extremely sensitive experiments searching for LFV. It is, furthermore, shown that within the framework of tensorial neutrino NSI, electromagnetic (EM) neutrino properties are also predicted, which are complementary to distinguish the Dirac or Majorana nature of neutrinos. For the case of neutrino EM interactions a thorough investigation is devoted demonstrating that neutrino-nucleus scattering is a promising probe to search for physics beyond the SM.

The first stage of our research involves the development of the mathematical formalism where the relevant NSI operators are parametrised assuming typical phenomenological four-fermion contact interaction Lagrangians. The impact of the nuclear structure properties is studied through the appropriate transformation of the quark-level Lagrangians to the nuclear-level one. The corresponding neutrino-nucleus cross sections are evaluated by employing the nuclear method of the multipole decomposition of the hadronic current, established by Donnelly-Walecka. In addition, the various flavour preserving and flavour changing interaction channels, predicted to occur within NSI, are taken into consideration through the evaluation of the respective matrix elements entering the relevant cross sections.

The nuclear physics aspects of these processes are systematically studied in the context of the state-of-the-art quasi-particle random phase approximation (QRPA). Specifically, for the case of coherent elastic neutrino-nucleus scattering (CENNS), the nuclear ground state is constructed by solving iteratively

the Bardeen-Cooper-Schrieffer (BCS) equations. This way, realistic strong two-nucleon pairing forces are taken into account maximising the reliability of the obtained results. Such nuclear structure corrections improve previous CENNS calculations ignoring the nuclear form factor, by even one order of magnitude.

From the experimental physics perspective, for the case of both conventional and exotic neutrino processes, the accuracy of the obtained cross sections is exploited in order to compute with high significance the corresponding convoluted cross sections that represent the signal expected to be recorded by terrestrial nuclear detectors. Furthermore, we evaluate reliably other important experimental observables such as the differential event rates and the number of neutrino scattering events expected to be measured in Supernova (SN), Spallation Neutron Source (SNS) and reactor neutrino experiments. We illustrate that, such measurements may be very sensitive to neutrino-quark NSI or neutrino EM interactions (magnetic moment, mean charge-radius, milli-charge) and could provide more severe constraints as compared to those expected in future neutrino factory experiments. To this end, our study involves extensive calculations for a set of promising target materials throughout the periodic table of nuclides. Focusing on astrophysical (SN) and laboratory (SNS and reactor) neutrino sources as well as dark matter and multipurpose experiments, our results refer to the ^{20}Ne , ^{40}Ar , ^{76}Ge and ^{132}Xe isotopes, i.e. the target nuclei of ongoing and future experiments including the COHERENT, TEXONO, GEMMA and the direct detection of Cold Dark Matter (CDM) experiments. Therefore, this type of calculations is of primary importance for experiments searching for WIMP-nucleus scattering, since CENNS events constitutes an irreducible background.

In view of the operation of extremely intense laboratory neutrino fluxes (at the SNS, J-PARC, Fermilab, PSI, etc.), the sensitivity to search for new physics will be largely increased, and, therefore, through CENNS measurements, several open questions (involving neutrino NSI, neutrino magnetic moment, sterile neutrino searches and others) may be answered. Our present results, in conjunction with those expected from sensitive muon-to-electron conversion experiments (Mu2e at Fermilab, COMET at J-PARC), may offer significant contribution to understand the fundamental nature of electroweak interactions in the leptonic sector and to constrain the parameters of beyond the SM Lagrangians.

Εκτεταμένη Περίληψη

Το αντικείμενο της παρούσας Διδακτορικής Διατριβής εντάσσεται στο χώρο επικάλυψης της πυρηνικής αστροφυσικής, της αστροσωματιδιακής φυσικής και των θεμελιωδών ηλεκτρασθενών αλληλεπιδράσεων. Κύριος σκοπός της εργασίας αυτής είναι η διερεύνηση των ανοιχτών ερωτημάτων της σύγχρονης έρευνας της φυσικής των νετρίνων, δίνοντας ιδιαίτερη έμφαση στη μελέτη των εξωτικών διαδικασιών ουδετέρου-ρεύματος των νετρίνων που λαμβάνουν χώρα στο πεδίο των πυρήνων και των νουκλεονίων. Οι εν λόγω αντιδράσεις προβλέπονται από θεωρίες πέραν του Καθιερωμένου Προτύπου (Standard Model, SM) των ηλεκτρασθενών αλληλεπιδράσεων ενώ παράλληλα αναζητούνται από εξαιρετικής ευαισθησίας πειράματα που λειτουργούν ή σχεδιάστηκαν να λειτουργήσουν στα ανά τον κόσμο μεγάλα Ερευνητικά Κέντρα.

Το ζήτημα των μη-συμβατικών αλληλεπιδράσεων (non-standard interactions, NSI) των νετρίνων διαδραματίζει σημαντικό ρόλο στη σύγχρονη έρευνα των διαδικασιών παραβίασης λεπτονικής γεύσης (lepton flavour violation, LFV) καθ' ότι το φαινόμενο των ταλαντώσεων των νετρίνων, με το οποίο έχει αποδειχθεί η εν λόγω παραβίαση στον λεπτονικό τομέα ουδετέρων σωματίων, έχει τεθεί πλέον σε ισχυρές βάσεις. Οι ανωτέρω αντιδράσεις προβλέπεται επίσης ότι λαμβάνουν χώρα υπό τις ακραίες συνθήκες που επικρατούν σε αστροφυσικό περιβάλλον (π.χ. συνθήκες έκρηξης Υπερκαινοφανούς αστέρα) επιβάλλοντας σημαντικές αλλαγές στα φαινόμενα εξέλιξης ενός Υπερκαινοφανούς κατάρρευσης καρδιάς (core collapse Supernova). Επιπρόσθετα, αναμένεται να παρατηρηθούν από επίγειους πυρηνικούς ανιχνευτές σύγχρονων εργαστηρίων όπως στο Oak Ridge National Lab (πείραμα COHERENT) καθώς και σε πειράματα νετρίνων πυρηνικών αντιδραστήρων ισχύος (πειράματα TEXONO, GEMMA, κλπ.). Πιο συγκεκριμένα, η παρούσα έρευνα επικεντρώνεται στη μελέτη της διανυσματικής συνιστώσας των NSI στη σκέδαση νετρίνων από πυρηνικούς ανιχνευτές σύγχρονων πειραμάτων υψηλής ευαισθησίας, η οποία οδηγεί σε παραβίαση της λεπτονικής γεύσης. Επιπλέον, καταδεικνύεται ότι η ταυστική συνιστώσα NSI των νετρίνων, συνεπάγεται την ύπαρξη ηλεκτρο-

μαγνητικών (EM) ιδιοτήτων των νετρίνων, οι οποίες μπορούν να συμβάλλουν στη διαλεύκανση της Dirac ή Majorana φύσης των νετρίνων. Σχετικά με τις EM ιδιότητες των νετρίνων, πραγματοποιείται εκτεταμένη μελέτη η οποία μέχρι τώρα έχει αναδείξει την σκέδαση νετρίνου-πυρήνα ως μία πολλά υποσχόμενη διαδικασία διερεύνησης της φυσικής πέρα από το SM.

Αρχικά, στην παρούσα εργασία, αναπτύσσεται κατάλληλος φορμαλισμός στον οποίο οι σχετικοί τελεστές των NSI παραμετροποιούνται θεωρώντας φαινομενολογικές Λαγκραντζιανές αλληλεπιδράσεως επαφής τεσσάρων-φερμιονίων (four-fermion contact interaction). Στο πλαίσιο της παρούσας Διατριβής, λαμβάνεται υπόψη η εξάρτηση της ενεργού διατομής σκέδασης από τις ιδιότητες της πυρηνικής δομής στην οποία μεταβαίνουμε μέσω κατάλληλου μετασχηματισμού των σχετικών Λαγκραντζιανών από το επίπεδο των κουάρκ, στο πυρηνικό επίπεδο. Στους λεπτομερειακούς υπολογισμούς των ενεργών διατομών υιοθετείται η μέθοδος της πολυπολικής ανάπτυξης του πυρηνικού αδρονικού ρεύματος (μεθόδος Donnelly-Walecka). Επιπρόσθετα, τα διάφορα κανάλια αλληλεπίδρασης, διατήρησης ή παραβίασης της λεπτονικής γεύσης, των οποίων η ύπαρξη προβλέπεται στο πλαίσιο των NSI, μελετώνται μέσω αντίστοιχων υπολογισμών των πυρηνικών στοιχείων πίνακα που υπεισέρχονται στην ενεργό διατομή της υπό μελέτη αντίδρασης.

Η συστηματική μελέτη των πτυχών της πυρηνικής δομής στις ανωτέρω διαδικασίες, επιτυγχάνεται χρησιμοποιώντας την μέθοδο της προσέγγισης τυχαίας φάσης με ημι-σωμάτια (quasi-particle random phase approximation, QRPA). Συγκεκριμένα, στην περίπτωση του συναφούς καναλιού ελαστικής σκέδασης νετρίνου-πυρήνα (coherent elastic neutrino-nucleus scattering, CENNS), η βασική πυρηνική κατάσταση κατασκευάζεται μέσω της επαναληπτικής επίλυσης των εξισώσεων Bardeen-Cooper-Schrieffer (BCS). Κατά συνέπεια λαμβάνεται υπόψη με ρεαλιστικό τρόπο η ισχυρή αλληλεπίδραση ζεύγους δύο-νουκλεονίων το οποίο οδηγεί σε ενίσχυση της αξιοπιστίας των ληφθέντων αποτελεσμάτων. Τέτοιου είδους υπολογισμοί, βασιζόμενοι στη λεπτομέρεια της πυρηνικής δομής, οδηγούν σε διαφορές έως και μίας τάξης μεγέθους των παρόντων αποτελεσμάτων σε σύγκριση με προηγούμενα στα οποία αγνοήθηκε πλήρως η εξάρτηση από τον πυρηνικό παράγοντα δομής.

Από πειραματική έποψη, στην περίπτωση των συμβατικών και εξωτικών διαδικασιών νετρίνου-πυρήνα, η ακρίβεια των ληφθέντων ενεργών διατομών αξιολογείται για τον υπολογισμό αντίστοιχων αναδιπλωμένων ενεργών διατομών, οι οποίες προσομοιάζουν το αναμενόμενο σήμα στους επίγειους πυρηνικούς ανιχνευτές. Επιπρόσθετα, στην παρούσα έρευνα πραγματοποιούνται ακριβείς υπολογισμοί σχετικοί με άλλες πολύ σημαντικές πειραματικές ποσότητες όπως, ο διαφορικός ρυθμός γεγονότων και ο ολικός αριθμός γεγονότων που αναμένεται να ανιχνευθούν σε πειράματα ανίχνευσης Υπερχαινοφανών νετρίνων, SNS νετρίνων καθώς και σε πειράματα νετρίνων αντιδραστήρων ισχύος (reactor neutrino experiments). Υπογραμμίζουμε ότι μετρήσεις τέτοιου είδους ενδέχεται να έχουν υψηλή ευαισθησία σε αλληλεπιδράσεις νετρίνου-κουάρκ ή EM φύσεως αλληλεπιδράσεις των νετρίνων (μαγνητική ροπή, μέση ακτίνα φορτίου, χιλιοστο-φορτίο) και κατά συνέπεια αναμένεται

να θέσει αυστηρότερα όρια στις προαναφερθείσες εξωτικές ιδιότητες των νετρίνων σε σχέση με μελλοντικά πειράματα που θα διεξαχθούν στα neutrino factories. Στην κατεύθυνση αυτή, η παρούσα μελέτη περιλαμβάνει υπολογισμούς οι οποίοι αναφέρονται σε διάφορα πυρηνικά συστήματα που καλύπτουν όλο το φάσμα του περιοδικού πίνακα ισοτόπων.

Η επικείμενη λειτουργία εξαιρετικά ισχυρών δεσμών εργαστηριακών νετρίνων (στα SNS, J-PARC, Fermilab, PSI, κλπ.), προϋποθέτει ότι, η ευαισθησία στην αναζήτηση νέας φυσικής θα αυξηθεί δραματικά και συνεπώς μέσω μετρήσεων της CENNS, πολλά ανοιχτά ζητήματα (όπως NSI νετρίνου, μαγνητική ροπή νετρίνου, η ύπαρξη sterile νετρίνο και άλλα) αναμένεται να διαλευκανθούν. Τα παρόντα αποτελέσματα, σε συνδυασμό με εκείνα που αναμένονται από τα πειράματα έρευνας της αντίδρασης μετατροπής μιονίου σε ηλεκτρόνιο, αφενός θα συνεισφέρουν σημαντικά στην κατανόηση των θεμελιωδών ηλεκτρασθενών αλληλεπιδράσεων στον λεπτονικό τομέα και αφετέρου στον περιορισμό των ορίων των παραμέτρων των Λαγκραντζιανών διάφορων μοντέλων που προχωρούν πέρα από το SM.

Η ύλη της παρούσας Διδακτορικής Διατριβής οργανώνεται ως εξής:

Έπειτα από μια γενική εισαγωγή στα ανωτέρω ερευνητικά θέματα (Κεφάλαιο 1), το Κεφάλαιο 2, περιλαμβάνει το θεωρητικό υπόβαθρο της Διατριβής από την άποψη της σωματιδιακής φυσικής. Αρχικά, παρατίθεται μια σύντομη επισκόπηση του Καθιερωμένου Προτύπου των ηλεκτρασθενών αλληλεπιδράσεων εστιάζοντας στις θεμελιώδεις διαδικασίες των νετρίνων με πολύπλοκους πυρήνες. Για λόγους πληρότητας, συζητούνται επιπλέον οι βασικές πτυχές των SM και NSI αντιδράσεων νετρίνου-ηλεκτρονίου ουδετέρου- και φορτισμένου-ρεύματος. Επιπρόσθετα παρουσιάζεται ο κύριος φορμαλισμός για την περιγραφή της σχέδασης νετρίνου-νουκλεονίου ουδετέρου-ρεύματος στο πλαίσιο του Καθιερωμένου Προτύπου καθώς και η απαραίτητη επέκτασή του ώστε να καταστεί δυνατή η περιγραφή των αντίστοιχων μη-συμβατικών αλληλεπιδράσεων νετρίνου-νουκλεονίου.

Στο Κεφάλαιο 3, αρχικά δίνεται ιδιαίτερη προσοχή στις μεθόδους μελέτης της δομής σύνθετων πυρήνων (με μαζικό αριθμό $A > 12$) μέσω μίας εκτεταμένης περιγραφής των σύγχρονων πυρηνικών μοντέλων που χρησιμοποιούνται. Η εκτενής μελέτη της δομής των πυρήνων που επιλέχθηκαν στην παρούσα έρευνα (βλέπε Κεφάλαια 4-8) από την άποψη της θεωρητικής πυρηνικής φυσικής γίνεται στο πλαίσιο μιας εκλέπτυνσης της QRPA και αποτελούν το βασικό θεωρητικό υπόβαθρο των Κεφαλαίων αυτών. Στην περίπτωση της CENNS, η βασική πυρηνική κατάσταση κατασκευάζεται μέσω της επαναληπτικής επίλυσης των εξισώσεων BCS. Τοιουτοτρόπως λαμβάνεται υπόψη με ρεαλιστικό τρόπο η ισχυρή αλληλεπίδραση ζεύγους δύο-νουκλεονίων θεωρώντας το δυναμικό (ανταλλαγής ενός-μεσονίου) Bonn C-D, το οποίο οδηγεί σε ενίσχυση της αξιοπιστίας των ληφθέντων αποτελεσμάτων. Στη συνέχεια, μέσω υπολογισμών πυρηνικής δομής της μεθόδου που αναπτύχθηκε στο πλαίσιο της παρούσας Διατριβής (σε γλώσσα προγραμματισμού FORTRAN 77), παρουσιάζονται αποτελέσματα πυρηνικών παραγόντων δομής (nuclear form factors). Ο έλεγχος της ανωτέρω μεθόδου και της ακρίβειας των αποτελεσμάτων, πραγματοποιήθηκε μέσω ανάπτυξης ειδικού κώδικα (με χρήση του πακέτου MATHEMAT-

ICA) ο οποίος υλοποιεί κατάλληλη επεξεργασία πειραματικών δεδομένων σκέδασης ηλεκτρονίου-ηλεκτρονίου και επιστρέφει τους αντίστοιχους παράγοντες δομής για άμεση σύγκριση. Στην κατεύθυνση αυτή, οι παράγοντες δομής μελετούνται περαιτέρω θεωρώντας το πυρηνικό μοντέλο φλοιών (nuclear shell model) καθώς και μέσω μιας εκλέπτυνσης της μεθόδου των μερικών πιθανοτήτων κατάλληλης (fractional occupation probabilities) των νουκλεονικών επιπέδων.

Στο Κεφάλαιο 4, με βάση τη θεωρία που ήδη περιγράφηκε στα Κεφάλαια 2 και 3, στο πλαίσιο του SM πραγματοποιείται λεπτομερής μελέτη της CENNS σε μία ομάδα πυρηνικών ισοτόπων που καλύπτουν ένα ευρύ φάσμα του Περιοδικού Πίνακα των νουκλεϊδίων. Στους λεπτομερειακούς υπολογισμούς των ενεργών διατομών υιοθετείται η πυρηνική μέθοδος της πολυπολικής ανάπτυξης του αδρονικού ρεύματος των Donnelly-Walecka, η ακρίβεια της οποίας αξιοποιείται στον αντίστοιχο υπολογισμό των αναδιπλωμένων ενεργών διατομών, οι οποίες προσομοιάζουν το αναμενόμενο σήμα ανίχνευσης των υπό συζήτηση αντιδράσεων στους επίγειους πυρηνικούς ανιχνευτές. Εστιάζοντας σε πειράματα νετρίνων, αστροφυσικών (SN) και εργαστηριακών (SNS) πηγών (αποτελούν ταυτόχρονα και πειράματα ανίχνευσης της σκοτεινής ύλης), δίνεται ιδιαίτερη έμφαση στη χρήση των πυρηνικών συστημάτων ^{20}Ne , ^{40}Ar , ^{76}Ge και ^{132}Xe . Τα ανωτέρω ισότοπα αποτελούν τα κύρια υλικά των ανιχνευτών του πρόσφατα σχεδιασθέντος πειράματος COHERENT που αποσκοπεί στην έρευνα της CENNS, καθώς και στην άμεση ανίχνευση της Ψυχρής Σκοτεινής Ύλης (CDM). Οι διορθώσεις στον υπολογισμό της πρωτογενούς ενεργού διατομής, οι οποίες προέρχονται από τα φαινόμενα της πυρηνικής φυσικής (βλέπε Κεφάλαιο 3) κρίνονται πολύ σημαντικές καθώς οδηγούν σε διαφορές άνω του 30% στα ληφθέντα αποτελέσματα. Κατά τον τρόπο αυτόν, για τα προαναφερθέντα πειράματα, παρουσιάζονται με μεγάλη ακρίβεια ο διαφορικός και ο ολικός ρυθμός γεγονότων που αναμένεται να ανιχνευθούν.

Στο Κεφάλαιο 5, επεκτείνεται η μέθοδος που αναπτύχθηκε στο Κεφάλαιο 4 και μελετάται η συνεισφορά της διανυσματικής συνιστώσας των μη-συμβατικών αλληλεπιδράσεων (NSI) στην ενεργό διατομή νετρίνου-πυρήνα. Οι σχετικοί τελεστές των NSI παραμετροποιούνται θεωρώντας φαινομενολογικές Λαγκραντζιανές αλληλεπιδράσεων επαφής τεσσάρων-φερμιονίων. Στο πλαίσιο της παρούσας Διατριβής, μελετάται εκτενώς η εξάρτηση από τις ιδιότητες της πυρηνικής δομής, μεταβαίνοντας μέσω κατάλληλου μετασχηματισμού των σχετικών Λαγκραντζιανών από το επίπεδο των κουάρκ, στο πυρηνικό επίπεδο. Επιπρόσθετα, τα διάφορα κανάλια διατήρησης ή παραβίασης της λεπτονικής γεύσης, η ύπαρξη των οποίων προβλέπεται στο πλαίσιο των NSI, μελετώνται μέσω υπολογισμών των αντίστοιχων πυρηνικών στοιχείων πίνακα που υπεισέρχονται στην ενεργό διατομή της εκάστοτε μελετούμενης αντίδρασης. Για τους επιμέρους υπολογισμούς (σε αναλογία με το Κεφάλαιο 4) χρησιμοποιήθηκαν ως πυρήνες-στόχοι τα ^{20}Ne , ^{40}Ar , ^{76}Ge και ^{132}Xe για την ανάλυση των εξωτικών διαδικασιών νετρίνου-πυρήνα στο πείραμα COHERENT. Επιπρόσθετα, μελετούνται οι (διαδικασίες υποβάθρου) NSI Υπερκαινοφανών νετρίνων με τα πυρηνικά συστήματα των ^{27}Al και ^{48}Ti , που επιλέχθηκαν ως ανιχνευτές στα μελλοντικά πειράματα αναζήτησης γεγονότων της εξωτικής

αντίδρασης της μετατροπής μιονίου σε ηλεκτρόνιο ($\mu^- \rightarrow e^-$ conversion) όπως το Mu2e στο Fermilab, και το COMET στο J-PARC. Εκμεταλευόμενοι την εξαιρετική ευαισθησία των πειραμάτων αυτών, κατέστη δυνατό να θέσουμε νέα άνω όρια για μερικές από τις παραμέτρους που χαρακτηρίζουν την ισχύ της NSI αλληλεπίδρασης.

Στο Κεφάλαιο 6, διερευνάται στο πλαίσιο των τανυστικών NSI αλληλεπιδράσεων των νετρίνων, η ύπαρξη ανιχνεύσιμων ηλεκτρομαγνητικών (EM) ιδιοτήτων των νετρίνων. Παρουσιάζονται και συζητούνται αναλυτικά οι προκύπτουσες τανυστικές NSI ενεργές διατομές καθώς και τα σχετικά πυρηνικά στοιχεία πίνακα. Επιπρόσθετα, διερευνώνται εκτενώς οι φαινομενολογικές συνέπειες της εν λόγω θεωρίας που σχετίζονται με ενδιαφέρουσες φυσικές ποσότητες όπως η μαγνητική ροπή (magnetic moment) και το χιλιοστο-φορτίο (milli-charge) του νετρίνου. Για τον σκοπό αυτό, μέσω της ευρέως χρησιμοποιούμενης στατιστικής μεθόδου χ^2 (chi-square fit), αναλύονται τα ληφθέντα αποτελέσματα που αφορούν τα ισότοπα ^{28}Si και ^{76}Ge για τους πυρηνικούς ανιχνευτές σε πειράματα νετρίνων αντιδραστήρων ισχύος, όπως τα TEXONO και GEMMA. Από την μελέτη αυτή, εξάγεται το συμπέρασμα ότι τα ανωτέρω πειράματα έχουν υψηλή ευαισθησία σε διαδικασίες που προβλέπονται στο πλαίσιο των τανυστικών NSI και επιπλέον η παρούσα έρευνα οδηγεί σε αυστηρότερα άνω όρια για τις παραμέτρους που υπεισέρχονται στις αντίστοιχες Λαγκραντζιανές της θεωρίας. Κατά συνέπεια, προϋποθέτονται βελτιωμένες τιμές στα άνω όρια για τη μαγνητική ροπή και το χιλιοστο-φορτίο του νετρίνου, βελτιώνοντας προηγούμενα αποτελέσματα.

Στο Κεφάλαιο 7, πραγματοποιείται διεξοδική έρευνα των EM ιδιοτήτων των νετρίνων τύπου Majorana (το σωματίο ν συμπίπτει με το αντισωματίο $\bar{\nu}$) μέσω της CENNS. Εκτιμάται η αποδοτικότητα των πειραμάτων COHERENT και TEXONO ως προς την ανίχνευση αλληλεπιδράσεων EM φύσεως λόγω μαγνητικών ροπών νετρίνου μιονίου (ν_μ) και ανινετρίνου ηλεκτρονίου ($\bar{\nu}_e$) αντίστοιχα. Τα αποτελέσματα της μελέτης μας καθιστούν πρόδηλη τη δυναμική των προαναφερθέντων πειραμάτων, ως προς την εύρεση νέας φυσικής πέρα από το Καθιερωμένο Πρότυπο μέσω της ανίχνευσης EM σημάτων νετρίνων. Συγκεκριμένα, παρουσιάζονται αυστηρότερα άνω όρια για τις ποσότητες μ_{ν_μ} και $\mu_{\bar{\nu}_e}$, βελτιώνοντας τα αντίστοιχα υπάρχοντα στην μέχρι τώρα διεθνή Βιβλιογραφία κατά 50%. Επιπρόσθετα ποσοτικοποιείται η ευαισθησία των προαναφερθέντων πειραμάτων αναφορικά με την μέση ακτίνα φορτίου των νετρίνων (neutrino mean charge radius). Στην περίπτωση αυτή, η βελτίωση ανέρχεται σε έως και μία τάξη μεγέθους. Επιπρόσθετα, εξετάζεται η προοπτική πραγματοποίησης ελέγχων ακριβείας των βασικών παραμέτρων του Καθιερωμένου Προτύπου. Εξάγεται το συμπέρασμα ότι μέσω της μέτρησης της σκέδασης νετρίνου-πυρήνα χαμηλών ενεργειών, καθίσταται δυνατός ο αυστηρός προσδιορισμός της γωνίας ανάμιξης των ηλεκτρασθενών αλληλεπιδράσεων (electroweak mixing angle, θ_W).

Στο Κεφάλαιο 8, μελετάται η δυνατότητα ανίχνευσης στείρων (sterile) νετρίνων μέσω της διαδικασίας σκέδασης νετρίνου-πυρήνα στα πειράματα TEXONO και COHERENT καθώς και η προοπτική μέτρησης των αντίστοιχων παραμέτρων ανάμιξης, χρησιμοποιώντας εξαιρετικά ευαίσθητους πυρηνικούς ανιχνευτές ^{76}Ge χαμηλού κατ-

ωφλίου ενέργειας. Εστιάζοντας στο μοντέλο (3+1) των sterile νετρίνων, τα αποτελέσματα που προέκυψαν καταδεικνύουν την CENNS ως ένα πολύτιμο εργαλείο στην έρευνα του πεδίου των ταλαντώσεων των νετρίνων σε εργαστηριακό επίπεδο. Με χρήση της μεθόδου που περιγράφηκε στα προηγούμενα Κεφάλαια, μέσω στατιστικής ανάλυσης των υπό μελέτη πειραμάτων, παρουσιάζονται οι σχετικές καμπύλες αποκλεισμού (exclusion curves) για τα επίπεδα $(\sin^2 2\theta_{ee}, \Delta m_{14}^2)$, $(\sin^2 2\theta_{\mu\mu}, \Delta m_{14}^2)$ και $(\sin^2 2\theta_{ee}, \Delta m_{14}^2)$. Επιπλέον, πραγματοποιείται μία σύντομη περιγραφή των φαινομενολογικών συνεπειών των σχετικών παραμέτρων ανάμιξης στην απλή διάσπαση-βήτα καθώς επίσης και στη διπλή διάσπαση-βήτα χωρίς νετρίνα. Οι ανωτέρω υπολογισμοί είναι χρήσιμοι για πειράματα που αναζητούν γεγονότα προερχόμενα από αντιδράσεις WIMP-πυρήνα, δεδομένου ότι τα CENNS αποτελούν αναπόφευκτα γεγονότα υποβάθρου.

Τα σημαντικότερα συμπεράσματα που εξήχθησαν από την έρευνα που πραγματοποιήθηκε στο πλαίσιο της παρούσας Διδακτορικής Διατριβής συνοψίζονται στο Κεφάλαιο 9. Επιπλέον παρατίθενται οι βασικές προοπτικές επέκτασης και εξέλιξης των υπό μελέτη θεωριών, που ενθαρρύνονται από την έμβαση της παρούσας εργασίας, περιλαμβάνοντας ενδιαφέροντα ανοιχτά θέματα του συναφούς αντικειμένου της εκπονηθείσας έρευνας.

Κλείνοντας, στα Παραρτήματα περιλαμβάνεται μια συνοπτική περιγραφή των συμβάσεων που υιοθετήθηκαν στην εργασία και συζητούνται οι απαραίτητες συμπληρωματικές πληροφορίες όπου κρίνεται απαραίτητο. Τέλος, παρατίθεται μία σύγχρονη και εκτενής Βιβλιογραφία η οποία αποτέλεσε το βασικό υπόβαθρο καθώς και το κίνητρο της Διδακτορικής Διατριβής.

List of Figures

2.1	Weak interaction neutral-current diagrams.	12
2.2	Weak interaction charged-current diagrams.	13
2.3	Low-energy CC Fermi contact interaction.	18
2.4	Low-energy NC Fermi contact interaction.	18
2.5	Constraints on SM parameters from neutrino-electron scattering. .	21
2.6	Constraints on NSI parameters from neutrino-electron scattering.	22
2.7	Differential and and total neutrino-nucleon NSI cross sections. . .	26
3.1	Woods-Saxon v.s. Harmonic Oscillator potential.	30
3.2	Feynman diagrams for the Bonn C-D potential.	45
3.3	The charge density distribution and the nuclear form factor. . . .	58
4.1	Feynman diagram for SM neutrino-nucleus scattering.	67
4.2	The $d\sigma/dT_N$, $d\sigma/d\cos\theta$ and σ_{tot} cross sections for ^{48}Ti	74
4.3	Total coherent cross sections for a set of nuclei.	75
4.4	Supernova neutrino energy spectra.	76
4.5	Stopped pion-muon beam neutrino energy spectra.	77
4.6	Convolved cross sections for Supernova and laboratory neutrinos.	78
4.7	Differential and total event rates for Supernova neutrinos.	80
4.8	Same as Fig. 4.7 but for ^{76}Ge and ^{132}Xe	81
4.9	Total number of expected events at the Spallation Neutron Source.	84
5.1	Nuclear level Feynman diagrams for NSI and cLFV processes. . . .	90
5.2	Coherent NSI cross sections $\sigma_{\lambda,\nu_\alpha}(E_\nu)$ for ^{48}Ti	95
5.3	Convolved NSI cross sections for Supernova neutrinos.	97
5.4	NSI Differential event rate for Supernova neutrinos.	98
5.5	Simulated signals for the $\sigma_{\nu_e \rightarrow \nu_\mu}^{\text{sign}}$ FCNC process.	99
5.6	Number of NSI events at the COHERENT experiment.	102
5.7	Same as Fig. 5.6.	103

6.1	Tree-level photon couplings with fermions and neutrinos.	108
6.2	Nuclear level Feynman diagram for μ_ν due to tensorial NSI.	118
6.3	$\Delta\chi^2$ profiles as function of the $\epsilon_{e\beta}^{dT}$ NSI parameters.	122
6.4	Allowed regions in the $\epsilon_{e\beta}^{dT}-\epsilon_{e\beta}^{uT}$ and $\epsilon_{\mu\beta}^{dT}-\epsilon_{\mu\beta}^{uT}$ parameter space.	124
6.5	The $d\sigma/dT_N$ cross sections for SM, EM and tensor NSI.	125
6.6	Reactor neutrino spectra.	125
6.7	Number of events due to vectorial NSI at TEXONO.	126
6.8	Number of events due to tensor NSI and NMM at TEXONO.	127
7.1	$\Delta\chi^2$ profiles in terms of $\sin^2\theta_W$ at COHERENT.	137
7.2	Combined $\Delta\chi^2$ profiles in terms of $\sin^2\theta_W$ at COHERENT.	139
7.3	$\Delta\chi^2$ profiles in terms of μ_{ν_μ} at COHERENT.	141
7.4	Combined $\Delta\chi^2$ profiles in terms of μ_{ν_μ} at COHERENT.	142
7.5	The 90% allowed $\mu_{\nu_\mu}(\mu_{\bar{\nu}_\mu})$ - $\sin^2\theta_W$ contours at COHERENT.	143
7.6	Same as Fig. 7.5 (left), but also for the 68% and 99% C.L.	143
7.7	Same as Fig. 7.5 (right), but also for the 68% and 99% C.L.	144
7.8	The 90% C.L. $\mu_{\bar{\nu}_\mu}-\mu_{\nu_e}$ contours at COHERENT.	144
7.9	$\Delta\chi^2$ profiles in terms of $\langle r_{\nu_\mu}^2 \rangle$ at COHERENT.	145
7.10	Combined $\Delta\chi^2$ profiles in terms of $\langle r_{\nu_\mu}^2 \rangle$ at COHERENT.	146
7.11	SM and EM $\langle \frac{d\sigma}{dT_N} \rangle$ and σ^{sign} for reactor neutrinos.	147
7.12	The quenching factor and the electron equivalent energy for ^{76}Ge	147
7.13	CENNS events for different quenching factors at TEXONO.	148
7.14	$\Delta\chi^2$ profiles in terms of $\sin^2\theta_W$ at TEXONO.	149
7.15	Sensitivity profiles in terms of the $\mu_{\bar{\nu}_e}$ and the detector mass.	150
7.16	$\Delta\chi^2$ profiles in terms of $\langle r_{\bar{\nu}_e}^2 \rangle$ at TEXONO.	152
7.17	Allowed regions in $(\sin^2\theta_W-\mu_{\bar{\nu}_e})$ and $(\langle r_{\bar{\nu}_e}^2 \rangle-\mu_{\bar{\nu}_e})$ planes at TEXONO.	153
8.1	The ratio $R = \langle \sigma \rangle_{\text{sterile}}/\langle \sigma \rangle_{\text{SM}}$ as a function of the baseline.	163
8.2	Contours of the number of events in the (3+1) scheme.	164
8.3	Allowed region in the $(U_{e4} ^2, \Delta m_{14}^2)$ plane in the (3+1) scheme.	164
8.4	Excluded region in the $(\sin^2 2\theta_{ee}, \Delta m_{14}^2)$ plane in the (3+1) scheme.	165
8.5	Excluded region in the $(\sin^2 2\theta_{\mu\mu}, \Delta m_{14}^2)$ plane in the (3+1) scheme.	165
8.6	Excluded region in the $(\sin^2 2\theta_{e\mu}, \Delta m_{14}^2)$ plane in the (3+1) scheme.	166
8.7	Contribution to $m_{2\beta}$ due to a sterile neutrino.	167
8.8	Contribution to m_β due to a sterile neutrino.	168

List of Tables

2.1	Fundamental couplings of the SM fermion fields to the Z -boson. . .	11
2.2	The three generations of leptons.	13
2.3	Higgs doublet eigenvalues in the $SU(3)_c \otimes SU(2)_L \otimes U(1)_Y$ group.	14
3.1	The values of proton g_{pair}^p and neutron g_{pair}^n pairs.	53
3.2	The exact f_λ and θ_λ coefficients in the nuclear Shell-Model.	55
4.1	Flux averaged cross sections for SN and laboratory neutrinos. . .	79
4.2	Total number of events for Supernova neutrinos.	82
5.1	The ratios R_{λ, ν_α}	94
5.2	Flux averaged cross sections, $\langle \sigma_{\lambda, \nu_\alpha} \rangle$, for Supernova neutrinos. . .	96
5.3	Sensitivity to NSI from $\mu^- \rightarrow e^-$ conversion experiments.	100
6.1	Sensitivity of COHERENT to tensor NSI.	123
6.2	Sensitivity of TEXONO to NSI parameters $\epsilon_{e\beta}^{fT}$	123
7.1	Summary of neutrino magnetic moment constraints.	131
7.2	Summary of the COHERENT detector concepts.	135
7.3	Sensitivity of COHERENT to $\sin^2 \theta_W(\nu_\alpha)$	138
7.4	Combined sensitivity of COHERENT to $\sin^2 \theta_W(\nu_\alpha)$	138
7.5	Expected upper limits on μ_ν at the COHERENT experiment. . .	140
7.6	Combined sensitivity of COHERENT to $\langle r_{\nu_\mu}^2 \rangle$	146
7.7	TEXONO sensitivities to $\sin^2 \theta_W$ and EM neutrino parameters. .	148
7.8	Comparison of binned and no-binned sensitivities at TEXONO. .	152
B.1	The coefficients $\mathcal{P}_\mu^{6,J}$ for the the $\langle j_1 \Delta_M^J j_2 \rangle$	181

1.1 The subject of the present research and motivation

The Standard Model (SM) of strong and electroweak interactions is for over three decades the most successful theory of elementary particle physics. Even though its predictions have been tested through various high-energy collider experiments resulting to exceptional agreement, our current understanding for the SM is that it only constitutes a low-energy approximation of a more complete “*theory of everything*”. Towards this direction, the scientific community has devoted a special effort towards formulating possible extensions of the basic theory in order to describe phenomena beyond the SM.

After the recent discovery of the Higgs boson, the neutrino remains the most enigmatic particle that exhibits the solid structure of the SM. The robust discovery of neutrino oscillations in the propagation of solar and atmospheric neutrinos, confirmed at accelerator and reactor neutrino sources, has provided us with a rather solid proof for the existence of neutrino masses and mixing and hence the clearest evidence for the need of physics beyond the SM. These results have prompted a great rush to produce adequate SM extensions with small neutrino masses. Many questions related to: the absolute neutrino mass, the total number of neutrino flavours, the Dirac or Majorana nature of neutrinos, potential exotic neutrino interactions, the neutrino electromagnetic (EM) properties and others remain yet open.

In recent years, a considerable part of research activities related to neutrino physics, focuses on interdisciplinary phenomena into the interplay between nuclear astrophysics, astroparticle physics and cosmology, both from a theoretical and experimental point of view. Despite the smallness of its mass and the weakness of its interaction with other particles, the neutrino constitutes a prime vehicle that plays instrumental role in astrophysical searches since it can escape from the interior of distant stars carrying away important information. It is, thus, not an

exaggeration to say that neutrinos serve as an excellent astronomical messenger and presently the most efficient nature's telescope to look deep inside the Earth, Sun, stars and so on up to Big Bang. Currently several experiments designed to operate with very high sensitivities, have put very stringent limits on various physical observables and/or particle model parameters while searching to see new physics beyond the current SM of electroweak interactions.

From the perspective of experimental nuclear physics, it became feasible that atomic nuclei provide a remarkable micro-laboratory to explore basic properties of the fundamental strong and electroweak interactions. In the latter interactions, among various processes that take place in the field of nuclei, neutrino-nucleus scattering plays a crucial role, while from a nuclear theory point of view, the accurate description of the nuclear states is of key importance. The nucleus, being a complex many-nucleon system, cannot be described with conventional methods to a satisfactory level and towards this purpose, advanced techniques have been developed over the last decades. Among the most prominent ones, the quasi-particle random phase approximation (QRPA) stands out as a highly efficient tool for studying the nuclear structure. The various modern versions of this method, based on the consideration of realistic strong two-nucleon forces, provides a reliable description for the nuclear transition matrix elements entering the cross section of lepton-nucleus processes.

The subject of the present study, falls within the overlap area of nuclear, astroparticle physics and cosmology. More specifically, this Thesis addresses the lepton flavour violating (LFV) non-standard neutrino interactions (NSI) that are not allowed to occur within the SM of particle physics. These processes, are also predicted to take place under the extreme conditions prevailing in an astrophysical environment (Supernova explosion) causing significant alterations to the expected evolution phenomena, e.g. those occurring during the core collapse Supernova. Moreover, they are very likely to be observed by terrestrial nuclear targets employed at: i) the Spallation Neutron Source facilities at Oak Ridge National Lab in the COHERENT experiment (SNS neutrinos) and ii) the experiments using neutrinos produced in nuclear reactor plants (reactor neutrinos) such as TEXONO and GEMMA.

Underpinning the ultimate origin of neutrino mass stands out as one of the biggest challenges in particle physics. A generic feature of many such schemes is the presence of non-vanishing neutrino EM properties. While the neutrino masses indicated by oscillation data are perhaps too small to induce sizeable magnetic moments, this issue is rather model dependent, and one cannot exclude this possibility on general grounds. If large enough, these may still play an important sub-leading role in precision neutrino studies, despite the good agreement found within the three-neutrino oscillation picture. Non-zero diagonal magnetic moments exist for massive Dirac neutrinos. In contrast, in the general Majorana neutrino case all magnetic moments are transition-type. Therefore, the study of neutrino magnetic moments would be a powerful tool towards distinguishing their

Dirac or Majorana character.

1.2 Overview of the Thesis

The material of the present Thesis has been organised as follows:

In Chapter 2, we briefly review the Standard electroweak model paying special attention on the fundamental neutrino interactions as they are described within the assumptions of this theory. For the sake of completeness, the main features of the SM and NSI neutrino-electron interactions are also addressed. In addition, we provide the basic aspects of the SM neutrino-nucleon interaction and we show how potential exotic neutrino-nucleon interactions may be obtained.

Chapter 3, is devoted to a thorough discussion of the basic theoretical background and the relevant theory describing the nuclear physics aspects considered in the calculations that are presented in the main research Chapters of the Thesis. We also discuss in detail and provide a compact mathematical description of the Bardeen-Cooper-Schrieffer (BCS) method which is employed for the explicit construction of the nuclear ground state in even-even nuclei. We proceed with the analysis of the quasi-particle random phase approximation (QRPA) and specifically, we illustrate the main features of the charge conserving pp-nn QRPA that is appropriate for the inelastic channels of the neutral-current neutrino processes. Eventually, apart from BCS, alternative complementary techniques for obtaining nuclear form factors of high accuracy, are presented and discussed.

In Chapter 4, we provide a detailed description for the SM neutrino scattering off complex nuclei by illustrating the relevant matrix elements which account for elastic and inelastic processes. In the context of the multipole decomposition theory of Donnelly-Walecka, the evaluated cross sections come out with high accuracy by incorporating the nuclear corrections addressed in Chapt. 3. For the case of coherent scattering, we furthermore, demonstrate convoluted cross sections calculations as well as differential and total event rates for a set of interesting nuclei. Focusing on Supernova and Spallation Source neutrinos as well as dark matter and multipurpose experiments, our results refer to the ^{20}Ne , ^{40}Ar , ^{76}Ge and ^{132}Xe isotopes, i.e. the target nuclei of ongoing and future experiments including the COHERENT and the direct detection of Cold Dark Matter (CDM) experiments GERDA, WARP, SuperCDMS, XENON100, etc.

In Chapter 5, we extend the formalism of Chapt. 4 and incorporate the vectorial NSI neutrino scattering off nuclei. Towards this direction, the adopted model is based on typical phenomenological four-fermion contact interaction Lagrangians, parametrised in terms of the NSI parameters. The latter parameters describe the existence of flavour-preserving (non-universal) and flavour-violating terms, leading to corrections of the SM weak interaction involving new physics phenomena. For the various exotic interaction channels, we provide the formalism for the NSI nuclear matrix elements entering the corresponding NSI cross

sections.

In Chapter 6, we review the basic theory describing the subject of neutrino EM properties and then we show that the context of tensorial NSI leads to EM neutrino interactions. The corresponding tensorial NSI cross sections and the relevant nuclear matrix elements are formulated and discussed. Predictions on NSI transition neutrino magnetic moments and neutrino milli-charges, are also addressed. Through a statistical χ^2 analysis of the coherent neutrino-nucleus events, we explore the sensitivity of COHERENT experiment to tensor NSI parameters.

In Chapter 7, we study the Majorana neutrino EM properties on the basis of a χ^2 fit analysis. Through neutral-current coherent neutrino-nucleus scattering, we examine the efficiency of experimental facilities that use stopped pion-muon beams and reactor plants in detecting the effects of neutrino EM interactions due to muon-neutrino and electron-antineutrino magnetic moments, respectively. We furthermore explore their expected sensitivity to probe the neutrino charge-radius and to perform SM precision tests through the determination of the weak-mixing angle.

In Chapter 8, we first review the basic theory of neutrino oscillations in propagation. Then, we illustrate the potentiality of TEXONO experiment to probe light sterile neutrinos through coherent neutrino-nucleus scattering. Furthermore, interesting phenomenological consequences of the corresponding mixing parameters on the simple beta-decay and the neutrinoless double-beta decay in the presence of massive Majorana neutrinos are discussed.

Chapter 9, summarises the main conclusions extracted in the present Thesis and discusses the prospect of extending the developed method for the study of dark matter physics and specifically (WIMP-nucleus processes), charged lepton flavour violating processes (muon-to-electron conversion in nuclei) as well as double charge exchanging processes (neutrinoless double-beta decay).

Eventually, the Appendices review the adopted notations and conventions as well as the required additional information and details related to the present study are included. Before closing, an extensive and modern Bibliography is also presented.

Chapter 2

The Standard Model and beyond

2.1 Introduction

In this Chapter we will review the main features of the Standard Model (SM) setting the framework on which, all aspects beyond the SM addressed in the present Thesis to be accommodated. Within the SM, the strong, electromagnetic, and weak interactions of elementary particles are described in the context of quantum field theory that consists of three sectors: quantum chromodynamics (QCD) to account for strong interactions, and quantum electrodynamics (QED) which involves the electromagnetic and weak forces, as introduced firstly by Weinberg [1], Glashow [2] and Salam [3]. Its main principle is gauge invariance which puts together in the same framework the matter particles, their interactions as well as the gauge vector bosons that mediate them. The SM is based on the local symmetry group $SU(3)_c \otimes SU(2)_L \otimes U(1)_Y$, with c , L and Y being the colour, left-handed chirality and weak hypercharge respectively, assuming that the interactions and the number of vector gauge bosons that correspond to the generators of the group are determined in a unique way. There are eight massless gluons, corresponding to the eight generators of $SU(3)_c$, that mediate strong interactions and four gauge bosons; three massive (W^\pm and Z) and one massless (γ), that correspond to the three generators of $SU(2)_L$ and the one generator of $U(1)_Y$, to mediate the electroweak interactions, while the fermions are assigned to the fundamental representations of the group.

2.2 Standard electroweak model

The electroweak interactions, based on the $SU(2)_L \otimes U(1)_Y$ part of the SM symmetry group, can be studied independently of the strong interactions since the symmetry under the colour group is unbroken, and thus, only $SU(2)_L$ and $U(1)_Y$ get mixed up in the process of symmetry breaking (there is no mixing

between $SU(3)_c$ and $SU(2)_L \otimes U(1)_Y$ sectors). The symmetry group $SU(2)_L$ is called weak isospin. The subscript, L , indicates that the elements of the group act in a nontrivial way only on the left-handed chiral components of the fermion fields (the right-handed chiral components are singlets under weak isospin transformations) [4]. The group generators, are denoted by T_a , $a = 1, 2, 3$ ¹. The symmetry group $U(1)_Y$, namely the hypercharge group, is generated by the hypercharge operator Y . The two group generators are related to the charge operator, Q , through the Gell-Mann-Nishijima relation

$$Q = T_3 + \frac{Y}{2}. \quad (2.1)$$

2.2.1 Gauge bosons

To satisfy local gauge invariance, the four gauge bosons characterising the electroweak sector of the SM are categorised into three vector gauge boson fields W_μ^i ($i = 1, 2, 3$ one for each generator $T_i = \tau_i/2$) that transform as the adjoint representation of $SU(2)_L$ and one vector gauge boson field B_μ associated with the generator, Y , of $U(1)_Y$. The latter are written in terms of the coupling constant g of $SU(2)_L$, the coupling constant g' of $U(1)_Y$, and the completely antisymmetric three dimensional tensor ϵ_{abc} , as [5]

$$\begin{aligned} W_{\mu\nu}^a &= \partial_\mu W_\nu^a - \partial_\nu W_\mu^a - g\epsilon_{abc}W_\mu^bW_\nu^c, \\ B_{\mu\nu} &= \partial_\mu B_\nu - \partial_\nu B_\mu. \end{aligned} \quad (2.2)$$

Then, the kinetic part of the electroweak Lagrangian being invariant under the separate local gauge transformations of $SU(2)_L$ and $U(1)_Y$, takes the compact form

$$\mathcal{L}_G = -\frac{1}{4}W_{\mu\nu}^aW_a^{\mu\nu} - \frac{1}{4}B_{\mu\nu}B^{\mu\nu}. \quad (2.3)$$

The gauge boson fields transform as

$$\begin{aligned} W_\mu^a \frac{\tau^a}{2} &\rightarrow W_\mu'^a \frac{\tau^a}{2} = U_L W_\mu^a \frac{\tau^a}{2} U_L^{-1} + \frac{i}{g} \partial_\mu U_L U_L^{-1}, \\ B_\mu &\rightarrow B_\mu' = B_\mu + \frac{i}{g'} \partial_\mu U_Y U_Y^{-1}, \end{aligned} \quad (2.4)$$

with

$$U_L = e^{i\alpha^a \frac{\tau^a}{2}}, \quad U_Y = e^{i\alpha_Y}, \quad \alpha^a \equiv \alpha(x)^a, \quad (2.5)$$

and τ^a being the Pauli matrices for isospin. For infinitesimal transformations, Eqs.(2.4) reduce to

$$\begin{aligned} \delta W_\mu^a &= -\epsilon^{abc} \alpha^b W_\mu^c - \frac{1}{g} \partial_\mu \alpha^a, \\ \delta B_\mu &= -\frac{1}{g'} \partial_\mu \alpha_Y. \end{aligned} \quad (2.6)$$

¹They satisfy the angular momentum commutation relations $[T_a, T_b] = i\epsilon_{abc}T_c$.

It should be noted that, boson self-couplings enter the Lagrangian (2.3), a conclusion being in agreement to what one would expect by recalling the non-Abelian nature of the $SU(2)_L$ group [5].

2.2.2 Matter fields

It is well-known that, within the SM the matter fields (leptons and quarks) are of fermionic nature and are classified into three generations. For the sake of convenience we distinguish the left and right helicity states as

$$\begin{aligned}\psi_L &= \frac{1 - \gamma^5}{2} \psi, \\ \psi_R &= \frac{1 + \gamma^5}{2} \psi,\end{aligned}\tag{2.7}$$

where the left-handed components are grouped into weak isospin doublets under the $SU(2)_L$ group while the right-handed components transform as singlets. In the SM, it is assumed that the neutrino fields have only left-handed components which furthermore implies that neutrinos are massless. For instance, the first generation matter fields are shown below

$$L_L = \begin{pmatrix} \nu_e \\ e^- \end{pmatrix}_L \equiv \begin{pmatrix} \nu_{eL} \\ e_L^- \end{pmatrix}, \quad Q_L = \begin{pmatrix} u \\ d \end{pmatrix}_L \equiv \begin{pmatrix} u_L \\ d_L \end{pmatrix}, \quad e_R^-, u_R, d_R.\tag{2.8}$$

Their transformation under finite local gauge transformation reads

$$\begin{aligned}\psi_L &\rightarrow \psi'_L = e^{i\alpha^a \frac{\tau^a}{2}} e^{i\alpha_Y \frac{Y}{2}} \psi_L, \\ \psi_R &\rightarrow \psi'_R = e^{i\alpha_Y \frac{Y}{2}} \psi_R.\end{aligned}\tag{2.9}$$

The principle of gauge invariance establishes that the component of the Lagrangian that describes the gauge interactions of the fermions, is obtained from the kinetic energy part of the Lagrangian, \mathcal{L}_G , after substituting the derivative by the covariant derivative [5]

$$\begin{aligned}\partial_\mu \psi_L &\rightarrow D_\mu \psi_L = \left(\partial_\mu + ig \frac{\tau^a}{2} W_\mu^a + ig' \frac{Y}{2} B_\mu \right) \psi_L, \\ \partial_\mu \psi_R &\rightarrow D_\mu \psi_R = \left(\partial_\mu + ig' \frac{Y}{2} B_\mu \right) \psi_R.\end{aligned}\tag{2.10}$$

The latter leads to the conclusion that the covariant derivatives have indeed the appropriate transformation properties, i.e.

$$\begin{aligned}D_\mu \psi_L &\rightarrow D_\mu \psi'_L = e^{i\alpha^a \frac{\tau^a}{2}} e^{i\alpha_Y \frac{Y}{2}} D_\mu \psi_L, \\ D_\mu \psi_R &\rightarrow D_\mu \psi'_R = e^{i\alpha_Y \frac{Y}{2}} D_\mu \psi_R.\end{aligned}\tag{2.11}$$

After symmetry breaking, by performing a rotation in the plane of the neutral gauge bosons W_μ^3 and B_μ through an angle θ_W (the weak mixing angle, also called the Weinberg angle), they mix giving a massless photon A_μ and one massive field Z_μ , as

$$\begin{aligned} W_\mu^3 &= \sin \theta_W A_\mu + \cos \theta_W Z_\mu, \\ B_\mu &= \cos \theta_W A_\mu - \sin \theta_W Z_\mu, \end{aligned} \quad (2.12)$$

with

$$e = g, \quad \sin \theta_W = g' \cos \theta_W, \quad \frac{g'}{g} = \tan \theta_W. \quad (2.13)$$

The field, W_μ , that annihilates W^+ bosons and creates W^- bosons, is defined as

$$W_\mu^\pm = \frac{W_\mu^1 \mp iW_\mu^2}{\sqrt{2}}. \quad (2.14)$$

Then, the covariant derivative for left- and right-handed fields can be cast in the more convenient form

$$\begin{aligned} D_\mu \psi_L &= \partial_\mu \psi_L + i \left[\frac{g}{\sqrt{2}} \begin{pmatrix} 0 & W_\mu^+ \\ 0 & 0 \end{pmatrix} + \frac{g}{\sqrt{2}} \begin{pmatrix} 0 & 0 \\ W_\mu^- & 0 \end{pmatrix} \right. \\ &\quad \left. + \frac{g}{\cos \theta_W} (T_3 - \sin^2 \theta_W) Z_\mu + eQ A_\mu \right] \psi_L, \\ D_\mu \psi_R &= \partial_\mu \psi_R + i \left[-\frac{g}{\cos \theta_W} \sin^2 \theta_W Q Z_\mu + eQ A_\mu \right] \psi_R, \end{aligned} \quad (2.15)$$

where Q is the charge (with respect to the elementary charge e) defined according to the charge operator in Eq.(2.1). Therefore, the kinetic Lagrangian for the fermion fields that is invariant under local gauge transformations reads (mixing among quarks are neglected)

$$\begin{aligned} \mathcal{L}_f^{\text{kinetic}} &= \sum_{\text{doublets}} i\bar{\psi}_L \gamma^\mu D_\mu \psi_L + \sum_{\text{singlets}} i\bar{\psi}_R \gamma^\mu D_\mu \psi_R \\ &= \sum_f i\bar{\psi}_f \gamma^\mu \partial_\mu \psi_f \\ &\quad - e \sum_f Q_f \bar{\psi}_f \gamma^\mu \psi_f A_\mu - \frac{g}{2 \cos \theta_W} \sum_f \bar{\psi}_f \gamma^\mu (g_V^f - g_A^f \gamma_5) \psi_f Z_\mu \\ &\quad - \frac{g}{2\sqrt{2}} \sum_{\text{doublets}} \bar{\psi}_u \gamma^\mu (1 - \gamma_5) \psi_d W_\mu^+ - \frac{g}{2\sqrt{2}} \sum_{\text{doublets}} \bar{\psi}_d \gamma^\mu (1 - \gamma_5) \psi_u W_\mu^-, \end{aligned} \quad (2.16)$$

where the last two terms involve summations over all doublets of the theory defined as

$$\psi_L = \begin{pmatrix} \psi_u \\ \psi_d \end{pmatrix}_L \equiv \begin{pmatrix} \nu_e \\ e^- \end{pmatrix}_L, \quad \begin{pmatrix} u \\ d \end{pmatrix}_L, \dots \quad (2.17)$$

Fermions	g_L^f	g_R^f	g_V^f	g_A^f
ν_e, ν_μ, ν_τ	$\frac{1}{2}$	0	$\frac{1}{2}$	$\frac{1}{2}$
e, μ, τ	$-\frac{1}{2} + s_W^2$	s_W^2	$-\frac{1}{2} + 2s_W^2$	$-\frac{1}{2}$
u, c, t	$\frac{1}{2} - \frac{2}{3}s_W^2$	$-\frac{2}{3}s_W^2$	$\frac{1}{2} - \frac{4}{3}s_W^2$	$\frac{1}{2}$
d, s, b	$-\frac{1}{2} - \frac{1}{3}s_W^2$	$-\frac{1}{3}s_W^2$	$-\frac{1}{2} + \frac{2}{3}s_W^2$	$-\frac{1}{2}$

Table 2.1: Fundamental couplings of the SM fermion fields to the Z -boson in terms of the weak mixing angle defined as $\sin^2 \theta_W \equiv s_W^2$.

In general, the coupling of a left- and right-handed SM fermion field f to the Z -boson is given by

$$g_L^f = T_3^f - Q_f \sin^2 \theta_W, \quad (2.18)$$

$$g_R^f = -Q_f \sin^2 \theta_W. \quad (2.19)$$

The corresponding vector and axial vector couplings read

$$g_V^f = g_L^f + g_R^f = T_3^f - 2Q_f \sin^2 \theta_W, \quad (2.20)$$

$$g_A^f = g_L^f - g_R^f = T_3^f, \quad (2.21)$$

where T_3^f is the third component of the weak isospin and Q_f the fermion charge. For the fermion fields, the corresponding values of g_L , g_R , g_V and g_A are listed in Table 2.1.

2.2.3 Neutral-current neutrino-lepton interactions

Focusing on the leptonic sector, and by assuming the diagonal parts of the interaction Lagrangian given in Eq.(2.16) we get the neutral-current (NC) interaction Lagrangian, which may be decomposed as

$$\mathcal{L}_{NC} = \mathcal{L}_\gamma + \mathcal{L}_Z. \quad (2.22)$$

The electromagnetic interactions are involved in the first term, written in terms of the elementary charge, e , and the electromagnetic field, A^μ , as follows

$$\mathcal{L}_\gamma = -e j_\gamma^\mu A_\mu, \quad (2.23)$$

with

$$j_\gamma^\mu = -\bar{e} \gamma^\mu e. \quad (2.24)$$

Neutrinos do not couple to the electromagnetic field since they are neutral particles. The second term in Eq.(2.22) is recognised as the leptonic weak NC Lagrangian and takes the form ²

$$\mathcal{L}_Z = -\frac{g}{2 \cos \theta_W} j_Z^\mu Z_\mu, \quad (2.25)$$

²Unless otherwise mentioned for the rest of the Thesis when we refer to the NC Lagrangian we will always assume that $\mathcal{L}_{NC} \equiv \mathcal{L}_Z$.

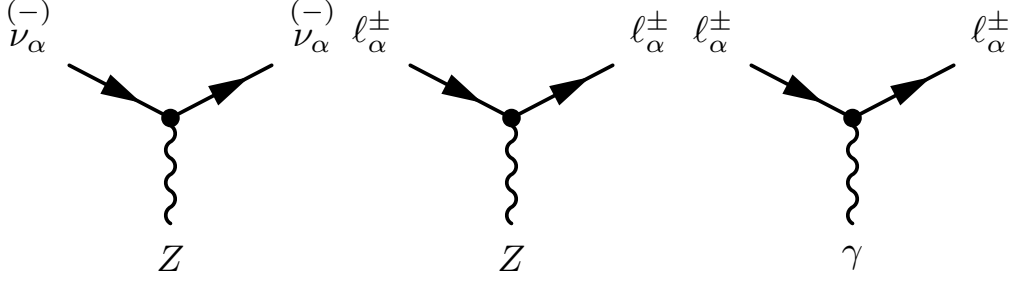


Figure 2.1: Weak interaction neutral-current diagrams demonstrating graphically the trilinear couplings arising from Lagrangian (2.22) (generalised to the three lepton generations).

where the associated leptonic weak NC reads

$$\begin{aligned} j_Z^\mu &= 2g_L^\nu \bar{\nu}_{eL} \gamma^\mu \nu_{eL} + 2g_L^l \bar{e}_L \gamma^\mu e_L + 2g_R^l \bar{e}_R \gamma^\mu e_R \\ &= \bar{\nu}_e \gamma^\mu (g_V^\nu - g_A^\nu \gamma_5) \nu_e + \bar{e} \gamma^\mu (g_V^l - g_A^l \gamma_5) e. \end{aligned} \quad (2.26)$$

In order to include the three lepton generations (see Table 2.2), we may generalise our discussion by writing the leptonic NC as

$$j_Z^\mu = 2g_L^\nu \sum_{\alpha=e,\mu,\tau} \bar{\nu}_{\alpha L} \gamma^\mu \nu_{\alpha L} + 2 \sum_{\alpha=e,\mu,\tau} (g_L^l \bar{l}_{\alpha L} \gamma^\mu l_{\alpha L} + g_R^l \bar{l}_{\alpha R} \gamma^\mu l_{\alpha R}). \quad (2.27)$$

The above expression can be cast in the more convenient form

$$j_Z^\mu = \frac{1}{2} \sum_{\alpha=e,\mu,\tau} \bar{\nu}_\alpha \gamma^\mu (1 - \gamma_5) \nu_\alpha = \sum_{\alpha=e,\mu,\tau} \bar{\nu}_{\alpha L} \gamma^\mu \nu_{\alpha L}, \quad (2.28)$$

with $\alpha = \{e, \mu, \tau\}$ being the neutrino flavour. Here, for simplicity we have not shown the contribution due to charged leptons. The corresponding Feynman diagrams are shown in Fig. 2.1.

2.2.4 Charged-current neutrino-lepton interactions

For the sake of completeness, we mention that the off-diagonal parts of the interaction Lagrangian given in Eq.(2.16) give rise to the charged-current (CC) interaction Lagrangian

$$\begin{aligned} \mathcal{L}_{CC} \equiv \mathcal{L}_W &= -\frac{g}{2\sqrt{2}} \bar{\nu}_e \gamma^\mu (1 - \gamma_5) e W_\mu + \text{h.c.} \\ &= -\frac{g}{2\sqrt{2}} j_{W,L}^\mu W_\mu + \text{h.c.}, \end{aligned} \quad (2.29)$$

where the leptonic CC is defined as

$$j_{W,L}^\mu \equiv \bar{\nu}_e \gamma^\mu (1 - \gamma_5) e = 2\bar{\nu}_{eL} \gamma^\mu e_L. \quad (2.30)$$

generation	particle	antiparticle	L_e	L_μ	L_τ
1 st	e^-	e^+	+1 (-1)	0	0
	ν_e	$\bar{\nu}_e$	+1 (-1)	0	0
2 nd	μ^-	μ^+	0	+1 (-1)	0
	ν_μ	$\bar{\nu}_\mu$	0	+1 (-1)	0
3 rd	τ^-	τ^+	0	0	+1 (-1)
	ν_τ	$\bar{\nu}_\tau$	0	0	+1 (-1)

Table 2.2: Summary Table of the three generations of leptons, including the lepton numbers of the particles. The lepton number of the antiparticles is shown within the brackets. Each of the three generations forms an SU(2) doublet.

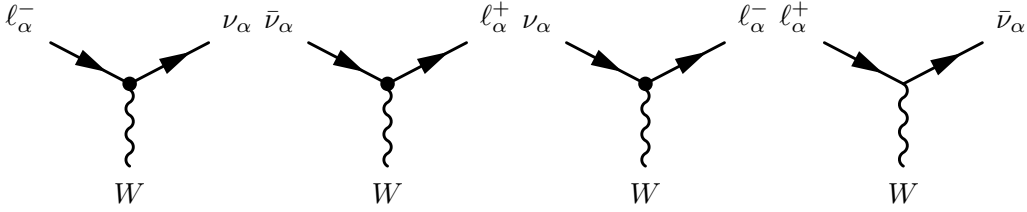


Figure 2.2: Weak interaction charged-current diagrams demonstrating graphically the trilinear couplings arising from (generalised to the three lepton generations) Lagrangian (2.29). The first two originate from Eq.(2.32) while the second two from the corresponding hermitian conjugate current.

The corresponding hermitian conjugated leptonic CC reads

$$j_{W,L}^{\mu\dagger} \equiv \bar{e} \gamma^\mu (1 - \gamma_5) \nu_e = 2 \bar{e}_L \gamma^\mu \nu_{eL}. \quad (2.31)$$

Analogously to the NC case, incorporating the previous lines in order to extend the formalism and taking into account the three lepton generations, the corresponding CC weak lepton currents can be trivially obtained through Eq.(2.30), as

$$j_{W,L}^\mu \equiv \sum_{\alpha=e,\mu,\tau} \bar{\nu}_\alpha \gamma^\mu (1 - \gamma_5) \ell_\alpha = 2 \sum_{\alpha=e,\mu,\tau} \bar{\nu}_\alpha \gamma^\mu \ell_\alpha, \quad (2.32)$$

with $\ell_\alpha = \{e^-, \mu^-, \tau^-\}$ denoting the charged leptons that correspond to the neutrino flavour α . The associated Feynman diagrams are shown in Fig. 2.2.

2.2.5 Mass generation

Up to this point, all fermions and gauge bosons are considered to be massless. Indeed, the invariant under $SU(3)_c \otimes SU(2)_L \otimes U(1)_Y$ Lagrangian (2.16) does not

Higgs doublet	ϕ^+	ϕ^0
T_3	$\frac{1}{2}$	$-\frac{1}{2}$
Y	1	1
Q	1	0

Table 2.3: Higgs doublet eigenvalues of the third component of the weak isospin T_3 , the hypercharge Y , and the charge Q with respect to the SM gauge group $SU(3)_c \otimes SU(2)_L \otimes U(1)_Y$.

contain any mass term, since the left- and right-handed components of the fermion fields transform differently under the gauge group. Moreover, there is no mass term for the gauge bosons compatible with the symmetry. In addition, it is impossible to add fermion and gauge bosons “by hand” because it would lead to gauge invariance breaking.

The Higgs mechanism (also called the Englert-Brout-Higgs-Guralnik-Hagen-Kibble mechanism) [6–8], is the relativistic extension of the spontaneous symmetry breaking theory [9], which introduces masses preserving the gauge invariance of the Lagrangian. In this context, a spontaneously broken symmetry is preserved by the Lagrangian, but it is not a symmetry of the ground state of the system. Thus, an $SU(2)_L$ scalar doublet Φ is introduced

$$\Phi(x) = \begin{bmatrix} \phi^+(x) \\ \phi^0(x) \end{bmatrix}, \quad (2.33)$$

where $\phi^+(x)$ and $\phi^0(x)$ are charged complex and neutral complex scalar fields respectively with the quantum numbers shown in Table 2.3.

We proceed our discussion, by writing the Lagrangians

$$\begin{aligned} \mathcal{L}_H &= (\mathcal{D}_\mu \Phi)^\dagger (\mathcal{D}_\mu \Phi) - \mu^2 \Phi^\dagger \Phi - \lambda (\Phi^\dagger \Phi)^2, \\ \mathcal{L}_{\text{Yuk}} &= - \sum_{ij} \left[Y_{ij}^\ell \bar{\ell}'_{iL} \Phi \ell'_{jR} + Y_{ij}^u \bar{u}'_{iL} \tilde{\Phi} u'_{jR} + Y_{ij}^d \bar{d}'_{iL} \Phi d'_{jR} + \text{h.c.} \right], \end{aligned} \quad (2.34)$$

where $\tilde{\Phi} = i\sigma_2 \Phi^*$ is a doublet with $Y = -1$ in order to make the Yukawa Lagrangian invariant under the gauge group. The coefficient of the quartic self-couplings of the Higgs fields must be positive, $\lambda > 0$, while the squared mass-like coefficient must be negative, $\mu^2 < 0$ so that the potential

$$V(\Phi) = \mu^2 \Phi^\dagger \Phi + \lambda (\Phi^\dagger \Phi)^2, \quad (2.35)$$

is bounded from below. By defining

$$v \equiv \sqrt{-\frac{\mu^2}{\lambda}}, \quad (2.36)$$

and neglecting the (irrelevant) constant term, $v^4/4$, the Higgs potential can be written in the form

$$V(\Phi) = \lambda \left(|\Phi|^2 - \frac{v^2}{2} \right)^2, \quad |\Phi|^2 \equiv \Phi^\dagger \Phi. \quad (2.37)$$

In a quantised theory, this leads to the appearance of a non-zero vacuum expectation value of Φ , as

$$\langle |\Phi| \rangle = \frac{v}{\sqrt{2}} = \sqrt{-\frac{\mu^2}{2\lambda}}. \quad (2.38)$$

Following Ref. [5], the prime notation for ℓ' , u' , d' is introduced in order to avoid confusion of the aforementioned weak eigenstates with the mass eigenstates that will be discussed below. The relevant covariant derivative reads

$$\begin{aligned} D_\mu &= \left[\partial_\mu + i \frac{g}{\sqrt{2}} (\tau^+ W_\mu^+ + \tau^- W_\mu^-) + i \frac{g}{2} \tau_3 W_\mu^3 + i \frac{g'}{2} B_\mu \right] \Phi \\ &= \left[\partial_\mu + i \frac{g}{\sqrt{2}} (\tau^+ W_\mu^+ + \tau^- W_\mu^-) + ieQA_\mu \right. \\ &\quad \left. + i \frac{g}{\cos \theta_W} \left(\frac{\tau_3}{2} - Q \sin^2 \theta_W \right) Z_\mu \right] \Phi. \end{aligned} \quad (2.39)$$

One can perturbatively expand Φ around one of the continuous set of true vacua, by parametrising the scalar field in terms of the three fields θ^a and H . According to the Goldstone theorem [10, 11], if the $SU(2)_L$ symmetry was a global symmetry of the Lagrangian, then θ^a would correspond to physical fields with vanishing mass. To gauge away the fields θ^a , it is convenient to adopt the unitary gauge (physical gauge) in which the physical states of the theory appear explicitly. To this purpose, the following transformations are used

$$\begin{aligned} \Phi(x) &\rightarrow \Phi'(x) = \exp \left(-i \frac{\theta^a(x) \tau^a}{v} \right) \Phi = \frac{1}{\sqrt{2}} \begin{bmatrix} 0 \\ v + H(x) \end{bmatrix}, \\ W_\mu^a &\rightarrow W_\mu'^a, \\ B_\mu &\rightarrow B'_\mu = B_\mu. \end{aligned} \quad (2.40)$$

By combining Eq.(2.34) with Eq.(2.40) and rotating the gauge bosons through Eq.(2.12) we arrive at the result

$$\begin{aligned} \mathcal{L}_H &= \frac{1}{2} (\partial_\mu H)^2 - \frac{1}{2} M_H^2 H^2 - \frac{1}{4} \lambda H^4 - \lambda v H^3 + \frac{1}{2} v g^2 W_\mu^+ W^{-\mu} H \\ &\quad + \frac{1}{4} v \frac{g^2}{\cos \theta_W} Z_\mu Z^\mu H + \frac{1}{4} g^2 W_\mu^+ W^{-\mu} H^2 + \frac{1}{8} \frac{g^2}{\cos \theta_W} Z_\mu Z^\mu H^2 \\ &\quad + \frac{1}{2} M_Z^2 Z_\mu Z^\mu + M_W^2 W_\mu^+ W^{-\mu} + \lambda \frac{v^4}{4}, \end{aligned} \quad (2.41)$$

with the masses M_W , M_Z , M_H given by

$$M_W = \frac{v}{2}g, \quad M_Z = \frac{v}{2}\sqrt{g^2 + g'^2} = \frac{M_W}{\cos\theta_W}, \quad M_H = \sqrt{-2\mu^2} = \sqrt{2\lambda v^2}. \quad (2.42)$$

Therefore, after spontaneous symmetry breaking, the fields Z and A are the physical mass eigenstates, while the photon remains massless since electromagnetism remains unbroken because the electric charge must be exactly conserved.

In the unitary gauge, the Yukawa Lagrangian is written as

$$\begin{aligned} \mathcal{L}_{\text{Yuk}} = & - \sum_{ij} \left[\bar{\ell}'_{iL} M_{ij}^\ell \ell'_{jR} + \bar{u}'_{iL} M_{ij}^u u'_{jR} + \bar{d}'_{iL} M_{ij}^d d'_{jR} \right. \\ & \left. + \frac{H}{\sqrt{2}} \bar{\ell}'_{iL} Y_{ij}^\ell \ell'_{jR} + \frac{H}{\sqrt{2}} \bar{u}'_{iL} Y_{ij}^u u'_{jR} + \frac{H}{\sqrt{2}} \bar{d}'_{iL} Y_{ij}^d d'_{jR} + \text{h.c.} \right], \end{aligned} \quad (2.43)$$

where the corresponding masses read

$$M_{ij}^\ell = Y_{ij}^\ell \frac{v}{2}, \quad M_{ij}^u = Y_{ij}^u \frac{v}{2}, \quad M_{ij}^d = Y_{ij}^d \frac{v}{2}. \quad (2.44)$$

By introducing the unitary matrices U_{ij}^f , the weak eigenstates are related to the mass eigenstates as follows

$$\begin{aligned} \ell_{iL} &= U_{Lij}^\ell \ell'_{jL}, & u_{iL} &= U_{Lij}^u u'_{jL}, & d_{iL} &= U_{Lij}^d d'_{jL}, \\ \ell_{iR} &= U_{Rij}^\ell \ell'_{jR}, & u_{iR} &= U_{Rij}^u u'_{jR}, & d_{iR} &= U_{Rij}^d d'_{jR}. \end{aligned} \quad (2.45)$$

We stress, however, that neutrinos remain massless since the SM does not contain right-handed neutrinos and we cannot write down any mass term. Then, the Yukawa Lagrangian can be cast in the form

$$\mathcal{L}_{\text{Yuk}} = - \sum_i \left[m_i^\ell \bar{\ell}_i \ell_i + m_i^u \bar{u}_i u_i + m_i^d \bar{d}_i d_i \right] + \dots, \quad (2.46)$$

with m_i^f being the physical fermion masses.

Within this framework, the charged-current Lagrangian that contains the physical mass eigenstates takes the form

$$\mathcal{L}_{CC} = - \frac{g}{2\sqrt{2}} \bar{u}_i \gamma^\mu (1 - \gamma_5) V_{ij}^{\text{CKM}} d_j W_\mu^+ + \text{h.c.}, \quad (2.47)$$

where

$$V^{\text{CKM}} = U_L^u U_L^{d\dagger} \quad (2.48)$$

is the so-called Cabibbo-Kobayashi-Maskawa matrix [12, 13].

The NC interaction couples fermions with the same electroweak charges and therefore it holds $U^f U^{f\dagger} = 1$. Thus, the corresponding NC Lagrangian, remains flavour-diagonal and reads

$$\mathcal{L}_{NC} = -e \sum_f Q_f \bar{\psi}_f \gamma^\mu A_\mu - \frac{g}{2\cos\theta_W} \sum_f \bar{\psi}_f \left(g_V^f - g_A^f \gamma_5 \right) \psi_f Z_\mu. \quad (2.49)$$

This notable result implies that within the SM, flavour changing neutral-current (FCNC) interactions are absent. This mechanism has been established long ago by Glashow-Iliopoulos-Maiani and it is well-known as the GIM mechanism [14].

2.3 Effective low-energy CC and NC Lagrangians

In the present Thesis, we are mainly interested in phenomena for which the energy involved is much lower than the masses of W and Z gauge bosons, an approximation which is also referred to as the low-energy regime (energies $\ll M_W$ and energies $\ll M_Z$). In this case the exact propagators of the W and Z boson fields [15, 16]

$$\begin{aligned} G_{\mu\nu}^W(x-x') &= \langle 0|T[W_\mu(x)W_\nu^\dagger(x')] |0\rangle = \lim_{\epsilon \rightarrow 0} i \int \frac{d^4p}{(2\pi)^4} \frac{-g_{\mu\nu} + \frac{p_\mu p_\nu}{M_W^2}}{p^2 - M_W^2 + i\epsilon} e^{-ip \cdot (x-x')}, \\ G_{\mu\nu}^Z(x-x') &= \langle 0|T[Z_\mu(x)Z_\nu(x')] |0\rangle = \lim_{\epsilon \rightarrow 0} i \int \frac{d^4p}{(2\pi)^4} \frac{-g_{\mu\nu} + \frac{p_\mu p_\nu}{M_Z^2}}{p^2 - M_Z^2 + i\epsilon} e^{-ip \cdot (x-x')}, \end{aligned} \quad (2.50)$$

for low momentum transfer can be well-approximated by

$$G_{\mu\nu}^W(p) = \xrightarrow{|k|^2 \ll M_W^2} i \frac{g_{\mu\nu}}{m_W^2}, \quad G_{\mu\nu}^Z(p) = \xrightarrow{|k|^2 \ll M_Z^2} i \frac{g_{\mu\nu}}{m_Z^2}. \quad (2.51)$$

This means, that the internal boson lines in the relevant Feynman diagrams can be contracted to a point, leading to the known effective four-fermion Fermi contact interaction. The graphical illustration of the latter approximation is shown in Figs. 2.3 and 2.4 for CC and NC processes respectively.

Specifically, for the case of CC processes the effective current-current Lagrangian is written in terms of the Fermi constant G_F , as

$$\mathcal{L}_{\text{CC}}^{\text{eff}} = -\frac{G_F}{\sqrt{2}} j_{W\mu}^\dagger j_W^\mu, \quad (2.52)$$

where

$$\frac{G_F}{\sqrt{2}} = \frac{g^2}{8M_W^2}. \quad (2.53)$$

In an analogous way, the NC low-energy Lagrangian is written as

$$\mathcal{L}_{\text{NC}}^{\text{eff}} = -\frac{G_F}{\sqrt{2}} j_{Z\mu} j_Z^\mu, \quad (2.54)$$

with

$$2\rho \frac{G_F}{\sqrt{2}} = \frac{g^2}{4 \cos^2 \theta_W M_Z^2}. \quad (2.55)$$

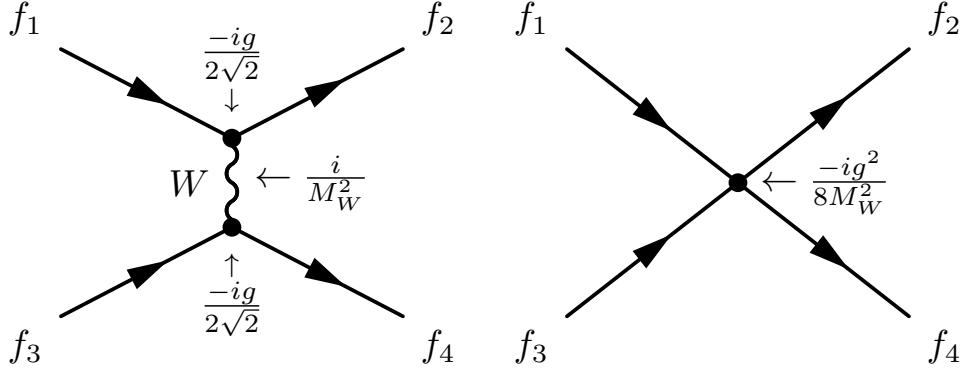


Figure 2.3: Point contraction of the W gauge propagator for low-energy charged-current processes involving generic fermions f_i .

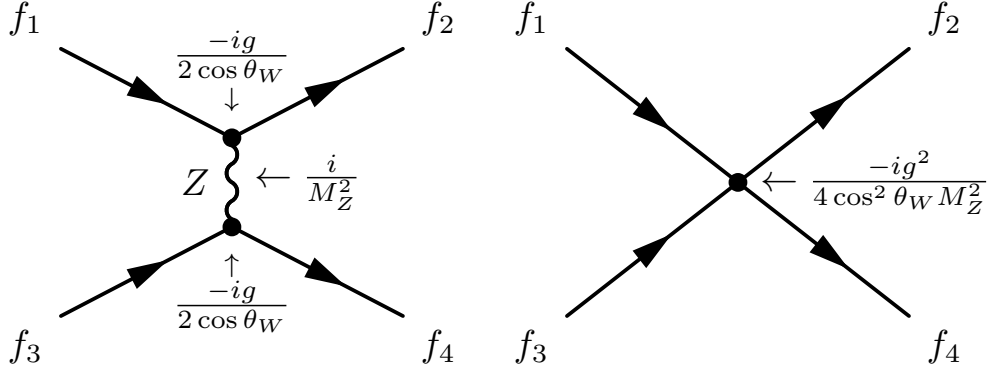


Figure 2.4: Point contraction of the Z gauge propagator for low-energy neutral-current processes involving generic fermions f_i .

The parameter, ρ , is defined as

$$\rho = \frac{M_W^2}{M_Z^2 \cos^2 \theta_W} \quad (2.56)$$

which, within the SM is set equal to unity, i.e. $\rho = 1$.

The Fermi constant can be also written in terms of the fine structure constant $a_{em} = e^2/4\pi$, the weak mixing-angle, θ_W , and the W (or Z) gauge boson mass, according to the relation

$$\frac{G_F}{\sqrt{2}} = \frac{\pi a_{em}}{2 \sin^2 \theta_W M_W^2} = \frac{\pi a_{em}}{2 \sin^2 \theta_W \cos^2 \theta_W M_Z^2}. \quad (2.57)$$

In the latter expressions we used the fact that $M_W^2 = \cos \theta_W M_Z^2$.

2.4 Standard and non-standard neutrino-electron interactions

The experimental confirmation of the existence of NC interactions was first established in 1973 through the observation of the $\bar{\nu}_\mu + e^- \rightarrow \bar{\nu}_\mu + e^-$ process in the Gargamelle experiment [17]. In this Section we review the basic formalism needed to describe the elastic NC interactions within the SM and we discuss briefly potential contributions to this process originating due to non-standard interactions beyond the SM, namely NSI. We stress that, these processes play key role in solar neutrino searches using water Cherenkov detectors.

At low-energies, neutrinos (or antineutrinos) of flavour $\alpha = \{e, \mu, \tau\}$ interact weakly with electrons through the elastic scattering process

$$\nu_\alpha + e^- \rightarrow \nu_\alpha + e^- . \quad (2.58)$$

For the case of electron-neutrinos, ν_e , this process receives contributions from both CC and NC interactions, while for ν_μ and ν_τ only the relevant NC diagram contributes.

2.4.1 SM neutrino-electron cross sections

In the picture of neutrino scattering, from the constituents of strongly bound systems like the nucleons inside a nucleus (see Subsect. 2.5.2), the scattering of neutrinos from point-like particles (e.g. electrons) will serve as a benchmark for our main study presented in the main research Chapters (see Chapt. 4–8).

After performing a Fierz reordering, the effective low-energy Lagrangian of Eq.(2.16) for $\nu_e e^-$ scattering is written as

$$\mathcal{L}_{eff}^{\text{CC+NC}} = -\frac{G_F}{\sqrt{2}} [\bar{\nu}_e \gamma^\mu (1 - \gamma_5) \nu_e] [\bar{e} \gamma_\mu ((1 + g_V^l) - (1 + g_A^l) \gamma_5) e] . \quad (2.59)$$

For $\nu_{\mu,\tau}$ scattering off electrons the corresponding effective Lagrangian contains only a NC term, as

$$\mathcal{L}_{eff}^{\text{NC}} = -\frac{G_F}{\sqrt{2}} [\bar{\nu}_\alpha \gamma^\mu (1 - \gamma_5) \nu_\alpha] [\bar{e} \gamma_\mu (g_V^l - g_A^l \gamma_5) e] , \quad \alpha = \{e, \mu\} . \quad (2.60)$$

The kinetic energy of the recoil electron, T_e , is one of the most interesting physical quantities measured by relevant experiments. The differential cross section with respect to T_e in the laboratory frame is written as

$$\frac{d\sigma(E_\nu, T_e)}{dT_e} = \frac{\sigma_0}{m_e} \left[g_1^2 + g_2^2 \left(1 - \frac{T_e}{E_\nu} \right)^2 - g_1 g_2 \frac{m_e T_e}{E_\nu^2} \right] , \quad (2.61)$$

where E_ν denotes the incident neutrino energy, m_e is the electron mass and

$$\sigma_0 = \frac{2G_F^2 m_e^2}{\pi} \approx 88.06 \times 10^{-46} \text{ cm}^2. \quad (2.62)$$

The parameters g_1 and g_2 entering the differential cross section of Eq.(2.61) depend on the flavour of the (anti-)neutrino. For ν_e and $\bar{\nu}_e$, we have

$$\begin{aligned} g_1^{(\nu_e)} = g_2^{(\bar{\nu}_e)} &= 1 + \frac{g_V^\ell + g_A^\ell}{2} = 1 + g_L^\ell = \frac{1}{2} + \sin^2 \theta_W, \\ g_2^{(\nu_e)} = g_1^{(\bar{\nu}_e)} &= \frac{g_V^\ell - g_A^\ell}{2} = g_R^\ell = \sin^2 \theta_W, \end{aligned} \quad (2.63)$$

while for $\nu_{\mu,\tau}$ and $\bar{\nu}_{\mu,\tau}$ the corresponding expressions are

$$\begin{aligned} g_1^{(\nu_{\mu,\tau})} = g_2^{(\bar{\nu}_{\mu,\tau})} &= \frac{g_V^\ell + g_A^\ell}{2} = g_L^\ell = -\frac{1}{2} + \sin^2 \theta_W, \\ g_2^{(\nu_{\mu,\tau})} = g_1^{(\bar{\nu}_{\mu,\tau})} &= \frac{g_V^\ell - g_A^\ell}{2} = g_R^\ell = \sin^2 \theta_W. \end{aligned} \quad (2.64)$$

The kinematics of the reaction allow to change variables by expressing the scattering angle, θ , in terms of the electron recoil energy as

$$T_e = \frac{2m_e E_\nu^2 \cos^2 \theta}{(m_e + E_\nu)^2 - E_\nu^2 \cos^2 \theta}, \quad (2.65)$$

and by differentiating we obtain

$$dT_e = \frac{4m_e E_\nu^2 (m_e + E_\nu)^2}{[(m_e + E_\nu)^2 - E_\nu^2 \cos^2 \theta]^2} \cos \theta d \cos \theta. \quad (2.66)$$

Then, the differential cross section with respect to the scattering angle is readily written as

$$\begin{aligned} \frac{d\sigma(E_\nu, \theta)}{d \cos \theta} &= \frac{4\sigma_0 E_\nu^2 (m_e + E_\nu)^2 \cos \theta}{[(m_e + E_\nu)^2 - E_\nu^2 \cos^2 \theta]^2} \left[g_1^2 + g_2^2 \left(1 - \frac{2m_e E_\nu \cos^2 \theta}{(m_e + E_\nu)^2 - E_\nu^2 \cos^2 \theta} \right)^2 \right. \\ &\quad \left. - g_1 g_2 \frac{2m_e^2 \cos^2 \theta}{(m_e + E_\nu)^2 - E_\nu^2 \cos^2 \theta} \right]. \end{aligned} \quad (2.67)$$

From Eq.(2.65), for forward-scattering ($\cos \theta = 1$) the maximum recoil energy, $T_{e\text{max}}$, is

$$T_{e\text{max}}(E_\nu) = \frac{2E_\nu^2}{m_e + 2E_\nu}, \quad (2.68)$$

while the minimum electron energy required to produce a given kinetic energy T_e reads

$$E_{\nu\text{min}} = \frac{T_e}{2} \left(1 + \sqrt{1 + \frac{2m_e}{T_e}} \right) = \begin{cases} \sqrt{m_e T_e/2} & \text{for } T_e \ll m_e, \\ T_e + m_e/2 & \text{for } T_e \gg m_e. \end{cases} \quad (2.69)$$

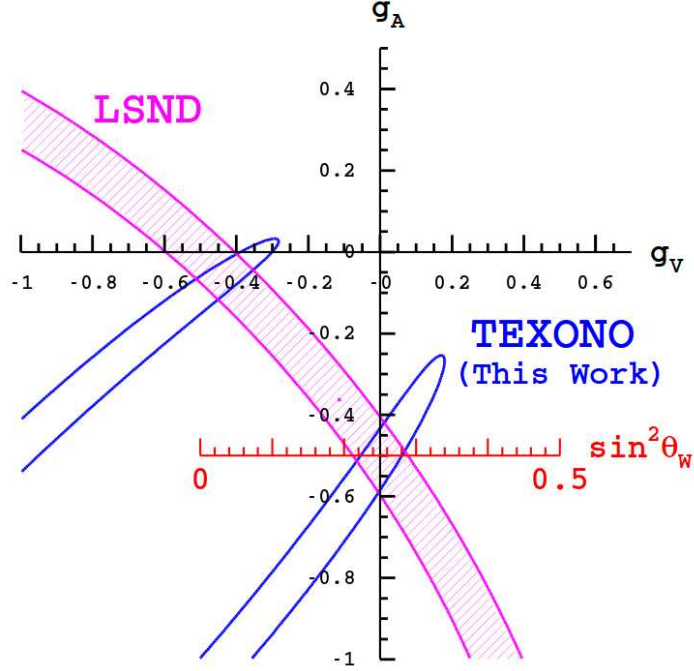


Figure 2.5: Allowed region for 1σ error in the $g_V - g_A$ plane and in the $\sin^2 \theta_W$ axis, extracted from a combined analysis of TEXONO reactor antineutrino and LSND neutrino electron scattering off electrons. (Figure adopted from Ref. [19]).

Neutrino-electron scattering is a purely leptonic process that is exactly evaluated in the electroweak theory. Its experimental cross section measurement with reactor neutrinos provides a new window to study the SM electroweak parameters [18]. Figure 2.5 presents the current status of experimental constraints of the SM parameters in the $g_V - g_A$ plane.

2.4.2 Non-standard neutrino-electron cross sections

Assuming a typical phenomenological Lagrangian at the four-fermion approximation, in principle one can also consider sub-dominant non-standard interactions (NSI) of neutrinos in addition to the SM ones. In this framework, the NC Lagrangian given in Eq.(2.60) will contain an additional part that accounts for NSI, as [20]

$$\mathcal{L}_{eff}^{NSI} = -\frac{G_F}{\sqrt{2}} \sum_{\alpha=e,\mu,\tau} [\bar{\nu}_\alpha \gamma^\mu (1 - \gamma_5) \nu_e] \left([\epsilon_{\alpha e}^{eL} \bar{e} \gamma_\mu (1 - \gamma_5) e] + [\epsilon_{\alpha e}^{eR} \bar{e} \gamma_\mu (1 + \gamma_5) e] \right). \quad (2.70)$$

The parameters $\epsilon_{\alpha e}^{eP}$, $P = \{L, R\}$ represent the left- and right-handed NSI of neutrinos with electrons, and are classified in non-universal (NU) ϵ_{ee}^{eP} and flavour-changing, $\epsilon_{\alpha e}^{eP}$, interactions.

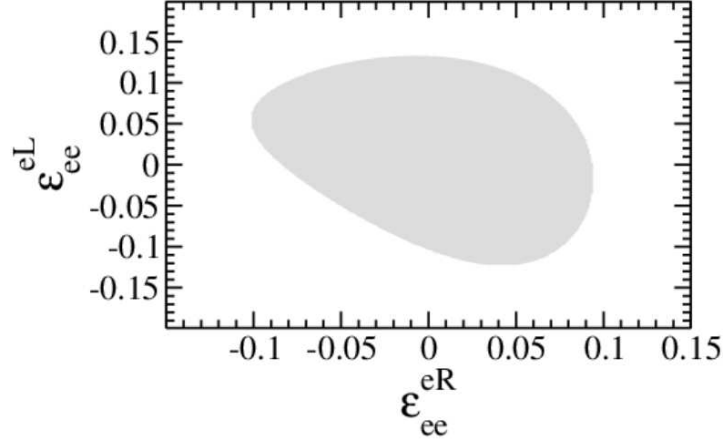


Figure 2.6: Constraints at 90% C.L. on the diagonal NSI parameters ϵ_{ee}^{eL} and ϵ_{ee}^{eR} , extracted from a combined analysis of TEXONO reactor antineutrino and LSND neutrino electron scattering off electrons. (Figure adopted from [24]).

Then, the differential cross section for the process $\nu_e e \rightarrow \nu_\alpha e$ becomes [21]

$$\begin{aligned} \frac{d\sigma(E_\nu, T_e)}{dT} = \frac{\sigma_0}{m_e} & \left[\left(\tilde{g}_L^2 + \sum_{\alpha \neq e} |\epsilon_{\alpha e}^{eL}|^2 \right) + \left(\tilde{g}_R^2 + \sum_{\alpha \neq e} |\epsilon_{\alpha e}^{eR}|^2 \right) \left(1 - \frac{T_e}{E_\nu^2} \right)^2 \right. \\ & \left. - \left(\tilde{g}_L \tilde{g}_R + \sum_{\alpha \neq e} |\epsilon_{\alpha e}^{eL}| |\epsilon_{\alpha e}^{eR}| \right) m_e \frac{T_e}{E_\nu^2} \right], \end{aligned} \quad (2.71)$$

with $\tilde{g}_L = g_1 + \epsilon_{ee}^{eL}$ and $\tilde{g}_R = g_2 + \epsilon_{ee}^{eR}$. Equation (2.71) is used to put upper limits on various NSI parameters [22, 23]. Figure 2.6 shows the most recent constraints on the diagonal NSI parameters ϵ_{ee}^{eL} and ϵ_{ee}^{eR} . For further information and a summary of the current status of the NSI parameters discussed above, the reader is referred to [24]. Motivated by the successful application of NSI in the leptonic sector, in the same spirit extensive details will be presented in Chapt. 5 and 6 for the case of NSI in neutrino-quark and neutrino-nucleon scattering.

2.5 Standard and non standard neutrino-nucleon interactions

2.5.1 Neutrino-nucleon cross sections

For NC coherent elastic neutrino scattering off complex nuclei, a rather detailed analysis focusing on possible alterations of the expected event rates due to NSI is performed in Refs. [25–27]. Motivated by the latter, here we first present an improved formalism and consider NC neutrino-nucleon reactions within the

framework of NSI. The studied processes are of the form

$$\nu_\alpha(\bar{\nu}_\alpha) + n \rightarrow \nu_\beta(\bar{\nu}_\beta) + n, \quad \nu_\alpha(\bar{\nu}_\alpha) + p \rightarrow \nu_\beta(\bar{\nu}_\beta) + p, \quad (2.72)$$

with $\alpha, \beta = \{e, \mu, \tau\}$ being the neutrino flavour. As we will see, these processes are closely related to the neutrino-nucleus scattering studied in Chapt. 4, 5 and 6.

2.5.2 NSI neutrino-nucleon cross sections

The study of the neutrino-nucleon cross sections, starts by writing down the matrix element of the processes (2.72) in the usual $V - A$ form

$$\mathcal{M} = \frac{iG_F}{2\sqrt{2}} j_\mu \langle N | J_Z^\mu | N \rangle = \frac{iG_F}{2\sqrt{2}} \bar{\nu}_\alpha \gamma^\mu (1 - \gamma_5) \nu_\beta \langle N | J_Z^\mu | N \rangle, \quad (2.73)$$

where j_μ (J_Z^μ) denotes the leptonic (hadronic) neutral-current. The hadronic matrix element $\langle N | J_Z^\mu | N \rangle$ (after neglecting the second class currents and the contribution of the pseudoscalar component) is expressed in terms of the well-known nucleon form factors as

$$\langle N | J_Z^\mu | N \rangle = \langle N | F_1^{\text{NC:p(n)}}(Q^2) + F_2^{\text{NC:p(n)}}(Q^2) \frac{i\sigma^{\mu\nu} q_\nu}{2m_N} + F_A^{\text{NC:p(n)}}(Q^2) \gamma^\mu \gamma^5 | N \rangle, \quad (2.74)$$

where $Q^2 = -q^2$ with q^2 being the four momentum transfer. In the latter expression $F_1^{\text{NC:p(n)}}(Q^2)$, $F_2^{\text{NC:p(n)}}(Q^2)$, $F_A^{\text{NC:p(n)}}(Q^2)$ denote the Dirac, Pauli and axial vector weak neutral-current form factors, respectively.

Relying on the above nucleon matrix elements, within the simple relativistic Fermi gas (RFG) model, for example, the SM differential cross section of the reactions (2.72) reads [28]

$$\frac{d\sigma}{dQ^2} = \frac{G_F^2 Q^2}{2\pi E_\nu^2} [A(Q^2) \pm B(Q^2)W + C(Q^2)W^2], \quad (2.75)$$

where the plus (minus) sign accounts for neutrino (antineutrino) scattering and

$$W = \frac{4E_\nu}{m_N} - \frac{Q^2}{m_N^2}. \quad (2.76)$$

(see e.g. Ref. [29]). In the latter expression, for the nucleon mass m_N we assume the value $m_N = 0.938$ GeV.

The form factors $A(Q^2)$, $B(Q^2)$ and $C(Q^2)$ are defined as follows [29]

$$A(Q^2) = \frac{1}{4} \left\{ \left(F_A^{\text{NC:p(n)}} \right)^2 (1 + \tau) - \left[\left(F_1^{\text{NC:p(n)}} \right)^2 - \tau \left(F_2^{\text{NC:p(n)}} \right)^2 \right] (1 - \tau) + 4\tau F_1^{\text{NC:p(n)}} F_2^{\text{NC:p(n)}} \right\}, \quad (2.77)$$

$$B(Q^2) = -\frac{1}{4} F_A^{\text{NC:p(n)}} \left(F_1^{\text{NC:p(n)}} + F_2^{\text{NC:p(n)}} \right),$$

$$C(Q^2) = \frac{m_N^2}{16Q^2} \left[\left(F_A^{\text{NC:p(n)}} \right)^2 + \left(F_1^{\text{NC:p(n)}} \right)^2 + \tau \left(F_2^{\text{NC:p(n)}} \right)^2 \right],$$

where their explicit Q^2 dependence has been suppressed and $\tau = Q^2/4m_N^2$.

As it is well-known, the electromagnetic Dirac and Pauli form factors are written in terms of the electric (E) and magnetic (M) form factors as follows [30]

$$\begin{aligned} F_1^{\text{EM:p(n)}} &= \frac{G_E^{\text{p(n)}}(Q^2) + \tau G_M^{\text{p(n)}}(Q^2)}{1 + \tau}, \\ F_2^{\text{EM:p(n)}} &= \frac{G_M^{\text{p(n)}}(Q^2) - \tau G_E^{\text{p(n)}}(Q^2)}{1 + \tau}. \end{aligned} \quad (2.78)$$

In this work, for the magnetic form factors we adopt the parametrisation of Ref. [31]

$$\frac{G_M^{\text{p(n)}}}{\mu_{\text{p(n)}}} = \frac{1 + \alpha_{\text{p(n),1}}^M \tau}{1 + b_{\text{p(n),1}}^M \tau + b_{\text{p(n),2}}^M \tau^2 + b_{\text{p(n),3}}^M \tau^3}, \quad (2.79)$$

where $\mu_{\text{p(n)}}$ denotes the proton (neutron) magnetic moment. The proton electric form factor in a similar manner can be cast as [32]

$$G_E^{\text{p(n)}} = \frac{1 + \alpha_{\text{p(n),1}}^E \tau}{1 + b_{\text{p(n),1}}^E \tau + b_{\text{p(n),2}}^E \tau^2 + b_{\text{p(n),3}}^E \tau^3}, \quad (2.80)$$

(for the fit parameters see Ref. [31]). The electric neutron form factor is usually expressed through the Galster-like parametrisation

$$G_E^{\text{m}}(Q^2) = \frac{A\tau}{1 + B\tau} G_D(Q^2), \quad (2.81)$$

with $A = 1.68$ and $B = 3.63$.

At this point, regarding the cross sections calculations performed below, we find it useful to devote a separate Subsection and discuss some significant details on the aforementioned form factors $A(Q^2)$, $B(Q^2)$ and $C(Q^2)$.

2.5.3 NSI nucleon form factors

As it is well known, within the SM, the weak NC Dirac and Pauli form factors are written in terms of the electromagnetic current form factors F_i^{EM} , $i = 1, 2$ (assuming the conserved vector current theory) [30]. We furthermore consider additional contributions originating from NSI that enter through the vector-type NSI form factors. The latter could be written in terms of the fundamental NSI neutrino-quark couplings $\epsilon_{\mu e}^{uV}$ ($\epsilon_{\mu e}^{dV}$) for u (d) quarks discussed in Refs. [25–27], and take the form

$$\begin{aligned}\varepsilon_{\mu e}^{\text{p}V}(Q^2) &= (2\epsilon_{\mu e}^{uV} + \epsilon_{\mu e}^{dV})G_D(Q^2), \\ \varepsilon_{\mu e}^{\text{n}V}(Q^2) &= (\epsilon_{\mu e}^{uV} + 2\epsilon_{\mu e}^{dV})G_D(Q^2).\end{aligned}\tag{2.82}$$

Here, the above NSI form factors are considered to have the same momentum dependence as those of the SM ones. Thus, the function $G_D(Q^2)$ may be assumed to be of a dipole type form factor as

$$G_D = \left(1 + \frac{Q^2}{M_V^2}\right)^{-2},\tag{2.83}$$

(for the vector mass a commonly used value is $M_V = 0.843$ GeV). A dipole approximation for $G_D(Q^2)$, apart from providing the correct momentum dependence, ensures also that the event rate coming out of NSI has the correct behaviour at high energies.

Then, the weak NC nucleon form factors for protons (plus sign) and neutrons (minus sign) employed in our present calculations read

$$F_{1,2}^{\text{NC:p(n)}}(Q^2) = \pm \frac{1}{2} \left[F_{1,2}^{\text{EM:p}}(Q^2) - F_{1,2}^{\text{EM:n}}(Q^2) \right] - 2 \sin^2 \theta_W F_{1,2}^{\text{EM:p(n)}} \pm \varepsilon_{\mu e}^{\text{p(n)}V}(Q^2).\tag{2.84}$$

For the case of the axial form factor $F_A^{\text{NC:p(n)}}$, needed for the incoherent channels of the NC neutrino-nucleus cross section, one may correspondingly take

$$F_A^{\text{NC:p(n)}}(Q^2) = \pm \frac{1}{2} g_A \left(1 + \frac{Q^2}{M_A^2}\right)^{-2},\tag{2.85}$$

with the static axial vector coupling g_A being $g_A = -1.267$ (it is determined as usually through neutron beta decay), and the axial mass being $M_A = 1.35$ GeV [33]. For simplicity, potential axial NSI form factors are neglected.

At first we calculate the differential cross sections of Eq. (2.75) for the SM weak neutral-current process (2.72) as well as for the case of NSI based on Eqs. (2.82)-(2.85). In Fig. 2.7 we demonstrate the total cross section evaluated through numerical integration of the differential cross section (2.75), as

$$\sigma(E_\nu) = \int_0^{Q_{\text{max}}^2(E_\nu)} \frac{d\sigma}{dQ^2} dQ^2,\tag{2.86}$$

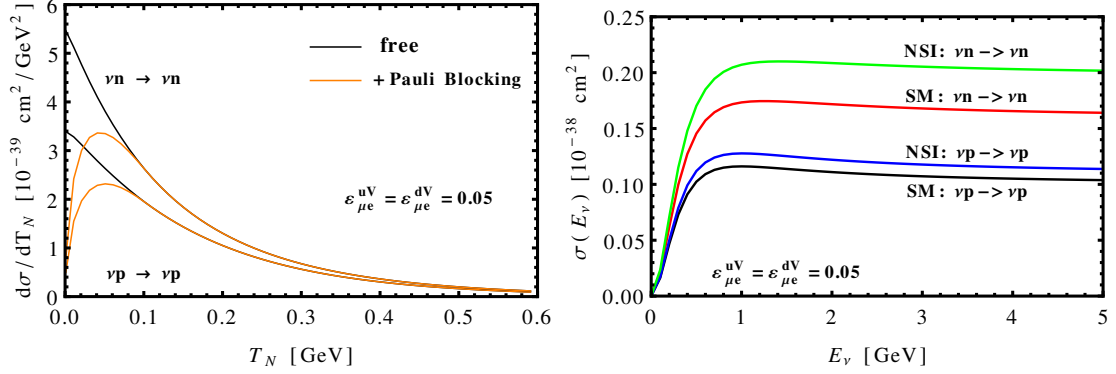


Figure 2.7: Differential (*left panel*) and total (*right panel*) cross section as function of the incoming neutrino energy due to SM and SM+NSI. Pauli blocking effects are also taken into account.

where, for the upper limit of the momentum transfer Q^2 we employ the value

$$Q_{\max}^2(E_\nu) = \frac{4m_N E_\nu^2}{m_N + 2E_\nu}. \quad (2.87)$$

Apparently, one sees that the integrated cross sections for both $\nu p \rightarrow \nu p$, $\nu n \rightarrow \nu n$ scattering channels are enhanced assuming potential non-zero NSI (in Chapt. 5 we used typical values of the flavour changing couplings). As expected the cross section for the $\nu - n$ process is much larger than that of the $\nu - p$ reaction, for both SM or NSI, which suggests the neutrino-nucleus scattering as a valuable probe to study the nuclear neutron form factor.

Chapter 3

Description of the Nuclear Structure

3.1 Introduction

In this Chapter, we devote a thorough discussion in order to present the nuclear physics methods employed in the present Thesis regarding the study of the nuclear physics aspects of the processes in question. We illustrate that the assumption under which the nucleus (A, Z) consists of point-like nucleons (N neutrons and Z protons), in many cases is not a sufficient approximation to provide reliable results.

From the perspective of nuclear theory, the nucleus is considered as a complex many-body system having internal structure. Apart from the strong interaction between the nucleons and the electromagnetic Coulomb force acting on the protons, a realistic description of this system requires to take into account the nuclear correlations arising from short and long range mesonic and quark degrees of freedom. To this contribution, various evolved nuclear physics methods have been formulated, a summary of which is presented below.

3.2 The nuclear Hamiltonian

In general, for nuclear systems with mass number $A > 10 - 12$ the corresponding A -nucleon Schrödinger equation cannot be solved exactly, and a reasonable diagonalisation of this many-body problem of strongly interacting particles, is required. To this purpose, a common approximation is to treat the strongly interacting system of particles as a system of weakly interacting quasi-particles with kinetic energy T and potential energy V . In this way, the many-body nuclear Hamiltonian contains (in addition to the kinetic energy T) the strong interaction between all pairs of nucleons i and j , $v(\mathbf{r}_i, \mathbf{r}_j)$ (realistic nucleon-nucleon potential).

Therefore, H can be cast in the form [34-38]

$$\begin{aligned} H = T + V &= \sum_{i=1}^A t(\mathbf{r}_i) + \sum_{i<j=1}^A v(\mathbf{r}_i, \mathbf{r}_j), \\ &= \sum_{i=1}^A \frac{-\hbar^2}{2m_N} \nabla_i^2 + \sum_{i<j=1}^A v(\mathbf{r}_i, \mathbf{r}_j), \end{aligned} \quad (3.1)$$

with \mathbf{r}_i denoting the spatial coordinates of the i -th nucleon m_N the nucleon mass. Within the context of the independent particle Shell-Model, each nucleon is assumed as moving independently within an overall attractive central potential V_{MF} that represents its interaction with the remaining $A - 1$ nucleons defined as

$$V_{\text{MF}} = \sum_{i=1}^A U(\mathbf{r}_i), \quad (3.2)$$

and thus the nuclear Hamiltonian is written as

$$\begin{aligned} H_{\text{MF}} &= \sum_{i=1}^A t(\mathbf{r}_i) + \sum_{i=1}^A U(\mathbf{r}_i) = \sum_{i=1}^A h(\mathbf{r}_i), \\ &= T + V_{\text{MF}}. \end{aligned} \quad (3.3)$$

In this sense, we define the scalar function, H_{res} , treated as a small perturbation written as

$$H_{\text{res}} \equiv H_{\text{res}}(\mathbf{r}_i, \mathbf{r}_j) = V - \sum_{i=1}^A U(\mathbf{r}_i) = \sum_{i<j=1}^A v(\mathbf{r}_i, \mathbf{r}_j) - \sum_{i=1}^A U(\mathbf{r}_i), \quad (3.4)$$

which implies that the many-body nuclear Hamiltonian of Eq.(3.1) is separated into a mean-field and a residual part as follows

$$H = \underbrace{\sum_{i=1}^A [t(\mathbf{r}_i) + U(\mathbf{r}_i)]}_{H_{\text{MF}}} + \underbrace{\left[\sum_{i<j=1}^A v(\mathbf{r}_i, \mathbf{r}_j) - \sum_{i=1}^A U(\mathbf{r}_i) \right]}_{H_{\text{res}}}. \quad (3.5)$$

Within the Born approximation (i.e. $H_{\text{res}} \approx 0$), the solution of the many-nucleon Schrödinger equation for the unperturbed mean-field Hamiltonian $H_{\text{MF}} = \sum_{i=1}^A h(\mathbf{r}_i)$ is constructed in terms of a complete set of single-nucleon wavefunctions, i.e. the solutions of the equation $h(\mathbf{r})\psi_\alpha(\mathbf{r}) = \varepsilon_\alpha\psi_\alpha(\mathbf{r})$. The nuclear state, $|f\rangle$, is a totally antisymmetric product of the wavefunctions $\psi_\alpha(\mathbf{r})$ and in its normalised form it is represented by the Slater determinant

$$|f\rangle = \frac{1}{\sqrt{A!}} \begin{pmatrix} \psi_{\alpha,1}(\mathbf{r}_1) & \psi_{\alpha,2}(\mathbf{r}_2) & \cdots & \psi_{\alpha,A}(\mathbf{r}_A) \\ \psi_{\alpha,1}(\mathbf{r}_1) & \psi_{\alpha,2}(\mathbf{r}_2) & \cdots & \psi_{\alpha,A}(\mathbf{r}_A) \\ \vdots & \vdots & \ddots & \vdots \\ \psi_{\alpha,1}(\mathbf{r}_1) & \psi_{\alpha,2}(\mathbf{r}_2) & \cdots & \psi_{\alpha,A}(\mathbf{r}_A) \end{pmatrix}. \quad (3.6)$$

More specifically, it is a product of single-particle wave functions obtained by solving the one-nucleon Schrödinger equation for an external potential ¹, that yields a set of A -identical equations

$$h(\mathbf{r}_i)\psi_\alpha(\mathbf{r}_i) = \varepsilon_\alpha\psi_\alpha(\mathbf{r}_i), \quad h(\mathbf{r}_i) = t(\mathbf{r}_i) + U(\mathbf{r}_i) = \frac{-\hbar^2}{2m_N}\nabla^2 + U(\mathbf{r}_i). \quad (3.7)$$

At this point it should be stressed that, in the general case, a central potential such as $V_{\text{MF}}(\mathbf{r})$ is not the optimum choice to describe non-spherical nuclei at a satisfactory level. The most important concern that should be taken into consideration in order to determine an appropriate potential, $V_{\text{MF}}(\mathbf{r})$, is to seek the particular one that minimises the residual interaction between the quasi-particles (see Sect. 3.4.1). This becomes possible through the Hartree-Fock method or by employing a phenomenological potential such as the Harmonic Oscillator or the Woods-Saxon potential. In this work, for the case of the mean-field we use the Woods-Saxon potential (see Sect. 3.3), while for the residual interaction we adopt the well-known Bonn C-D potential (see Sect. 3.4.7).

3.3 The Woods-Saxon potential

For the purposes of the present work, as central potential we employ the Woods-Saxon potential (see also the Appendix D.1)

$$V_{\text{WS}}(r) = \frac{-V_0}{1 + e^{\frac{r-R}{\alpha}}}, \quad (3.8)$$

where V_0 is the potential well depth parameter, R is the nuclear radius and α the surface-thickness (or surface diffuseness) parameter. The well depth is adopted to be different for neutrons and protons (see e.g. the left panel of Fig. 3.1). Figure 3.1 (right panel) illustrates graphically a comparison between the Woods-Saxon potential and the Harmonic Oscillator potential defined as

$$V_{\text{HO}}(r) = -V_1 + kr^2 = -V_1 + \frac{m_N\omega}{2}r^2, \quad (3.9)$$

(more details are given in Appendix D.2).

To obtain higher reliability of our present results we include Coulomb corrections (only for protons) and we also take into account contributions originating from the spin-orbit $\mathbf{l}\cdot\mathbf{s}$ interaction. More specifically, assuming a uniformly charged sphere, the static Coulomb potential of the nucleon inside the nucleus reads

$$V_c(r) = (Z-1)e^2 \begin{cases} \frac{3-(r/R_c)^2}{2R_c}, & r \leq R_c, \\ \frac{1}{r}, & r > R_c. \end{cases} \quad (3.10)$$

¹Indeed the A -nucleon Schrödinger equation $H_{\text{MF}}\Psi_0(\mathbf{r}_1, \mathbf{r}_2, \dots, \mathbf{r}_A) = E\Psi_0(\mathbf{r}_1, \mathbf{r}_2, \dots, \mathbf{r}_A)$ is separated using the fact that $\Psi_0(\mathbf{r}_1, \mathbf{r}_2, \dots, \mathbf{r}_A) = \prod_{i=1}^A \psi_{\alpha i}(\mathbf{r}_i)$ and the definition $E = \sum_{i=1}^A \varepsilon_{\alpha i}$.

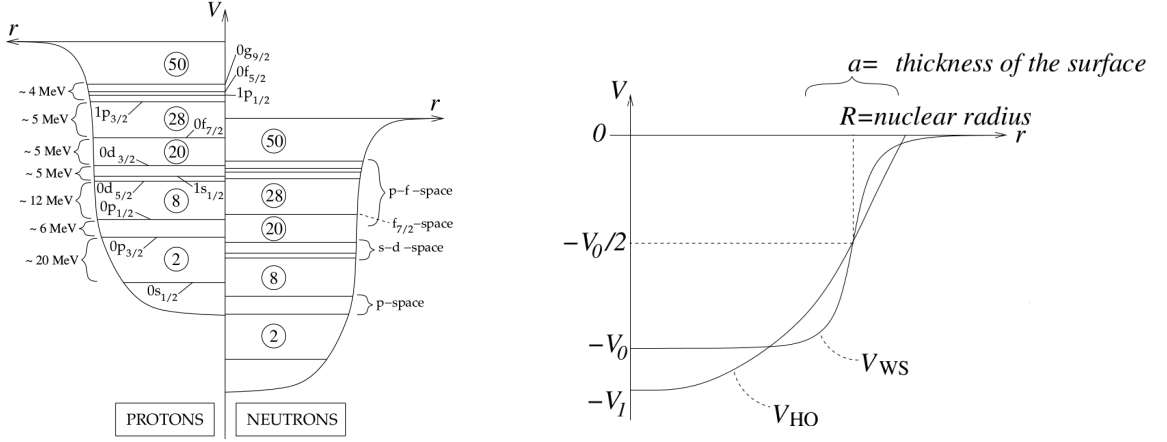


Figure 3.1: (*Left panel*) The Woods-Saxon potential for protons and neutrons. The magic numbers and shells of states are indicated with rough energies. (*Right panel*) Comparison between the Woods-Saxon and the Harmonic Oscillator potential. The parameters in both cases are selected so that they become approximately equivalent. (The figure is reproduced from Ref. [38]).

The Coulomb interaction yields an additional difference between the single-particle potential for neutrons and protons, i.e. the nuclear depth for protons is deeper.

To achieve higher reproducibility of the experimental data of the single-particle energies, the employed spin-orbit correction is described by the potential

$$V_{ls}(r) = \left(\frac{\hbar}{m_N c^2} \right)^2 \frac{1}{r} \frac{d}{dr} \left(\frac{V_s}{1 + e^{(r-R_s)/\alpha_s}} \right) \mathbf{l} \cdot \mathbf{s}, \quad (3.11)$$

where \mathbf{l} denotes the orbital angular momentum and \mathbf{s} the spin of the nucleon. With the latter correction, Mayer and Jensen [39] achieved reproducibility of the energy gaps which correspond to the so-called magic numbers (2, 8, 20, 28, 50, 82, 126, etc.). Indeed, this becomes possible since the $\mathbf{l} \cdot \mathbf{s}$, splits the states that correspond to a given quantum number l as $j = l \pm 1/2$, with j being the total single-particle angular momentum. Eventually, the mean-field Coulomb corrected Woods-Saxon potential with additional spin-orbit corrections as described above, is given by

$$V_{MF} = \sum_{i=1}^A U(\mathbf{r}_i) = \sum_{i=1}^A [V_{WS}(\mathbf{r}_i) + V_c(\mathbf{r}_i) + V_{ls}(\mathbf{r}_i)]. \quad (3.12)$$

In this work the adopted parametrisation for the parameters entering the defini-

tion of the Woods-Saxon potential follows Ref. [40]

$$\begin{aligned} V_{0n} &= -53.3 + 27.0 \frac{(N - Z)}{A}, \\ V_{0p} &= -53.3 - 27.0 \frac{(N - Z)}{A} - 0.4 \frac{Z}{A^{1/3}}, \end{aligned} \tag{3.13}$$

with $\alpha = 0.65$, $R = 1.25$, while for the spin-orbit interaction we have $R_s = 1.25$, $\alpha_s = 0.47$ and $V_s = 15.0$. Our code however, offers the possibility to employ the corresponding parametrisation established by Bohr and Motelson [41] or Bertch and Esbensen [42]. Moreover, in the literature, one may also find the Tanaka parametrisation (that is beyond our scope) which is appropriate for very heavy nuclei [43].

3.4 Theoretical description of the nuclear ground state

Long ago, experimental data showed that the nucleons within the field of a nucleus have the tension to couple in pairs so as their total angular momentum vanishes. This nuclear physics phenomenon in 1950 inspired Mayer [44] who provided a reasonable explanation to the question: why even-even nuclei carry vanishing total spin, whereas in odd-odd nuclei the total spin is equal to the spin of the last non-coupled particle. Soon after, in 1952, Flowers and simultaneously Racoli and Talmi introduced the seniority scheme for the description of the coupling in nuclear physics.

In 1957, Bardeen, Cooper and Schrieffer formulated the so-called BCS theory in order to provide a microscopic description of the superconductivity of metals [45]. Its main feature is that the long-range effective attraction between two electrons is mediated by quantised lattice vibrations, lattice phonons (the correlated electrons form pairs with total spin zero). On the basis of the pairing phenomenon in nuclei, Bohr, Mottelson and Pines [46] in 1958 and Belyaev [47] in 1959 proposed the application of the BCS theory for the description of nuclei, which become a standard part of nuclear structure calculations.

3.4.1 The nuclear BCS wavefunction

BCS is an advanced many-body theory that can be viewed as a Rayleigh-Ritz variational problem and can be applied by using a relatively simple pairing force. In this framework, the concept of quasi-particles, made out of particle and hole components with certain occupation amplitudes, is introduced. Under these considerations, the nucleons are assumed to couple in pairs with vanishing angular momentum forming bosonic states and behave as being in a superconducting state.

In analogy to the BCS theory who determined the ground state of a semiconductor, in the nuclear BCS theory the ground state (*g.s.*) wavefunction of an even-even nucleus can be represented by the ansatz [34]

$$|BCS\rangle = \prod_{\alpha>0} (u_\alpha - v_\alpha c_\alpha^\dagger \tilde{c}_\alpha^\dagger) |\text{core}\rangle. \quad (3.14)$$

Note that, some authors [34, 36] use an opposite sign in the definition of $|BCS\rangle$. This choice results to a different definition for the Bogoliubov-Valatin transformation [see also Eq.(3.21)]. In Eq.(3.14) the operator $c_\alpha^\dagger \tilde{c}_\alpha^\dagger$ creates an identical nucleonic pair and c_α^\dagger (c_α) is the creation (annihilation) operator for physical particles. The product runs only over half the configuration space, as indicated by $\alpha > 0$, while for each state $\alpha > 0$ there exists a conjugate state $\tilde{\alpha} < 0$ [36]. In our present study we adopt the Baranger notation [48] $\alpha \equiv (a, m_\alpha)$, where $a \equiv (n_a, l_a, j_a)$, thus, for the assumed spherical nuclei the u_a and v_a parameters are independent of the projection quantum number m_α . For instance, in the case where a given Hamiltonian is invariant under time reversal, such as the Harmonic Oscillator basis (spherical basis) one would readily write

$$|\alpha\rangle = |n_a l_a j_a; m_\alpha\rangle \quad |\tilde{\alpha} \equiv -\alpha\rangle = |n_a l_a j_a; -m_\alpha\rangle, \quad m_\alpha > 0. \quad (3.15)$$

In this context, u_a and v_a , are considered as variational parameters representing the probability amplitudes, (v_a^2 and u_a^2 constitute the probability that a conjugate pair state ($\alpha, \tilde{\alpha}$) is occupied or unoccupied respectively). However, the latter are not independent and obey the condition $|u_a|^2 + |v_a|^2 = 1$, that represents the normalisation of each single-nucleon state. In this context, the optimum wavefunction is found by varying the model parameters to achieve minimum energy. The BCS wavefunction is only fixed to within a phase factor and therefore it is always possible to choose the coefficients of u_a to be real and positive and thus write

$$u_a^2 + v_a^2 = 1 \quad \text{for all } a, \quad (3.16)$$

(in principle, the phase of v_a has to be determined by the variation of the energy expectation value).

A weak feature of the method is the absence of a fixed number of particles and therefore it is not an eigenstate of the number operator

$$\hat{n} = \sum_{\alpha} c_{\alpha}^{\dagger} c_{\alpha}. \quad (3.17)$$

Indeed, via a Taylor expansion, the BCS state can be expressed as a sum of

eigenstates $|N\rangle$ as follows

$$\begin{aligned}
|BCS\rangle &= \prod_{\alpha>0} (u_\alpha - v_\alpha c_\alpha^\dagger \tilde{c}_\alpha^\dagger) |\text{core}\rangle = \prod_{\alpha>0} u_\alpha \left(1 - \frac{v_\alpha}{u_\alpha} c_\alpha^\dagger \tilde{c}_\alpha^\dagger\right) |\text{core}\rangle \\
&= \prod_{\beta>0} u_\beta \prod_{\alpha>0} \exp\left(-\frac{v_\alpha}{u_\alpha} c_\alpha^\dagger \tilde{c}_\alpha^\dagger\right) |\text{core}\rangle \\
&= \prod_{\beta>0} u_\beta \exp\left(-\sum_{\alpha>0} \frac{v_\alpha}{u_\alpha} c_\alpha^\dagger \tilde{c}_\alpha^\dagger\right) |\text{core}\rangle \\
&= \prod_{\beta>0} u_\beta \sum_n \frac{1}{n!} \left(-\sum_{\alpha>0} \frac{v_\alpha}{u_\alpha} c_\alpha^\dagger \tilde{c}_\alpha^\dagger\right)^n |\text{core}\rangle.
\end{aligned} \tag{3.18}$$

This means that we can regard $|N\rangle$ as a projection onto the N -particle space of the wavefunction

$$|BCS\rangle = \prod_{\beta>0} u_\beta \sum_{N=\text{even}} \frac{1}{(N/2)!} |N\rangle, \tag{3.19}$$

with

$$|N\rangle \equiv \left(-\sum_{\alpha>0} \frac{v_\alpha}{u_\alpha} c_\alpha^\dagger \tilde{c}_\alpha^\dagger\right)^{N/2} |\text{core}\rangle, \tag{3.20}$$

implying that the BCS vacuum does not possess good particle number and that it is not a normalised eigenstate to the nucleon number N , respectively. Apparently, the BCS as given in Eq.(3.14) is more convenient as compared to that of the number-conserving state $|N\rangle$, since $|BCS\rangle$ is the vacuum for BCS quasi-particles (see Subsect. 3.4.2).

3.4.2 BCS quasi-particles

At this point, we define the quasi-particle creation (annihilation) operator a^\dagger (a) as linear combinations of particle operators via the Bogoliubov-Valatin (BV) transformation [49, 50]

$$\begin{aligned}
a_\alpha^\dagger &= u_\alpha c_\alpha^\dagger + v_\alpha \tilde{c}_\alpha, & c_\alpha^\dagger &= u_\alpha a_\alpha^\dagger - v_\alpha \tilde{a}_\alpha, \\
\tilde{a}_\alpha^\dagger &= u_\alpha \tilde{c}_\alpha^\dagger - v_\alpha c_\alpha, & \tilde{c}_\alpha^\dagger &= u_\alpha \tilde{a}_\alpha^\dagger + v_\alpha a_\alpha, \\
a_\alpha &= u_\alpha c_\alpha + v_\alpha \tilde{c}_\alpha^\dagger, & c_\alpha &= u_\alpha a_\alpha - v_\alpha \tilde{a}_\alpha^\dagger, \\
\tilde{a}_\alpha &= u_\alpha \tilde{c}_\alpha - v_\alpha c_\alpha^\dagger, & \tilde{c}_\alpha &= u_\alpha \tilde{a}_\alpha + v_\alpha a_\alpha^\dagger.
\end{aligned} \tag{3.21}$$

The corresponding anticommutation relations preserve the basic commutation relations (i.e. BV is a quantum mechanical canonical transformation), as

$$\{a_\alpha^\dagger, a_\beta^\dagger\} = 0, \quad \{a_\alpha, a_\beta\} = 0, \quad \{a_\alpha, a_\beta^\dagger\} = \delta_{\alpha\beta}, \tag{3.22}$$

emphasising that the quasi-particles are (generalised) fermions like the physical particles they are built from.

It should be noticed that the quasi-particle is to be viewed as *partly particle* and simultaneously *partly hole*, rather than bare particle or bare hole. In other words, the operator a_α^\dagger creates a quasi-particle, in an orbital α , that is a particle with probability amplitude u_a and a hole with probability amplitude v_a . The corresponding annihilation operator is a_α with $\tilde{a}_\alpha = (-1)^{j_a+m_\alpha} a_{-\alpha}$, and $-\alpha = (a, -m_\alpha)$. Moreover, we stress that above the Fermi surface (v_a^2 small) it is nearly particle, while below the Fermi surface (u_a^2 small) it is nearly hole. In this framework, a j orbital, is occupied with $(2j+1)v_j^2$ particles and $(2j+1)u_j^2$ holes. In addition, through the BV transformation, it is achieved a representation of the ground state of pairwise interacting particles in terms of a gas of non-interacting quasi-particles. The disadvantage however, is that the BV transformation does not conserve the particle number due to the mixing of creation and annihilation operators.

The BV transformation is written in matrix form as

$$\begin{pmatrix} c_\alpha^\dagger \\ \tilde{c}_\alpha \end{pmatrix} = \begin{bmatrix} u_a & -v_a \\ v_a & u_a \end{bmatrix} \begin{pmatrix} a_\alpha^\dagger \\ \tilde{a}_\alpha \end{pmatrix}, \quad (3.23)$$

and can be inverted as

$$\begin{pmatrix} a_\alpha^\dagger \\ \tilde{a}_\alpha \end{pmatrix} = \begin{bmatrix} u_a & v_a \\ -v_a & u_a \end{bmatrix} \begin{pmatrix} c_\alpha^\dagger \\ \tilde{c}_\alpha \end{pmatrix}. \quad (3.24)$$

Before closing this discussion, we give the result of the a_α and \tilde{a}_α operations on the BCS vacuum, that is

$$a_\alpha |BCS\rangle = 0, \quad \tilde{a}_\alpha |BCS\rangle = 0. \quad (3.25)$$

The corresponding contraction properties are written as

$$\overline{a_\alpha a_\beta^\dagger} \equiv \langle BCS | a_\alpha a_\beta^\dagger | BCS \rangle = \delta_{\alpha\beta}, \quad \text{all other contractions} = 0, \quad (3.26)$$

which imply that the quasi-particles are defined in terms of normal ordered operators. Furthermore, recalling the BV transformations of Eq.(3.21) and using Eq.(3.26), one may write the contractions of the physical particle operators with respect to the BCS vacuum, as follows

$$\begin{aligned} \overline{c_\alpha c_\beta^\dagger} &= u_a^2 \delta_{\alpha\beta}, \\ \overline{c_\alpha^\dagger c_\beta} &= v_a^2 \delta_{\alpha\beta}, \\ \overline{c_\alpha^\dagger c_\beta^\dagger} &= u_a v_a (-1)^{j_a - m_\alpha} \delta_{\alpha, -\beta}, \\ \overline{\tilde{c}_\alpha \tilde{c}_\beta} &= u_a v_a (-1)^{j_a + m_\alpha} \delta_{\alpha, -\beta}. \end{aligned} \quad (3.27)$$

3.4.3 Two-body interactions

The two-body interaction V entering the nuclear Hamiltonian is usually written as

$$V = \frac{1}{4} \sum_{\alpha\beta\gamma\delta} \bar{v}_{\alpha\beta\gamma\delta} c_{\alpha}^{\dagger} c_{\beta}^{\dagger} c_{\delta} c_{\gamma}. \quad (3.28)$$

The antisymmetrised two-nucleon interaction matrix elements are denoted by

$$\bar{v}_{\alpha\beta\gamma\delta} = \langle \alpha\beta | V | \gamma\delta \rangle - \langle \alpha\beta | V | \delta\gamma \rangle, \quad (3.29)$$

and fulfil the symmetry properties

$$\bar{v}_{\alpha\beta\gamma\delta} = -\bar{v}_{\beta\alpha\gamma\delta} = -\bar{v}_{\alpha\beta\delta\gamma} = -\bar{v}_{\beta\alpha\delta\gamma} = \bar{v}_{\gamma\delta\alpha\beta}^*. \quad (3.30)$$

The normalised and antisymmetrised two-nucleon states with respect to the appropriate particle vacuum $|0\rangle$ (e.g. $|0\rangle \equiv |\text{core}\rangle$ in our case) are given by

$$|\alpha\beta\rangle = c_{\alpha}^{\dagger} c_{\beta}^{\dagger} |0\rangle, \quad |\gamma\delta\rangle = c_{\gamma}^{\dagger} c_{\delta}^{\dagger} |0\rangle. \quad (3.31)$$

In angular-momentum-coupled representation, the normalised two-nucleon state takes the form

$$|ab; JM\rangle = \mathcal{N}_{ab}(J) [c_a^{\dagger} c_b^{\dagger}]_{JM} |0\rangle, \quad (3.32)$$

with

$$\mathcal{N}_{ab}(J) = \frac{\sqrt{1 + \delta_{ab}(-1)^J}}{1 + \delta_{ab}}. \quad (3.33)$$

These wavefunctions describe a two-body nucleonic system for all possible combinations (proton-proton, neutron-neutron or proton-neutron). To express the uncoupled wavefunction $|\alpha\beta\rangle$ in terms of the coupled wavefunctions $|ab; JM\rangle$ we write the operators $c_{\alpha}^{\dagger} c_{\beta}^{\dagger}$ using the Clebsch-Gordan coefficients (see Appendix C.1) as

$$c_{\alpha}^{\dagger} c_{\beta}^{\dagger} = \sum_{JM} (j_a m_{\alpha} j_b m_{\beta} | JM) [c_a^{\dagger} c_b^{\dagger}]_{JM}. \quad (3.34)$$

Acting on the vacuum we get

$$|\alpha\beta\rangle = \sum_{JM} (j_a m_{\alpha} j_b m_{\beta} | JM) [\mathcal{N}_{ab}(J)]^{-1} |ab; JM\rangle. \quad (3.35)$$

A direct substitution of the latter expression to Eq.(3.28) yields

$$V = \frac{1}{4} \sum_{\substack{abcd \\ JM J' M'}} [\mathcal{N}_{ab}(J) \mathcal{N}_{cd}(J')]^{-1} \langle ab; JM | V | cd; J' M' \rangle \\ \times [c_a^{\dagger} c_b^{\dagger}]_{JM} (-1)^{J'+M'+1} [\tilde{c}_c \tilde{c}_d]_{J', -M'}. \quad (3.36)$$

To proceed, we use the Wigner-Eckart theorem (see Appendix C.6) and express the matrix element of the above equation in the following form

$$\begin{aligned}
\langle ab; JM|V|cd; J'M'\rangle &= (-1)^{J-M} \begin{pmatrix} J & 0 & J' \\ -M & 0 & M' \end{pmatrix} \langle ab; J||V||cd; J'\rangle \\
&= \delta_{JJ'} \delta_{MM'} \left[\hat{J} \right]^{-1} \langle ab; J||V||cd; J'\rangle \\
&= \delta_{JJ'} \delta_{MM'} \langle ab; J|V|cd; J\rangle,
\end{aligned} \tag{3.37}$$

where in the second line we used the symmetry properties of the 3-j symbols (see Appendix C.2 and Ref. [51]) and adopted the commonly used abbreviation $\hat{J} = \sqrt{2J+1}$. We note that, the last term in the right hand side of the equality is not expressed in terms of a reduced matrix element since the matrix element is diagonal in J and M and therefore has no dependence on M . Then, in a straightforward manner we obtain the two-body quasi-particle residual interaction in the form

$$\begin{aligned}
V &= -\frac{1}{4} \sum_J \sum_{abcd} [\mathcal{N}_{ab}(J)\mathcal{N}_{cd}(J)]^{-1} \langle ab; J|V|cd; J\rangle \\
&\quad \times \sum_M (-1)^{J+M} [c_a^\dagger c_b^\dagger]_{JM} [\tilde{c}_c \tilde{c}_d]_{J,-M}.
\end{aligned} \tag{3.38}$$

Thus, by using Eq.(C.21), we arrive at the expression

$$V = -\frac{1}{4} \sum_J \sum_{abcd} [\mathcal{N}_{ab}(J)\mathcal{N}_{cd}(J)]^{-1} \hat{J} \langle ab; J|V|cd; J\rangle \left[[c_a^\dagger c_b^\dagger]_J [\tilde{c}_c \tilde{c}_d]_J \right]_{00}. \tag{3.39}$$

Isospin representation of coupled two-body matrix elements

At this point we find it useful to provide the corresponding relations for the coupled two-body matrix elements in the isospin representation, that are needed for our purposes. The interaction in this case is isoscalar and satisfies the relation

$$\langle ab; JM; TM_T|V|cd; JM; T'M'_T\rangle = \delta_{TT'} \delta_{M_T M'_T} \langle ab; JT|V|cd; JT\rangle, \tag{3.40}$$

standing out as an extension of the matrix elements entering the second and third line of Eq.(3.37). The latter, relates the matrix elements with angular momentum coupling to those with angular momentum plus isospin coupling in a compact way.

The required proton-proton and neutron-neutron two-body matrix elements can be cast in the simple form

$$\begin{aligned}
\langle p_1 p_2; J|V|p_3 p_4; J\rangle &= \langle a_1 a_2; JT = 1|V|a_3 a_4; JT = 1\rangle, \\
\langle n_1 n_2; J|V|n_3 n_4; J\rangle &= \langle a_1 a_2; JT = 1|V|a_3 a_4; JT = 1\rangle.
\end{aligned} \tag{3.41}$$

The corresponding proton-neutron and neutron-proton matrix elements read

$$\begin{aligned} \langle p_1 n_2; J|V|p_3 n_4; J \rangle &= \langle n_1 p_2; J|V|n_3 p_4; J \rangle \\ &= \frac{1}{2} \left\{ \sqrt{[1 + \delta_{a_1 a_2}(-1)^J][1 + \delta_{a_3 a_4}(-1)^J]} \langle a_1 a_2; JT = 1|V|a_3 a_4; JT = 1 \rangle \right. \\ &\quad \left. + \sqrt{[1 - \delta_{a_1 a_2}(-1)^J][1 - \delta_{a_3 a_4}(-1)^J]} \langle a_1 a_2; JT = 0|V|a_3 a_4; JT = 0 \rangle \right\}, \end{aligned} \quad (3.42)$$

$$\begin{aligned} \langle n_1 p_2; J|V|p_3 n_4; J \rangle &= \langle p_1 n_2; J|V|n_3 p_4; J \rangle \\ &= \left\{ \frac{1}{2} \sqrt{[1 + \delta_{a_1 a_2}(-1)^J][1 + \delta_{a_3 a_4}(-1)^J]} \langle a_1 a_2; JT = 1|V|a_3 a_4; JT = 1 \rangle \right. \\ &\quad \left. - \sqrt{[1 - \delta_{a_1 a_2}(-1)^J][1 - \delta_{a_3 a_4}(-1)^J]} \langle a_1 a_2; JT = 0|V|a_3 a_4; JT = 0 \rangle \right\}. \end{aligned} \quad (3.43)$$

The above expressions obey the simple symmetries

$$\begin{aligned} \langle ab; J|V|cd; J \rangle &= \langle cd; J|V|ab; J \rangle, \\ \langle ab; JT|V|cd; JT \rangle &= \langle cd; JT|V|ab; JT \rangle, \end{aligned} \quad (3.44)$$

and also the phase symmetries

$$\begin{aligned} \langle ab; J|V|cd; J \rangle &= (-1)^{j_a + j_b + J + 1} \langle ba; J|V|cd; J \rangle \\ &= (-1)^{j_c + j_d + J + 1} \langle ab; J|V|dc; J \rangle, \\ \langle ab; JT|V|cd; JT \rangle &= (-1)^{j_a + j_b + J + T} \langle ba; JT|V|cd; JT \rangle \\ &= (-1)^{j_c + j_d + J + T} \langle ab; JT|V|dc; JT \rangle. \end{aligned} \quad (3.45)$$

3.4.4 The BCS nuclear Hamiltonian

We proceed our discussion with a description of the required steps towards obtaining the quasi-particle representation of the nuclear Hamiltonian within the context of BCS. In the second quantisation language the many-body nuclear Hamiltonian, $H = T + V$, is expressed as a sum of a one-quasi-particle term that describes the quasi-particle mean-field, and a residual interaction, as

$$H = \sum_{\alpha} \varepsilon_{\alpha} c_{\alpha}^{\dagger} c_{\alpha} + \frac{1}{4} \sum_{\alpha\beta\gamma\delta} \bar{v}_{\alpha\beta\gamma\delta} c_{\alpha}^{\dagger} c_{\beta}^{\dagger} c_{\delta} c_{\gamma}, \quad (3.46)$$

where the first sum represents the one-body kinetic energy, T , of the Hamiltonian, while the second sum represents the two-body potential V .

Focusing on the two-body part only and by applying the Wick's theorem we

get ² [38]

$$\begin{aligned}
4V &= \sum_{\alpha\beta\gamma\delta} \bar{v}_{\alpha\beta\gamma\delta} c_{\alpha}^{\dagger} c_{\beta}^{\dagger} c_{\delta} c_{\gamma} = \sum_{\alpha\beta\gamma\delta} \bar{v}_{\alpha\beta\gamma\delta} \mathcal{N} \left[c_{\alpha}^{\dagger} c_{\beta}^{\dagger} c_{\delta} c_{\gamma} \right] \\
&+ \sum_{\alpha\beta\gamma\delta} \bar{v}_{\alpha\beta\gamma\delta} \langle BCS | c_{\alpha}^{\dagger} c_{\beta}^{\dagger} | BCS \rangle \mathcal{N} [c_{\delta} c_{\gamma}] - \sum_{\alpha\beta\gamma\delta} \bar{v}_{\alpha\beta\gamma\delta} \langle BCS | c_{\alpha}^{\dagger} c_{\delta} | BCS \rangle \mathcal{N} [c_{\beta}^{\dagger} c_{\gamma}] \\
&+ \sum_{\alpha\beta\gamma\delta} \bar{v}_{\alpha\beta\gamma\delta} \langle BCS | c_{\alpha}^{\dagger} c_{\gamma} | BCS \rangle \mathcal{N} [c_{\beta}^{\dagger} c_{\delta}] + \sum_{\alpha\beta\gamma\delta} \bar{v}_{\alpha\beta\gamma\delta} \langle BCS | c_{\beta}^{\dagger} c_{\delta} | BCS \rangle \mathcal{N} [c_{\alpha}^{\dagger} c_{\gamma}] \\
&- \sum_{\alpha\beta\gamma\delta} \bar{v}_{\alpha\beta\gamma\delta} \langle BCS | c_{\beta}^{\dagger} c_{\gamma} | BCS \rangle \mathcal{N} [c_{\alpha}^{\dagger} c_{\delta}] + \sum_{\alpha\beta\gamma\delta} \bar{v}_{\alpha\beta\gamma\delta} \langle BCS | c_{\delta} c_{\gamma} | BCS \rangle \mathcal{N} [c_{\alpha}^{\dagger} c_{\beta}^{\dagger}] \\
&+ \sum_{\alpha\beta\gamma\delta} \bar{v}_{\alpha\beta\gamma\delta} \langle BCS | c_{\alpha}^{\dagger} c_{\beta}^{\dagger} | BCS \rangle \langle BCS | c_{\delta} c_{\gamma} | BCS \rangle \\
&- \sum_{\alpha\beta\gamma\delta} \bar{v}_{\alpha\beta\gamma\delta} \langle BCS | c_{\alpha}^{\dagger} c_{\delta} | BCS \rangle \langle BCS | c_{\beta}^{\dagger} c_{\gamma} | BCS \rangle \\
&+ \sum_{\alpha\beta\gamma\delta} \bar{v}_{\alpha\beta\gamma\delta} \langle BCS | c_{\alpha}^{\dagger} c_{\gamma} | BCS \rangle \langle BCS | c_{\beta}^{\dagger} c_{\delta} | BCS \rangle .
\end{aligned} \tag{3.47}$$

By using the BV transformation of Eq.(3.21) and Eq.(3.27) one finds

$$\bar{v}_{-\alpha, -\beta, -\gamma, -\delta} = (-1)^{j_a - m_{\alpha} + j_b - m_{\beta} + j_c - m_{\gamma} + j_d - m_{\delta}} \bar{v}_{\alpha\beta\gamma\delta} . \tag{3.48}$$

Then, after some straightforward elaboration one gets

$$\begin{aligned}
4V &= \sum_{\alpha\beta\gamma\delta} \bar{v}_{\alpha\beta\gamma\delta} \mathcal{N} \left[c_{\alpha}^{\dagger} c_{\beta}^{\dagger} c_{\delta} c_{\gamma} \right] + 2 \sum_{\alpha\beta} \bar{v}_{\alpha\beta\alpha\beta} v_a^2 v_b^2 \\
&+ \sum_{\alpha\beta} \bar{v}_{\alpha, -\alpha, \beta, -\beta} (-1)^{j_a - m_{\alpha} + j_b - m_{\beta}} u_a v_a u_b v_b \\
&+ 2 \sum_{\alpha\gamma\delta} \bar{v}_{\alpha, -\alpha, -\gamma, \delta} (-1)^{j_a - m_{\alpha} + j_c - m_{\gamma}} u_a v_a (u_d v_c + v_d u_c) a_{\gamma}^{\dagger} a_{\delta} \\
&+ 4 \sum_{\alpha\gamma\delta} \bar{v}_{\alpha\gamma\alpha\delta} v_a^2 (u_c u_d - v_d v_c) a_{\gamma}^{\dagger} a_{\delta} \\
&+ 4 \sum_{\alpha\gamma\delta} \bar{v}_{\alpha\delta\alpha, -\gamma} (-1)^{j_c - m_{\gamma}} v_a^2 u_d v_c (a_{\gamma}^{\dagger} a_{\delta}^{\dagger} + a_{\delta} a_{\gamma}) \\
&+ \sum_{\alpha\gamma\delta} \bar{v}_{\alpha, -\alpha, \gamma\delta} (-1)^{j_a + m_{\alpha}} u_a v_a (v_c v_d - u_c u_d) (a_{\gamma}^{\dagger} a_{\delta}^{\dagger} + a_{\delta} a_{\gamma}) .
\end{aligned} \tag{3.49}$$

We now use the properties of the Clebsch-Gordan coefficients (see Appendix C.1)

²Recall the normal ordering operation $\mathcal{N} [c_{\alpha}^{\dagger} c_{\beta} c_{\gamma}^{\dagger} c_{\delta}] = (-1)^1 c_{\alpha}^{\dagger} c_{\gamma}^{\dagger} c_{\beta} c_{\delta} = (-1)^2 c_{\alpha}^{\dagger} c_{\gamma}^{\dagger} c_{\delta} c_{\beta}$ and that $\mathcal{N} [ABC \dots] \equiv : ABC \dots :$, where the two colons ($: \dots :$) separate the product of the arbitrary operators A, B, C, \dots to be normal ordered.

and rewrite contracted terms of the previous summation as follows

$$2 \sum_{\alpha\beta} \bar{v}_{\alpha\beta\alpha\beta} v_a^2 v_b^2 = 2 \sum_{ab} v_a^2 v_b^2 \sum_J \hat{J}^2 [\mathcal{N}_{ab}(J)]^{-2} \langle ab; J|V|ab; J \rangle, \quad (3.50)$$

$$\sum_{\alpha\beta} \bar{v}_{\alpha,-\alpha,\beta,-\beta} (-1)^{j_a - m_\alpha + j_b - m_\beta} u_a v_a u_b v_b = 2 \sum_{ab} \hat{j}_a \hat{j}_b u_a v_a u_b v_b \langle aa; 0|V|bb; 0 \rangle, \quad (3.51)$$

$$2 \sum_{\alpha\gamma\delta} \bar{v}_{\alpha,-\alpha,-\gamma,\delta} (-1)^{j_a - m_\alpha + j_c - m_\gamma} u_a v_a (u_d v_c + v_d u_c) a_\gamma^\dagger a_\delta = \\ - 2\sqrt{2} \sum_{acd} \hat{j}_a u_a v_a (u_d v_c + v_d u_c) [\mathcal{N}_{cd}(0)]^{-1} \delta_{j_c j_d} \langle aa; 0|V|cd; 0 \rangle [a_c^\dagger \tilde{a}_d]_{00}, \quad (3.52)$$

$$4 \sum_{\alpha\gamma\delta} \bar{v}_{\alpha\gamma\alpha\delta} v_a^2 (u_c u_d - v_d v_c) a_\gamma^\dagger a_\delta = 4 \sum_{acd} [\hat{j}_c]^{-1} v_a^2 (u_c u_d - v_d v_c) \\ \times \sum_J \hat{J}^2 [\mathcal{N}_{ac}(J) \mathcal{N}_{ad}(J)]^{-1} \delta_{j_c j_d} \langle ac; J|V|ad; J \rangle [a_c^\dagger \tilde{a}_d]_{00}, \quad (3.53)$$

$$4 \sum_{\alpha\gamma\delta} \bar{v}_{\alpha\delta\alpha,-\gamma} (-1)^{j_c - m_\gamma} v_a^2 u_d v_c (a_\gamma^\dagger a_\delta^\dagger + a_\delta a_\gamma) = 4 \sum_{acd} [\hat{j}_c]^{-1} v_a^2 u_d v_c \\ \times \sum_J \hat{J}^2 [\mathcal{N}_{ad}(J) \mathcal{N}_{ac}(J)]^{-1} \delta_{j_d j_c} \langle ad; J|V|ac; J \rangle \left([a_c^\dagger a_d^\dagger]_{00} - [\tilde{a}_d \tilde{a}_c]_{00} \right), \quad (3.54)$$

$$\sum_{\alpha\gamma\delta} \bar{v}_{\alpha,-\alpha,\gamma\delta} (-1)^{j_a + m_\alpha} u_a v_a (v_c v_d - u_c u_d) (a_\gamma^\dagger a_\delta^\dagger + a_\delta a_\gamma) = \sqrt{2} \sum_{acd} \hat{j}_a u_a v_a \\ \times (u_c u_d - v_c v_d) [\mathcal{N}_{cd}(0)]^{-1} \delta_{j_c j_d} \langle aa; 0|V|cd; 0 \rangle \left([a_c^\dagger a_d^\dagger]_{00} - [\tilde{a}_d \tilde{a}_c]_{00} \right). \quad (3.55)$$

In the same spirit, the one-body kinetic energy, i.e. the first sum in Eq.(3.46), takes the form

$$T = \sum_\alpha \varepsilon_\alpha c_\alpha^\dagger c_\alpha = \sum_a \varepsilon_a \hat{j}_a^2 v_a^2 + \sum_a \varepsilon_a \hat{j}_a (u_a^2 - v_a^2) [a_a^\dagger \tilde{a}_a]_{00} \\ + \sum_a \varepsilon_a \hat{j}_a u_a v_a \left([a_a^\dagger a_a^\dagger]_{00} - [\tilde{a}_a \tilde{a}_a]_{00} \right). \quad (3.56)$$

Following [38] (within a good approximation it is reasonable to make the replacement $\delta_{j_c j_d} \rightarrow \delta_{cd}$) and after collecting all terms for the Eqs.(3.50–3.56),

the quasi-particle representation of the nuclear Hamiltonian can be cast in the form

$$H = H_0 + \sum_b H_{11}(b) [a_b^\dagger \tilde{a}_b]_{00} + \sum_b H_{20}(b) \left([a_b^\dagger a_b^\dagger]_{00} - [\tilde{a}_b \tilde{a}_b]_{00} \right) + V_{\text{res}}, \quad (3.57)$$

where

$$\begin{aligned} H_0 = & \sum_a \varepsilon_a \hat{j}_a^2 v_a^2 + \frac{1}{2} \sum_{abJ} v_a^2 v_b^2 \hat{J}^2 [\mathcal{N}_{ab}(J)]^{-2} \langle ab; J | V | ab; J \rangle \\ & + \frac{1}{2} \sum_{ab} \hat{j}_a \hat{j}_b u_a v_a u_b v_b \langle aa; 0 | V | bb; 0 \rangle, \end{aligned} \quad (3.58)$$

$$\begin{aligned} H_{11}(b) = & \varepsilon_b \hat{j}_b (u_b^2 - v_b^2) - 2u_b v_b \sum_a \hat{j}_a u_a v_a \langle aa; 0 | V | bb; 0 \rangle \\ & + [\hat{j}_b]^{-1} (u_b^2 - v_b^2) \sum_{aJ} v_a^2 [\mathcal{N}_{ab}(J)]^{-2} \langle ab; J | V | ab; J \rangle, \end{aligned} \quad (3.59)$$

$$\begin{aligned} H_{20}(b) = & \varepsilon_b \hat{j}_b u_b v_b + [\hat{j}_b]^{-1} u_b v_b \sum_{aJ} v_a^2 \hat{J}^2 [\mathcal{N}_{ab}(J)]^{-2} \langle ab; J | V | ab; J \rangle \\ & + \frac{1}{2} (u_b^2 - v_b^2) \sum_a \hat{j}_a u_a v_a \langle aa; 0 | V | bb; 0 \rangle. \end{aligned} \quad (3.60)$$

Eventually, the residual two-body interaction is compactly expressed in its normal ordered form with respect to the BCS vacuum, as

$$V_{\text{res}} = \frac{1}{4} \sum_{\alpha\beta\gamma\delta} \bar{v}_{\alpha\beta\gamma\delta} \mathcal{N} \left[c_\alpha^\dagger c_\beta^\dagger c_\delta c_\gamma \right]_{BCS}. \quad (3.61)$$

Further manipulation leads to $V_{\text{res}} \equiv H_{40} + H_{31} + H_{22}$ (for details, see Appendix D.4).

3.4.5 BCS equations

The BCS equations can be derived by minimising the BCS ground-state expectation value

$$E = \langle BCS | H | BCS \rangle, \quad (3.62)$$

which can be viewed as a constrained variational problem with respect to the occupation amplitudes u_α and v_α . To this purpose, the weak point of the method (i.e. the non-conservation of the particle number as mentioned in Subsect. 3.4.1) serves as the actual tool to (self-) heal it. More specifically, the variational problem is forced to reproduce the correct average particle number, $\bar{n} \equiv (Z, N)$, subject to the constraint

$$\langle BCS | H | BCS \rangle = \bar{n}. \quad (3.63)$$

Towards this direction, the number operator given in Eq.(3.17) is written [analogously to Eq.(3.56)] as

$$\begin{aligned} \hat{n} = \sum_{\alpha} c_{\alpha}^{\dagger} c_{\alpha} &= \sum_a \hat{j}_a^2 v_a^2 + \sum_a \hat{j}_a^2 (u_a^2 - v_a^2) [a_a^{\dagger} \tilde{a}_a^{\dagger}]_{00} \\ &+ \sum_a \hat{j}_a^2 u_a v_a ([a_a^{\dagger} a_a^{\dagger}]_{00} - [\tilde{a}_a^{\dagger} \tilde{a}_a^{\dagger}]_{00}) . \end{aligned} \quad (3.64)$$

In this respect, \bar{n} acquires contributions only from the constant term of the above expression and therefore

$$\bar{n} = \sum_a \hat{j}_a^2 v_a^2 . \quad (3.65)$$

In numerical calculations, protons and neutrons are treated separately (proton-neutron pairing is ignored). The variational problem is then solved by employing the method of the Lagrange multipliers (in order to become unconstrained) which enter via the definition of the auxiliary X•amiltonian

$$\mathcal{H} \equiv H - \lambda n . \quad (3.66)$$

In this context, the parameter λ , namely the chemical potential (or the Fermi energy), is determined through the variational problem

$$\delta \langle BCS | \mathcal{H} | BCS \rangle = 0 , \quad (3.67)$$

or equivalently

$$\delta \left(H_0 - \lambda \sum_a \hat{j}_a^2 v_a^2 \right) \equiv \delta \mathcal{H}_0 = 0 . \quad (3.68)$$

Recalling Eq.(3.58), we simply write

$$\begin{aligned} \mathcal{H}_0 &= \sum_a (\varepsilon_a - \lambda) \hat{j}_a^2 v_a^2 + \frac{1}{2} \sum_{abJ} v_a^2 v_b^2 \hat{J}^2 [\mathcal{N}_{ab}(J)]^{-2} \langle ab; J | V | ab; J \rangle \\ &+ \frac{1}{2} \sum_{ab} \hat{j}_a \hat{j}_b u_a v_a u_b v_b \langle aa; 0 | V | bb; 0 \rangle , \end{aligned} \quad (3.69)$$

thus, the single-particle energies ε_a are sifted as $\varepsilon_a \rightarrow \varepsilon_a - \lambda$, which implies that $\mathcal{H}_0|_{\varepsilon} = H_0|_{\varepsilon-\lambda}$ (the same occurs for H_{11} and H_{20}). At this stage, it is convenient to introduce the following abbreviations

$$\begin{aligned} \Delta_b &\equiv - \left[\hat{j}_b \right]^{-1} \sum_a \hat{j}_a u_a v_a \langle aa; 0 | V | bb; 0 \rangle , \\ \mu_b &\equiv - \left[\hat{j}_b \right]^{-2} \sum_{aJ} v_a^2 \hat{J}^2 [\mathcal{N}_{ab}(J)]^{-2} \langle ab; J | V | ab; J \rangle , \\ \eta_b &\equiv \varepsilon_b - \lambda - \mu_b , \end{aligned} \quad (3.70)$$

which correspond to physical quantities (see below) and write

$$\mathcal{H}_0 = \sum_b \hat{j}_b^2 \left[v_b^2 \left(\eta_b + \frac{1}{2} \mu_b \right) - \frac{1}{2} u_b v_b \Delta_b \right], \quad (3.71)$$

$$\mathcal{H}_{11}(b) = \hat{j}_b \left[(u_b^2 - v_b^2) \eta_b + 2u_b v_b \Delta_b \right], \quad (3.72)$$

$$\mathcal{H}_{20}(b) = \hat{j}_b \left[u_b v_b \eta_b - \frac{1}{2} (u_b^2 - v_b^2) \Delta_b \right]. \quad (3.73)$$

The quantity Δ_b is called the pairing-gap (for more details see Subsect. 3.4.6 below). The quantity μ_a , namely the self-energy, describes a renormalisation of the single-particle energy, ε_a , due to the fact that the energy of a nucleon in the orbital, a , gets additional contributions from its interactions with the other nucleons. The physical interpretation of the chemical potential, λ , is understood as follows. From the definition of the auxiliary Hamiltonian given in Eq.(3.66), we have

$$\mathcal{H}_0 = \langle BCS | H | BCS \rangle - \lambda n. \quad (3.74)$$

The number constraint in the variational problem means that the derivative of \mathcal{H}_0 with respect to the particle number, n , must vanish at the correct required particle number, i.e. $n = \bar{n}$. Taking the derivative of the latter expression with respect to n and setting it to zero yields

$$\lambda = \left. \frac{\partial}{\partial n} \langle BCS | H | BCS \rangle \right|_{n=\bar{n}}. \quad (3.75)$$

The latter expression describes how much the energy of the BCS ground state increases when one particle is added to it.

3.4.6 The gap equation

To perform the variational calculation that leads to the BCS equations, taking also into consideration Eq.(3.16)³, we require that

$$\frac{\partial}{\partial v_c} \mathcal{H}_0 = 0, \quad \text{for all } c. \quad (3.76)$$

³This also gives

$$\frac{\partial u_b}{\partial v_c} = -\delta_{bc} \frac{v_c}{u_c}.$$

This requirement yields the result

$$\begin{aligned}
0 = \frac{\partial}{\partial v_c} \mathcal{H}_0 &= \sum_b \hat{j}_b^2 \left[-\frac{1}{2} v_b^2 \frac{\partial \mu_b}{\partial v_c} + 2v_b \delta_{bc} \left(\eta_b + \frac{1}{2} \mu_b \right) \right. \\
&\quad \left. - \frac{1}{2} u_b v_b \frac{\partial \Delta_b}{\partial v_c} - \frac{1}{2} u_b \delta_{bc} \Delta_b + \frac{1}{2} \delta_{bc} \frac{v_b}{u_c} v_b \Delta_b \right] \\
&= v_c \sum_{bJ} v_b^2 \hat{J}^2 [\mathcal{N}_{bc}(J)]^{-2} \langle bc; J|V|bc; J \rangle + 2\hat{j}_c^2 v_c \left(\eta_c + \frac{1}{2} \mu_c \right) \\
&\quad + \hat{j}_c \frac{u_c^2 - v_c^2}{2u_c} \sum_b \hat{j}_b u_b v_b \langle bb; 0|V|cc; 0 \rangle - \frac{1}{2} \hat{j}_c^2 u_c \Delta_c + \frac{1}{2} \hat{j}_c^2 \frac{v_c^2}{u_c} \Delta_c \\
&= 2\hat{j}_c^2 v_c \eta_c + \hat{j}_c^2 \frac{v_c^2 - u_c^2}{u_c} \Delta_c,
\end{aligned} \tag{3.77}$$

where by using Eq.(3.30) we have performed the derivatives

$$\begin{aligned}
\frac{\partial}{\partial v_c} \left(\eta_b + \frac{1}{2} \mu_b \right) &= -\frac{1}{2} \frac{\partial \mu_b}{\partial v_c}, \\
\frac{\partial \mu_b}{\partial v_c} &= -2 \left[\hat{j}_b \right]^{-2} v_c \sum_J \hat{J}^2 [\mathcal{N}_{bc}(J)]^{-2} \langle bc; J|V|bc; J \rangle, \\
\frac{\partial \Delta_b}{\partial v_c} &= -\left[\hat{j}_b \right]^{-1} \hat{j}_c \frac{u_c^2 - v_c^2}{u_c} \langle bb; 0|V|cc; 0 \rangle.
\end{aligned} \tag{3.78}$$

Then, Eq.(3.77) implies that

$$(u_c^2 - v_c^2) \Delta_c = 2u_c v_c \eta_c, \tag{3.79}$$

or by squaring both sides

$$u_c^2 v_c^2 = \frac{\Delta_c^2}{4(\eta_c^2 + \Delta_c^2)}. \tag{3.80}$$

The latter, is solved with respect to the occupation amplitudes giving

$$\begin{aligned}
u_c &= \frac{1}{\sqrt{2}} \sqrt{1 + \frac{\eta_c}{E_c}}, \\
v_c &= \frac{1}{\sqrt{2}} \sqrt{1 - \frac{\eta_c}{E_c}},
\end{aligned} \tag{3.81}$$

where the quasi-particle energy reads

$$E_c \equiv \sqrt{\eta_c^2 + \Delta_c^2}. \tag{3.82}$$

Substituting the positive root of Eq.(3.80), i.e.

$$u_c v_c = \frac{\Delta_c}{2E_c} \tag{3.83}$$

into the expression for Δ_b as given in Eq.(3.70), yields the so-called gap-equation

$$2\hat{j}_b\Delta_b = -\sum_a \frac{\hat{j}_a\Delta_a}{\sqrt{\eta_a^2 + \Delta_a^2}} \langle aa; 0|V|bb; 0 \rangle. \quad (3.84)$$

By inserting the conditions of Eqs.(3.79),(3.81),(3.84) in Eq.(3.73), one finds

$$\begin{aligned} \mathcal{H}_0 &= \frac{1}{2} \sum_b \frac{\hat{j}_b^2}{E_b} \left[(E_b - \eta_b) \left(\eta_b + \frac{1}{2}\mu_b \right) - \frac{1}{2}\Delta_b^2 \right], \\ \mathcal{H}_{11}(b) &= \hat{j}_b E_b, \\ \mathcal{H}_{20}(b) &= 0, \end{aligned} \quad (3.85)$$

and thus, the auxiliary Hamiltonian in terms of the quasi-particle energy, E_b , takes the form

$$\mathcal{H} = \mathcal{H}_0 + \sum_b \hat{j}_b E_b \left[a_b^\dagger \tilde{a}_b \right]_{00} + V_{\text{res}}. \quad (3.86)$$

The first two terms entering the above Hamiltonian, carry a large part of the original residual interaction and they describe non-interacting quasi-particles with energies E_b . The residual interaction, V_{res} , produces configuration mixing between many-quasi-particle states. In the present Thesis, this mixing is handled within the framework of the quasi-particle random phase approximation (QRPA) (see Sect. 3.5).

The constant term, H_0 , in the definition of the original nuclear Hamiltonian takes the form

$$H_0 = \mathcal{H}_0 + \lambda \sum_a \hat{j}_a^2 v_a^2 = \mathcal{H}_0 + \lambda \bar{n}, \quad (3.87)$$

which may be rewritten by combining Eq.(3.73) with Eq.(3.81), as follows

$$H_0 = \frac{1}{2} \sum_b \frac{\hat{j}_b^2}{E_b} \left[(E_b - \eta_b) \left(\varepsilon_b - \frac{1}{2}\mu_b \right) - \frac{1}{2}\Delta_b^2 \right]. \quad (3.88)$$

3.4.7 Pairing interaction in the Bonn C-D potential

The Bonn Full Model (BFM), is considered as a comprehensive phenomenological meson-exchange theory for the reliable description of the nucleon-nucleon interaction [52]. Within the framework of the BFM, the concept of meson-exchange for nuclear forces as well as its validity range may be systematically tested, representing a good point of departure for alternative theories (on the basis of quark models, chiral perturbation theory, etc.) towards explaining the nuclear force. In this context the predicted charge-dependence (C-D), i.e. the invariance under any rotation in isospin space, is reproduced accurately through a refinement of the BFM, namely the Bonn C-D potential [53]. The off-shell behaviour of Bonn C-D

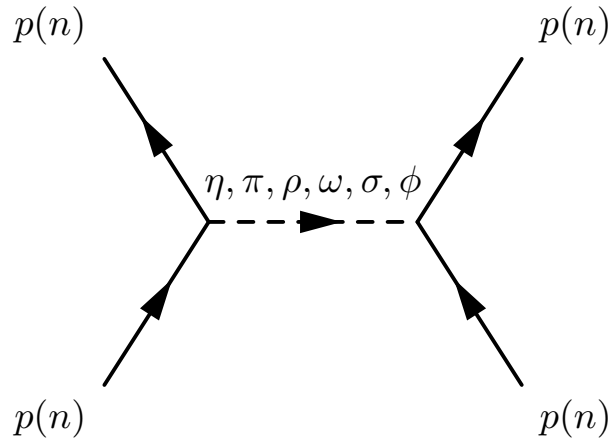


Figure 3.2: Tree level meson-exchange Feynman diagrams describing the nucleon-nucleon interaction (Bonn C-D potential).

is based upon the relativistic Feynman amplitudes for meson-exchange, thus it differs off-shell from conventional nucleon-nucleon potentials, a fact that has attractive consequences in nuclear structure applications [54]. Our QRPA code, for the two-nucleon residual interaction utilises the C-D version of the well-known Bonn potential. The mesons, η , π , ρ , ω , σ , ϕ with spin and isospin $(J^\pi, T) = (0^-, 0)$, $(0^-, 1)$, $(1^-, 1)$, $(1^-, 0)$, $(0^+, 0)$, $(1^-, 0)$ respectively, that are assumed to mediate the strong interaction are indicated in the relevant Feynman diagrams shown in Fig. 3.2.

As has been stressed in Ref. [38], the interaction of pairs with $J = 0$ is much stronger than those with $J \neq 0$ pairs. Therefore, we may consider the interaction in a single j shell by making the approximation that only the $J = 0$ channel contributes. Starting from the general two-body interaction of Eq.(3.39), we

write

$$\begin{aligned}
V_{res} &= -\frac{1}{2} \sum_J \hat{J} \langle jj; J | V | jj; J \rangle \left[[c_j^\dagger c_j^\dagger]_J [\tilde{c}_j \tilde{c}_j]_J \right]_{00} \\
&= -\frac{1}{2} \sum_J \hat{J} \langle jj; J | V | jj; J \rangle \left[[c_j^\dagger c_j^\dagger]_J [\tilde{c}_j \tilde{c}_j]_J \right]_{00} \\
&\stackrel{\text{pairing}}{\approx} -\frac{1}{2} \langle jj; 0 | V | jj; 0 \rangle [c_j^\dagger c_j^\dagger]_0 [\tilde{c}_j \tilde{c}_j]_0 \\
&= -\frac{1}{2} \langle jj; 0 | V | jj; 0 \rangle \left[\hat{j} \right]^{-2} \sum_{mm'} (-1)^{j-m+j-m'} c_{jm}^\dagger c_{j,-m}^\dagger \tilde{c}_{jm'} \tilde{c}_{j,-m'} \\
&= \frac{1}{2} \langle jj; 0 | V | jj; 0 \rangle \left[\hat{j} \right]^{-2} \sum_{mm'} c_{jm}^\dagger \tilde{c}_{jm}^\dagger \tilde{c}_{jm'} c_{jm'} \\
&= 2 \langle jj; 0 | V | jj; 0 \rangle \left[\hat{j} \right]^{-2} \sum_{\substack{m>0 \\ m'>0}} c_{jm}^\dagger \tilde{c}_{jm}^\dagger \tilde{c}_{jm'} c_{jm'} ,
\end{aligned} \tag{3.89}$$

where we have used the anticommutation relations of Eq.(3.22) and the simple Clebsch-Gordan coefficient $(jmjm'|00) = (-1)^{j-m} \left[\hat{j} \right]^{-1} \delta_{m,-m'}$.

For the reliable description of the nucleon-nucleon interaction in the dense nuclear medium, our code solves the Bethe-Goldstone equation which yields the two-nucleon matrix elements of the residual interaction within a given model space. Thus, by employing the Bonn C-D potential as the residual interaction, we obtain the G-matrix elements. In the particular case of the pairing interaction, by introducing the abbreviation

$$2 \langle jj; 0 | V | jj; 0 \rangle \hat{j}^{-2} \equiv -G , \tag{3.90}$$

the pairing interaction, V_{pair} , for a single j shell takes the form

$$V_{pair} = -G \sum_{mm'>0} c_{jm}^\dagger \tilde{c}_{jm}^\dagger \tilde{c}_{jm'} c_{jm'} . \tag{3.91}$$

For completeness, we also give its generalisation to several j shells , as

$$V_{pair} = -G \sum_{jj'} \sum_{mm'>0} c_{jm}^\dagger \tilde{c}_{jm}^\dagger \tilde{c}_{j'm'} c_{j'm'} . \tag{3.92}$$

(in our case it includes all shells of the chosen model space). It is worth noting that the pairing interaction is a short range attractive force, thus G is positive.

For a single j shell the above pairing interaction is diagonalised as follows. We choose the single-particle energies as $\varepsilon_j = 0$ and the two-particle basis states to be

$$A_{jm}^\dagger |0\rangle \equiv c_{jm}^\dagger \tilde{c}_{jm}^\dagger |0\rangle, \quad m > 0 . \tag{3.93}$$

The relevant matrix elements read

$$\begin{aligned} \langle 0 | A_{jm} V_{pair} A_{jm'}^\dagger | 0 \rangle &= -G \sum_{m_1 m_2 > 0} \langle 0 | \tilde{c}_{jm} c_{jm} c_{jm_1}^\dagger \tilde{c}_{jm_1}^\dagger \tilde{c}_{jm_2} c_{jm_2} c_{jm'}^\dagger \tilde{c}_{jm'}^\dagger | 0 \rangle \\ &= -G. \end{aligned} \quad (3.94)$$

Then, the interaction matrix is

$$V_{pair} = -G \begin{pmatrix} 1 & 1 & \cdots & 1 \\ 1 & 1 & \cdots & 1 \\ \vdots & \vdots & \ddots & \vdots \\ 1 & 1 & \cdots & 1 \end{pmatrix}, \quad (3.95)$$

being an $\Omega \times \Omega$ matrix, where

$$\Omega \equiv \frac{1}{2}(2j+1) \quad (3.96)$$

is the pair degeneracy.

After diagonalising the latter matrix, the eigenstate that is associated to the lowest eigenvalue takes the form

$$|\Psi_1\rangle = \frac{1}{\sqrt{\Omega}} \begin{pmatrix} 1 \\ 1 \\ \vdots \\ 1 \end{pmatrix}, \quad (3.97)$$

which in occupation number representation is written as

$$\begin{aligned} |\Psi_1\rangle &= \frac{1}{\sqrt{\Omega}} \sum_{m>0} A_{jm}^\dagger |0\rangle = \frac{1}{\sqrt{2}} \sum_m \frac{(-1)^{j+m}}{\hat{j}} c_{jm}^\dagger c_{j,-m}^\dagger |0\rangle \\ &= -\frac{1}{\sqrt{2}} [c_j^\dagger c_j^\dagger]_{00} |0\rangle \\ &= -|j^2; J=0, M=0\rangle. \end{aligned} \quad (3.98)$$

This result implies that the diagonalisation of the pairing matrix in the uncoupled basis indeed gives a zero-coupled pair as the lowest eigenstate.

From the above discussion we extract the following concluding remarks. The behaviour of the pairing force is understood as a direct consequence of its definition. Specifically, the $J \neq 0$ pairs are non-interacting and remain at their unperturbed energy $2\varepsilon_j$. On the other hand, the $J = 0$ pairs are interacting and are lowered in energy by the attractive force.

In analogy to the above description, the pair creation operator is defined as

$$A^\dagger \equiv \frac{1}{\sqrt{\Omega}} \sum_{m>0} A_{jm}^\dagger = \frac{1}{\sqrt{\Omega}} \sum_{m>0} c_{jm}^\dagger \tilde{c}_{jm}^\dagger, \quad (3.99)$$

that creates a zero-coupled pair. The pairing interaction operator is subsequently written as

$$V_{pair} = -G\Omega A^\dagger A. \quad (3.100)$$

Furthermore, in this framework by defining the particle number operator, as

$$\hat{n} \equiv \sum_m c_{jm}^\dagger c_{jm} = \sum_{m>0} \left(c_{jm}^\dagger c_{jm} + \tilde{c}_{jm}^\dagger \tilde{c}_{jm} \right), \quad (3.101)$$

the following commutation relations hold

$$\begin{aligned} [A, A^\dagger] &= 1 - \hat{n}/\Omega, \\ [A^\dagger, \hat{n}] &= -2A^\dagger, \\ [V_{pair}, A^\dagger] &= -GA^\dagger(\Omega - \hat{n}) = -G(\Omega - \hat{n} + 2)A^\dagger. \end{aligned} \quad (3.102)$$

3.5 Quasi-particle random phase approximation (QRPA)

A general quasi-particle pair, i.e. a pair referred to two orbitals a and b , coupled to angular momentum J with projection M and parity π , is described by the operator

$$A_{ab}^\dagger(JM) = \mathcal{N}_{ab}(J) [a_a^\dagger a_b^\dagger]_{JM}, \quad (3.103)$$

while its hermitian conjugate is

$$\tilde{A}_{ab}(JM) = (-1)^{J+M} A_{ab}(J, -M) = -\mathcal{N}_{ab}(J) [\tilde{a}_a \tilde{a}_b]_{JM}. \quad (3.104)$$

An appropriate framework to accommodate the pair excitations of the quasi-particles from the ground state is the so-called quasi-particle random phase approximation (QRPA). In the present Thesis, after constructing the quasi-particle base through the solution of the BCS equations, we proceed by performing QRPA calculations in order to find the excited states of the studied nuclear isotopes. As we will see below, for each nuclear system, our computational method takes into account the residual interaction, which is renormalised through the parameters g^{ph} (particle-hole) and g^{pp} (particle-particle).

In this context, the QRPA excitation, $|\omega\rangle$, is defined in terms of the QRPA phonon creation operator, Q_ω^\dagger , as

$$|\omega\rangle = Q_\omega^\dagger |QRPA\rangle, \quad (3.105)$$

whereas the QRPA vacuum reads

$$Q_\omega |QRPA\rangle = 0, \quad \text{for all } \omega. \quad (3.106)$$

The QRPA excitation operator (QRPA phonon creation operator), Q_ω^\dagger , can be cast in the form

$$Q_\omega^\dagger = \sum_{a \leq b} \left[X_{ab}^\omega A_{ab}^\dagger(JM) - Y_{ab}^\omega \tilde{A}_{ab}^\dagger(JM) \right]. \quad (3.107)$$

The annihilation operator (that deletes the vacuum), is the hermitian conjugate of the latter

$$Q_\omega = \sum_{a \leq b} \left[X_{ab}^{\omega*} A_{ab}(JM) - Y_{ab}^{\omega*} \tilde{A}_{ab}^\dagger(JM) \right]. \quad (3.108)$$

We note that from Eq.(3.107), it can be seen that $Q_\omega^\dagger |BCS\rangle \neq 0$, meaning that the BCS vacuum is not the vacuum for the QRPA.

In the previous expressions we defined $\omega = nJ^\pi M$, where the quantum number, n , stands for the different QRPA solutions that correspond to the same value of angular momentum and parity, while the summation is restricted to avoid double counting. The scattering amplitudes are introduced to describe forward-scattering X_{ab}^ω , and back-scattering Y_{ab}^ω respectively. They obey the orthogonality as well as the completeness condition. Eventually, we stress that the amplitude, Y_{ab}^ω , is required to be small in order to prevent QRPA breaking. Furthermore, the QRPA equations can be obtained and expressed through the commutators, as

$$\langle QRPA | [A_{ab}, \mathcal{H}, Q_\omega^\dagger] | QRPA \rangle = E_\omega \langle QRPA | [A_{ab}, Q_\omega^\dagger] | QRPA \rangle, \quad (3.109)$$

$$\langle QRPA | [\tilde{A}_{ab}^\dagger, \mathcal{H}, Q_\omega^\dagger] | QRPA \rangle = E_\omega \langle QRPA | [\tilde{A}_{ab}^\dagger, Q_\omega^\dagger] | QRPA \rangle, \quad (3.110)$$

where, E_ω is the excitation energy of the nuclear state.

The two quasi-particle operators, A_{ab}^\dagger and \tilde{A}_{ab} [see Eqs.(3.103) and (3.104)], have been obtained under the assumption of the quasi-boson approximation (QBA). This allows us to substitute the exact QRPA ground state with that of the BCS ground state (see Appendix D.3)⁴. Thus, the QRPA operators satisfy the bosonic condition

$$[Q_\omega, Q_{\omega'}^\dagger] = \delta_{\omega\omega'}, \quad (3.111)$$

which represents the expectation value of the operator of two QRPA phonons with respect to the BCS vacuum. As a consequence, the QRPA equations are not derived through a variational principle.

The (non-hermitian) eigenvalue problem, i.e. the charge conserving QRPA equations, are then written in matrix form as

$$\begin{pmatrix} \mathcal{A} & \mathcal{B} \\ -\mathcal{B}^* & -\mathcal{A}^* \end{pmatrix} \begin{pmatrix} X^\omega \\ Y^\omega \end{pmatrix} = E_\omega \begin{pmatrix} X^\omega \\ Y^\omega \end{pmatrix}. \quad (3.112)$$

⁴We consider $|QRPA\rangle = |BCS\rangle +$ small corrections, where the small corrections are four-quasi-particle, eight-quasi-particle, etc., components.

The QRPA matrices satisfy the relations $\mathcal{A}^\dagger = \mathcal{A}$ (i.e. hermitian) and $\mathcal{B}^T = \mathcal{B}$ (i.e. symmetric). In the BCS ground state, the QRPA matrices $\mathcal{A}(J)$, $\mathcal{B}(J)$ have elements

$$A_{ab,cd}(J) \equiv \langle BCS | \left[A_{ab}(JM), \mathcal{H}, A_{cd}^\dagger(JM) \right] | BCS \rangle, \quad (3.113)$$

$$B_{ab,cd}(J) \equiv -\langle BCS | \left[A_{ab}(JM), \mathcal{H}, \tilde{A}_{cd}(JM) \right] | BCS \rangle. \quad (3.114)$$

Since the matrix elements of the two latter expressions are independent of M , the scattering amplitudes entering the QRPA equations (3.112) must be also independent of M .

The hermitian matrix, \mathcal{A} , is called the QTDA matrix (after quasi-particle Tamm-Dancoff Approximation), since it can be solved by employing a simple quasi-particle pair approximation, namely the Quasi-particle Tamm-Dancoff Approximation. The symmetric matrix, \mathcal{B} , is introduced due to the more complicated QRPA excitation and is called the correlation matrix. It can be written as

$$B_{ab,cd}(J) = \langle BCS | A_{ab}(JM) \tilde{A}_{cd}(JM) \mathcal{H} | BCS \rangle, \quad (3.115)$$

(the explicit expression for the matrix elements is shown in Appendix D.5).

The application of the QBA approximation yields the relations for the orthogonality

$$\sum_{a < b} \left(X_{ab}^{nJ\pi*} X_{ab}^{n'J\pi} - Y_{ab}^{nJ\pi*} Y_{ab}^{n'J\pi} \right) = \delta_{nn'}, \quad (3.116)$$

and the relations for the completeness (or closure)

$$\sum_n \left(X_{ab}^{nJ\pi} X_{cd}^{nJ\pi*} - Y_{ab}^{nJ\pi*} Y_{cd}^{nJ\pi} \right) = \delta_{ac} \delta_{bd} \quad a \leq b, \quad c \leq d, \quad (3.117)$$

$$\sum_n \left(X_{ab}^{nJ\pi} Y_{cd}^{nJ\pi*} - Y_{ab}^{nJ\pi*} X_{cd}^{nJ\pi} \right) = 0, \quad a \leq b, \quad c \leq d. \quad (3.118)$$

From the above expressions, we conclude that the QRPA solutions are doubled and only the positive-energy solutions are physical. Hence, the eigenvalue index, n , in the completeness relations Eq.(3.117) and Eq.(3.118) runs only over the positive-energy solutions. These can be combined in matrix form as

$$\sum_{\substack{n \\ E_n > 0}} \left[\begin{pmatrix} X^\omega \\ Y^\omega \end{pmatrix} (X^{\omega\dagger}, -Y^{\omega\dagger}) - \begin{pmatrix} Y^{\omega*} \\ X^{\omega*} \end{pmatrix} (Y^{\omega T}, -X^{\omega T}) \right] = \begin{pmatrix} 1 & 0 \\ 0 & 1 \end{pmatrix}. \quad (3.119)$$

It should be mentioned that for a sufficiently strong two-body interaction the QRPA problem breaks down. In this case, the lowest root of the QRPA equation (3.112) becomes imaginary, emphasising the need for a deformed mean field as the starting point of the calculation. The dynamics of the breaking point can be tangibly seen in the elementary case of one active two-quasi-particle excitation. In actual QRPA calculations, the bare two-body interaction is renormalised

with the aid of two parameters. The first multiplies the particle-particle interaction (g^{pp}) and the second the particle-hole interaction (g^{ph}). By adjusting these parameters, we modify the QRPA solution so as physical energy eigenvalues (reproducing the experimental spectrum) to be obtained.

3.5.1 The proton-proton and neutron-neutron QRPA

For the charge conserving nuclear reactions we are interested in the present study, the appropriate type of QRPA is the so called proton-proton and neutron-neutron QRPA (pp-nn QRPA). In this case, the structure of the correlation QRPA matrix, \mathcal{B} , has the general form

$$\mathcal{B} = \begin{pmatrix} V_{QRPA}(pp - pp) & V_{QRPA}(pp - nn) \\ V_{QRPA}(nn - pp) & V_{QRPA}(nn - nn) \end{pmatrix}. \quad (3.120)$$

In the previous Section, it has been mentioned that the correlation matrix is symmetric. Thus, if the proton and neutron two-quasi-particle bases are the same, the non-diagonal blocks are symmetric. Moreover, when the single-particle energies and interactions are the same for protons and neutrons the diagonal blocks are the same [38].

The $pp - pp$ and $nn - nn$ blocks contain proton-proton and neutron-neutron matrix elements, while the $pp - nn$ and $nn - pp$ blocks contain only particle-hole matrix elements. For instance, the $pp - pp$ blocks in isospin notation are expressed as

$$\begin{aligned} \langle p_1 p_2^{-1}; J | V_{res} | p_3 p_4^{-1}; J \rangle &\rightarrow \langle a_1 a_4; J'T = 1 | V | a_3 a_2; J'T = 1 \rangle, \\ \langle p_1 p_2^{-1}; J | V_{res} | p_4 p_3^{-1}; J \rangle &\rightarrow \langle a_1 a_3; J'T = 1 | V | a_4 a_2; J'T = 1 \rangle, \end{aligned} \quad (3.121)$$

(the neutron-neutron case is trivially obtained) while the matrix elements for the $pp - nn$ and $nn - pp$ blocks read

$$\begin{aligned} \langle p_1 p_2^{-1}; J | V_{res} | n_3 n_4^{-1}; J \rangle &\rightarrow \langle a_1 a_4; J'T = 1, 0 | V | a_3 a_2; J'T = 1, 0 \rangle, \\ \langle p_1 p_2^{-1}; J | V_{res} | n_4 n_3^{-1}; J \rangle &\rightarrow \langle a_1 a_3; J'T = 1, 0 | V | a_4 a_2; J'T = 1, 0 \rangle. \end{aligned} \quad (3.122)$$

To proceed, we make use of the known Pandya transformation and define the quantities

$$\begin{aligned} \mathcal{M}_{abcd}^{(1)}(J) &\equiv - \sum_{J'} \hat{J}'^2 [\mathcal{N}_{ad}(J') \mathcal{N}_{cb}(J')]^{-1} \begin{Bmatrix} j_a & j_b & J \\ j_c & j_d & J' \end{Bmatrix} \\ &\times \langle ad; J'1 | V_{res} | cb; J'1 \rangle_{A_1=1}, \end{aligned} \quad (3.123)$$

and

$$\begin{aligned} \mathcal{M}_{abcd}^{(2)}(JT) &\equiv \frac{1}{2} (-1)^T \sum_{J'} \hat{J}'^2 \sqrt{[1 - (-1)^{J'+T} \delta_{ad}][1 - (-1)^{J'+T} \delta_{cb}]} \\ &\times \begin{Bmatrix} j_a & j_b & J \\ j_c & j_d & J' \end{Bmatrix} \langle ad; J'T | V_{res} | cb; J'T \rangle_{A_T=1}. \end{aligned} \quad (3.124)$$

Then, the particle-hole matrix elements are given by $\mathcal{M}_{phph}^{(1)}(J)$ and $\mathcal{M}_{phph}^{(2)}(JT)$, as

$$\begin{aligned} \langle p_1 p_2^{-1}; J | V_{res} | p_3 p_4^{-1}; J \rangle &= \langle n_1 n_2^{-1}; J | V_{res} | n_3 n_4^{-1}; J \rangle \\ &= A_1 \mathcal{M}_{a_1 a_2 a_3 a_4}^{(1)}(J), \end{aligned} \quad (3.125)$$

$$\begin{aligned} \langle p_1 p_2^{-1}; J | V_{res} | n_3 n_4^{-1}; J \rangle &= \langle n_1 n_2^{-1}; J | V_{res} | p_3 p_4^{-1}; J \rangle \\ &= A_1 \mathcal{M}_{a_1 a_2 a_3 a_4}^{(2)}(J1) + A_0 \mathcal{M}_{a_1 a_2 a_3 a_4}^{(2)}(J0). \end{aligned} \quad (3.126)$$

3.6 Evaluation of the nuclear form factors

3.6.1 Nuclear Structure calculations

The main nuclear physics aspects of the present Thesis are studied through a detailed evaluation of the nuclear form factor $F(\mathbf{q}^2)$ of the nuclear system in question. Towards this aim, at first, we study the nuclear structure details of the matrix elements entering the neutrino-nucleus cross sections discussed in Chapt. 4–8. Such results reflect the dependence of the coherent cross section on the incident-neutrino energy E_ν and the scattering angle θ (or the recoil energy T_N). We mention that for the even-even nuclei this study involves realistic QRPA calculations for the differential cross sections $d\sigma_{\nu\alpha}/d\cos\theta$ and $d\sigma_{\nu\alpha}/dT_N$, performed after constructing the nuclear ground state, $|g.s.\rangle$, by solving iteratively the BCS equations (see Sect. 3.4.5). The solution of these equations provides the probability amplitudes $u_{N_n}^j$ and $v_{N_n}^j$ of the j -th single nucleon level to be occupied or unoccupied, respectively [see Eq.(3.81)]. Moreover, the latter equations provide the single quasi-particle energies, based on the single-particle energies of the nuclear field (a Coulomb corrected Woods-Saxon potential in our case) as well as the pairing part of the residual two-body interaction (Bonn C-D potential in our case).

The nuclear form factors for protons (neutrons) are obtained as [55]

$$F_{N_n}(\mathbf{q}^2) = \frac{1}{N_n} \sum_j \hat{j} \langle j | j_0(|\mathbf{q}|r) | j \rangle (v_{N_n}^j)^2, \quad (3.127)$$

with $N_n = Z$ (or N). For each nuclear system studied, the chosen active model space, the Harmonic Oscillator (h.o.) parameter b and the values of the two parameters $g_{\text{pair}}^{p(n)}$ for proton (neutron) pairs that renormalise the monopole (pairing) residual interaction (obtained from the Bonn C-D two-body potential describing the strong two-nucleon forces), are presented in Table 3.1. The adjustment of $g_{\text{pair}}^{p(n)}$ is achieved through the reproducibility of the pairing gaps $\Delta_p(n)$. To this purpose, the gap-equation given in Eq.(3.84) is written in the form

$$\Delta_b = -\frac{g_{\text{pair}}^{p(n)}}{2\hat{j}_b} \sum_a \frac{\hat{j}_a \Delta_a}{\sqrt{\eta_a^2 + \Delta_a^2}} \langle aa; 0 | V | bb; 0 \rangle, \quad (3.128)$$

Nucleus	model-space	b	Δ_p	Δ_n	g_{pair}^p	g_{pair}^n
^{12}C	8 (no core)	1.522	4.68536	4.84431	1.12890	1.19648
^{16}O	8 (no core)	1.675	3.36181	3.49040	1.06981	1.13636
^{20}Ne	10 (no core)	1.727	3.81516	3.83313	1.15397	1.27600
^{28}Si	10 (no core)	1.809	3.03777	3.14277	1.15568	1.23135
^{32}S	15 (no core)	1.843	2.03865	2.09807	0.8837	0.95968
^{40}Ar	15 (no core)	1.902	1.75518	1.76002	0.94388	1.01348
^{48}Ti	15 (no core)	1.952	1.91109	1.55733	1.05640	0.99890
^{76}Ge	15 (no core)	2.086	1.52130	1.56935	0.95166	1.17774
^{114}Cd	18 (core ^{16}O)	2.214	1.41232	1.35155	1.03122	0.98703
^{132}Xe	15 (core ^{40}Ca)	2.262	1.19766	1.20823	0.98207	1.13370

Table 3.1: The values of proton g_{pair}^p and neutron g_{pair}^n pairs that renormalise the residual interaction and reproduce the respective empirical pairing gaps Δ_p and Δ_n . The active model space and the Harmonic Oscillator parameter, for each isotope, are also presented.

while the pairing gaps are obtained through the three-point formula as follows

$$\begin{aligned}\Delta_n^{\text{exp}} &= -\frac{1}{4} [S_n(A-1, Z) - 2S_n(A, Z) + S_n(A+1, Z)] , \\ \Delta_p^{\text{exp}} &= -\frac{1}{4} [S_p(A-1, Z-1) - 2S_p(A, Z) + S_p(A+1, Z+1)] ,\end{aligned}\tag{3.129}$$

where, S_n (S_p) denotes the experimental separation energy for neutrons (protons), respectively, of the target nucleus (A, Z) and the neighbouring nuclei ($A\pm 1, Z\pm 1$) and ($A\pm 1, Z$).

3.6.2 Other methods for obtaining the nuclear form factors

The point-nucleon charge density distributions $\rho(\mathbf{r})$, are defined as the expectation value of the density operator

$$\hat{\rho}(\mathbf{r}) = \sum_{j=1}^A \frac{1}{2} (1 + \tau_{3j}) \delta(\mathbf{r} - \mathbf{r}_j) ,\tag{3.130}$$

where the $+$ ($-$) sign corresponds to the point-proton (neutron) charge density distribution. If we assume that the ground state of a nucleus (A, Z), is approximately described by a Slater determinant constructed from single-particle wave-functions, the distributions of Eq.(3.130) are simply the sum of the squares of the point-nucleon wavefunctions. For closed (sub)shell nuclei $\rho(\mathbf{r})$ is spherically symmetric and the more interesting radial ($r = |\mathbf{r}|$) proton charge density

distribution, $\rho_p(r)$, is simply given by

$$\rho_p(r) = \frac{1}{4\pi} \sum_{\substack{(n,l)j \\ \text{occupied}}} (2j+1) |R_{nlj}(r)|^2, \quad (3.131)$$

where $R_{nlj}(r)$ is the radial component of the single-particle wavefunction with quantum numbers n , l and j .

The nuclear form factor, which is the Fourier transform of the nuclear charge density distribution, $\rho_p(r)$, is defined as

$$F_Z(\mathbf{q}^2) = \frac{4\pi}{Z} \int \rho_p(r) j_0(|\mathbf{q}|r) r^2 dr, \quad (3.132)$$

with $j_0(x)$ being the zero-order Spherical Bessel function and depends on the magnitude of the three momentum transfer squared, $\mathbf{q}^2 \equiv |\mathbf{q}|^2$. Due to the significance of the nuclear form factors in our calculations and for the benefit of the reader we devote a separate discussion to summarise some useful possibilities of obtaining these observables.

i) *Use of available experimental data*

For many nuclei and especially for odd-A isotopes, the proton nuclear form factors $F_Z(\mathbf{q}^2)$, are computed by means of a model independent analysis (using the Fourier-Bessel expansion model or others defined in Appendix F.1) of the electron scattering data for the proton charge density $\rho_p(r)$ [56] wherever, possible. The absence of similar data for neutron densities, restricts us to assume that $F_N(\mathbf{q}^2) = F_Z(\mathbf{q}^2)$. In this work, we consider this method only for the case of the very heavy doubly closed ^{208}Pb nucleus.

ii) *Fractional occupation probabilities in a simple Shell-Model*

In Ref. [57] the form factor $F_Z(\mathbf{q}^2)$, for Harmonic Oscillator wavefunctions has been written as [58, 59]

$$F_Z(\mathbf{q}^2) = \frac{1}{Z} e^{-(|\mathbf{q}|b)^2/4} \Phi(|\mathbf{q}|b, Z), \quad \Phi(|\mathbf{q}|b, Z) = \sum_{\lambda=0}^{N_{\max}} \theta_{\lambda} (|\mathbf{q}|b)^{2\lambda}, \quad (3.133)$$

where $N_{\max} = (2n+l)_{\max}$ stands for the number of quanta of the highest occupied proton (neutron) level. The coefficients θ_{λ} read

$$\theta_{\lambda} = \frac{\sqrt{\pi}}{4^{\lambda}} \sum_{\substack{(n,l)j \\ (2n+l>\lambda)}}^{N_{\max}} \sum_{m=s}^{2n} \frac{(2j+1)n! C_{nl}^m \Lambda_{\lambda}(m+l, 0) (l+m)!}{2\Gamma(n+l+\frac{3}{2})}, \quad (3.134)$$

where $\Gamma(x)$ is the Gamma function and the index s is defined as

$$s = \begin{cases} 0, & \text{if } \lambda - l \leq 0 \\ \lambda - l & \text{if } \lambda - l > 0 \end{cases}, \quad (3.135)$$

$Z (N)$	$(nl)j$	$\lambda = 0$	$\lambda = 1$	$\lambda = 2$	$\lambda = 3$	$\lambda = 4$
2	$0s_{1/2}$	2 (2)				
6	$0p_{3/2}$	2 (6)	$\frac{8}{3}$ ($-\frac{2}{3}$)			
8	$0p_{1/2}$	2 (8)	4 (-1)			
14	$0d_{5/2}$	2 (14)	4 (-3)	$\frac{8}{3}$ ($\frac{1}{10}$)		
18	$0d_{3/2}$	2 (18)	4 ($-\frac{13}{3}$)	$\frac{8}{3}$ ($\frac{1}{6}$)		
20	$1s_{1/2}$	5 (20)	0 (-5)	4 ($\frac{1}{4}$)		
22	$1p_{1/2}$	5 (22)	$\frac{10}{3}$ (-6)	$\frac{4}{3}$ ($\frac{13}{3}$)	$\frac{8}{15}$ ($-\frac{1}{120}$)	
30	$0f_{7/2}$	5 (30)	$\frac{10}{3}$ (-10)	$\frac{4}{3}$ ($\frac{1}{5}$)	$\frac{7}{15}$ ($-\frac{1}{56}$)	
34	$1p_{3/2}$	5 (34)	10 (-12)	-4 ($\frac{16}{5}$)	$\frac{232}{105}$ ($-\frac{29}{840}$)	
40	$0f_{5/2}$	5 (40)	10 (-15)	-4 ($\frac{13}{5}$)	$\frac{8}{15}$ ($-\frac{1}{24}$)	
50	$0h_{9/2}$	5 (50)	10 ($-\frac{65}{3}$)	-4 ($\frac{19}{2}$)	$\frac{16}{3}$ ($-\frac{4}{56}$)	$\frac{32}{189}$ ($\frac{1}{1512}$)

Table 3.2: The exact coefficients $f_\lambda (\theta_\lambda)$, that determine the proton and neutron density and momentum distributions (form factors) up to ^{50}Sn , within the chosen model space. For more details see the text.

and

$$\Lambda_k(n, l) = \frac{(-)^k}{k!} \binom{n+l+1/2}{n-k}, \quad C_{nl}^m = \sum_{k=0}^m \Lambda_{m-k}(n, l) \Lambda_k(n, l). \quad (3.136)$$

The radial nuclear charge density distribution, $\rho_p(r)$, entering the definition of Eq.(3.132), is written in the following compact form [58, 59]

$$\rho_p(r) = \frac{1}{\pi^{3/2} b^3} e^{-(r/b)^2} \Pi\left(\frac{r}{b}, Z\right), \quad \Pi(\chi, Z) = \sum_{\lambda=0}^{N_{\max}} f_\lambda \chi^{2\lambda}, \quad (3.137)$$

where $\chi = r/b$, with b denoting the Harmonic Oscillator size parameter. The coefficients, f_λ , are expressed as

$$f_\lambda = \sum_{(n,l)j} \frac{\pi^{1/2} (2j+1) n! C_{nl}^{\lambda-l}}{2\Gamma(n+l+\frac{3}{2})}. \quad (3.138)$$

As a first step of our calculational procedure, we evaluated the θ_λ and f_λ coefficients, required for the form factor and the proton charge density of the ^{48}Ti nucleus. Specifically, an inversion of the $(nl)j$ levels compared to that assumed in Ref [57], results in the present work, in order to fit the experimental data for ^{48}Ti . These coefficients are listed below in Table 3.2. As mentioned in Ref. [57], an interchange of the sequence of the levels, does not affect the coefficients of the core nucleus (e.g. our results for the ^{40}Ca nucleus coincide with those of Ref. [57]).

Up to this point, the proton occupation probabilities entering Eq.(3.132) Eq.(3.133) have been considered equal to unity for the states below the Fermi

surface and zero for those above the Fermi surface. In Ref. [57], the authors introduced depletion and occupation numbers, to parametrise the partially occupied levels of the states. These parameters satisfy the relation

$$\sum_{\substack{(n,l)j \\ \text{all}}} \alpha_{nlj}(2j+1) = N_n. \quad (3.139)$$

Within this context, the ‘‘active’’ surface nucleons (above or below the Fermi level) have non-zero occupation probability $\alpha_{nlj} \neq 0$, smaller than unity, while the ‘‘core’’ levels have occupation probability $\alpha_{nlj} = 1$. In this Thesis, we extend the work of Ref. [57] where three parameters $\alpha_1, \alpha_2, \alpha_3$ are used to describe the partial occupation probabilities of the surface orbits. We improve the formalism by introducing more parameters, increasing this way the number of ‘‘active’’ nucleons in the studied nuclear system and come out with higher reproducibility of the experimental data [56]. To this aim, we introduce four parameters α_i , $i = 1, 2, 3, 4$ in Eq.(3.139). Then, the assumed ‘‘active’’ single-particle levels are five and Eq.(16) of Ref. [57] becomes

$$\begin{aligned} \Pi(\chi, Z, \alpha_i) = & \Pi(\chi, Z_2) \frac{\alpha_1}{Z_1 - Z_2} + \Pi(\chi, Z_1) \left[\frac{\alpha_2}{Z_c - Z_1} - \frac{\alpha_1}{Z_1 - Z_2} \right] \\ & + \Pi(\chi, Z_c) \left[\frac{Z' - Z}{Z' - Z_c} - \frac{\alpha_2}{Z_c - Z_1} - \frac{\alpha_3}{Z' - Z_c} \right] \\ & + \Pi(\chi, Z') \left[\frac{Z - Z_c}{Z' - Z_c} + \frac{\alpha_3}{Z' - Z_c} - \frac{\alpha_4}{Z'' - Z'} \right] \\ & + \Pi(\chi, Z'') \left[\frac{\alpha_4}{Z'' - Z'} - \frac{\lambda}{Z''' - Z''} \right] + \Pi(\chi, Z''') \frac{\lambda}{Z''' - Z''}, \end{aligned} \quad (3.140)$$

with $\lambda = \alpha_1 + \alpha_2 - \alpha_3 - \alpha_4$. By substituting the polynomial $\Pi(\chi, Z)$ of Eq.(3.137) with that of the latter expression and using the experimental data [56], we fit the parameters α_i (and similarly for the form factor of Eq.(3.133)). As an example, for the ^{40}Ar isotope we have, $Z_2 = 10, Z_1 = 12, Z = Z_c = 18, Z' = 20, Z'' = 22, Z''' = 30$. The resulting fractional occupation probabilities that fit the experimental charge density distribution are $\alpha_1 = 0.85, \alpha_2 = 1.25, \alpha_3 = 0.85, \alpha_4 = 0.75$. Similarly for the ^{48}Ti nucleus, we have $Z_2 = 18, Z_1 = 20, Z = Z_c = 22, Z' = 30, Z'' = 34, Z''' = 40$ and the fitting parameters are $\alpha_1 = 1.0, \alpha_2 = 1.5, \alpha_3 = 0.35, \alpha_4 = 0.1$. In Fig. 3.3 the prediction of the method is compared with that of the simple Shell-Model and the experimental data. We note that in the momentum transfer range of our interest (i.e. $\mathbf{q} < 2 \text{ fm}^{-1}$) the form factor has excellent behaviour. We however mention that even though the FOP method presents very high reproducibility of the experimental data, it is not always applicable, e.g. for deformed nuclei (where BCS appears to be still successful).

iii) *Use of effective expressions for the nuclear form factors*

We finally discuss one of the most accurate effective methods for calculating the nuclear form factor by Ref. [60]

$$F(\mathbf{q}^2) = \frac{3j_1(|\mathbf{q}|R_0)}{|\mathbf{q}|R_0} \exp\left[-\frac{1}{2}(|\mathbf{q}|s)^2\right], \quad (3.141)$$

where $j_1(x)$ is the known first-order Spherical-Bessel function and $R_0^2 = R^2 - 5s^2$, with R and s being the radius and surface thickness parameters of the nucleus respectively. The radius parameter is usually given from the semi-empirical form $R = 1.2A^{1/3}$ fm while s is of the order of 0.5 fm (see Ref. [56]).

It is worth noting that, by inserting the form factors $F_{Z(N)}$ obtained as described above in Eq.(4.69), the resulting cross sections have a rather high confidence level. In the next part of the Thesis the results show that the momentum dependence of the nuclear form factors becomes crucial, especially for intermediate and high energies. In some cases, differences of even an order of magnitude may occur as compared to the calculations neglecting the momentum dependence of the nuclear form factors.

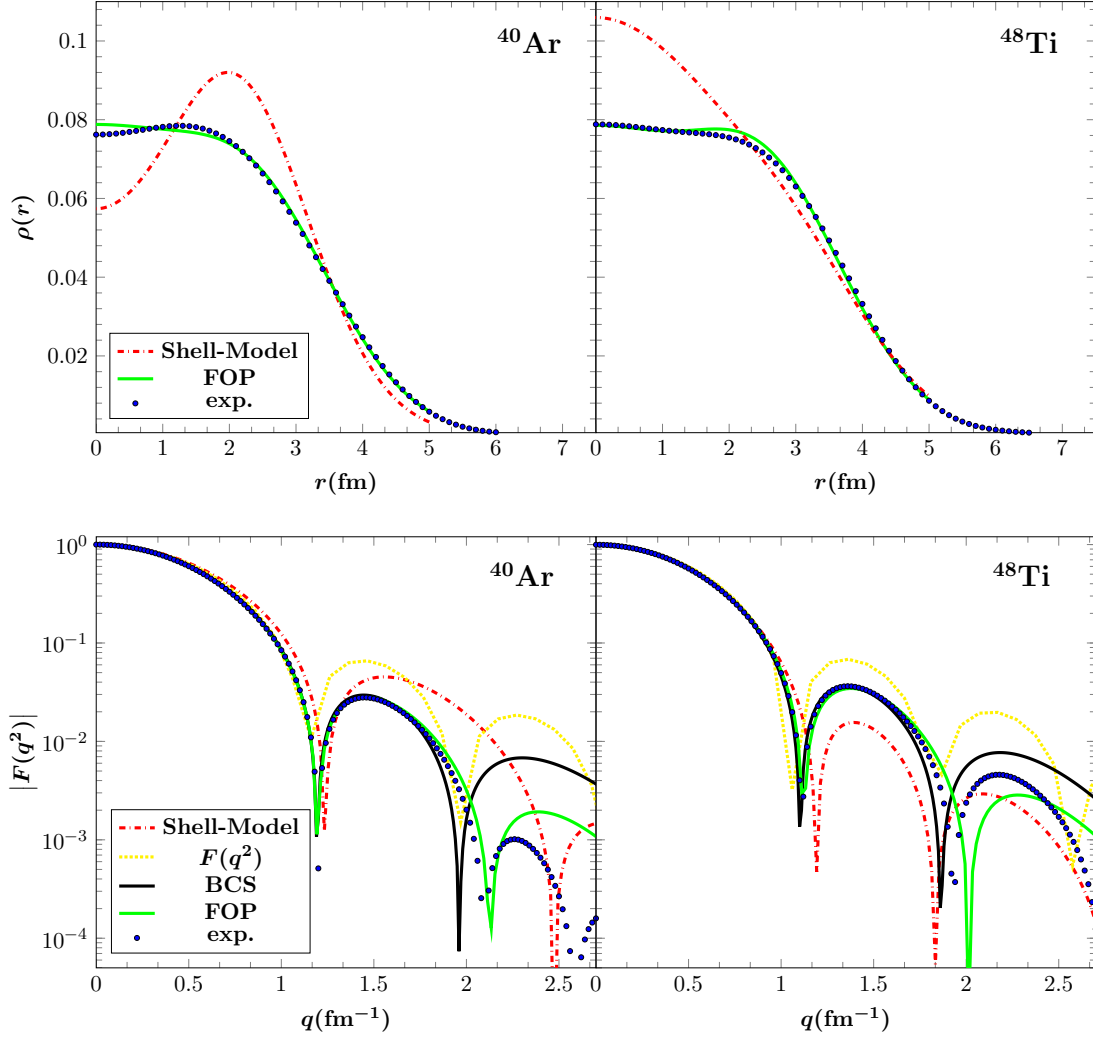


Figure 3.3: The charge density distribution (*left*) and the nuclear form factor as a function of the momentum transfer (*right*), for the cases of ^{40}Ar and ^{48}Ti nuclei. The introduction of fractional occupation probabilities (FOP) of the states provides higher reproducibility of the experimental data, compared to the simple Shell-Model and that of Eq.(3.141). The BCS nuclear neutron form factor $F_N(\mathbf{q}^2)$ is also presented and compared.

Chapter 4

Neutrino-nucleus processes within the SM

4.1 Introduction

Open neutrino physics issues require precision studies, both theoretical and experimental ones, and towards this aim coherent neutral-current neutrino-nucleus scattering events are expected to be observed soon. In this Chapter, we explore neutrino-nucleus processes from a nuclear theory point of view and obtain results with high confidence level based on accurate nuclear structure cross sections calculations. Besides cross sections, the present study includes simulated signals expected to be recorded by nuclear detectors, differential event rates as well as total number of events predicted to be measured. Our original cross sections calculations are focused on measurable rates for the Standard Model process. We concentrate on the possibility of detecting (i) Supernova neutrinos by using massive detectors like those of the GERDA and SuperCDMS dark matter experiments and (ii) laboratory neutrinos produced near the spallation neutron source facilities (at Oak Ridge National Lab) by the COHERENT experiment.

4.2 The role of neutrino-nucleus processes

Coherent scattering of neutrinos on complex nuclei was proposed long ago [61–63] as a prominent probe to study neutral-current (NC) neutrino-nucleus processes, but up to now no events have been experimentally measured. Neutrino detection, constitutes an excellent probe to search for a plethora of conventional neutrino physics applications and new-physics open issues [64–66]. In principle, low-energy astrophysical and laboratory neutrino searches provide crucial information towards understanding the underlying physics of the fundamental electroweak interactions within and beyond the SM [67, 68]. Well-known neutrino sources include (i) Supernova neutrinos (with energies up to 60-100 MeV) and (ii) labor-

atory neutrinos (with energies up to 52.8 MeV) emerging from stopped-pion and muon decays at muon factories (Fermilab, PSI, JPARC, etc.) and at the Spallation Neutron Source (SNS) at Oak Ridge National Lab [69]. Recently, it became feasible [70] to detect neutrinos by exploiting the neutral-current interactions and measuring the nuclear recoil signals through the use of very low threshold-energy detectors [71, 72]. To this purpose, great experimental effort has been put and new experiments have been proposed to be performed at facilities with stopped-pion neutrino beams, based on promising nuclear detectors like those of the COHERENT experiment [73–75] and others [76] at the SNS, or alternative setups at the Booster Neutrino Beam (BNB) at Fermilab [77, 78]. The nuclear neutrino detectors adopted by the relevant experiments include liquid noble gases, such as ^{20}Ne , ^{40}Ar , ^{132}Xe as well as, ^{76}Ge and CsI[Na] detection materials [79].

On the theoretical side, the neutrino signals of low-energy neutrinos, expected to be recorded in sensitive nuclear detectors [80–82], could be simulated through nuclear calculations of neutrino-nucleus scattering cross sections. Such results may provide useful information relevant for the evolution of distant stars, the core collapse Supernovae, explosive nucleosynthesis and other phenomena [40, 83–85]. In fact, coherent neutral-current neutrino-nucleus scattering events are expected to be observed by using the high intensity stopped-pion neutrino beams [86, 87] and nuclear targets for which recoil energies are of the order of a few to tens of keV, and therefore appropriate for detection of WIMPs [88, 89], candidates of Cold Dark Matter [90, 91]. Such detectors are e.g. the SuperCDMS [92], GERDA [93] and other multi-purpose detectors [94–96]. For low-energies, the dominant vector components of NC interactions lead to a coherent contribution of all nucleons (actually all neutrons) in the target nucleus [97–99].

It is worth mentioning that, after the discovery [100–105] of neutrino oscillations in propagation, the challenge of neutral and charged lepton flavour violation (LFV) is further investigated by extremely sensitive experiments [106–109] searching for physics beyond the current Standard Model (SM) [110]. To this end, neutrino-nucleus coherent scattering experiments may probe new physics beyond the SM involved in exotic neutrino-nucleus interactions [22, 25, 70, 111], an undoubtable signature of non-standard physics. Therefore, new data and insights will be provided to the physics of flavour changing neutral-current (FCNC) processes, in the leptonic sector, in non-standard neutrino oscillation effects [112–114], in neutrino transition magnetic moments [115], in sterile neutrino search [116] and others [117]. Furthermore, such experimental sensitivity may also inspire advantageous probes to shed light on various open issues in nuclear astrophysics [118, 119].

In recent works [25], neutral-current (NC) non-standard interactions (NSI) involving (anti)neutrino scattering processes on leptons, nucleons and nuclei have been investigated. The reactions of this type that take place in nuclei are represented by

$$\nu_\alpha(\bar{\nu}_\alpha) + (A, Z) \rightarrow \nu_\beta(\bar{\nu}_\beta) + (A, Z), \quad (4.1)$$

($\alpha, \beta = e, \mu, \tau$ with $\alpha \neq \beta$). It has been suggested [120] that, theoretically the latter processes, can be studied with the same nuclear methods as the exotic cLFV process of $\mu^- \rightarrow e^-$ conversion in nuclei [121–124]. The corresponding Lagrangians may be derived within the context of various extensions of the SM [67, 68, 125], like the four-fermion contact interaction, seesaw model [126, 127], left-right symmetric models [128], gluonic operator model [129], etc.

It is well-known that neutrino NSI may have rather significant impact in many areas of modern physics research and thus, motivate a great number of similar studies [130]. Especially in astrophysical applications, constraints coming out of some Supernova explosion scenarios [21, 131, 132], may be affected and eventually lead to the necessity of further investigation of NSI in both LFV and cLFV processes that may occur in solar and Supernova environment [55, 58, 59, 133, 134]. Such open issues motivated our present work too.

One of our main purposes in this Chapter, is to comprehensively study the above issues by performing nuclear structure calculations for a set of experimentally interesting nuclei. We estimate reliably the nuclear matrix elements describing the Standard Model component of the neutrino-nucleus processes, i.e. we consider $\alpha = \beta$ in the reactions of Eq.(4.1). Exotic neutrino-nucleus events are computed in Chapt. 5. By exploiting our accurate original cross sections, we obtain simulated neutrino signals and flux averaged cross sections which are experimentally interesting quantities for both Supernova and SNS neutrinos. The total number of events expected to be recorded over the energy threshold for the studied nuclear targets are also presented for both cases.

We stress that, we have devoted special effort to obtain results of high accuracy by constructing the nuclear ground state within the context of the quasi-particle random phase approximation (QRPA), i.e. by solving iteratively the BCS equations for realistic pairing interactions (the Bonn C-D potential) [135, 136], and achieving high reproducibility of the available experimental data [56]. In addition, we made comparisons with the results of other methods evaluating the nuclear form factors that enter the coherent rate [31, 137] as the one which employs fractional occupation probabilities (FOP) of the states (on the basis of analytic expressions) [57], and other well-known methods [60].

4.3 The Donnelly-Walecka method

From a nuclear theory point of view, it is important to evaluate the transition matrix elements entering the cross sections and other observables of electroweak processes with reliable many-body nuclear wave functions. For any semi-leptonic electroweak interaction, the partial (exclusive) reaction rate $\Gamma_{i \rightarrow f}$ between an initial $|i\rangle$ and a final $|f\rangle$ (many-body) nuclear states, are based on the nuclear matrix elements of the interaction Hamiltonian, \hat{H}_{eff}

$$\Gamma_{i \rightarrow f} \propto |\langle f | \hat{H}_{eff} | i \rangle|^2 \quad (4.2)$$

(i.e. the Fourier transform of the nuclear matrix elements of the hadronic current density $\hat{\mathcal{J}}_\mu$). The Hamiltonian, \hat{H}_{eff} , can be deduced by assuming the exchange of intermediate particles between the leptonic $\hat{\ell}_\mu^{\text{lept}}$ and hadronic $\hat{\mathcal{J}}_\mu$ current densities and in the low-energy approximation takes the form

$$\hat{H}_{eff} = \frac{G}{\sqrt{2}} \int \hat{\ell}_\mu^{\text{lept}}(\mathbf{x}) \hat{\mathcal{J}}^\mu(\mathbf{x}) d^3\mathbf{x}, \quad (4.3)$$

($G = G_F$, the Fermi coupling constant for neutral-current processes or $G = G_F \cos \theta_c$, θ_c the Cabbibo angle, for charged-current processes.)

From theoretical nuclear physics perspectives, the computation of the transition amplitudes, $\langle f | \hat{H}_{eff} | i \rangle$, for lepton-nucleus processes, is based on the multipole decomposition analysis of the hadronic current density (see Appendix B.1). Then, the transition amplitudes are expressed as [37]

$$\begin{aligned} \langle f | \hat{H}_{eff} | i \rangle = & -\frac{G}{\sqrt{2}} \langle f | \left\{ \sum_{J \geq 0} \sqrt{4\pi(2J+1)} (-i)^J \left(l_3 \hat{\mathcal{L}}_{J0}(\kappa) - l_0 \hat{\mathcal{M}}_{J0}(\kappa) \right) \right. \\ & \left. + \sum_{\lambda = \pm 1} \sum_{J \geq 1} \sqrt{2\pi(2J+1)} (-i)^J l_\lambda \left(\lambda \hat{\mathcal{T}}_{J-\lambda}^{\text{mag}}(\kappa) + \hat{\mathcal{T}}_{J-\lambda}^{\text{el}}(\kappa) \right) \right\} | i \rangle. \end{aligned} \quad (4.4)$$

By using the Wigner-Eckart theorem (see C.6), the matrix elements of the irreducible operators are given by

$$\begin{aligned} \Gamma_{i \rightarrow f} \propto & \frac{1}{2J_i + 1} \sum_{M_i} \sum_{M_f} |\langle f | \hat{H}_{eff} | i \rangle|^2 = \frac{G^2}{2} \frac{1}{2J_i + 1} \left\{ \sum_{\lambda = \pm 1} l_\lambda l_\lambda^* \sum_{J \geq 1} 2\pi \right. \\ & \times |\langle J_f || \lambda \hat{\mathcal{T}}_J^{\text{mag}} + \hat{\mathcal{T}}_J^{\text{el}} || J_i \rangle|^2 + \sum_{J \geq 0} 4\pi \left[l_3 l_3^* |\langle J_f || \hat{\mathcal{L}}_J || J_i \rangle|^2 \right. \\ & \left. + l_0 l_0^* |\langle J_f || \hat{\mathcal{M}}_J || J_i \rangle|^2 - 2\Re \left(l_3 l_0^* \langle J_f || \hat{\mathcal{L}}_J || J_i \rangle \langle J_f || \hat{\mathcal{M}}_J || J_i \rangle \right) \right] \left. \right\}, \end{aligned} \quad (4.5)$$

where the average of the summation over the final nuclear states for non-oriented spherical targets is taken. Then, sorting term-by-term the latter expression one

has

$$\begin{aligned}
\Gamma_{i \rightarrow f} &\propto \frac{1}{2J_i + 1} \sum_{M_i} \sum_{M_f} |\langle f | \hat{H}_{eff} | i \rangle|^2 = \frac{G^2}{2} \frac{4\pi}{2J_i + 1} \\
&\times \left\{ \sum_{J \geq 0} \left[l_3 l_3^* |\langle J_f \| \hat{\mathcal{L}}_J \| J_i \rangle|^2 + l_0 l_0^* |\langle J_f \| \hat{\mathcal{M}}_J \| J_i \rangle|^2 \right. \right. \\
&- 2\Re \left(l_3 l_0^* \langle J_f \| \hat{\mathcal{L}}_J \| J_i \rangle \langle J_f \| \hat{\mathcal{M}}_J \| J_i \rangle^* \right) \\
&+ \sum_{J \geq 1} \left[\frac{1}{2} (\mathbf{1} \cdot \mathbf{1}^* - l_3 l_3^*) \left(|\langle J_f \| \hat{\mathcal{T}}_J^{mag} \| J_i \rangle|^2 + |\langle J_f \| \hat{\mathcal{T}}_J^{el} \| J_i \rangle|^2 \right) \right. \\
&\left. \left. - \frac{i}{2} (\mathbf{1} \times \mathbf{1}^*)_3 \left(2\Re \langle J_f \| \hat{\mathcal{T}}_J^{mag} \| J_i \rangle \langle J_f \| \hat{\mathcal{T}}_J^{el} \| J_i \rangle^* \right) \right] \right\}. \quad (4.6)
\end{aligned}$$

To evaluate the partial transition rate between an initial $|i\rangle$ and a final $|f\rangle$ state of the studied semi-leptonic process it is required to take the average of the summation over the final spin states of the incoming lepton

$$\Gamma_{fi} \propto \frac{1}{2} \sum_{\text{lepton spins}} \frac{1}{2J_i + 1} \sum_{M_i} \sum_{M_f} |\langle f | \hat{H}_{eff} | i \rangle|^2. \quad (4.7)$$

4.3.1 Multipole operators

In the context of the Donnelly-Walecka multipole decomposition method the eight linearly independent irreducible tensor operators (see below), are written in terms of the Spherical Bessel functions, j_l , and the Spherical Harmonics, Y_M^L , or the vector Spherical Harmonics, $\mathbf{Y}_M^{(L,1)J}$, as [51]

$$M_M^J(\kappa \mathbf{r}) = \delta_{LJ} j_L(\kappa r) Y_M^L(\hat{r}), \quad (4.8)$$

$$\mathbf{M}_M^{(L,1)J}(\kappa \mathbf{r}) = j_L(\kappa r) \mathbf{Y}_M^{(L,1)J}(\hat{r}), \quad (4.9)$$

with

$$\mathbf{Y}_M^{(L,1)J}(\hat{r}) = \sum_{M_L, \lambda} \langle LM_L 1\lambda | JM \rangle Y_{M_L}^L(\hat{r}) \mathbf{e}_\lambda. \quad (4.10)$$

For later convenience, in the present Thesis the magnitude of the three-momentum transfer $|\mathbf{q}|$, where $q_\mu = (q_0, \mathbf{q})$ is defined as $\kappa = |\mathbf{q}|$. Note, that our convention is different to that adopted in Ref. [135]

In this framework, four operators are defined for the polar vector component $\hat{J}_\lambda = (\hat{\rho}, \hat{\mathbf{J}})$ and four for the the axial vector component $\hat{J}_\lambda^5 = (\hat{\rho}^5, \hat{\mathbf{J}}^5)$ of the hadronic current respectively

$$\hat{\mathcal{M}}_{JM}(\kappa) = \hat{M}_{JM}^{coul} - \hat{M}_{JM}^{coul5} = \int d\mathbf{r} M_M^J(\kappa\mathbf{r}) \hat{\mathcal{J}}_0(\mathbf{r}), \quad (4.11)$$

$$\hat{\mathcal{L}}_{JM}(\kappa) = \hat{L}_{JM} - \hat{L}_{JM}^5 = i \int d\mathbf{r} \left(\frac{1}{\kappa} \nabla M_M^J(\kappa\mathbf{r}) \right) \cdot \hat{\mathcal{J}}(\mathbf{r}), \quad (4.12)$$

$$\hat{\mathcal{T}}_{JM}^{el}(\kappa) = \hat{T}_{JM}^{el} - \hat{T}_{JM}^{el5} = \int d\mathbf{r} \left(\frac{1}{q} \nabla \times \mathbf{M}_M^{JJ}(\kappa\mathbf{r}) \right) \cdot \hat{\mathcal{J}}(\mathbf{r}), \quad (4.13)$$

$$\hat{\mathcal{T}}_{JM}^{mag}(\kappa) = \hat{T}_{JM}^{mag} - \hat{T}_{JM}^{mag5} = \int d\mathbf{r} \mathbf{M}_M^{JJ}(\kappa\mathbf{r}) \cdot \hat{\mathcal{J}}(\mathbf{r}), \quad (4.14)$$

due to the V-A structure of the weak interaction

$$\hat{\mathcal{J}}_\mu = \hat{J}_\mu - \hat{J}_\mu^5 = (\hat{\rho}, \hat{\mathbf{J}}) - (\hat{\rho}^5, \hat{\mathbf{J}}^5). \quad (4.15)$$

The latter operators from a mathematical point of view constitute tensor operators of rank J which act in the Hilbert space of the studied nuclear system. Then, seven operators $T_i^{JM}(\kappa\mathbf{r})$, $i = 1, 2, \dots, 7$ may be defined as

$$\hat{M}_{JM}^{coul}(\kappa\mathbf{r}) = F_1^V(Q^2) M_M^J(\kappa\mathbf{r}), \quad (4.16)$$

$$\hat{L}_{JM}(\kappa\mathbf{r}) = \frac{q_0}{\kappa} \hat{M}_{JM}^{coul}(\kappa\mathbf{r}), \quad (4.17)$$

$$\hat{T}_{JM}^{el}(\kappa\mathbf{r}) = \frac{\kappa}{m_N} \left[F_1^V(Q^2) \Delta_M^J(\kappa\mathbf{r}) + \frac{1}{2} \mu^V(Q^2) \Sigma_M^J(\kappa\mathbf{r}) \right], \quad (4.18)$$

$$i\hat{T}_{JM}^{mag}(\kappa\mathbf{r}) = \frac{\kappa}{m_N} \left[F_1^V(Q^2) \Delta_M^J(\kappa\mathbf{r}) - \frac{1}{2} \mu^V(Q^2) \Sigma_M^J(\kappa\mathbf{r}) \right], \quad (4.19)$$

$$i\hat{M}_{JM}^5(\kappa\mathbf{r}) = \frac{\kappa}{m_N} \left[F_A(Q^2) \Omega_M^J(\kappa\mathbf{r}) + \frac{1}{2} (F_A(Q^2) + q_0 F_P(Q^2)) \Sigma_M^J(\kappa\mathbf{r}) \right], \quad (4.20)$$

$$-i\hat{L}_{JM}^5(\kappa\mathbf{r}) = \left[F_A(Q^2) - \frac{\kappa^2}{2m_N} F_P(Q^2) \right] \Sigma_M^J(\kappa\mathbf{r}), \quad (4.21)$$

$$-i\hat{T}_{JM}^{el5}(\kappa\mathbf{r}) = F_A(Q^2) \Sigma_M^J(\kappa\mathbf{r}), \quad (4.22)$$

$$\hat{T}_{JM}^{mag5}(\kappa\mathbf{r}) = F_A(Q^2) \Sigma_M^J(\kappa\mathbf{r}). \quad (4.23)$$

To proceed, by introducing the operators $\hat{\mathcal{M}}_{JM}$, $\hat{\mathcal{L}}_{JM}$, $\hat{\mathcal{T}}_{JM}^{el}$, $\hat{\mathcal{T}}_{JM}^{mag}$ we write the above expressions in a more compact form, as follows

$$\begin{aligned}\hat{\mathcal{M}}_{JM}(\kappa r) &= \hat{M}_{JM}^{coul} + \hat{M}_{JM}^{coul5} \\ &= F_1^V M_M^J(\kappa r) - i \frac{\kappa}{M_N} [F_A \Omega_M^J(\kappa r) + \frac{1}{2}(F_A + q_0 F_P) \Sigma_M''^J(\kappa r)],\end{aligned}\quad (4.24)$$

$$\begin{aligned}\hat{\mathcal{L}}_{JM}(\kappa r) &= \hat{L}_{JM} + \hat{L}_{JM}^5 \\ &= \frac{q_0}{\kappa} F_1^V M_M^J(\kappa r) + i F_A \Sigma_M''^J(\kappa r),\end{aligned}\quad (4.25)$$

$$\begin{aligned}\hat{\mathcal{T}}_{JM}^{el}(\kappa r) &= \hat{T}_{JM}^{el} + \hat{T}_{JM}^{el5} \\ &= \frac{\kappa}{M_N} [F_1^V \Delta_M'^J(\kappa r) + \frac{1}{2} \mu^V \Sigma_M^J(\kappa r)] + i F_A \Sigma_M'^J(\kappa r),\end{aligned}\quad (4.26)$$

$$\begin{aligned}\hat{\mathcal{T}}_{JM}^{mag}(\kappa r) &= \hat{T}_{JM}^{mag} + \hat{T}_{JM}^{mag5} \\ &= -\frac{q}{M_N} [F_1^V \Delta_M^J(\kappa r) - \frac{1}{2} \mu^V \Sigma_M^J(\kappa r)] + i F_A \Sigma_M^J(\kappa r),\end{aligned}\quad (4.27)$$

entering between the initial $|J_i^\pi, T_i\rangle$ and final $|J_f^\pi, T_f\rangle$ nuclear state. The free nucleon form factors $F_X(Q^2)$, $X=1, A, P$ and $\mu^V(Q^2)$, entering Eqs. (4.16)-(4.23) are discussed in Appendix B.3.

It can be seen that within the aforementioned operators, only seven are linearly independent. The polar-vector component yields the following operators, namely Coulomb M_{JM}^{coul} , longitudinal L_{JM} , transverse electric T_{JM}^{el} (with normal parity $\pi = (-)^J$) and transverse magnetic T_{JM}^{mag} (with abnormal parity $\pi = (-)^{J+1}$). For the case of the axial-vector component the defined operators are M_{JM}^{coul5} , L_{JM}^5 , T_{JM}^{el5} (with abnormal parity) and T_{JM}^{mag5} (with normal parity).

To proceed, the latter are written in terms of the matrix elements (ME) of seven basic irreducible tensor operators, which in our convention are [120, 135]

$$\langle j_1 || T_i^J || j_2 \rangle = e^{-y} y^{\beta/2} \sum_{\mu=0}^{n_{max}} \mathcal{P}_\mu^{i, J} y^\mu, \quad i = 1, \dots, 7. \quad (4.28)$$

Therefore, their evaluation is necessary for performing nuclear cross sections calculations (more details are given in Appendix B.2). These coefficients, $\mathcal{P}_\mu^{i, J}$, have been computed recently in Refs. [120, 135]. The operators $T_i^{JM}(\kappa \mathbf{r})$,

$i = 1, 2, \dots, 7$ in the proton-neutron representation read

$$T_1^{JM} \equiv M_M^J(\kappa\mathbf{r}) = \delta_{LJ} j_L(\kappa\mathbf{r}) Y_M^L(\hat{r}), \quad (4.29)$$

$$T_2^{JM} \equiv \Sigma_M^J(\kappa\mathbf{r}) = \mathbf{M}_M^{JJ} \cdot \boldsymbol{\sigma}, \quad (4.30)$$

$$T_3^{JM} \equiv \Sigma'_M{}^J(\kappa\mathbf{r}) = -i \left[\frac{1}{\kappa} \boldsymbol{\nabla} \times \mathbf{M}_M^{JJ}(\kappa\mathbf{r}) \right] \cdot \boldsymbol{\sigma}, \quad (4.31)$$

$$T_4^{JM} \equiv \Sigma''_M{}^J(\kappa\mathbf{r}) = \left[\frac{1}{\kappa} \boldsymbol{\nabla} M_M^J(\kappa\mathbf{r}) \right] \cdot \boldsymbol{\sigma}, \quad (4.32)$$

$$T_5^{JM} \equiv \Delta_M^J(\kappa\mathbf{r}) = \mathbf{M}_M^{JJ}(\kappa\mathbf{r}) \cdot \frac{1}{\kappa} \boldsymbol{\nabla}, \quad (4.33)$$

$$T_6^{JM} \equiv \Delta'_M{}^J(\kappa\mathbf{r}) = -i \left[\frac{1}{\kappa} \boldsymbol{\nabla} \times \mathbf{M}_M^{JJ}(\kappa\mathbf{r}) \right] \cdot \frac{1}{\kappa} \boldsymbol{\nabla}, \quad (4.34)$$

$$T_7^{JM} \equiv \Omega_M^J(\kappa\mathbf{r}) = M_M^J(\kappa\mathbf{r}) \boldsymbol{\sigma} \cdot \frac{1}{\kappa} \boldsymbol{\nabla}. \quad (4.35)$$

4.3.2 Coherent and incoherent neutrino-nucleus cross sections

At low and intermediate energies, considered in the present study, any semi-leptonic process is described by an effective interaction Hamiltonian, written in terms of the leptonic j_μ^{lept} and hadronic \mathcal{J}_μ currents as

$$\mathcal{H}_{\text{eff}} = \frac{G_F}{\sqrt{2}} j_\mu^{\text{lept}}(x) \mathcal{J}^\mu(x), \quad (4.36)$$

where G_F is the well-known Fermi constant. In the Donnelly-Walecka multipole decomposition method, the neutral-current, double differential SM cross section from an initial $|J_i\rangle$ to a final $|J_f\rangle$ nuclear state reads [137, 138]

$$\frac{d^2\sigma_{i \rightarrow f}}{d\Omega d\omega} = \frac{G_F^2}{\pi} F(Z, \varepsilon_f) \frac{|\mathbf{k}_f| \varepsilon_f}{(2J_i + 1)} \left(\sum_{J=0}^{\infty} \sigma_{\text{CL}}^J + \sum_{J=1}^{\infty} \sigma_{\text{T}}^J \right), \quad (4.37)$$

where ε_f ($|\mathbf{k}_f|$) is the final energy (momentum) of the outgoing lepton and $\omega = \varepsilon_i - \varepsilon_f$ is the excitation energy of the nucleus, with ε_i being the initial neutrino energy. The Fermi function $F(Z, \varepsilon_f)$, takes into account the final state interaction of the outgoing charged particle the case of charged-current processes, while for neutral-current processes it holds $F(Z, \varepsilon_f) = 1$.

The summations in Eq.(4.37) contain the contributions of Coulomb $\hat{\mathcal{M}}$, longitudinal $\hat{\mathcal{L}}$, transverse electric $\hat{\mathcal{T}}^{el}$ and transverse magnetic $\hat{\mathcal{T}}^{mag}$ with both vector and axial vector components (see the text below). The cross sections σ_{CL}^J (for the Coulomb-longitudinal operators) and σ_{T}^J are written in terms of the reduced matrix elements (ME) of eight basic irreducible tensor operators (for the tensor

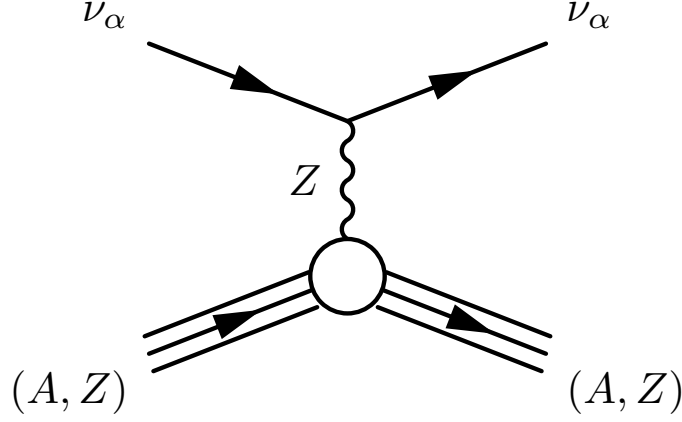


Figure 4.1: Feynman diagram contributing to neutrino-nucleus scattering within the SM.

operators) [137]

$$\begin{aligned} \sigma_{\text{CL}}^J &= (1 + a \cos \theta) |\langle J_f | \hat{\mathcal{M}}_J(\kappa) | J_i \rangle|^2 \\ &\quad + (1 + a \cos \theta - 2b \sin^2 \theta) |\langle J_f | \hat{\mathcal{L}}_J(\kappa) | J_i \rangle|^2 \\ &\quad + \left[\frac{\omega}{\kappa} (1 + a \cos \theta) + d \right] 2\Re e |\langle J_f | \hat{\mathcal{L}}_J(\kappa) | J_i \rangle \langle J_f | \hat{\mathcal{M}}_J(\kappa) | J_i \rangle|^*, \end{aligned} \quad (4.38)$$

$$\begin{aligned} \sigma_{\text{T}}^J &= (1 - a \cos \theta + b \sin^2 \theta) \left[|\langle J_f | \hat{\mathcal{T}}_J^{\text{mag}}(\kappa) | J_i \rangle|^2 + |\langle J_f | \hat{\mathcal{T}}_J^{\text{el}}(\kappa) | J_i \rangle|^2 \right] \\ &\quad \mp \left[\frac{(\varepsilon_i + \varepsilon_f)}{\kappa} (1 - a \cos \theta) - d \right] 2\Re e |\langle J_f | \hat{\mathcal{T}}_J^{\text{mag}}(\kappa) | J_i \rangle \langle J_f | \hat{\mathcal{T}}_J^{\text{el}}(\kappa) | J_i \rangle|^*, \end{aligned} \quad (4.39)$$

where the plus (minus) sign is for neutrino (antineutrino) scattering and θ is the scattering angle. The parameters a , b , d are given from the relations

$$a = \frac{|\mathbf{k}_f|}{\varepsilon_f} = \sqrt{1 - \left(\frac{m_f}{\varepsilon_f} \right)^2}, \quad b = \frac{\varepsilon_i \varepsilon_f a^2}{\kappa^2}, \quad d = \frac{m_f^2}{\kappa \varepsilon_f}. \quad (4.40)$$

In our convention ($\hbar = c = 1$) the square of the four momentum transfer is determined from the kinematics of the process in question, as

$$q^2 \equiv q_\mu q^\mu = q_0^2 - \mathbf{q}^2, \quad (4.41)$$

and to avoid confusion we define the magnitude of the three momentum transfer, as

$$\kappa = |\mathbf{q}| \equiv |\vec{q}| = [\omega^2 + 2\varepsilon_i \varepsilon_f (1 - a \cos \theta) - m_f^2]^{1/2}. \quad (4.42)$$

For neutral-current coherent neutrino-nucleus scattering (see Fig. 4.1), the kinematics of the reaction imply: $m_f = 0$ and $|\mathbf{k}_f| = \varepsilon_f$, hence $a = 1$ and $d = 0$. For the case of coherent neutrino-nucleus scattering, the momentum transfer is written in terms of the incoming neutrino energy E_ν (we adopt the usual notation $\varepsilon_i = \varepsilon_f = E_\nu$) and the scattering angle θ (laboratory frame), as

$$Q^2 = -q^2 = 4E_\nu^2 \sin^2 \frac{\theta}{2}. \quad (4.43)$$

hence, one has $\omega = 0$, and thus $\kappa = \sqrt{-q^2} = \sqrt{Q^2}$. In this case, only the Coulomb operator, $T_0^0 \equiv \hat{\mathcal{M}}_{00}$ contributes, while precise cross sections calculations become possible by explicitly solving the BCS equations [55]. The corresponding differential cross section reads

$$\frac{d\sigma}{d\cos\theta} = \frac{G_F^2}{2\pi} E_\nu^2 (1 + \cos\theta) |\langle g.s. || \hat{\mathcal{M}}_{00}(Q) || g.s. \rangle|^2, \quad (4.44)$$

where the $g.s. \rightarrow g.s.$ transition ME is given in terms of the ground state nuclear elastic form factors for protons, $F_Z(Q^2)$, and neutrons, $F_N(Q^2)$.

$$\langle g.s. || \hat{\mathcal{M}}_{00}(Q) || g.s. \rangle = \frac{1}{2} [(1 - 4\sin^2\theta_W) Z F_Z(Q^2) - N F_N(Q^2)]. \quad (4.45)$$

From an experimental physics point of view, experiments are more sensitive to the kinetic energy of the recoiling nucleus given by

$$T_N = Q^2/2M, \quad (4.46)$$

rather than the orientation of the scattered neutrino. Thus, expressing the differential cross section with respect to the nuclear recoil energy T_N , in the low energy approximation $T_N \ll E_\nu$, one finds

$$\frac{d\sigma}{dT_N} = \frac{G_F^2 M}{4\pi} \left(1 - \frac{MT_N}{2E_\nu^2}\right) |\langle g.s. || \hat{\mathcal{M}}_{00}(Q) || g.s. \rangle|^2, \quad (4.47)$$

where M stands for the mass of the target nucleus. In the latter equations, the BCS form factors for protons (neutrons) are given from Eq.(3.127)

$$F_{N_n} = \frac{1}{N_n} \sum_j \hat{j} \langle g.s. || j_0(\kappa r) || g.s. \rangle \left(v_{p(n)}^j\right)^2. \quad (4.48)$$

The above method is more accurate compared to those used by other authors. As a concrete example, we mention the differential cross section with respect to the scattering neutrino angle [63]

$$\frac{d\sigma}{d\cos\theta} = \frac{G_F^2}{8\pi} E_\nu^2 (1 + \cos\theta) Q_W^2 F^2(Q^2), \quad (4.49)$$

where the weak charge is defined as $Q_W = [(1 - 4 \sin^2 \theta_W) Z - N]$. It can be seen from Eq.(4.49) that the nuclear form factor, $F(Q^2)$, has been taken into account, which from a nuclear physics point of view cannot be neglected, due to the finite nuclear size, however many authors take $F(Q^2) = 1$ for simplicity. Eventually, we note that in the approximation $F_Z(Q^2) \approx F_N(Q^2) \equiv F(Q^2)$ Eq.(4.44) coincides with Eq.(4.49).

4.4 Derivation of coherent neutrino-nucleus cross section

The effective (quark-level) SM neutrino-nucleus interaction Lagrangian, \mathcal{L}_{SM} at low and intermediate neutrino energies, is written as

$$\mathcal{L}_{\text{SM}} = -2\sqrt{2}G_F \sum_{\substack{P=L,R \\ f=u,d \\ \alpha=e,\mu,\tau}} g_{\alpha\alpha}^{f,P} [\bar{\nu}_\alpha \gamma_\rho L \nu_\alpha] [\bar{f} \gamma^\rho P f], \quad (4.50)$$

where $g_L^u = \frac{1}{2} - \frac{2}{3} \sin^2 \theta_W$ and $g_R^u = -\frac{2}{3} \sin^2 \theta_W$ are the left- and right-handed couplings of the u -quark to the Z -boson and $g_L^d = -\frac{1}{2} + \frac{1}{3} \sin^2 \theta_W$ and $g_R^d = \frac{1}{3} \sin^2 \theta_W$ are the corresponding couplings of the d -quark (θ_W is the Weinberg mixing angle) [137].

In the general case, through the application of Feynman rules, the invariant amplitude of the process is written as

$$-i\mathcal{M} = - \left(\frac{ig}{2 \cos \theta_W} \right)^2 \bar{\nu}(k_f) \gamma_\mu (g_V^\nu - g_A^\nu \gamma_5) \nu(k_i) i \frac{g^{\mu\nu} - q^\mu q^\nu / M_Z^2}{q^2 - M_Z^2} \times \langle (Z, N)(p_f) | J_Z | (Z, N)(p_i) \rangle. \quad (4.51)$$

The nuclear matrix element for $Z \neq N$, scalar nuclei, is written as [62]

$$\langle (Z, N)(p_f) | J_Z | (Z, N)(p_i) \rangle = \frac{1}{(2\pi)^3} \frac{(p_i + p_f)^\mu}{(2E_i 2E_f)^{1/2}} [a_0 \mathcal{F}_{(T=0)}(Q^2) + a_1 \mathcal{F}_{(T=1)}(Q^2)], \quad (4.52)$$

where the current coupled to isospin has been taken into account (for $Z = N$ nuclei, the third component of isospin vanishes, $T_3 = \frac{1}{2}(Z - N)$ and only the isoscalar current contributes). In the above expression, $a_0 = -\sin^2 \theta_W$ and $a_1 = 1 - 2 \sin^2 \theta_W$. Focusing on $S = 0$, $T = 0$ nuclei, the nuclear matrix element is conveniently expressed as

$$\begin{aligned} \langle (Z, N)(p_f) | J_Z^V | (Z, N)(p_i) \rangle &= \int d^3x e^{i\mathbf{q}\cdot\mathbf{x}} (g_V^n \rho_n(x) N + g_V^p \rho_p(x) Z) \\ &= g_V^n N F_N^V(Q^2) + g_V^p Z F_Z^V(Q^2) \\ &\equiv G_V, \end{aligned} \quad (4.53)$$

where $\rho_n(x)$ ($\rho_p(x)$) and $F_N^V(Q^2)$ ($F_Z^V(Q^2)$) denote the nuclear charge density distribution and the corresponding vector form factors for neutrons (protons), while Z and N represent the number of protons and neutrons in the nucleus. The corresponding axial vector matrix element is written in the form [111]

$$\begin{aligned} \langle (Z, N)(p_f) | J_Z^A | (Z, N)(p_i) \rangle &= g_A^n (N_+ - N_-) F_N^A(Q^2) + g_A^p (Z_+ - Z_-) F_Z^A(Q^2) \\ &\equiv G_A, \end{aligned} \quad (4.54)$$

where Z_+ (Z_-) and N_+ (N_-) denote the number of protons and neutrons with spin up (spin down) respectively and $F_N^A(Q^2)$ ($F_Z^A(Q^2)$) being the axial vector nuclear form factors¹. Apparently, G_A vanishes for spin-zero nuclei.

For low momentum transfer ($Q^2 \ll M_Z^2$), the propagator can be approximated as follows

$$i \frac{g^{\mu\nu} - q^\mu q^\nu / M_Z^2}{q^2 - M_Z^2} \rightarrow i \frac{g^{\mu\nu}}{M_Z^2}, \quad (4.55)$$

leading to the usual four-fermion contact interaction, that imposes a redefinition of the Fermi constant in terms of the electroweak parameters which reads [see also Eq.(2.55)]

$$\frac{G_F}{\sqrt{2}} = \frac{g^2}{8M_W^2} = \frac{g^2}{8M_Z^2 \cos^2 \theta_W}. \quad (4.56)$$

Then, by using this equality and substituting the neutrino couplings given in Table 2.1 as well as the nuclear matrix elements for vector and axial vector couplings, the invariant amplitude becomes

$$\begin{aligned} \mathcal{M} &= 2 \frac{G_F}{\sqrt{2}} \left\{ \left[\frac{1}{2} \bar{\nu}_\beta \gamma_\mu (1 - \gamma_5) \nu_\alpha \right] [\bar{q} \gamma^\mu (G_V - G_A \gamma_5) q] \right\} \\ &= \frac{G_F}{\sqrt{2}} \left\{ [\bar{\nu}_\beta \gamma_\mu (1 - \gamma_5) \nu_\alpha] [\bar{q} \gamma^\mu (G_V - G_A \gamma_5) q] \right\}. \end{aligned} \quad (4.57)$$

The spin-averaged invariant amplitude squared is written as

$$\overline{|\mathcal{M}|^2} = \frac{1}{(2s_\nu + 1)} \frac{1}{(2s_q + 1)} \sum_{\text{spins}} |\mathcal{M}|^2 = \frac{1}{2} \sum_{\text{spins}} |\mathcal{M}|^2, \quad (4.58)$$

with s_ν and s_q being the spin degrees of freedom of the neutrino and quark respectively. Note, that neutrinos are always in the state corresponding to the negative helicity while quarks assume both states. Then, the spin-averaged matrix

¹From now on, unless otherwise mentioned, we will always denote $F_N^V(Q^2) \equiv F_N(Q^2)$ and $F_Z^V(Q^2) \equiv F_Z(Q^2)$.

elements can be calculated from first principles as

$$\begin{aligned}
\overline{|\mathcal{M}|^2} &= \frac{G_F^2}{4} \text{tr} [\bar{\nu}_\beta(k_f) \gamma_\mu (1 - \gamma_5) \nu_\alpha(k_i)] [\bar{\nu}_\beta(k_f) \gamma_\nu (1 + \gamma_5) \nu_\alpha(k_i)] \\
&\quad \times \text{tr} [\bar{q}(p_f) \gamma^\mu (G_V - G_A \gamma_5) q(p_i)] [\bar{q}(p_f) \gamma^\nu (G_V + G_A \gamma_5) q(p_i)] \\
&= \frac{G_F^2}{4} \text{tr} [\gamma_\mu (1 - \gamma_5) \not{k}_i \gamma_\nu (1 - \gamma_5) \not{k}_f] \\
&\quad \times \text{tr} \left[\gamma^\mu (G_V - G_A \gamma_5) (\not{p}_i + M) \gamma^\nu (G_V - G_A \gamma_5) (\not{p}_f + M) \right] \quad (4.59) \\
&= \frac{G_F^2}{4} \left\{ \text{tr} [2\gamma_\mu \not{k}_i \gamma_\nu \not{k}_f] + \text{tr} [2\gamma_5 \gamma_\mu \not{k}_i \gamma_\nu \not{k}_f] \right\} \\
&\quad \times \left\{ \text{tr} (G_V^2 + G_A^2) [\gamma^\mu \not{p}_i \gamma^\nu \not{p}_f] + \text{tr} (2G_V G_A) [\gamma_5 \gamma^\mu \not{p}_i \gamma^\nu \not{p}_f] \right. \\
&\quad \left. + \text{tr} (G_V^2 - G_A^2) [\gamma^\mu \gamma^\nu M^2] + \text{tr} (2G_V G_A) [\gamma_5 \gamma^\mu \gamma^\nu M] \right\}.
\end{aligned}$$

By using the properties of the gamma-matrices (see Appendix A.2), we evaluate the traces, and the above expression becomes

$$\begin{aligned}
\overline{|\mathcal{M}|^2} &= \frac{G_F^2}{4} \left\{ 2 (G_V^2 + G_A^2) 32 [(k_i \cdot p_i)(k_f \cdot p_f) + (k_i \cdot p_f)(k_f \cdot p_i)] \right. \\
&\quad + 2 (2G_V G_A) 32 [(k_i \cdot p_i)(k_f \cdot p_f) - (k_i \cdot p_f)(k_f \cdot p_i)] \\
&\quad + [8 (k_{i\mu} k_{f\nu} + k_{i\nu} k_{f\mu} - (k_i \cdot k_f) g_{\mu\nu}) + 8i \epsilon_{\mu\lambda\nu\tau} k_i^\lambda k_f^\tau] \\
&\quad \left. \times [(G_V^2 - G_A^2) 4M^2 g^{\mu\nu} + 0] \right\} \\
&= \frac{G_F^2}{4} \left\{ 64 (G_V + G_A)^2 (k_i \cdot p_i)(k_f \cdot p_f) \right. \\
&\quad + 64 (G_V - G_A)^2 (k_i \cdot p_f)(k_f \cdot p_i) \\
&\quad \left. + 32M^2 (G_V^2 - G_A^2) (-2k_i \cdot k_f) \right\} \quad (4.60) \\
&= 4 G_F^2 \left\{ (G_V + G_A)^2 (2k_i \cdot p_i)(2k_f \cdot p_f) \right. \\
&\quad + (G_V - G_A)^2 (2k_i \cdot p_f)(2k_f \cdot p_i) \\
&\quad \left. - 2M^2 (G_V^2 - G_A^2) (2k_i \cdot k_f) \right\}.
\end{aligned}$$

This matrix element is more conveniently expressed in terms of the Mandelstam variables (see Appendix A.3) as

$$\begin{aligned}
\overline{|\mathcal{M}|^2} &= 4 G_F^2 \left\{ (G_V + G_A)^2 (s - M^2)^2 + (G_V - G_A)^2 (u - M^2)^2 \right. \\
&\quad \left. - 2M^2 (G_V^2 - G_A^2) t \right\}. \quad (4.61)
\end{aligned}$$

The cross section in the center of mass frame can be cast in the form

$$\frac{d\sigma}{dQ^2} = \frac{\overline{|\mathcal{M}|^2}}{64\pi M^2 E_\nu^2}, \quad (4.62)$$

or through the change of variables $Q^2 = 2MT_N$ is written in terms of the nuclear recoil energy, T_N , as

$$\frac{d\sigma}{dT_N} = \frac{|\overline{\mathcal{M}}|^2}{32\pi ME_\nu^2}. \quad (4.63)$$

By substituting the matrix element of Eq.(4.61) in the differential cross section given above, we get

$$\frac{d\sigma}{dT_N} = \frac{4G_F^2}{32\pi ME_\nu^2} \left\{ (G_V + G_A)^2 (s - M^2)^2 + (G_V - G_A)^2 (u - M^2)^2 - 2M^2 (G_V^2 - G_A^2) t \right\}, \quad (4.64)$$

or equivalently

$$\frac{d\sigma}{dT_N} = \frac{G_F^2}{8\pi ME_\nu^2} \left\{ (G_V + G_A)^2 (2ME_\nu)^2 + (G_V - G_A)^2 (2ME'_\nu)^2 - 2M^2 (G_V^2 - G_A^2) 2M (E_\nu - E'_\nu) \right\}, \quad (4.65)$$

where we substituted the Mandelstam variables. Then, from the definition of the nuclear recoil energy

$$T_N = E' - M = E_\nu - E'_\nu, \quad (4.66)$$

the final expression for the differential neutrino-nucleus cross section takes the compact form

$$\frac{d\sigma}{dT_N} = \frac{G_F^2 M}{2\pi} \left\{ (G_V + G_A)^2 + (G_V - G_A)^2 \left(1 - \frac{T_N}{E_\nu}\right)^2 - (G_V^2 - G_A^2) \frac{MT_N}{E_\nu^2} \right\}. \quad (4.67)$$

For the case of coherent scattering, $G_A = 0$, and the differential cross section with respect to the nuclear recoil energy, T_N , takes the form

$$\frac{d\sigma_{SM,\nu\alpha}}{dT_N} = \frac{G_F^2 M}{\pi} \left(1 - \frac{MT_N}{2E_\nu^2}\right) \left| \langle g.s. || \hat{\mathcal{M}}_{00}(Q) || g.s. \rangle \right|^2. \quad (4.68)$$

The operator $\hat{\mathcal{M}}_{00}$ in the nuclear matrix element of the latter equation is the Coulomb operator which is equal to the product of the zero-order Spherical Bessel function times the zero-order Spherical Harmonic [135, 137]. This matrix element can be cast in the form [55]

$$|\mathcal{M}_{V,\nu\alpha}^{SM}|^2 \equiv \left| \langle g.s. || \hat{\mathcal{M}}_{00}(Q) || g.s. \rangle \right|^2 = [g_V^p Z F_Z(Q^2) + g_V^n N F_N(Q^2)]^2, \quad (4.69)$$

where, the polar-vector couplings of protons g_V^p and neutrons g_V^n with the Z boson, are written as

$$\begin{aligned} g_V^p &= 2(g_L^u + g_R^u) + (g_L^d + g_R^d) = \frac{1}{2} - 2\sin^2\theta_W, \\ g_V^n &= (g_L^u + g_R^u) + 2(g_L^d + g_R^d) = -\frac{1}{2}, \end{aligned} \quad (4.70)$$

respectively. As can be easily seen, the vector contribution of all protons is very small ($g_V^p \sim 0.04$), hence the coherence in Eq.(4.69) essentially refers to all neutrons only of the studied nucleus.

After some straightforward elaboration the SM angle-differential cross section reads

$$\frac{d\sigma_{\text{SM},\nu\alpha}}{d\cos\theta} = \frac{G_F^2}{2\pi} E_\nu^2 (1 + \cos\theta) \left| \langle g.s. | \hat{\mathcal{M}}_{00}(Q) | g.s. \rangle \right|^2. \quad (4.71)$$

In this Chapter, we perform Standard model cross sections calculations for a set of nuclei throughout the periodic table up to ^{208}Pb . We adopt various nuclear models (see Sect. 3.6) to compute the nuclear form factors. Then, for a great part of the cross section results (except differential cross sections) we evaluate folded cross sections, and event rates.

4.5 Results and discussion

The next step of our study was to apply the form factor discussed previously and using Eqs.(4.44, 4.47) to perform nuclear cross sections calculations (see upper and central panel of Fig. 4.2). We note that large differences appear if the form factor dependence is neglected and hence $F = 1$ is not reliable. However, at low neutrino energies, i.e. $E_\nu \leq 20$ MeV that are relevant for solar neutrinos, the agreement of these two approximations is rather good. On the contrary, for the case of Supernova neutrinos (or neutrinos from other sources with higher energies), a difference of some orders of magnitude may exist. The scattering angle, has found to play significant role in the angular dependence of the differential cross section $d\sigma/d\cos\theta$. Forward scattering, ($\theta = 0$) leads to maximum $d\sigma/d\cos\theta$ and obviously in that case the form factor is equal to unity due to zero momentum transfer, see Eq.(4.43).

4.5.1 Integrated coherent neutrino-nucleus cross sections

The next phase of our calculational procedure is related to the total coherent neutrino-nucleus cross sections, obtained through numerical integration of Eq.(4.44) over angles [or Eq.(4.47) over T_N] as

$$\sigma_{\nu\alpha}(E_\nu) = \int \frac{d\sigma_{\nu\alpha}}{d\cos\theta}(\theta, E_\nu) d\cos\theta. \quad (4.72)$$

The results for the Standard Model cross sections, for a set of different promising targets throughout the periodic table, are presented in the lower panel of Fig. 4.2 [for the case of ^{48}Ti only, using the method of fraction occupation probabilities, (FOP)] and in Fig. 4.3 (using the BCS method). As can be seen, the present nuclear structure calculations indicate that between light and heavy nuclear systems, the cross sections may differ by even two orders of magnitude (or more)

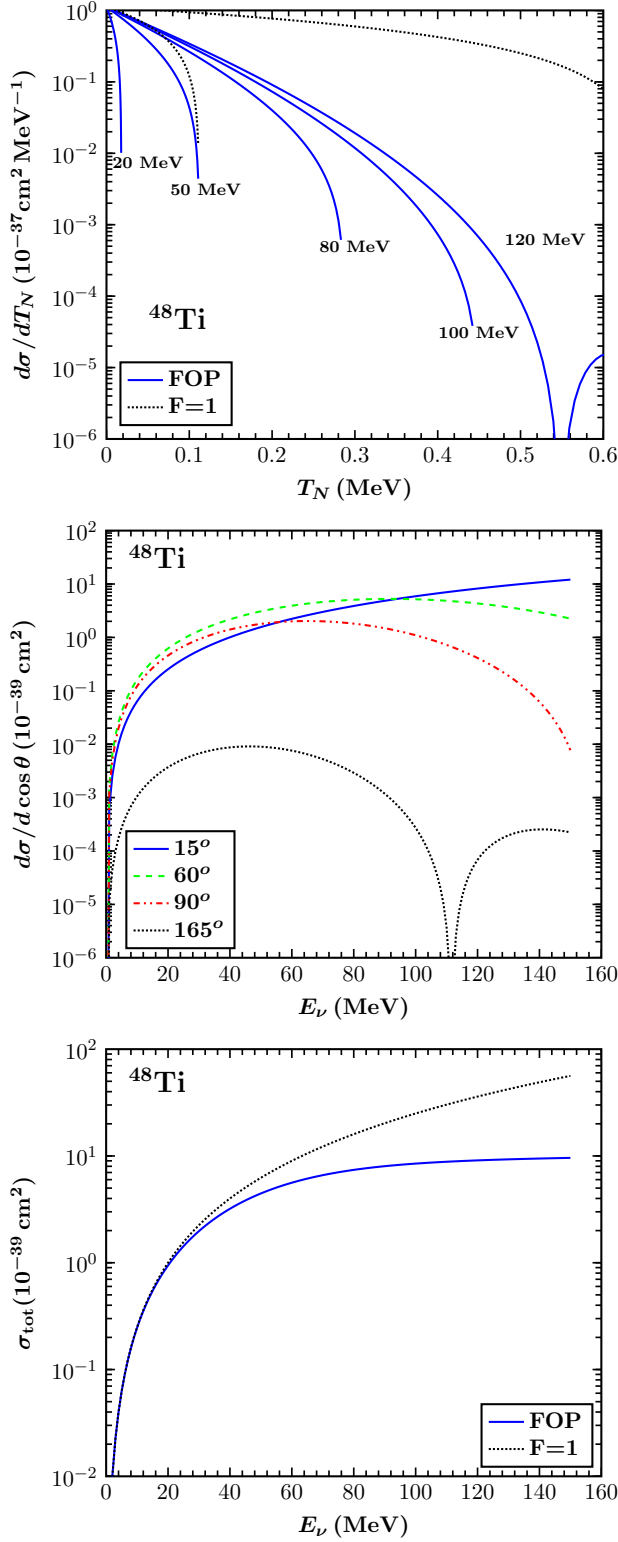


Figure 4.2: *Top:* The differential cross section $d\sigma/dT_N$ (in units $10^{-37} \text{cm}^2/\text{MeV}$) as a function of the nuclear recoil energy T for various neutrino energies. $d\sigma/dT_N$ is compared to that of point-like nucleus ($F = 1$) for $E_\nu = 50$ and $E_\nu = 120$ MeV. For rather low energies the results coincide, however for intermediate or high energies this is not the case.

Middle: The differential cross section $d\sigma/d \cos \theta$ (in units 10^{-39}cm^2) as a function of the incoming neutrino energy E_ν , for some typical angles. We observe the important affect of the scattering angle on $d\sigma/d \cos \theta$, e.g. for backward scattering, even not shown here, the cross section is minimised.

Bottom: The total coherent cross section, σ_{tot} (in units 10^{-39}cm^2) as a function of the incident neutrino energy in MeV (bottom), for ^{48}Ti . σ_{tot} appears to have an asymptotic behaviour at neutrino energies $E_\nu \geq 80$ MeV or higher.

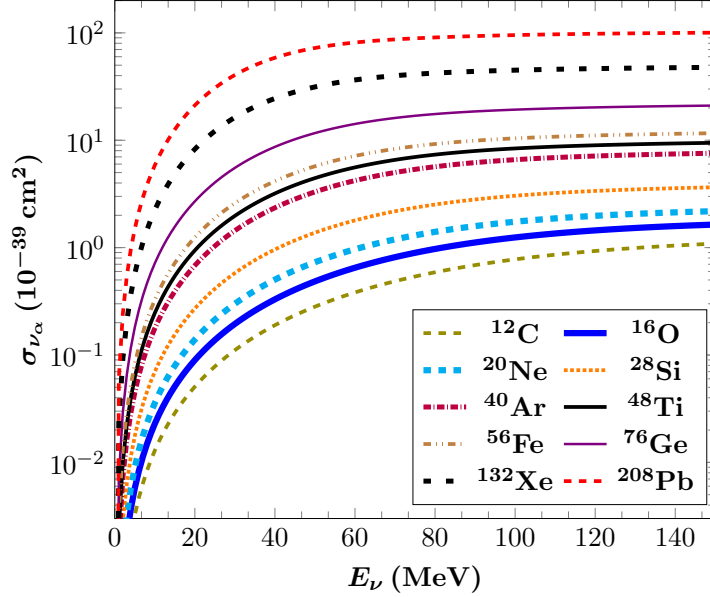


Figure 4.3: Total coherent cross sections $\sigma_{\nu_\alpha(\bar{\nu}_\alpha)}(E_\nu)$ in units 10^{-39}cm^2 for a set of nuclei as a function of the incoming neutrino energy E_ν , for the SM neutrino processes $\nu_\alpha(\bar{\nu}_\alpha) + (A, Z) \rightarrow \nu_\alpha(\bar{\nu}_\alpha) + (A, Z)$.

as a consequence of the dependence on the nuclear parameters (i.e. mass, form factors, etc.). We also see that for heavier nuclei the cross sections flatten more quickly (at lower neutrino energies) compared to that of lighter nuclear isotopes. The latter conclusion originates mainly from the fact that, for heavy nuclei the suppression of the cross sections due to the nuclear form factors becomes more significant. Thus, for heavy material the nuclear effects become important even at low energies. Such original cross section results are helpful for the simulations of the Standard Model signals of neutrino detection experiments (see below).

4.5.2 Supernova neutrino simulations

As discussed previously, our present calculations may also be useful for ongoing and future neutrino experiments related to Supernova (SN) neutrino detection, since as it is known, the neutrinos emitted in SN explosions transfer the maximum part of the total the energy released. Then, the total neutrino flux, $\Phi(E_\nu)$, arriving at a terrestrial detector as a function of the SN neutrino energy E_ν , the number of emitted (anti)neutrinos, N_{ν_α} , at a distance, d , from the source (here we consider $d = 10$ kpc), reads [88, 99]

$$\Phi(E_\nu) = \sum_{\nu_\alpha} \Phi_{\nu_\alpha} \eta_{\nu_\alpha}^{\text{SN}}(E_\nu) = \sum_{\nu_\alpha} \frac{N_{\nu_\alpha}}{4\pi d^2} \eta_{\nu_\alpha}^{\text{SN}}(E_\nu), \quad (4.73)$$

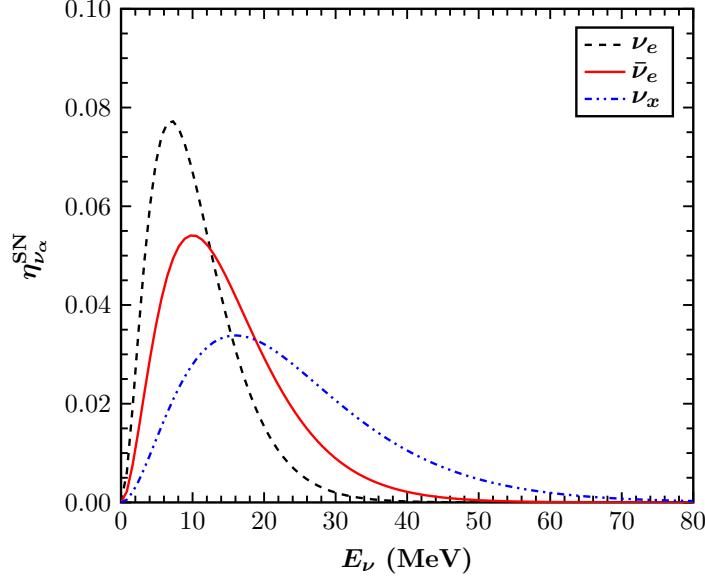


Figure 4.4: Normalised Supernova neutrino energy spectra, $\eta_{\nu_\alpha}^{\text{SN}}$, parametrised with Maxwell-Boltzmann distributions for zero chemical potential. Each neutrino flavour has different temperature dependence (see the text).

($\alpha = e, \mu, \tau$) where $\eta_{\nu_\alpha}^{\text{SN}}$ denotes the energy-distribution of the (anti)neutrino flavour α .

The emitted SN-neutrino energy spectra (see Fig. 4.4), $\eta_{\nu_\alpha}^{\text{SN}}(E_\nu)$, may be parametrised by Maxwell-Boltzmann distributions that depend only on the temperature, T_{ν_α} , of the (anti)neutrino flavour ν_α or $\bar{\nu}_\alpha$ (assuming zero chemical potential) we have

$$\eta_{\nu_\alpha}^{\text{SN}}(E_\nu) = \frac{E_\nu^2}{2T_{\nu_\alpha}^3} e^{-E_\nu/T_{\nu_\alpha}}, \quad (4.74)$$

($T_{\nu_e} = 3.5\text{MeV}$, $T_{\bar{\nu}_e} = 5.0\text{MeV}$, $T_{\nu_x, \bar{\nu}_x} = 8.0\text{MeV}$, $x = \mu, \tau$ [97]). For each flavour, the total number of emitted neutrinos, N_{ν_α} , is obtained from the mean neutrino energy [25]

$$\langle E_{\nu_\alpha} \rangle = 3T_{\nu_\alpha} \quad (4.75)$$

and the total energy released from a SN explosion, $U = 3 \times 10^{53}\text{erg}$ [80, 81]. Thus, the equipartition of energy yields $N_{\nu_e} = 3.0 \times 10^{57}$, $N_{\bar{\nu}_e} = 2.1 \times 10^{57}$ and $N_{\nu_x} = 5.2 \times 10^{57}$.

In the literature, apart from Maxwell-Boltzmann, there exist alternative choices for the SN-neutrino energy spectra. The most interesting choices, include those resembling Fermi-Dirac or power-law distributions (see Appendix E.1).

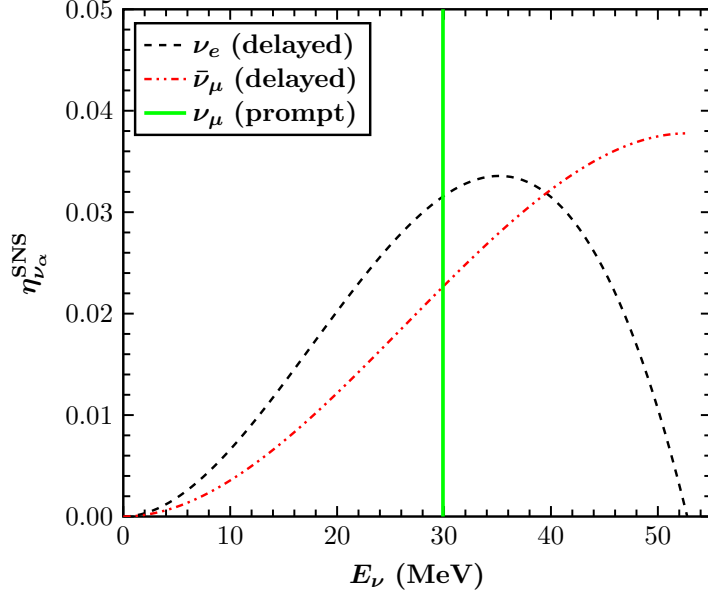


Figure 4.5: Normalised stopped pion-muon beam neutrino energy spectra, $\eta_{\nu_\alpha}^{\text{SNS}}$, for delayed (ν_e and $\bar{\nu}_\mu$) and prompt (ν_μ) beams (see the text).

4.5.3 Laboratory neutrino simulations

The Spallation Neutron Source (SNS) at Oak Ridge National Lab [69] produces neutrons by firing a pulsed proton beam at a liquid mercury target [117]. The main aim of the COHERENT proposal [73–75] (or of other similar conceptual [76]) concerns with possible detection of neutrino-nucleus coherent scattering events at the SNS. Our simulations here, are mainly motivated by previous studies [70, 78, 79, 116] and the hope to provide our accurate nuclear structure calculations. In stopped pion-muon sources, neutrinos are produced by the pion decay chain. Pion decay at rest $\pi^+ \rightarrow \mu^+ \nu_\mu$, ($\tau = 26$ ns) produces monochromatic muon neutrinos ν_μ at 29.9 MeV, followed by electron neutrinos ν_e and muon antineutrinos $\bar{\nu}_\mu$ that are produced by the muon-decay $\mu^+ \rightarrow \nu_e e^+ \bar{\nu}_\mu$ ($\tau = 2.2$ μ s) [86, 87]. For pulsed beams in time-scales narrower than μ s, ν_e 's and $\bar{\nu}_\mu$'s will be delayed with the beam while ν_μ 's will be prompt with the beam [70]. In Fig. 4.5, the emitted ν_e and $\bar{\nu}_\mu$ neutrino spectra are described by the high precision normalised distributions, known as the Michel spectrum [72]

$$\begin{aligned} \eta_{\nu_e}^{\text{SNS}} &= 96 E_\nu^2 m_\mu^{-4} (m_\mu - 2E_\nu) , \\ \eta_{\bar{\nu}_\mu}^{\text{SNS}} &= 16 E_\nu^2 m_\mu^{-4} (3m_\mu - 4E_\nu) , \end{aligned} \quad (4.76)$$

($m_\mu = 105.6$ MeV is the muon rest mass). The maximum neutrino energy in the latter distributions is $E_\nu^{\text{max}} = m_\mu/2 = 52.8$ MeV (see e.g. [71]).

The Spallation Neutron Source (SNS) at Oak Ridge National Lab is currently the most powerful facility to detect for a first time neutrino-nucleus coherent scat-

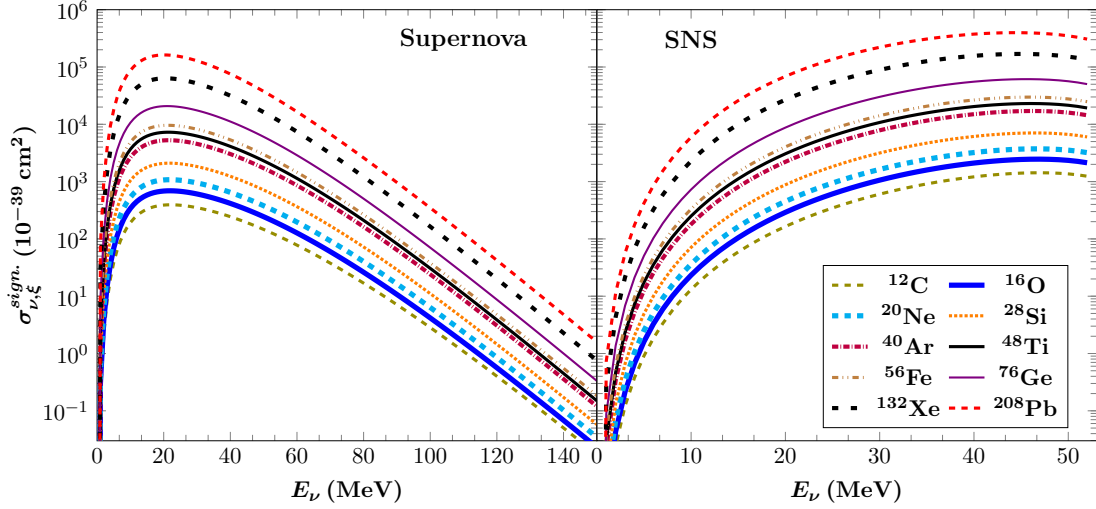


Figure 4.6: The signal cross sections that represent the expected signal to be recorded on a terrestrial nuclear neutrino detector, (*left*) for Supernova neutrinos ($\xi = \text{SN}$), evaluated with Maxwell-Boltzmann distributions at $d = 10$ kpc, and (*right*) for SNS neutrinos ($\xi = \text{SNS}$), at 20 m from the source. For the case of SNS neutrinos the figure takes into account only the delayed beam, evaluated with the generic flux of $\Phi_{\nu_\alpha} \sim 10^7 \nu\text{s}^{-1}\text{cm}^{-2}$. Different nuclear detectors have been studied.

tering events, since it provides exceptionally intense fluxes $\Phi_{\nu_\alpha} = 2.5 \times 10^7 \nu\text{s}^{-1}\text{cm}^2$ at 20 m and $\Phi_{\nu_\alpha} = 6.3 \times 10^6 \nu\text{s}^{-1}\text{cm}^2$ at 40 m from the source [86, 87]. The simulated laboratory neutrino signals $\sigma_{\nu, \text{SNS}}^{\text{sign}}$ coming out of our calculations for the adopted nuclear targets are discussed below.

4.5.4 Simulated neutrino signals

By weighting the integrated cross section $\sigma_{\nu_\alpha}(E_\nu)$ with the neutrino distributions of Eq.(4.74), for SN neutrinos, or Eq.(4.76), for laboratory neutrinos, the total signal produced on a terrestrial detector is described by [136]

$$\sigma_{\nu, \xi}^{\text{sign}}(E_\nu) = \sum_{\nu_\alpha} \sigma_{\nu_\alpha}(E_\nu) \eta_{\nu_\alpha}^\xi(E_\nu), \quad \xi = \text{SN}, \text{SNS}. \quad (4.77)$$

The resulting signals, $\sigma_{\nu, \xi}^{\text{sign}}(E_\nu)$, obtained by inserting in Eq.(4.77) the cross sections σ_{ν_α} of Fig. 4.3, are plotted in Fig. 4.6.

In Ref. [25] we have shown that the simulated cross sections reflect the characteristics of the incident neutrino spectrum of the specific neutrino flavour α and therefore, such a simulated signal is characterised by its own position of the maximum peak and width of the distribution $\eta_{\nu_\alpha}^{\text{SN}}$. We, however, remind that

Nucleus	^{12}C	^{16}O	^{20}Ne	^{28}Si	^{40}Ar	^{48}Ti	^{56}Fe	^{76}Ge	^{132}Xe	^{208}Pb
$\langle\sigma_\nu\rangle_{\text{SN}}$	1.46	2.51	3.91	7.52	18.59	25.43	33.29	70.63	207.56	514.93
$\langle\sigma_\nu\rangle_{\text{SNS}}$	3.07	5.33	8.13	15.52	37.91	51.50	67.02	139.83	395.59	949.50

Table 4.1: Flux averaged cross sections $\langle\sigma_\nu\rangle_\xi$ in units 10^{-40}cm^2 for the adopted Supernova ($d = 10\text{ kpc}$) and laboratory (delayed flux only) neutrino spectra. For the case of SNS neutrinos, we adopt the generic flux, i.e. $\Phi_{\nu_\alpha} \sim 10^7\text{ }\nu\text{s}^{-1}\text{cm}^2$ at 20 m for all nuclear targets.

within the framework of the SM, coherent neutrino scattering is a flavour blind and a particle-antiparticle blind process. For this particular case our results are shown in Fig. 4.6 for Supernova and laboratory (SNS) neutrinos.

In neutrino simulations, another useful quantity is the flux averaged cross section [66] which in our notation is written as

$$\langle\sigma_\nu\rangle_\xi = \sum_{\nu_\alpha} \int \sigma_{\nu_\alpha}(E_\nu) \eta_{\nu_\alpha}^\xi(E_\nu) dE_\nu. \quad (4.78)$$

The results for $\langle\sigma_\nu\rangle_\xi$, obtained by using the angle-integrated cross sections of Fig. 4.3 are listed in Table 4.1 for both neutrino sources.

4.5.5 Differential and total event rates

From experimental physics perspectives, predictions for the differential event rate, Y_{ν_α} , of a neutrino detector are crucial [88]. The usual expression for computing the yield in events is based on the neutrino flux, and is defined as [99]

$$Y_{\nu_\alpha}(T_N) = \frac{dN}{T_N} = K \sum_{\nu_\alpha} \Phi_{\nu_\alpha} \int \eta_{\nu_\alpha}^\xi dE_\nu \int \frac{d\sigma_{\nu_\alpha}}{d\cos\theta} \delta\left(T_N - \frac{Q^2}{2M}\right) d\cos\theta, \quad (4.79)$$

where $K = N_{\text{targ.}} t_{\text{tot.}}$ accounts for the total number of nuclei (atoms) in the detector material $N_{\text{targ.}}$ times the total time of exposure $t_{\text{tot.}}$. Using the latter equation, one concludes that, the lower the energy recoil, the larger the potentially detected number of events (see Fig. 4.7 and Fig. 4.8). In principle, in order to maximise the potential detection of a rare event process like the neutrino-nucleus scattering, detector materials with very low energy-recoil threshold and low-background are required. In the last stage of our study we make predictions for the total number of coherent scattering events, the most important quantity, both from theoretical and experimental perspectives. To this purpose, we evaluate the number of expected counts, for the studied detector materials, by performing numerical integration of Eq.(4.79) over the nuclear recoil threshold T_N^{thres} (see Table 4.2).

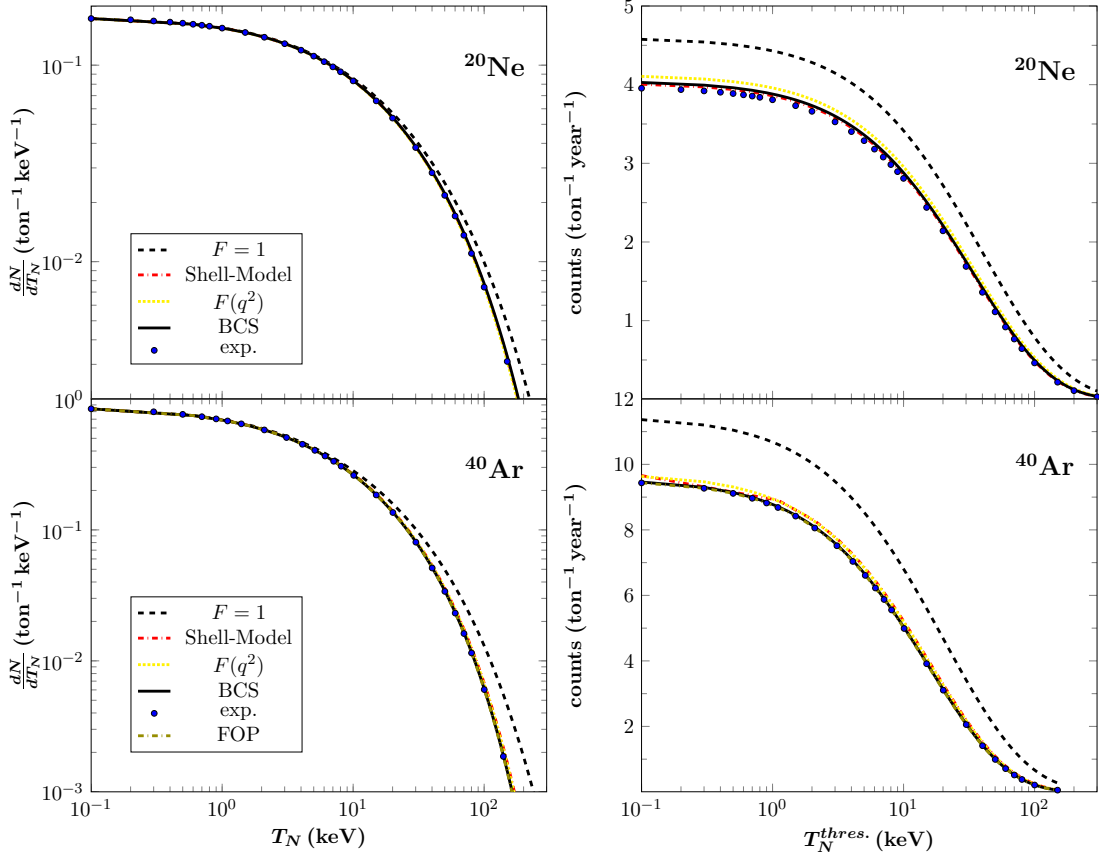
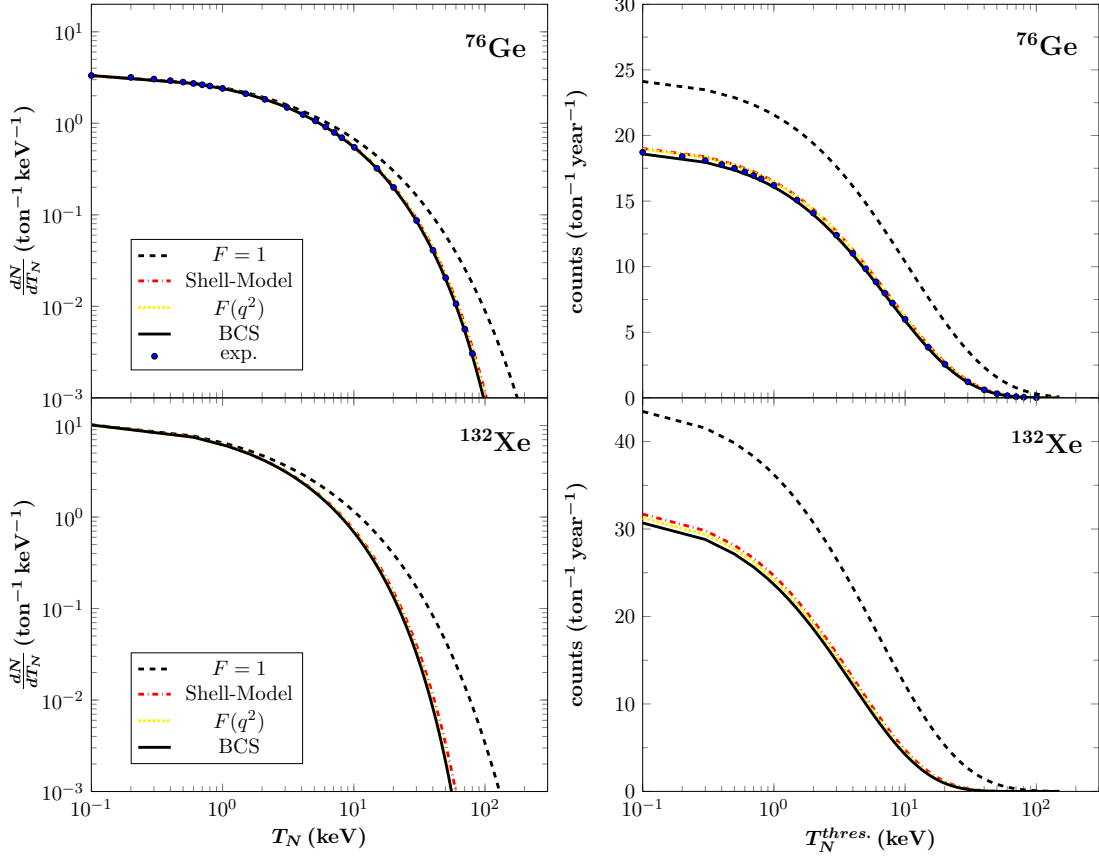


Figure 4.7: Yield in events (*left*) and total number of events over nuclear recoil threshold T_N^{thres} (*right*), for Supernova neutrinos at $d = 10$ kpc. Here, 1 ton of perfectly efficient ^{20}Ne and ^{40}Ar detectors have been considered and also possible neutrino oscillation in propagation effects are neglected. For heavier nuclear targets the differences become rather significant. In this figure, $F(q^2)$ stands for Eq.(3.141) and FOP for the method of fractional occupation probabilities of the states. For more details see the text.

As has been discussed previously [88, 89], SN neutrino detection might become possible by the massive dark matter detectors [94] which have very good energy resolution and low threshold capabilities [99]. These experiments are designed (or planned) to search for WIMPs [90, 91] and/or other rare events such as the neutrinoless double beta decay. The latter, use heavy nuclei as nuclear detectors, e.g. Ge (GERDA [93] and SuperCDMS [92] experiments). In addition we report that SN neutrino events can be potentially detected by experiments using noble gases like Ne (CLEAN detector [94]), Ar (WARP programme [95]) and Xe (XENON 100 Collaboration [96]).

As mentioned in Sect. 3.6, in order to test our nuclear calculations we have also employed other nuclear methods. To this purpose, we have compared our

Figure 4.8: Same as Fig. 4.7 but for ^{76}Ge and ^{132}Xe .

original results evaluated with the BCS method with those obtained as discussed in Subsect. 3.6.2 and concluded that for the case of the coherent channel all available nuclear methods are in good agreement, but their results differ significantly from those obtained assuming $F_Z(Q^2) = F_N(Q^2) = 1$ (see Fig. 4.7 and Fig. 4.8). We stress however, that, since the cross section is mostly sensitive to the neutron distribution of the target nucleus, the most accurate method (at low and intermediate energies) is the BCS method which provides realistic proton as well as neutron form factors. All other methods employed here consider only the proton distribution and assume $F_Z(Q^2) = F_N(Q^2)$, which especially for heavy nuclei, is a rather crude approximation. We remark, however, that the aforementioned nuclear methods offer reliable results on the differential and total event rates for low energies (see Fig. 4.7 and Fig. 4.8), but in order to correctly estimate the neutron form factor, methods like the BSC are probably more appropriate.

Our present nuclear structure calculations for laboratory (SNS) neutrinos [69] (see Fig. 4.9), are in good agreement with previous results [70]. They imply that a comparably large number of coherent neutrino scattering events is expected to be measured by using LNe, LAr, LXe, Ge and CsI[Na] materials adopted by

Nucleus	T_N	$T_N > 5$ keV	$T_N > 10$ keV	$T_N > 25$ keV	$T_N > 50$ keV
^{12}C	2.52	2.25	2.05	1.60	1.14
^{16}O	3.29	2.84	2.51	1.83	1.19
^{20}Ne	4.03	3.35	2.87	1.96	1.16
^{27}Al	5.78	4.53	3.71	2.27	1.17
^{32}S	6.23	4.68	3.72	2.12	0.99
^{40}Ar	9.46	6.63	5.01	2.53	1.00
^{48}Ti	10.73	7.04	5.06	2.27	0.76
^{56}Fe	12.00	7.36	5.04	2.01	0.57
^{76}Ge	18.58	9.61	5.82	1.70	0.30
^{114}Cd	26.08	9.79	4.68	0.73	0.05
^{132}Xe	30.68	9.84	4.16	0.46	0.01
^{208}Pb	46.93	7.86	1.95	0.03	$< 10^{-3}$

Table 4.2: Total number of events per ton of the target materials for a Supernova at a distance of 10 kpc. We assume various energy thresholds 5, 10, 25 or 50 keV. Our present results are in excellent agreement with those of Refs. [88, 99].

the COHERENT Collaboration [73–75]. The predictions of the BCS method for these nuclei are illustrated in Fig. 4.9 and compared with those of other promising nuclear targets. Because the neutrino flux produced at the SNS is very high, (of the order of $\Phi_{\nu_\alpha} \sim 10^7 \nu s^{-1} \text{cm}^{-2}$ per flavour at 20 m from the source [86]), even kg-scale experiments expect to measure neutrino-nucleus coherent scattering events at significantly higher rates than those of Supernova neutrinos.

It is worth noting that, the choice of the target nucleus plays also a crucial role, since a light nuclear target may yield almost constant number of events throughout the energy range, but small number of counts. On the other hand, a heavy nuclear target provides more counts, but yields low-energy recoil making the detection more difficult. This leads to the conclusion that the most appropriate choice for a nuclear detector might be a combination of light and heavy nuclear isotopes, like the scintillation detectors discussed in Ref. [99].

4.6 Conclusions

The evaluation of all required nuclear matrix elements, related to Standard Model neutrino-nucleus processes is formulated, and realistic nuclear structure calculations of neutrino-nucleus cross sections for a set of interesting nuclear targets are performed. The first stage involves cross sections calculations for the dominant coherent channel in the range of incoming neutrino energies $0 \leq E_\nu \leq 150$ MeV (it includes neutrino energies of stopped pion-muon neutrino decay sources, Supernova neutrinos, etc.).

Additionally, new results for the total number of events expected to be observed in one ton of various neutrino detector materials are provided and the potentiality of detecting Supernova as well as laboratory neutrino-nucleus events is in detail explored. The calculations are concentrated on interesting nuclei, like ^{20}Ne and ^{40}Ar , ^{76}Ge and ^{132}Xe which are important detector materials for several rare event experiments, like the COHERENT at Oak Ridge National Laboratory, and also experiments searching for dark matter events as the GERDA, SuperCDMS, XENON 100, CLEAN, etc. By comparing our results with those of other methods, we see that the nuclear physics aspects (reflecting the accuracy of the required neutrino-nucleus cross sections), appreciably affect the coherent $g.s. \rightarrow g.s.$ transition rate, a result especially useful for Supernova neutrino detection probes.

In this Chapter, the QRPA method that considers realistic nuclear forces has been adopted in evaluating the nuclear form factors, for both categories of neutrino-nucleus processes, the conventional and the exotic ones. Also, a comparison with other simpler methods as (i) effective methods and (ii) the method of fractional occupation probabilities, which improves over the simple Shell-Model and gives higher reproducibility of the available experimental data, is presented and discussed. We conclude that among all the adopted methods the agreement is quite good, especially for light and medium nuclear isotopes. However, since coherent neutrino-nucleus scattering can probe the neutron nuclear form factors, methods like the BCS provide more reliable results.

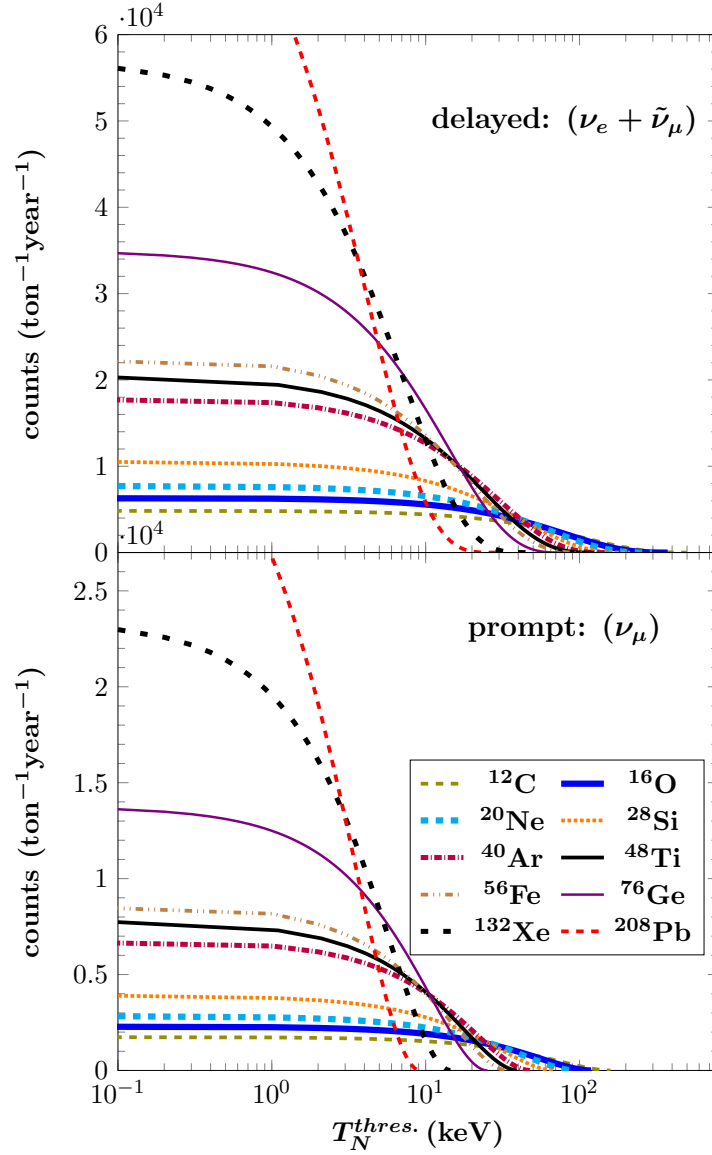


Figure 4.9: Total number of expected events over nuclear recoil threshold for 1 ton of various nuclear targets at 20 m from the source ($\Phi_{\nu_\alpha} \sim 10^7 \nu\text{s}^{-1}\text{cm}^{-2}$). The upper (lower) panel assumes the delayed (prompt) flux of laboratory stopped-pion neutrino sources. This figure assumes a perfectly efficient detector and negligible neutrino oscillation effects.

Chapter 5

Exotic neutrino-nucleus processes

5.1 Introduction

The nuclear aspects of flavour changing neutral-current (FCNC) processes, predicted by various new-physics models to occur in the presence of nuclei, are examined by computing the relevant nuclear matrix elements within the context of the QRPA using realistic strong two-body forces. One of our aims is to explore the role of the non-standard interactions (NSI) in the leptonic sector and specifically: (i) in lepton flavour violating (LFV) processes involving the neutral particles ν_ℓ and $\bar{\nu}_\ell$, $\ell = e, \mu, \tau$ and (ii) in charged lepton flavour violating (cLFV) processes involving the charged leptons ℓ^- or ℓ^+ . As concrete nuclear systems we have chosen the stopping targets of $\mu^- \rightarrow e^-$ conversion experiments, i.e. the ^{48}Ti nucleus of the PRIME/PRISM experiment at J-PARC and the ^{27}Al of the COMET at J-PARC as well as of the Mu2e at Fermilab. These experiments have been designed to reduce the single event sensitivity down to 10^{-16} – 10^{-18} in searching for charged lepton mixing events. Our goal is, by taking advantage of our detailed nuclear structure calculations and using the present limits or the sensitivity of the aforementioned exotic $\mu^- \rightarrow e^-$ experiments, to put stringent constraints on the parameters of NSI Lagrangians.

5.2 The role of neutrino NSI interactions in nuclear physics

In recent years, ongoing extremely sensitive experiments searching for physics beyond the current Standard Model (SM) expect to see new physics or to set severe limits on various physical observables and particle model parameters [110, 139, 140]. In particular, current experiments searching for flavour changing neutral current (FCNC) processes in the leptonic sector [105–109, 140] may provide insights and new results into the physics of charged lepton flavour viol-

ation (cLFV), neutrino oscillation in propagation [105] and others. The cLFV experiments, although they have not yet discovered any event, represent a very important probe to search for charged lepton mixing with significant implications on understanding various open issues in particle, nuclear physics and astrophysics [22, 111, 118, 119]. To this purpose, exotic $\mu^- \rightarrow e^-$ conversion studies are interesting worldwide theoretically [122, 126] as well as experimentally with two experiments: (i) the COMET at J-PARC, Japan [106, 107], and (ii) the Mu2e at Fermilab, USA [108, 109]. Both ambitious experiments expect to reach a single event sensitivity down to 10^{-16} – 10^{-18} .

The best previous limit for the $\mu^- \rightarrow e^-$ conversion was obtained by the SINDRUM-II collaboration at the Paul Scherrer Institute (PSI), Switzerland, on the reaction



as $R_{\mu e}^{\text{Ti}} < 6.1 \times 10^{-13}$ [141] (many authors use the published upper limit $R_{\mu e}^{\text{Ti}} < 4.3 \times 10^{-12}$ [142]), where $R_{\mu e}^{\text{Ti}}$ denotes the branching ratio of the $\mu^- \rightarrow e^-$ conversion rate divided by the total μ^- -capture rate in the ${}^{48}\text{Ti}$ nucleus. The COMET experiment, is expected to reach a high sensitivity, $R_{\mu e}^{\text{Al}} < 10^{-16}$ [106, 107] using ${}^{27}\text{Al}$ as muon-stopping target while the Mu2e experiment aims to improve $R_{\mu e}^{\text{Al}}$ even further, i.e. to a single event sensitivity 2×10^{-17} , which with a background of 0.5 events will reach a target sensitivity $R_{\mu e}^{\text{Al}} < 6 \times 10^{-17}$ [108, 109]. The next decade experiments for cLFV, need very high intensity and quality muon beams, like those planed to be built at Fermilab for the Mu2e at Project-X and at J-PARC for the PRIME/PRISM experiments. The use of Project-X beams by the Mu2e experiment, expects to further decrease the upper bound to $R_{\mu e}^{\text{Al}} < 2 \times 10^{-18}$ [143], while the PRIME experiment, based on the superior properties of the muon beam at J-PARC that can be delivered to the ${}^{48}\text{Ti}$, may reach the sensitivity of $R_{\mu e}^{\text{Ti}} < 10^{-18}$ [144, 145].

We should mention the most stringent upper bounds on purely leptonic cLFV processes presently available for $\mu - e$ transitions, namely, the new limit on the branching ratio of the $\mu^+ \rightarrow e^+ \gamma$ process, $Br(\mu^+ \rightarrow e^+ \gamma) < 5.7 \times 10^{-13}$, set very recently by the MEG experiment at PSI using one of the most intense continuous μ^+ beams in the world [146], and that of the $\mu \rightarrow eee$ process set previously by the SINDRUM II collaboration in the value $Br(\mu^+ \rightarrow e^+ e^+ e^-) < 1.0 \times 10^{-12}$ [147].

In recent works, neutral-current (NC) neutrino scattering processes on leptons, nucleons and nuclei involving interactions that go beyond the SM (non-standard interactions, NSI, for short) have been examined [22, 111, 118]. Such processes may be predicted from several extensions of the SM such as various realisations of the seesaw mechanism in the SM [67, 68, 126, 127], and left-right symmetric models [128]. The reactions of this type that take place in nuclei are represented by

$$\nu_\alpha(\bar{\nu}_\alpha) + (A, Z) \rightarrow \nu_\beta(\bar{\nu}_\beta) + (A, Z), \quad (5.2)$$

($\alpha, \beta = e, \mu, \tau$) and theoretically they can be studied under the same nuclear

methods as the exotic cLFV process of $\mu^- \rightarrow e^-$ conversion in nuclei. Among the interesting applications of the reactions (5.2), those connected with the Supernova physics may allow ν_e neutrinos to change flavour during core collapse creating ν_e neutrino holes in the electron-neutrino sea [130] which may allow e^- -capture on nucleons and nuclei to occur and subsequently decrease the value of the electron fraction Y_e . Such non-standard interactions [70, 112–114] may suggest alterations in the mechanisms of neutrino-propagation through the Supernova (SN) envelope and affect constraints put on the physics beyond the SM as well as on some scenarios of Supernova explosion [21, 131, 132]. This motivated the investigation of the NSI in both LFV and cLFV processes in solar and Supernova environment [55, 133, 134] and motivated our present work too. Furthermore, the impact of non-standard neutrino interactions on SN physics was the main motivation of works examining their effect on Supernova when the neutrino self-interaction is taken into account [119]. The extreme conditions under which neutrinos propagate after they are created in the SN core, may lead to strong matter effects. It is known that, in particular, the effect of small values of the NSI parameters can be dramatically enhanced in the inner strongly deleptonised regions [119].

In general, low-energy astrophysical and laboratory neutrino searches provide crucial information towards understanding the fundamental electroweak interactions, within and beyond the SM. Well-known astrophysical neutrino sources like the solar, Supernova, Geoneutrinos, etc., constitute excellent probes in searching for a plethora of neutrino physics applications and new-physics open issues [66]. Since neutrinos interact extremely weakly with matter, they may travel astronomical distances and reach the Earth [100–102], etc. The recorded neutrino signals in sensitive terrestrial nuclear detectors of low-energy neutrinos [80–82], could be simulated providing useful information relevant to the evolution of distant stars, the core collapse Supernovae, explosive nucleosynthesis [83], neutrino oscillation effects and others. Recently it became feasible to detect neutrinos by exploiting the NC interactions and measuring the nuclear recoil signal by employing detectors with very low-threshold energies [71, 72]. The NC interactions, through their vector components can lead to an additive contribution (coherence) of all nucleons in the target nucleus [61, 63, 88, 89, 97–99, 137].

Our main purpose is to explore the nuclear physics aspects of the neutrino-nucleus reactions of Eq.(5.2) focusing on the role of the NSI which have not been studied in detail up to now. We should stress that, our strategy in studying the nuclear aspects of FCNC in nuclei, is to carry out realistic cross sections calculations for the exotic processes (5.1) and (5.2), including NSI terms in the relevant effective Lagrangian. The required nuclear matrix elements are evaluated within the context of the QRPA, considering both coherent and incoherent processes by applying the advantageous state-by-state method developed in Refs. [55, 136, 148]. As a first step, we perform calculations for $g.s. \rightarrow g.s.$ transitions of the reactions (5.2) by solving the BCS equations, for even-even nuclear systems, and employing

the experimental nuclear charge densities [56] for odd- A nuclei. For comparison of our results with those of other methods [88, 99, 111, 118, 130], SM cross sections calculations are also carried out. More specifically, our present results refer to the even-even ^{48}Ti isotope, the stopping target of SINDRUM II and PRIME/PRISM $\mu^- \rightarrow e^-$ experiments. We perform similar calculations for processes (5.2) in the ^{27}Al nucleus proposed as detector material in Mu2e and COMET experiments. Finally, we will use the experimental upper limits of the cLFV processes to put robust bounds on model parameters of the relevant Lagrangians and the ratios of the NSI contributions with respect to the SM ones.

5.3 Neutrino non-standard interactions

With no doubt, up to now the SM of particle physics is by far the most accurate theory, predicting a vast number of observables at high precision level from only few fitted parameters. The Higgs boson, predicted by the SM as a direct result of the electroweak symmetry breaking in order to provide masses, constituted the only missing piece of the SM puzzle until 2012, when the celebrated announcement of its discovery by the ATLAS and CMS experiments [149, 150] at CERN, culminated the success of the SM. However, there is yet a notable number of observations as well as fundamental theoretical problems, for which sufficient explanation within the framework of the SM is still absent. The latter include the existence of dark matter, the exclusion of gravity, the observation of neutrino oscillations in propagation, the hierarchy problem, etc., indicating that the SM is to be viewed as a low-energy approximation of a more general theory.

The SM can be subsequently seen as an effective theory and thus higher-dimensional operators, suppressed by powers of a new mass scale Λ , should be naturally introduced into the SM Lagrangian. Therefore, for rather low energy scales, the additional effective operators are expected to generate only small corrections. This concept is further motivated since the only known gauge invariant operator allowed at dimension five (i.e. suppressed by one power of Λ), is the Weinberg operator [151], that yields a Majorana mass term for the case of left-handed neutrinos. For this reason, after the discovery of neutrino oscillations in propagation (that required neutrino mass-squared differences), it will not be surprising if further sub-leading effects of non-zero neutrino masses will be among the first signs of new physics beyond the SM.

Apart from the fact that the Weinberg operator is appropriate to provide the neutrino masses, tiny deviations from the expected neutrino conversion amplitudes during the phenomenon of neutrino oscillations might arise due to the presence of higher-order operators. Indeed, since neutrino physics is entering a precision era, such alterations will provide key insights into the field of high-energy neutrino physics and in particular will shed light on to determine the mechanism that is responsible for neutrino mass generation. It is, thus, of significant im-

portance to exploit the exceptional experimental sensitivity of neutrino-nucleus experiments and study the potential impact of higher-order operators, such as those involving NSI (for a recent review, see Ref. [24]).

In the present work, the assumed NSI operators are effective four-fermion operators of the form [23]

$$\mathcal{O} = (\bar{f}_1 \gamma^\mu P f_2) (\bar{f}_3 \gamma_\mu P f_4) + \text{h.c.}, \quad (5.3)$$

with f_i , $i = 1, 2, 3, 4$ being the SM fermion fields and $P = \{L, R\}$ denoting the left- and right-handed projectors. Since the latter operators are of dimension six, an effective coupling constant of dimension minus two will enter the effective interaction Lagrangian. Concentrating on the neutrino NSI, we stress that at least one of the fermion fields, f_i , is taken to be a neutrino field, implying that the respective projection operator is left-handed. Specifically, for neutrino-matter NSI, one has either charged-current interactions of the form [152]

$$\mathcal{O}_{\alpha\beta}^{f'P} = (\bar{\ell}_\alpha \gamma^\mu L \nu_\beta) (\bar{f} \gamma_\mu P f') + \text{h.c.}, \quad (5.4)$$

or neutral-current ones [153, 154]

$$\mathcal{O}_{\alpha\beta}^{fP} = (\bar{\nu}_\alpha \gamma^\mu L \nu_\beta) (\bar{f} \gamma_\mu P f) + \text{h.c.}, \quad (5.5)$$

with $\alpha, \beta = \{e, \mu, \tau\}$ being the neutrino flavour, ℓ denoting a charged lepton, f is a charged lepton or a first generation quark $q = \{u, d\}$ and f' its SU(2) partner.

In this Thesis we will focus on the latter process. As discussed in Ref. [20], we have taken a phenomenological approach, assuming that the new physics which induces these non-standard neutral-current operators does not generate the SU(2) related charged lepton operators at tree level¹. However, neutral-current operators of the form $(\bar{\nu}\nu)(\bar{f}f)$ nonetheless induce a $(\bar{\ell}\ell)(\bar{f}f)$ and/or $(\bar{\ell}\nu)(\bar{f}f)$ operator, via external one-loop SM dressing, and therefore, bounds on charged lepton operators set model independent bounds on the NSI operators [22]. Currently, such constraints are important only in the case of μ - e flavour changing operators (for example $\mu^- \rightarrow e^-$ conversion in nuclei), since the loop suppression is smaller. Furthermore, loop-NSI may yield flavour dependent corrections to the decay rates of the electroweak gauge bosons, and subsequently put relevant limits on flavour diagonal NSI.

5.4 Description of the formalism

The non-standard neutrino-nucleus processes (5.2) and the exotic cLFV $\mu^- \rightarrow e^-$ conversion in nuclei [110, 121, 122, 126, 133, 134], can be predicted within the aforementioned new-physics models [126]. In Fig. 5.1 we show the nuclear-level

¹This could be the case if the operators in Eq.(5.3) are of dimension eight or larger.

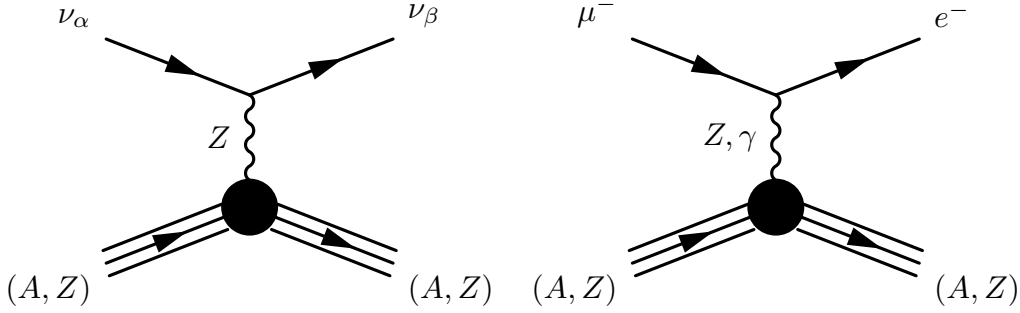


Figure 5.1: Nuclear level Feynman diagrams for: (*left*) non-standard Z -exchange neutrino-nucleus reactions and (*right*) Z -exchange and photon-exchange $\mu^- \rightarrow e^-$ in the presence of a nucleus (muon-to-electron conversion). The non-standard (cLFV or LFV) physics enters in the complicated vertex denoted by the blob \bullet .

Feynman diagrams representing the exchange of a Z -boson between a lepton and a nucleon for the cases of neutrino-nucleus scattering within the context of the non-standard interactions of neutrinos with nuclei (left panel) and the exchange of a Z -boson or a γ -photon in the $\mu^- \rightarrow e^-$ conversion (right panel). The leptonic vertex in both cases is a complicated one. A general effective Lagrangian that involves SM interactions (\mathcal{L}_{SM}) and NSI (\mathcal{L}_{NSI}) with a non-universal (NU) term and a flavour changing (FC) term can be written as

$$\mathcal{L}_{\text{tot}} = \mathcal{L}_{\text{SM}} + \mathcal{L}_{\text{NSI}} = \mathcal{L}_{\text{SM}} + \mathcal{L}_{\text{NU}} + \mathcal{L}_{\text{FC}}. \quad (5.6)$$

The individual components \mathcal{L}_{SM} and \mathcal{L}_{NSI} of this Lagrangian are explained in the next Subsections.

For a concrete example, it has been proposed [67, 68] that, even small deviation from unitary lepton mixing matrix, may cause sizeable NSI effects and potentially large LFV [127]. The non-trivial structure of electroweak currents in low-scale seesaw Lagrangians leads to non-unitary lepton mixing matrix $N_{\alpha\beta}$, which can be parametrised as $N \equiv (1 - n)U$. $U_{\alpha\beta}$ is a unitary matrix and $n_{\alpha\beta}$ a model depended non-standard matrix ($\alpha, \beta = e, \mu, \tau$) which takes specific form within seesaw mechanisms [127].

5.4.1 Non-standard neutrino-nucleus reaction cross sections

The neutral-current non-standard neutrino interactions addressed here, are described by a quark-level Lagrangian, \mathcal{L}_{NSI} , parametrised (for energies $\ll M_Z$)

as [21, 70, 111]

$$\mathcal{L}_{\text{NSI}} = -2\sqrt{2}G_F \sum_{\substack{P=L,R \\ f=u,d \\ \alpha,\beta=e,\mu,\tau}} \epsilon_{\alpha\beta}^{fP} [\bar{\nu}_\alpha \gamma_\rho L \nu_\beta] [\bar{f} \gamma^\rho P f], \quad (5.7)$$

where three light neutrinos ν_α with Majorana masses are considered, f denotes a first generation SM quark and $P = \{L, R\}$ are the chiral projectors. The Lagrangian (5.7) contains flavour preserving non-SM terms, known as non-universal (NU) interactions that are proportional to $\epsilon_{\alpha\alpha}^{fP}$, as well as flavour-changing (FC) terms proportional to $\epsilon_{\alpha\beta}^{fP}$, $\alpha \neq \beta$. These couplings are taken with respect to the strength of the Fermi coupling constant G_F . For the polar-vector couplings we are mainly interested in the present work, it holds

$$\epsilon_{\alpha\beta}^{fV} = \epsilon_{\alpha\beta}^{fL} + \epsilon_{\alpha\beta}^{fR}, \quad (5.8)$$

while for the axial-vector couplings

$$\epsilon_{\alpha\beta}^{fA} = \epsilon_{\alpha\beta}^{fL} - \epsilon_{\alpha\beta}^{fR}. \quad (5.9)$$

The nuclear physics aspects of the non-standard neutrino-matter reactions can be studied by transforming the Lagrangian (5.7) to the nuclear level where the hadronic current is written in terms of NC nucleon form factors (functions of the four momentum transfer) [133, 134]. In the general case of the inelastic scattering of neutrinos on nuclei, the magnitude of the three momentum transfer, $\kappa = |\mathbf{q}|$, obtained from the kinematics of the reaction, is a function of the scattering angle of the outgoing neutrino θ (laboratory frame), the initial, ε_i , and final, ε_f , neutrino energies, as well as the excitation energy of the target nucleus ω as, $\kappa^2 = \omega^2 + 2\varepsilon_i\varepsilon_f(1 - \cos\theta)$ [136, 137]. In the special case of the coherent (elastic) channel we focus in this Chapter ($\omega = 0$ and $\varepsilon_i = \varepsilon_f \equiv E_\nu$), only $g.s. \rightarrow g.s.$ transitions occur (for spin-zero nuclei) and we have $Q^2 = 2E_\nu^2(1 - \cos\theta)$ or $Q = 2E_\nu \sin(\theta/2)$.

The coherent differential cross section with respect to the scattering angle θ for NSI neutrino-nucleus processes is written as

$$\frac{d\sigma_{\text{NSI},\nu_\alpha}}{d\cos\theta} = \frac{G_F^2}{2\pi} E_\nu^2 (1 + \cos\theta) |\langle g.s. || G_{V,\nu_\alpha}^{\text{NSI}}(Q) || g.s. \rangle|^2, \quad (5.10)$$

($\alpha = e, \mu, \tau$, denotes the flavour of incident neutrinos) where $|g.s.\rangle$ represents the nuclear ground state (for even-even nuclei, like the ^{48}Ti , $|g.s.\rangle = |J^\pi\rangle \equiv |0^+\rangle$). The nuclear matrix element, that arises from the Lagrangian (5.7), takes the form

$$\begin{aligned} |\mathcal{M}_{V,\nu_\alpha}^{\text{NSI}}|^2 &\equiv |\langle g.s. || G_{V,\nu_\alpha}^{\text{NSI}}(Q) || g.s. \rangle|^2 = \\ &[(2\epsilon_{\alpha\alpha}^{uV} + \epsilon_{\alpha\alpha}^{dV}) ZF_Z(Q^2) + (\epsilon_{\alpha\alpha}^{uV} + 2\epsilon_{\alpha\alpha}^{dV}) NF_N(Q^2)]^2 \\ &+ \sum_{\beta \neq \alpha} [(2\epsilon_{\alpha\beta}^{uV} + \epsilon_{\alpha\beta}^{dV}) ZF_Z(Q^2) + (\epsilon_{\alpha\beta}^{uV} + 2\epsilon_{\alpha\beta}^{dV}) NF_N(Q^2)]^2, \end{aligned} \quad (5.11)$$

($\beta = e, \mu, \tau$) where $F_{Z(N)}$ denote the nuclear (electromagnetic) form factors for protons (neutrons) entered due to the CVC theory. We note that in the adopted NSI model, the coherent NC neutrino-nucleus reaction is not a flavour blind process. By considering the nuclear structure details, the cross sections provided by Eq.(5.10), become more realistic and accurate [70] (in Ref. [111] the variation versus the momentum transfer of the nuclear form factor is neglected, which for Supernova neutrino studies is a rather crude approximation). The structure of the Lagrangian (5.6), implies that in the r.h.s. of Eq.(5.11) the first term is the NU matrix element, $\mathcal{M}_{V,\nu_\alpha}^{\text{NU}}$, and the summation is the FC matrix element, $\mathcal{M}_{V,\nu_\alpha}^{\text{FC}}$, hence we write

$$|\mathcal{M}_{V,\nu_\alpha}^{\text{NSI}}|^2 = |\mathcal{M}_{V,\nu_\alpha}^{\text{NU}}|^2 + |\mathcal{M}_{V,\nu_\alpha}^{\text{FC}}|^2. \quad (5.12)$$

From an experimental physics point of view, many neutrino detectors are more sensitive to the recoil energy of the nuclear target, T_N , than to the scattering angles, θ . Therefore, it is also important to compute the differential cross sections $d\sigma/dT_N$. For coherent scattering the nucleus recoils (intrinsically it remains unchanged) with energy which, in the approximation $T_N \ll E_\nu$ (low-energy limit), is maximised as, $T_N^{\text{max}} = 2E_\nu^2/(M + 2E_\nu)$, with M being the nuclear mass [89, 97, 98]. Then, to a good approximation, the square of the four momentum transfer, is equal to $Q^2 = 2MT_N$, and the coherent NSI differential cross section with respect to T_N is written as

$$\frac{d\sigma_{\text{NSI},\nu_\alpha}}{dT_N} = \frac{G_F^2 M}{\pi} \left(1 - \frac{MT_N}{2E_\nu^2}\right) |\langle g.s. || G_{V,\nu_\alpha}^{\text{NSI}}(Q) || g.s. \rangle|^2. \quad (5.13)$$

Both Eqs. (5.10) and (5.13) are useful for studying the nuclear physics of NSI of neutrinos with matter.

The Lagrangian \mathcal{L}_{tot} of Eq.(5.6), contains the flavour preserving (FP) part, equal to

$$\mathcal{L}_{\text{FP}} \equiv \mathcal{L}_{\text{NU}} + \mathcal{L}_{\text{SM}}, \quad (5.14)$$

which can be evaluated through the Coulomb matrix element

$$|\mathcal{M}_{V,\nu_\alpha}^{\text{FP}}|^2 = |\mathcal{M}_{V,\nu_\alpha}^{\text{SM}} + \mathcal{M}_{V,\nu_\alpha}^{\text{NU}}|^2. \quad (5.15)$$

Subsequently, the total coherent cross section may be computed on the basis of the matrix element

$$|\mathcal{M}_{V,\nu_\alpha}^{\text{tot}}|^2 = |\mathcal{M}_V^{\text{FP}}|^2 + |\mathcal{M}_{V,\nu_\alpha}^{\text{FC}}|^2. \quad (5.16)$$

Furthermore, by performing numerical integrations in Eq.(5.10) over the scattering angle θ or in Eq.(5.13) over the recoil energy T_N , one can obtain integrated (total) coherent NSI cross sections, $\sigma_{\text{NSI},\nu_\alpha}$. The individual cross sections $\sigma_{\text{NU},\nu_\alpha}$ and $\sigma_{\text{FC},\nu_\alpha}$ may be evaluated accordingly.

5.5 Results and discussion

At first, we studied the nuclear structure details of the matrix elements entering Eqs.(5.10)–(5.13) that reflect the dependence of the coherent cross section on the incident neutrino-energy E_ν and the scattering angle θ (or the recoil energy T_N). For the even-even ^{48}Ti nucleus, the stopping target of the PSI [141, 142] and PRIME [144, 145] experiments, this study involves realistic nuclear structure calculations for the cross sections $d\sigma_{\lambda,\nu_\alpha}/d\cos\theta$ and $d\sigma_{\lambda,\nu_\alpha}/dT_N$, performed after constructing the nuclear ground state $|g.s.\rangle$ by solving iteratively the BCS equations. The nuclear BCS form factors for protons (neutrons) are obtained through Eq.(3.127). The chosen active model space consists of the lowest 15 single-particle j -orbits, $j \equiv (n, l, 1/2)j$ without core, up to major Harmonic Oscillator quanta $N = 4\hbar\omega$. The required monopole (pairing) residual interaction, obtained from a Bonn C-D two-body potential was slightly renormalised with the two parameters $g_{\text{pair}}^{p,n}$ ($g_{\text{pair}}^p = 1.056$, for proton pairs, and $g_{\text{pair}}^n = 0.999$, for neutron pairs).

We note that, we have devoted a special effort on the accurate construction of the nuclear ground state, (i) because the coherent channel is the dominant one for the neutral-current SM neutrino-nucleus processes and we assumed that this holds also for NSI processes, and (ii) because in a next step we are intended to perform extensive incoherent cross sections calculations where all accessible final nuclear states will be built on the present ground state.

For the odd- A ^{27}Al nucleus (its ground state spin is $|g.s.\rangle = |J^\pi\rangle = |(5/2)^+\rangle$), the stopping target of Mu2e and COMET experiments, we obtained the form factor $F_Z(Q^2)$, through a model independent analysis (using the Fourier-Bessel expansion model defined in the Appendix F.1) of the electron scattering data for the charge density distribution of this isotope [56]. Since similar data for $F_N(Q^2)$ ^{27}Al are not available, we considered (to a rather satisfactory approximation) that $F_N \simeq F_Z$ (a difference up to about 10% usually appears for medium and heavy nuclear systems [56]). The momentum dependence of the nuclear form factors was ignored by some authors [111] which at low neutrino-energies relevant for solar neutrinos is practically a good approximation, but for energies relevant to Supernova neutrinos addressed in this work, it may lead to differences of even an order of magnitude.

5.5.1 Integrated coherent neutrino-nucleus NSI cross sections

As in the SM case (see Chapt. 4), for the case of NSI we obtained angle-integrated coherent neutrino-nucleus cross sections by integrating numerically Eq.(5.10) over angles [or Eq.(5.13) over T_N] for the various interaction components as

$$\sigma_{\lambda,\nu_\alpha}(E_\nu) = \int \frac{d\sigma_{\lambda,\nu_\alpha}}{d\cos\theta}(\theta, E_\nu) d\cos\theta, \quad (5.17)$$

ν_α	(A, Z)	R_{tot}	R_{NU}	R_{FP}	$R_{\nu_\alpha \leftrightarrow \nu_e}$	$R_{\nu_\alpha \leftrightarrow \nu_\mu}$	$R_{\nu_\alpha \leftrightarrow \nu_\tau}$
ν_e	^{48}Ti	1.037	0.002	0.905	-	0.121×10^{-4}	0.130
	^{27}Al	1.044	0.003	0.902	-	0.130×10^{-4}	0.139
ν_μ	^{48}Ti	1.293	0.001	0.929	0.121×10^{-4}	-	0.361
	^{27}Al	1.318	0.001	0.927	0.130×10^{-4}	-	0.387

Table 5.1: The ratios R_{λ, ν_α} (for the definition see Eq.(5.18) in the text) of all possible $\nu_\alpha + (A, Z) \rightarrow \nu_\beta + (A, Z)$ processes. They have been evaluated in their asymptotic values reached at $E_\nu \approx 120$ MeV.

($\lambda = \text{tot}, \text{SM}, \text{NU}, \text{FP}, \text{FC}$). The results for the individual cross sections, $\sigma_{\text{tot}}, \sigma_{\text{SM}}, \sigma_{\text{NU}}, \sigma_{\text{FP}}, \sigma_{\text{FC}}$ (incoming neutrino energies in the range $0 \leq E_\nu \leq 150$ MeV) are illustrated in Fig. 5.2. We found that the exotic FCNC processes $\nu_\alpha \rightarrow \nu_\beta$ in ^{48}Ti have significantly lower cross section compared to the SM one. From the obtained FCNC neutrino-nucleus cross sections the most challenging result corresponds to the $\nu_\mu \rightarrow \nu_e$ transition (and to its lepton conjugate process, $\nu_e \rightarrow \nu_\mu$). This is mainly due to the severe constraint $\epsilon_{\mu e}^{fP} = 2.9 \times 10^{-4}$ inserted in the Lagrangian (5.7) which has been derived from the nuclear $\mu^- \rightarrow e^-$ conversion experimental limits on cLFV branching ratio [106–109]. We remind that, in this work we have employed the NSI parameters $\epsilon_{\alpha\beta}^{fV}$ (except the $\epsilon_{\mu e}^{fV}$) derived from various experimental bounds in Ref. [22].

By exploiting our cross sections $\sigma_{\lambda, \nu_\alpha}(E_\nu)$, we find it interesting to estimate the ratio of each of the individual cross sections, $\sigma_{\lambda, \nu_\alpha}$, with respect to the SM cross sections defined as

$$R_{\lambda, \nu_\alpha}(E_\nu) = \frac{\sigma_{\lambda, \nu_\alpha}(E_\nu)}{\sigma_{\text{SM}}(E_\nu)}, \quad \lambda = \text{tot}, \text{NU}, \text{FP}, \text{FC}. \quad (5.18)$$

For ^{48}Ti , the latter ratios initially are slowly increasing functions of E_ν , but eventually (for energies higher than about 80–120 MeV) they tend asymptotically to the values listed in Table 5.1. For ^{27}Al , however, the ratios R_{λ, ν_α} are energy independent which is a consequence of the different treatment applied in studying the nuclear structure details than that followed for ^{48}Ti . From the comparison of the results of Table 5.2 with those of the method [111], we conclude that our realistic calculations are important in the case of ^{48}Ti nucleus, where the BCS method gave us $F_N \neq F_Z$ and, hence, the results obtained for R_{λ, ν_α} differ from those given by Ref. [111]. For ^{27}Al , however, for which we considered $F_N \simeq F_Z$, the dependence on the nuclear structure parameters in the numerator and denominator of Eq.(5.18) cancel out and, then, our predictions for R_{λ, ν_α} are equal to those of Ref. [111].

It is worth noting that, some constraints coming from solar [113] and atmospheric [114] neutrino data indicate that the NSI might be large, while according

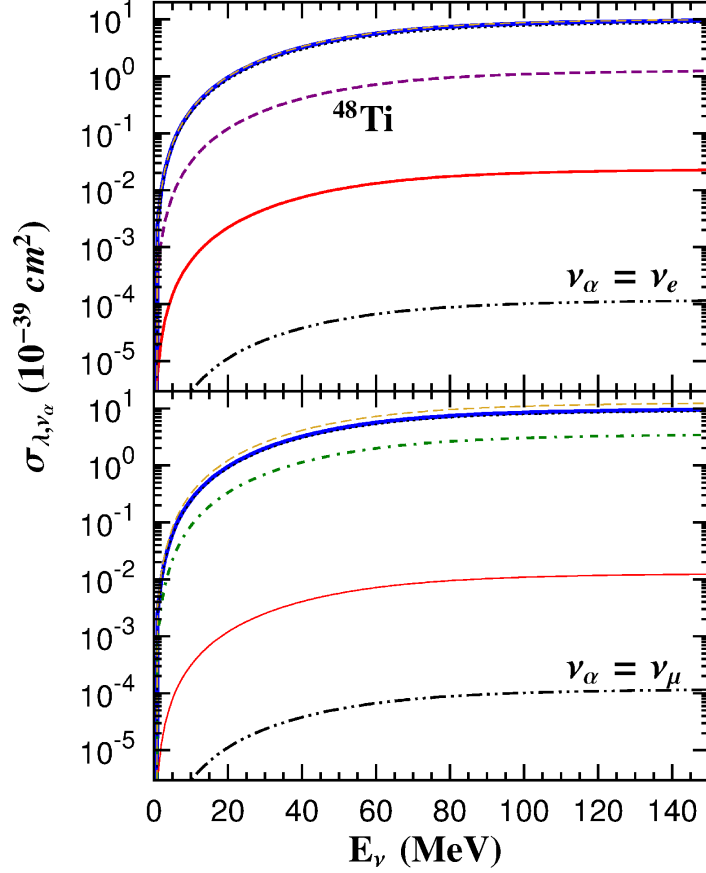


Figure 5.2: Integrated coherent cross sections $\sigma_{\lambda, \nu_\alpha}(E_\nu)$ versus the incoming neutrino-energy E_ν , for neutrino processes of the form $\nu_\alpha + {}^{48}\text{Ti} \rightarrow \nu_\beta + {}^{48}\text{Ti}$, with $\alpha \neq \beta$. As expected, the NSI channels (labelled as NU, FP, $\nu_e \leftrightarrow \nu_\mu$, $\nu_e \leftrightarrow \nu_\tau$, $\nu_\mu \leftrightarrow \nu_\tau$) have significantly smaller contributions compared to that of the SM one (continuous bold line). The line labelling is same to that of Fig. 5.3.

to the present experimental data, $\epsilon_{\tau\tau}^{fV}$ is unacceptably large and, consequently, it derives unrealistic results (the corresponding FP and NU cross sections, not included here, are larger than the SM ones) [22, 70].

5.5.2 NSI of Supernova neutrinos

One of the most interesting connections of our present calculations with ongoing and future neutrino experiments is related to Supernova neutrino detection. As it is known, in SN explosions most of the energy is released by neutrino emission. We assume that the emitted SN-neutrino-energy spectra, $\eta_{\nu_\alpha}^{\text{SN}}(E_\nu)$, resemble Maxwell-Boltzmann distributions that depend on the temperature, T_{ν_α} , of the (anti)neutrino flavour ν_α ($\bar{\nu}_\alpha$). By convoluting the integrated NSI cross

ν_α	(A, Z)	$\langle\sigma_{\text{tot}}\rangle$	$\langle\sigma_{\text{SM}}\rangle$	$\langle\sigma_{\text{NU}}\rangle$	$\langle\sigma_{\text{FP}}\rangle$	$\langle\sigma_{\nu_\alpha\rightarrow\nu_e}\rangle$	$\langle\sigma_{\nu_\alpha\rightarrow\nu_\mu}\rangle$	$\langle\sigma_{\nu_\alpha\rightarrow\nu_\tau}\rangle$
ν_e	^{48}Ti	5.32	5.15	1.20×10^{-2}	4.66	-	6.07×10^{-5}	6.50×10^{-1}
	^{27}Al	1.57	1.50	3.83×10^{-3}	1.35	-	1.95×10^{-5}	2.09×10^{-1}
ν_μ	^{48}Ti	19.6	15.2	1.93×10^{-2}	14.2	1.80×10^{-4}	-	5.36
	^{27}Al	6.07	4.61	6.42×10^{-3}	4.27	6.00×10^{-5}	-	1.78

Table 5.2: Flux averaged cross sections $\langle\sigma_{\lambda,\nu_\alpha}\rangle$ (in 10^{-40} cm^2) for various Supernova neutrino spectra parametrised by Maxwell-Boltzmann distributions.

section, $\sigma_{\lambda,\nu_\alpha}(E_\nu)$, with the neutrino distributions, the NSI signal produced on a terrestrial detector may be simulated as

$$\sigma_{\lambda,\nu_\alpha}^{\text{sign}}(E_\nu) = \sigma_{\lambda,\nu_\alpha}(E_\nu) \eta_{\nu_\alpha}^{\text{SN}}(E_\nu). \quad (5.19)$$

We note, the obvious difference between the above equation and Eq.(4.77) in Chapt. 4.

The resulting NSI signals, $\sigma_{\lambda,\nu_\alpha}^{\text{sign}}(E_\nu)$, obtained by inserting in Eq.(5.19) the cross sections $\sigma_{\lambda,\nu_\alpha}$, are plotted in Fig. 5.3. Note that, in contrast to the original cross sections, now $\sigma_{\nu_\alpha\rightarrow\nu_\beta}^{\text{sign}} \neq \sigma_{\nu_\beta\rightarrow\nu_\alpha}^{\text{sign}}$. Figure 5.3 shows that for incoming ν_μ neutrinos the signal $\sigma_{\lambda,\nu_\mu}^{\text{sign}}$ presents an appreciably wider energy range compared to that of ν_e and that the maximum peak is shifted towards higher energies following the features of the distributions $\eta_{\nu_\alpha}^{\text{SN}}(E_\nu)$. The simulated cross sections of Fig. 5.3 reflect the characteristics of the incident neutrino spectrum of a specific flavour α having its own position of the maximum peak and width of the distribution $\eta_{\nu_\alpha}^{\text{SN}}$. We remind that, as usually, for incoming ν_e neutrinos, the distribution $(\eta_{\nu_e}^{\text{SN}} + \eta_{\bar{\nu}_e}^{\text{SN}})/2$ is used.

In SN neutrino simulations, another useful quantity is the flux averaged cross section [66] which in our notation is written as

$$\langle\sigma_{\lambda,\nu_\alpha}\rangle = \int \sigma_{\lambda,\nu_\alpha}(E_\nu) \eta_{\nu_\alpha}^{\text{SN}}(E_\nu) dE_\nu. \quad (5.20)$$

The results for $\langle\sigma_{\lambda,\nu_\alpha}\rangle$, obtained by using our angle-integrated cross sections are listed in Table 5.2. We note that our flux averaged cross sections differ by about 30% from those of [111].

From experimental physics perspectives, it is also interesting to make predictions for the differential event rate of a neutrino detector [88, 99, 148]. The usual expression for computing the yield in events is based on the neutrino flux, Φ_{ν_α} . To include the NSI of neutrinos with nuclei, the yield in events, $Y_{\lambda,\nu_\alpha}(T_N)$, is [88, 99]

$$Y_{\lambda,\nu_\alpha}(T_N) = N_t \int \Phi_{\nu_\alpha} dE_\nu \int \frac{d\sigma_{\lambda,\nu_\alpha}}{d\cos\theta} \delta\left(T_N - \frac{Q^2}{2M}\right) d\cos\theta, \quad (5.21)$$

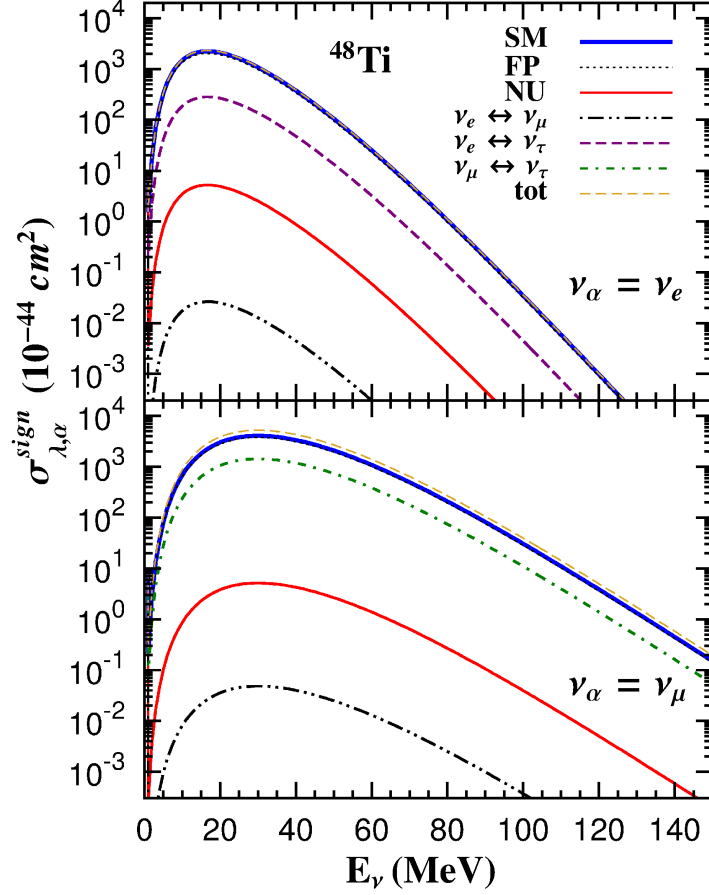


Figure 5.3: The convoluted cross sections, evaluated with Maxwell-Boltzmann distributions, that represent the expected signal to be recorded on a ^{48}Ti neutrino detector, $\sigma_{\lambda,\nu_\alpha}^{\text{sign}}(E_\nu)$. Due to the flavour dependence of the SN neutrino distribution, the energy-window of ν_e neutrinos signal is more narrow compared to those of ν_μ and ν_τ neutrinos.

where N_t is the total number of nuclei in the detector material. Within this formalism, apparently Eq.(4.79) is recovered for the channel $\lambda = \text{SM}$ in Eq.(5.21). Assuming a detector filled with one ton ^{48}Ti , we evaluated differential event rates $Y_{\lambda,\nu_\alpha}(T_N)$ for several Supernova scenarios. These results, are plotted in Fig. 5.4 where for each particular interaction, the corresponding neutrino flux has been considered. We see that, the respective results for the NU and FC processes, especially the case of $\nu_\mu \rightarrow \nu_e$ transition, present appreciably small contributions and that, the lower the energy recoil, the larger the potentially detected number of events. Hence, for the observation of non-standard neutrino-nucleus events, detector medium with very low energy-recoil threshold is required.

With the above results for $Y_{\lambda,\nu_\alpha}(T_N)$, one can obtain the total number of

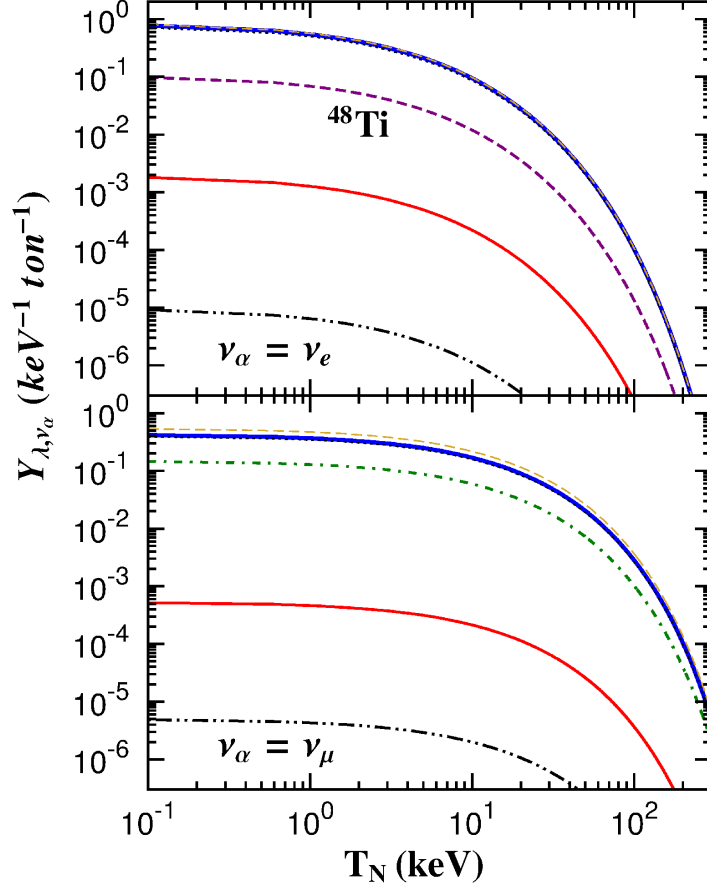


Figure 5.4: Differential event rate, $Y_{\lambda, \nu_\alpha}(T_N)$, as a function of the nuclear recoil energy, T_N , for a ^{48}Ti neutrino detector. The line labelling is same to that of Fig. 5.2.

counts by integrating Eq.(5.21) above the energy threshold, T_N^{thres} , of the detector in question. For the ^{48}Ti nucleus, assuming $T_N^{\text{thres}} \approx 1$ keV, we find about 13.5 events/ton for the SM process but only 10^{-3} events/ton for the flavour changing $\nu_\mu \leftrightarrow \nu_e$ reaction, i.e. about four orders of magnitude less events. We also conclude that, for making accurate predictions of the total number of counts, the nuclear structure parameters play significant role. Thus, for the $\nu_\mu \rightarrow \nu_e$ transition we end up with about 29% less events, compared to those given by the approximation of Ref. [111]. On the other hand, adding up the total number of events for the three SM processes of the form, $\nu_\alpha \rightarrow \nu_\alpha$, we end up with only 2% less events than those provided from the formalism of Refs. [88, 99].

It is worth noting that, the choice of the target nucleus plays also a key role, since a light nuclear target may yield high energy recoil tails but less counts. On the contrary, a heavy nuclear target provides more counts and yields low-energy

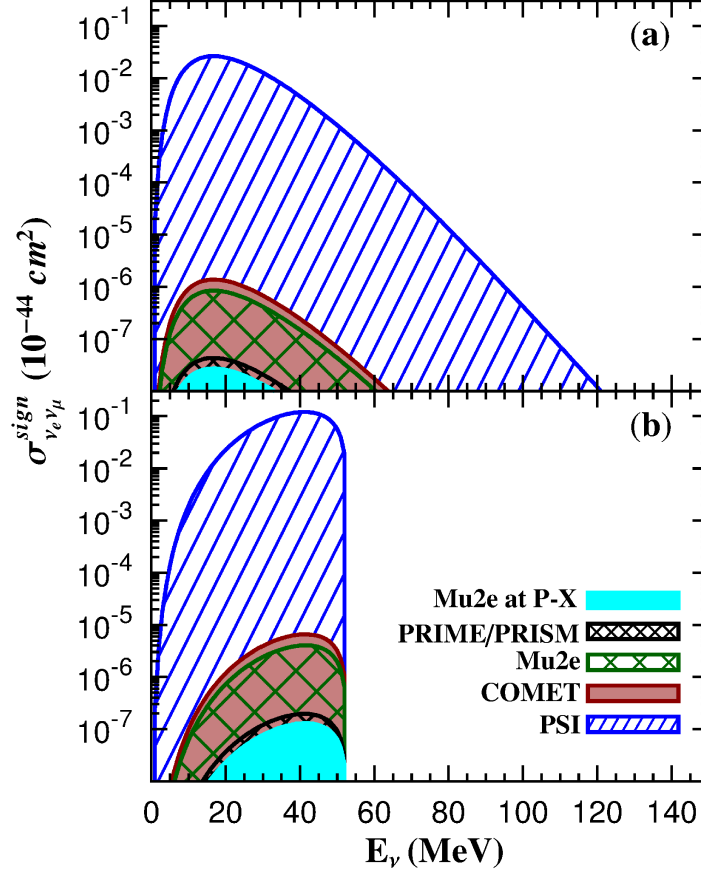


Figure 5.5: Simulated neutrino signal, $\sigma_{\nu_e \nu_\mu}^{sign}$, of the FCNC process $\nu_e + (A, Z) \rightarrow \nu_\mu + (A, Z)$ in ^{48}Ti , for the PSI and PRIME/PRISM experiments and in ^{27}Al , for the COMET, Mu2e and Mu2e at Project-X: (a) for Supernova neutrinos and (b) for pion-muon stopped neutrinos. The shaded area represents the excluded region of observation by the increased sensitivity of the designed experiments. For each plot the relevant NSI parameter $\epsilon_{\mu e}^{fP}$ of Table 5.3 has been employed.

recoils making the detection more difficult. This leads to the conclusion that the best choice for a nuclear detector must consist of a combination of light and heavy nuclear isotopes.

5.5.3 New stringent limits on $\epsilon_{\mu e}^{fV}$ from $\mu^- \rightarrow e^-$ conversion

In the last part of this analysis, we exploit our channel-by-channel cross sections calculations in order to provide new limits for the NSI parameters $\epsilon_{\mu e}^{fP}$, coming out of the present and future experimental constraints of cLFV $\mu^- \rightarrow e^-$ conversion as follows. The authors of Ref. [22] (assuming that cLFV arises from loop diagrams involving virtual W's) found that the couplings of charged leptons

Parameter	COMET	Mu2e	Project-X	PRIME
$\epsilon_{\mu e}^{fV} \times 10^{-6}$	3.70	2.87	0.52	0.37
$R_{\nu_\mu \leftrightarrow \nu_e} \times 10^{-10}$	21.2	13.0	0.42	0.19

Table 5.3: Upper limits on the NSI parameters $\epsilon_{\mu e}^{fV}$ and the ratios $R_{\nu_\mu \leftrightarrow \nu_e}$ for the FC $\nu_\mu \leftrightarrow \nu_e$ reaction channel resulting from the sensitivity of the $\mu^- \rightarrow e^-$ conversion experiments.

with quarks are given by $C\epsilon_{\alpha\beta}^{fP}$, where $C \approx 0.0027$. Consequently, for the $\nu_\mu \leftrightarrow \nu_e$ transition the NSI parameters are related with the experimental upper limits of $\mu^- \rightarrow e^-$ conversion as [22]

$$\epsilon_{\mu e}^{fP} = C^{-1} \sqrt{R_{\mu e}^{(A,Z)}}. \quad (5.22)$$

In our calculations, up to this point we used the value $\epsilon_{\mu e}^{fV} = 2.9 \times 10^{-4}$ resulting from the PSI upper limit, $R_{\mu e}^{Ti} < 6.1 \times 10^{-13}$ [141] (occasionally, this value is a more severe constraint compared to the value $\epsilon_{\mu e}^{fV} = 7.7 \times 10^{-4}$ used in [22] which came out of the upper limit $R_{\mu e}^{Ti} < 4.3 \times 10^{-12}$ [142]).

Significantly lower upper limits on the NSI $\epsilon_{\mu e}^{fP}$ parameters of Eq.(5.18), are expected to be derived from the COMET, Mu2e, Mu2e at Project-X and PRIME/PRISM $\mu^- \rightarrow e^-$ conversion experiments. Then, one may compute new ratios $R_{\nu_\mu \leftrightarrow \nu_e}$ of the FC $\nu_e \leftrightarrow \nu_\mu$ reaction channel. The results for the NSI parameters $\epsilon_{\mu e}^{fV}$ and the respective ratios $R_{\nu_\mu \leftrightarrow \nu_e}$ are listed in Table 5.3.

Before closing we find interesting to plot the expected neutrino signals $\sigma_{\nu_\mu \rightarrow \nu_e}^{sign}(E_\nu)$ resulting by using the limits of Table 5.3 in two cases of neutrino spectra: (i) Supernova neutrinos, and (ii) laboratory neutrinos originating e.g from the BNB (Booster Neutrino Beamline) at Fermilab known as pion decay-at-rest (DAR) neutrinos [71, 72]. In the first case the simulated cross sections are obtained by employing the Supernova neutrino spectra, $\eta_{\nu_\alpha}^{SN}$, discussed before [88, 99] and the results are illustrated in Fig. 5.5(a). In the second case, the simulated cross sections are obtained by considering the laboratory neutrino distribution of the stopped pion-muon neutrinos produced according to the reactions $\pi^+ \rightarrow \mu^+ + \nu_\mu$, $\mu^+ \rightarrow e^+ + \nu_e + \bar{\nu}_\mu$ [71, 72]. In these experiments the emitted ν_e neutrino spectrum is described by the normalised distribution $\eta_{\nu_\alpha}^{lab.}$, $\alpha = e, \mu$ [66, 148]. The simulated laboratory neutrino signal, $\sigma_{\nu_e \rightarrow \nu_\mu}^{sign}$, is shown in Fig. 5.5(b).

As can be seen, in both cases the exceedingly high sensitivity of the designed experiments reduces drastically (compare Figs. 5.3 and 5.5) the area of observation of the neutrino signals $\sigma_{\nu_e \rightarrow \nu_\mu}^{sign}(E_\nu)$.

We should note that for models based on non-unitary lepton mixing matrix (including seesaw), constraints on $n_{\alpha\beta}$ (related to $\epsilon_{\alpha\beta}^{fP}$ within normalisation factors [127]) may similarly come out. Obviously, for NSI considering both d and

u quarks, $n_{\alpha\beta}$ enter the nuclear matrix elements of Eq.(5.11).

5.5.4 NSI of neutrinos from spallation neutron sources

The multi-target approach of the COHERENT experiment [73–75] aiming on neutrino detection can also explore non-standard physics issues such as NSI [25, 111], neutrino magnetic moment [115] and sterile neutrino [116]. In this Subsection we find it interesting to evaluate the non-standard neutrino-nucleus events that could be potentially detected by this experiment in each of the proposed nuclear targets. The high intensity SNS neutrino beams [69] and the two promising neutrino detectors, liquid ^{20}Ne (391 kg) and liquid ^{40}Ar (456 kg) [116], firstly proposed by the CLEAR [76] and CLEAN [94] designs (located at distance 20 m from the source), constitute excellent probes to search for the exotic neutrino reactions. Other possibilities [73–75] include medium and heavy weight targets like ^{76}Ge (100 kg) inspired by the dark matter SuperCDMS [92] detector (located at 20 m) and ^{132}Xe (100 kg located at 40 m).

In Fig. 5.6 and Fig. 5.7 the resulting number of exotic events are illustrated and compared with the SM predictions. We note, however, that especially for the case of the flavour changing (FC) channel $\nu_\mu \rightarrow \nu_e$, by using the extremely high sensitivity of the ongoing $\mu^- \rightarrow e^-$ conversion experiments (COMET [106, 107] and Mu2e [140]), very robust bounds have been set on the vector parameters $\epsilon_{\mu e}^{fV}$ [25]. To this end, we conclude that, if the Mu2e and COMET experiments will not detect muon to electron conversion events, then the new $\epsilon_{\mu e}^{fV}$ parameters extracted in [25] will lead to undetectable coherent rates at the SNS facility for this channel.

For our present calculations we use the current bounds [25] set by the sensitivity of the PSI experiment [141] and found countable number of events for the near detectors in the case of the corresponding $\nu_\mu \rightarrow \nu_e$ reaction. The other exotic parameters, i.e. $\epsilon_{\alpha\alpha}^{fV}$ with $\alpha = e, \mu$ and $\epsilon_{e\tau}^{fV}$ have been taken from Ref. [22]. As discussed in Ref. [25], we do not take into account the $\epsilon_{\tau\tau}^{fV}$ contribution, since the corresponding limits are poorly constrained and eventually predict unacceptably high rates.

Before closing, it is worth noting that, the present calculations indicate significant possibility of detecting exotic neutrino-nucleus events through coherent scattering in the aforementioned experiments. Since neutrino-physics enters a precision era [70], a difference from the Standard Model predictions leads to an undoubtable evidence of non-standard neutrino-nucleus interactions (NSI). We recall that, in order to experimentally constrain simultaneously all the exotic parameters at high precision, the detector material should consist of maximally different ratio $k = (A + N)/(A + Z)$ [70, 111].

Our Future plans include estimation of the incoherent channel which may provide a significant part of the total cross section, especially for energies higher than $E_\nu \approx 20 - 40$ MeV (depending on the nuclear target [135] and the particle

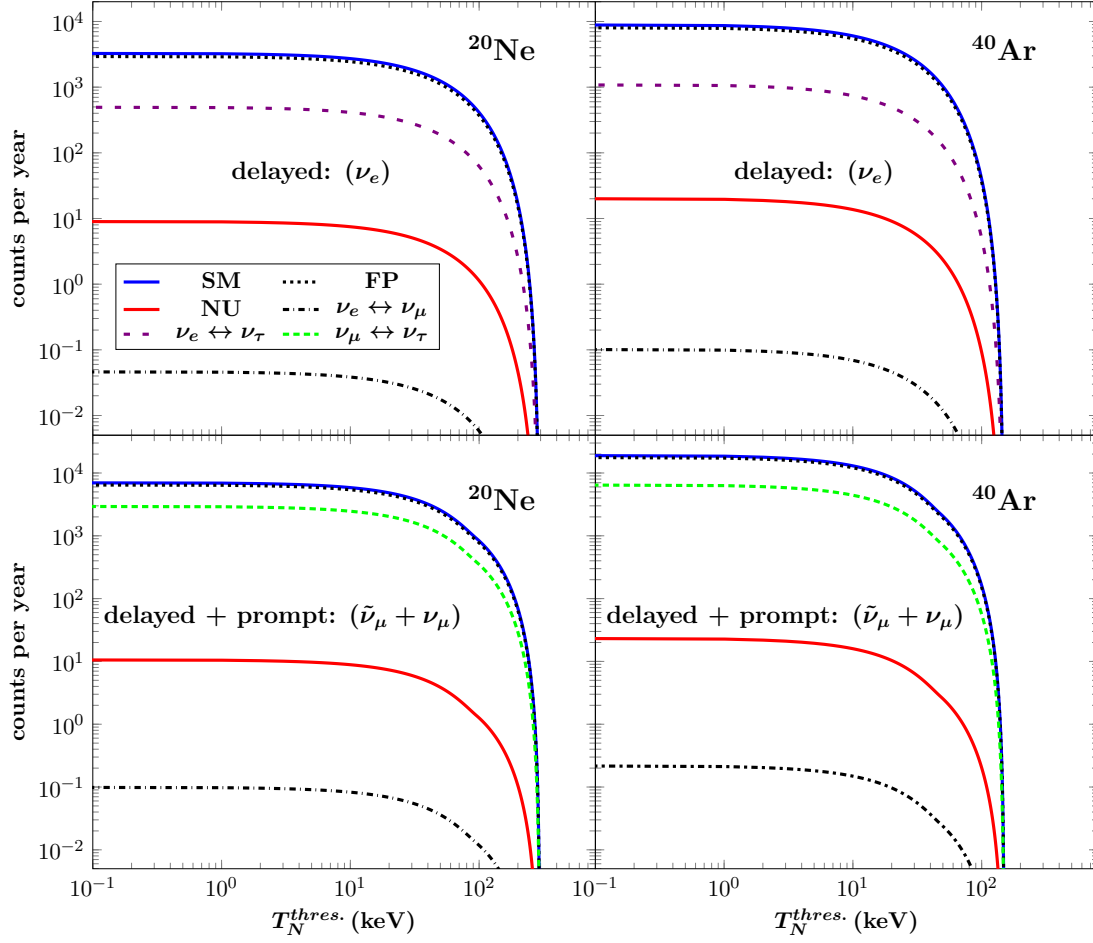


Figure 5.6: The expected non-standard neutrino scattering events over the recoil energy threshold at the COHERENT detector, filled with (*left*) 391 kg of liquid ^{20}Ne and (*right*) 456 kg of liquid ^{40}Ar , both located at a distance of 20 m ($\Phi_{\nu_\alpha} = 2.5 \times 10^7 \text{ } \nu \text{s}^{-1} \text{cm}^{-2}$) from the source. A perfectly efficient detector and negligible neutrino oscillation effects are assumed.

model predicting the exotic process).

5.6 NSI in SUSY theories

Within the context of Supersymmetry (SUSY) each particle has a partner with opposite spin statistics². The minimum number of fields to describe the known SM particles and their superpartners are described within the Minimal Supersymmetric Model (MSSM). R-parity stands out as an additional discrete

²For each boson there exist a corresponding fermion partner and vice versa.

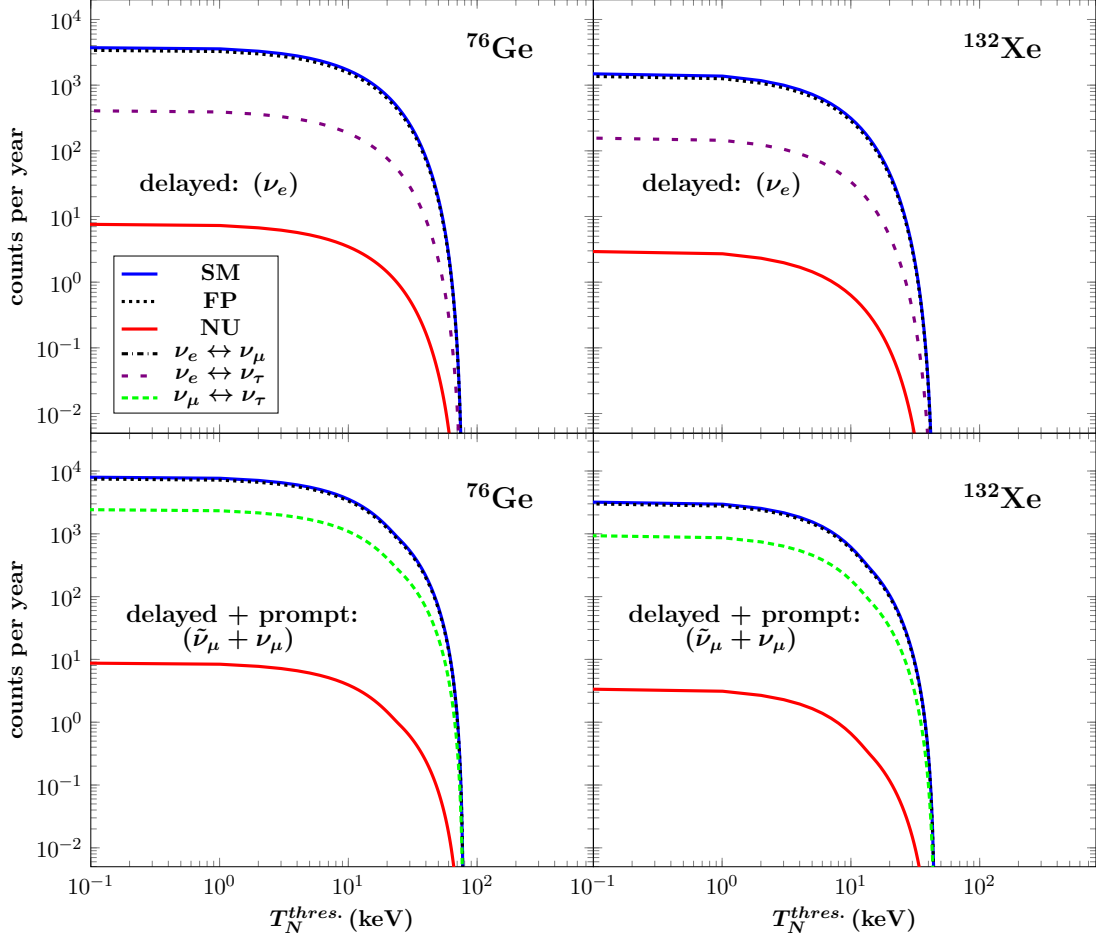


Figure 5.7: Same as Fig. 5.6, but for 100 kg of ^{76}Ge at 20 m ($\Phi_{\nu_\alpha} = 2.5 \times 10^7 \nu\text{s}^{-1}\text{cm}^{-2}$) and 100 kg of liquid ^{132}Xe at 40 m ($\Phi_{\nu_\alpha} = 6.3 \times 10^6 \nu\text{s}^{-1}\text{cm}^{-2}$) from the source.

symmetry whose main feature is it requires that an interaction must have an even number of SUSY particles. Specifically, R-parity violating interactions also violate lepton number, L , or baryon number, B .

Reference [118] explores possible NSI contributions that arise by considering lepton number violating terms in the superpotential, of the form

$$\lambda_{ijk} L_i L_j E_k^c, \quad \lambda'_{ijk} L_i Q_j D_k^c. \quad (5.23)$$

with, L_i and Q_i denoting lepton and quark $\text{SU}(2)$ doublet superfields, while E_i^c and D_i^c are lepton and quark singlet superfields. The couplings, λ_{ikj} , are anti-symmetric in i and j (family indices: $e, d = 1, \mu, s = 2$ and $\tau, b = 3$). These terms lead to the following interaction Lagrangians

$$\mathcal{L} = \lambda_{ijk} \left[\tilde{\nu}_L^i \bar{e}_R^k e_L^j + \tilde{e}_L^j \bar{e}_R^k \nu_L^i + (\tilde{e}_R^k)^* \bar{\nu}_L^i e_L^j - (i \leftrightarrow j) \right] + \text{h.c.}, \quad (5.24)$$

$$\begin{aligned} \mathcal{L} = \lambda'_{ijk} & \left[\tilde{\nu}_L^i \bar{d}_R^k d_L^j + \tilde{d}_L^j \bar{d}_R^k \nu_L^i + (\tilde{d}_R^k)^* \bar{\nu}_L^i d_L^j \right. \\ & \left. - \tilde{e}_L^i \bar{d}_R^k u_L^j - \tilde{u}_L^j \bar{d}_R^k e_L^i - (\tilde{d}_R^k)^* \bar{e}_L^i u_L^j \right] + \text{h.c.}, \end{aligned} \quad (5.25)$$

where the sparticles are denoted with the tilde.

For low energy scattering (negligible squark momentum in the propagator), concentrating on the relevant terms involving neutrino-quark interactions and after a Fierz transformation the R-breaking SUSY Lagrangian reads

$$\mathcal{L}_{\text{eff}} = [\bar{\nu}^j \gamma^\mu (1 - \gamma_5) \nu^i] \sum_{q=u,d} \left[\bar{q} \gamma^\mu (\kappa_{V_{ij}}^q + \kappa_{A_{ij}}^q \gamma_5) q \right], \quad (5.26)$$

where the exchange of a d squark is assumed. For the case of neutrino scattering off a d -quark, the relevant vector- and axial-vector couplings are written as [118]

$$\kappa_{V_{ij}}^d = \frac{1}{8} \sum_k \left[\frac{\lambda'_{ik1} (\lambda'_{j1k})^*}{m_{\tilde{d}_R^k}^2} - \frac{\lambda'_{ik1} (\lambda'_{jk1})^*}{m_{\tilde{d}_L^k}^2} \right], \quad (5.27)$$

$$\kappa_{A_{ij}}^d = \frac{1}{8} \sum_k \left[\frac{\lambda'_{ik1} (\lambda'_{j1k})^*}{m_{\tilde{d}_R^k}^2} + \frac{\lambda'_{ik1} (\lambda'_{jk1})^*}{m_{\tilde{d}_L^k}^2} \right]. \quad (5.28)$$

These couplings, are the SUSY analogous of those given in Eq.(5.8) and Eq.(5.9) respectively. Then, the corresponding cross section for the scattering channel, $(\bar{\nu}_i) \nu_i + (A, Z) \rightarrow (\bar{\nu}) \nu_j + (A, Z)$,

$$\frac{d\sigma_{ij}}{dQ^2} = \frac{1}{\pi} \left| (2\kappa_{V_{ij}}^u + \kappa_{V_{ij}}^d) Z + (\kappa_{V_{ij}}^u + 2\kappa_{V_{ij}}^d) N \right|^2 \left[1 - \left(\frac{Q}{2E_\nu} \right)^2 \right]. \quad (5.29)$$

5.7 Conclusions

In this Chapter, we explored NC non-standard neutrino-nucleus processes with realistic nuclear structure calculations. As a first step, we evaluated cross sections for the dominant coherent channel (incoming neutrino energies $0 \leq E_\nu \leq 150$ MeV, which include neutrinos coming from stopped pion-muon decay, Supernova, etc.). We have examined partial, integrated and total coherent cross sections and determined constraints for the ratios $R_{\nu_\alpha \rightarrow \nu_\beta}$ of all relevant reaction channels with respect to the SM cross section. Furthermore, we provided results for the differential event rates and the total number of events assuming the interesting detector materials employed at the COHERENT experiment. In view of operation of the muon-to-electron conversion experiments, searching for the exotic $\mu^- \rightarrow e^-$ conversion, we concentrated on the ^{48}Ti nucleus used previously as stopping target by the PSI experiment and recently proposed to be used by the PRIME experiment at J-PARC. Similarly we have studied the ^{27}Al as neutrino detector,

proposed to be used as muon stopping target in the sensitive Mu2e and COMET experiments.

New stringent upper limits (up to even three orders of magnitude lower than those previously put) on the NSI (FC) parameters $\epsilon_{\mu e}^{fV}$ are extracted by using the experimental sensitivity of the $\mu^- \rightarrow e^-$ conversion experiments and our present results. By comparing our results with those of other methods we conclude that the nuclear physics aspects (reflecting the reliability and accuracy of the cross sections), largely affect the coherent $g.s. \rightarrow g.s.$ transition rate, a result especially useful for Supernova neutrino detection probes and low-energy laboratory neutrinos.

Finally, we would like to remark that, $\mu^- \rightarrow e^-$ transition experiments at sensitivities down to $10^{-16} - 10^{-18}$ have excellent capabilities to search for evidence of new physics and to study its flavour structure. These well designed experiments at Fermilab and at J-PARC, could be the starting point of such a new effort, which would complement the neutrino programs. They have significant potential to constrain the NSI parameters and shed light on FCNC processes in the leptonic sector and specifically on the existence of the charged-lepton mixing.

Chapter 6

Electromagnetic neutrino properties in NSI theories

6.1 Introduction

Tensorial non-standard neutrino interactions are studied through a combined analysis of nuclear structure calculations and a sensitivity χ^2 -type of neutrino events expected to be measured at the COHERENT experiment, recently planned to operate at the Spallation Neutron Source (Oak Ridge). Potential sizeable predictions on transition neutrino magnetic moments and other electromagnetic parameters, such as neutrino milli-charges, are also addressed. The non-standard neutrino-nucleus processes, explored from nuclear physics perspectives within the context of the QRPA, are exploited in order to estimate the expected number of events originating from vector and tensor exotic interactions for the case of reactor neutrinos, studied with TEXONO and GEMMA neutrino detectors.

6.1.1 Dirac neutrinos

In the SM, the interaction of a fermionic field $f(x)$ with the electromagnetic field $A(x)$ is given by the interaction Hamiltonian

$$\mathcal{H}_{em}^{(f)} = j_{\mu}^{(f)}(x)A^{\mu}(x) = \mathbf{q}_f \bar{f}(x)\gamma_{\mu}f(x)A^{\mu}(x), \quad (6.1)$$

where \mathbf{q}_f is the fermionic charge¹. Figure 6.1(left panel) shows the corresponding tree-level Feynman diagram (the photon γ is the quantum of the electromagnetic field $A_{\mu}(x)$).

For neutrinos the electric charge is zero and there are no electromagnetic interactions at tree level. However, such interactions can arise at the quantum level from loop diagrams at higher order of the perturbative expansion of the

¹Note, that in Chapt. 2, instead of \mathbf{q}_f we used the notation Q_f .

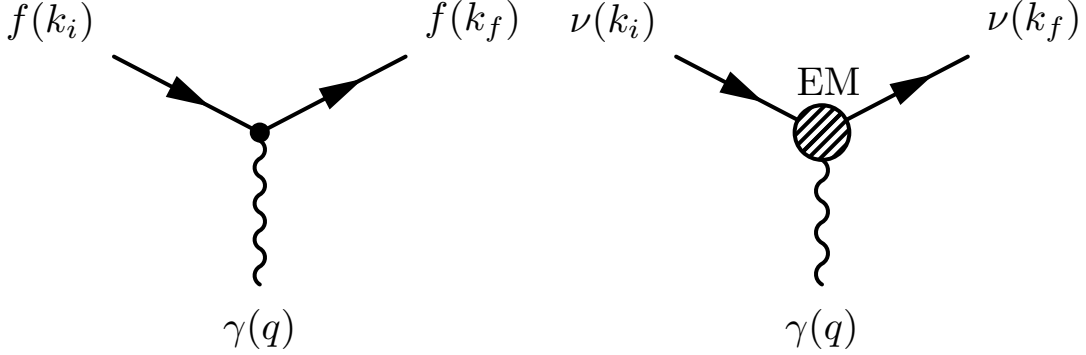


Figure 6.1: Tree-level coupling of a charged fermion f with a photon (*left*), and electromagnetic vertex of a neutrino with a photon (*right*).

interaction. In the one-photon approximation, the electromagnetic interactions of a neutrino field, $\nu(x)$, can be described by the effective interaction Hamiltonian

$$\mathcal{H}_{em}^{(\nu)}(x) = j_{\mu}^{(\nu)}(x)A^{\mu}(x) = \bar{\nu}(x)\Lambda_{\mu}\nu(x)A^{\mu}(x), \quad (6.2)$$

where, $j_{\mu}^{(\nu)}(x)$ is the neutrino effective electromagnetic current four-vector and Λ_{μ} is a 4×4 matrix in spinor space which can contain space-time derivatives, such that $j_{\mu}^{(\nu)}(x)$ transforms as a four-vector. Since radiative corrections are generated by weak interactions which are not invariant under a parity transformation, $j_{\mu}^{(\nu)}(x)$ can be a sum of polar and axial parts. The corresponding diagram for the interaction of a neutrino with a photon is shown in Fig. 6.1(right panel), where the blob represents the quantum loop contributions.

The neutrino electromagnetic properties corresponding to the diagram in Fig. 6.1(right panel) include charge and magnetic form factors. It is worth mentioning that these neutrino electromagnetic properties can exist even if neutrinos are elementary particles, without an internal structure, because they are generated by quantum loop effects. Thus, the neutrino charge and magnetic form factors have a different origin from the neutron charge and magnetic form factors (also called Dirac and Pauli form factors), which are mainly due to its internal quark structure. For example, the neutrino magnetic moment which is the magnetic form factor for interactions with real photons, i.e. $q^2 = 0$ in Fig. 6.1(right panel) have the same quantum origin as the anomalous magnetic moment of the electron (see Ref. [155]).

We are interested in the neutrino part of the amplitude corresponding to the diagram in Fig. 6.1(right panel), which is given by the matrix element

$$\langle \nu(k_f, h_f) | j_{\mu}^{(\nu)}(x) | \nu(k_i, h_i) \rangle, \quad (6.3)$$

with $k_i, (h_i)$ and $k_f, (h_f)$ is the initial and final four-momentum (helicity) of the neutrino respectively. The derivative of the electromagnetic current is expressed

in terms of the four-momentum operator as

$$\partial^\mu j_\mu^{(\nu)}(x) = i [\mathcal{K}^\mu, j_\mu^{(\nu)}(x)] , \quad (6.4)$$

which implies that the effective electromagnetic current can be cast in the form

$$j_\mu^{(\nu)}(x) = e^{i\mathcal{K}\cdot x} j_\mu^{(\nu)}(0) e^{-i\mathcal{K}\cdot x} , \quad (6.5)$$

and therefore the matrix element reads ²

$$\langle \nu(k_f, h_f) | j_\mu^{(\nu)}(x) | \nu(k_i, h_i) \rangle = e^{-i(k_i - k_f)\cdot x} \langle \nu(k_f, h_f) | j_\mu^{(\nu)}(0) | \nu(k_i, h_i) \rangle , \quad (6.6)$$

thus the neutrino-photon interaction strength is determined by the matrix element on the r.h.s. The incoming and outgoing neutrinos are free particles described by free Dirac fields. Their Fourier expansion gives [156]

$$\langle \nu(k_f) | j_\mu^{(\nu)}(0) | \nu(k_i) \rangle = \bar{u}(k_f) \mathcal{U}_\mu(k_f, k_i) u(k_i) . \quad (6.7)$$

The electromagnetic properties of neutrinos are embodied by the vertex function $\mathcal{U}_\mu(k_f, k_i)$, which is a matrix in spinor space and can be decomposed in terms of linearly independent products of Dirac gamma matrices and the available kinematical four-vectors k_i, k_f . As shown in Ref. [156], the most general decomposition can be written as function of six Lorentz-invariant form factors \mathbf{f}_ξ , $\xi = 1, \dots, 6$ in the following form

$$\begin{aligned} \mathcal{U}_\mu(k_f, k_i) = & \mathbf{f}_1(q^2) q_\mu + \mathbf{f}_2(q^2) q_\mu \gamma_5 + \mathbf{f}_3(q^2) \gamma_\mu + \mathbf{f}_4(q^2) \gamma_\mu \gamma_5 \\ & + \mathbf{f}_5(q^2) \sigma_{\mu\nu} q^\nu + \mathbf{f}_6(q^2) \epsilon_{\mu\nu\rho\tau} q^\nu \sigma^{\rho\tau} , \end{aligned} \quad (6.8)$$

where from energy-momentum conservation the momentum of the photon is $q = k_f - k_i$ ³.

The hermiticity of the interaction Hamiltonian and the electromagnetic field imply that the effective electromagnetic current is Hermitian i.e. $j_\mu^{(\nu)}(x) = j_\mu^{(\nu)\dagger}(x)$ and therefore the corresponding matrix element satisfies the relation

$$\langle \nu(k_f) | j_\mu^{(\nu)}(0) | \nu(k_i) \rangle = \langle \nu(k_f) | j_\mu^{(\nu)}(0) | \nu(k_i) \rangle^* . \quad (6.9)$$

Then, $\mathcal{U}_\mu(q)$ obeys the constraint

$$\mathcal{U}_\mu(q) = \gamma^0 \mathcal{U}_\mu^\dagger(-q) \gamma^0 , \quad (6.10)$$

and recalling the Dirac algebra, from the latter expression we conclude that $\mathbf{f}_2, \mathbf{f}_3, \mathbf{f}_4$ are real and $\mathbf{f}_1, \mathbf{f}_5, \mathbf{f}_6$ are imaginary. Moreover, the gauge invariance of the interaction Hamiltonian [i.e. the electromagnetic tensor $F^{\mu\nu} = \partial^\mu A^\nu - \partial^\nu A^\mu$

²Note, that $\mathcal{K}^\mu |\nu(k)\rangle = k^\mu |\nu(k)\rangle$.

³Note, that \mathbf{f}_ξ depend only on q^2 being the only Lorentz-invariant kinematical quantity (since $(k_i + k_f)^2 = 4m^2 - q^2$), and therefore from now on we will write $\mathcal{U}_\mu(k_f, k_i) \equiv \mathcal{U}_\mu(q)$.

being invariant under the transformation $A^\mu(x) \rightarrow A^\mu(x) + \partial^\mu \phi(x)$, for any $\phi(x)$] imposes current conservation, $\partial^\mu j_\mu^{(\nu)}$ leading to

$$\langle \nu(k_f) | [\mathcal{K}^\mu, j_\mu^{(\nu)}(x)] | \nu(k_i) \rangle = 0, \quad (6.11)$$

which subsequently in the momentum space translates to the constraint

$$q^\mu \bar{u}(k_f) \mathcal{U}_\mu(q) u(k_i) = 0. \quad (6.12)$$

Then, from the latter expression one has

$$\mathfrak{f}_1(q^2)q^2 + \mathfrak{f}_2(q^2)q^2\gamma_5 + 2m\mathfrak{f}_4(q^2)\gamma_5 = 0, \quad (6.13)$$

and furthermore due to the linear independence of the unitary matrix and γ_5 the following constraints are extracted

$$\mathfrak{f}_1(q^2) = 0, \quad \mathfrak{f}_4(q^2) = -\mathfrak{f}_2(q^2)\frac{q^2}{2m}. \quad (6.14)$$

Incorporating the above discussion, the most general vertex function consistent with Lorentz and electromagnetic gauge invariance, is written as [157, 158]

$$\mathcal{U}_\mu(q) = f_Q(q^2)\gamma_\mu - if_M(q^2)\sigma_{\mu\nu}q^\nu + f_E(q^2)\sigma_{\mu\nu}q^\nu\gamma_5 + f_A(q^2)(q^2\gamma_\mu - q_\mu\not{q})\gamma_5, \quad (6.15)$$

where the real charge, dipole magnetic and electric, and anapole neutrino form factors read

$$f_Q = \mathfrak{f}_3, \quad f_M = i\mathfrak{f}_5, \quad f_E = -2i\mathfrak{f}_6, \quad f_A = -\mathfrak{f}_2/2m, \quad (6.16)$$

where we also used the fact that

$$\bar{u}(k_f)\not{q}\gamma^5 u(k_i) = 2m\bar{u}(k_f)\gamma^5 u(k_i). \quad (6.17)$$

The latter take the following static (at $q^2 = 0$ e.g. couplings with real photons) values

$$f_Q(0) = \mathfrak{q}_\nu, \quad f_M(0) = \mu, \quad f_E(0) = \epsilon, \quad f_A(0) = \mathfrak{a}_\nu, \quad (6.18)$$

namely, the the neutrino (milli-)charge, magnetic moment, electric moment, and anapole moment.

6.1.2 Charge-radius

Even if the electric charge of a neutrino is zero, the electric form factor, $f_Q(q^2)$, can contain nontrivial information about the neutrino electric properties. In fact, a neutral particle can be characterised by a (real or virtual) superposition of two different charge distributions of opposite signs, which is described by a form factor $f_Q(q^2)$ which is non-zero for $q^2 \neq 0$.

The neutrino charge-radius is determined by the second term in the expansion of the neutrino charge form factor $f_Q(q^2)$ in a series of powers of q^2 as

$$f_Q(q^2) \simeq f_Q(0) + q^2 \left. \frac{df_Q(q^2)}{dq^2} \right|_{q^2=0} + \dots \quad (6.19)$$

Recalling the ‘‘Breit frame’’, where $q_0 = 0$, the charge form factor $f_Q(q^2)$ depends only on $\kappa \equiv |\mathbf{q}| = \sqrt{-q^2}$ and can be interpreted as the Fourier transform of a spherically symmetric charge distribution $\rho_\nu(r)$, with $r = |\mathbf{x}|$

$$\begin{aligned} f_Q(q^2) &= \int d^3x \rho_\nu(r) e^{-i\mathbf{q}\cdot\mathbf{x}} \\ &= \int d^3x \rho_\nu(r) \frac{\sin(\kappa r)}{\kappa r} \\ &= \int dr 4\pi \rho_\nu(r) r^2 j_0(\kappa r). \end{aligned} \quad (6.20)$$

Evaluating the derivative one finds

$$\frac{df_Q(q^2)}{dq^2} = \int d^3x \rho_\nu(r) \frac{\sin(\kappa r) - \kappa r \cos(\kappa r)}{2\kappa^3 r}, \quad (6.21)$$

which in the limit of zero momentum transfer gives

$$\lim_{q^2 \rightarrow 0} \frac{df_Q(q^2)}{dq^2} = \int d^3x \frac{r^2}{6} \equiv \frac{\langle r_\nu^2 \rangle}{6}. \quad (6.22)$$

Thus, the root mean squared neutrino charge-radius is related to the charge form factor by

$$\langle r_\nu^2 \rangle = 6 \left. \frac{df_Q(q^2)}{dq^2} \right|_{q^2=0}. \quad (6.23)$$

We note, however, that the latter can be negative, because the charge density, $\rho(r)$, is not a positively defined quantity. Recalling Eq.(6.19) and Eq.(6.23), in the SM, one defines the neutrino electromagnetic form factor for low momentum transfer as

$$f(q^2) \simeq \left(\frac{\langle r_\nu^2 \rangle}{6} - \mathbf{a}_\nu \right) q^2, \quad (6.24)$$

where \mathbf{a}_ν is the anapole moment⁴. Hence, in the SM this form factor can be interpreted as a neutrino charge-radius or as an anapole moment (or as a combination of both).

There has been a lot of controversial discussion on whether the neutrino charge-radius is a physical quantity or not. An ultraviolet divergent result has

⁴Note, that for the case of massless left-handed Weyl neutrinos as in the SM, the latter vanishes.

been obtained from studies in the unitary gauge [159] as well as in the general R_ξ gauge [160] implying that the neutrino charge-radius is not a physical quantity. However, within the unitary gauge, taking into account terms arising from Z -boson diagrams, a gauge dependent and finite result was derived [161], while further studies concluded that a finite and gauge independent value for the neutrino charge-radius could be obtained by considering additional box diagrams [162]. The neutrino electroweak radius was then introduced as a physical observable through calculations performed in the one-loop approximation including additional terms from the $\gamma - Z$ boson mixing and box diagrams involving W - and Z -bosons, leading to the gauge invariant result for the neutrino charge-radius [163]

$$\langle r_{\nu_\ell}^2 \rangle_{\text{SM}} = \frac{G_F}{4\sqrt{2}\pi^2} \left[3 - 2 \log \left(\frac{m_\ell^2}{M_W^2} \right) \right], \quad (6.25)$$

where M_W and m_ℓ denote the W -boson and lepton mass, $\ell = \{e, \mu, \tau\}$. Numerically, Eq.(6.25) gives

$$\begin{aligned} \langle r_{\nu_e}^2 \rangle_{\text{SM}} &= 4.1 \times 10^{-33} \text{ cm}^2, \\ \langle r_{\nu_\mu}^2 \rangle_{\text{SM}} &= 2.4 \times 10^{-33} \text{ cm}^2, \\ \langle r_{\nu_\tau}^2 \rangle_{\text{SM}} &= 1.5 \times 10^{-33} \text{ cm}^2. \end{aligned} \quad (6.26)$$

6.2 Majorana neutrino magnetic moment

In the general Majorana neutrino case, the effective Hamiltonian for the spin component of the neutrino electromagnetic vertex, takes the form [68, 164]

$$H_{em}^{\text{M}} = \frac{1}{4} \nu_L^\top C^{-1} \lambda \sigma^{\alpha\beta} \nu_L F_{\alpha\beta} + \text{h.c.}, \quad (6.27)$$

where $F_{\alpha\beta}$ is the electromagnetic field tensor, and $\lambda = \mu - i\epsilon$ is an antisymmetric complex matrix $\lambda_{\alpha\beta} = -\lambda_{\beta\alpha}$, so that $\mu^\top = -\mu$ and $\epsilon^\top = -\epsilon$ are imaginary. Hence for Majorana neutrinos, three complex or six real parameters are required. The Hamiltonian of Eq.(6.27) should be confronted to the Dirac neutrino case where the corresponding one reads

$$H_{em}^{\text{D}} = \frac{1}{2} \bar{\nu}_R \lambda \sigma^{\alpha\beta} \nu_L F_{\alpha\beta} + \text{h.c.}, \quad (6.28)$$

with $\lambda = \mu - i\epsilon$ denoting an arbitrary complex matrix, subject to the hermiticity constraints $\mu = \mu^\dagger$ and $\epsilon = \epsilon^\dagger$. Symmetry principles as well as neutrino properties place constraints to the matrices μ_{ij} and ϵ_{ij} . Contrary to the Dirac case, Majorana neutrinos require $\mu_{ii} = \epsilon_{ii} = 0$ which implies the vanishing of the diagonal moments. This notable difference indicates that neutrino electromagnetic properties constitute a valuable tool to distinguish between Dirac and Majorana neutrinos.

The Majorana magnetic and electric transition moments have been explicitly calculated in the simplest $SU(2)_L \otimes U(1)_Y$ model to be [165]

$$\mu_{ij}^M = -\frac{3ieG_F}{16\pi^2\sqrt{2}}(m_{\nu i} + m_{\nu j}) \sum_{\alpha=e,\mu,\tau} \Im m \left[U_{\alpha i}^* U_{\alpha j} \left(\frac{m_{l\alpha}}{M_W} \right)^2 \right], \quad (6.29)$$

$$\epsilon_{ij}^M = \frac{3ieG_F}{16\pi^2\sqrt{2}}(m_{\nu i} - m_{\nu j}) \sum_{\alpha=e,\mu,\tau} \Re e \left[U_{\alpha i}^* U_{\alpha j} \left(\frac{m_{l\alpha}}{M_W} \right)^2 \right]. \quad (6.30)$$

The corresponding results for the Dirac case read

$$\mu_{ij}^D = \frac{eG_F}{8\pi^2\sqrt{2}}(m_{\nu i} + m_{\nu j}) \sum_{\alpha=e,\mu,\tau} f(a_\alpha) U_{\alpha i}^* U_{\alpha j}, \quad (6.31)$$

$$\epsilon_{ij}^D = -\frac{ieG_F}{8\pi^2\sqrt{2}}(m_{\nu i} - m_{\nu j}) \sum_{\alpha=e,\mu,\tau} f(a_\alpha) U_{\alpha i}^* U_{\alpha j}, \quad (6.32)$$

where

$$f(a_\alpha) \simeq \frac{3}{2} \left(1 - \frac{a_\alpha}{2} \right), \quad a_\alpha \equiv \frac{m_{l\alpha}^2}{M_W^2}. \quad (6.33)$$

apparently, Eq.(6.33), emphasises the absence of diagonal electric moments, while the diagonal Dirac magnetic moment reads

$$\mu_{ii} \simeq \frac{3eG_F}{8\pi^2\sqrt{2}} m_{\nu i}. \quad (6.34)$$

We furthermore note, that irrespectively of whether we are involved with Dirac or Majorana neutrinos, for vanishing neutrino masses the magnetic and electric moments also vanish. Reference [67] states that a Dirac neutrino is equivalent to two Majorana neutrinos of same mass and opposite CP phases, which implies that

$$\mu_{ij}^M = 2\mu_{ij}^D, \quad \epsilon_{ij}^D = 0, \quad (6.35)$$

while for the same CP phases it holds

$$\mu_{ij}^M = 0, \quad \epsilon_{ij}^M = 2\epsilon_{ij}^D. \quad (6.36)$$

6.2.1 Effective neutrino magnetic moments

In scattering experiments the neutrino is created at some distance, L , from the detector as a flavour neutrino, which in reality is a superposition of massive neutrinos. The interpretations of experimental results depend on the exact neutrino compositions at the detectors. The observable, μ_ν ,

$$\mu_{\nu\alpha}^2(L, E_\nu) = \sum_j \left| \sum_i U_{\alpha i}^* e^{-i\Delta m_{ij}^2 L/2E_\nu} (\mu_{ij} - i\epsilon_{ij}) \right|^2, \quad (6.37)$$

is not that of a massive neutrino, but an effective and convoluted parameter which takes into account neutrino mixing and the oscillations during the propagation between source and detector [166, 167]. We note, that there can be only a phase difference between $\mu_{\nu_\alpha}^2$ and $\mu_{\nu_\beta}^2$, which is induced by neutrino oscillations.

From a phenomenological point of view, in general, the parameter $\mu_\nu \equiv \mu_{eff}$ describing the effective neutrino magnetic moment can be expressed through neutrino amplitudes of positive and negative helicity states which we denote as the 3-vectors a_+ and a_- , respectively and the magnetic moment matrix, λ ($\tilde{\lambda}$) in flavour (mass) basis

$$\lambda = \begin{pmatrix} 0 & \Lambda_\tau & -\Lambda_\mu \\ -\Lambda_\tau & 0 & \Lambda_e \\ \Lambda_\mu & -\Lambda_e & 0 \end{pmatrix}, \quad \tilde{\lambda} = \begin{pmatrix} 0 & \Lambda_3 & -\Lambda_2 \\ -\Lambda_3 & 0 & \Lambda_1 \\ \Lambda_2 & -\Lambda_1 & 0 \end{pmatrix}. \quad (6.38)$$

Here, we have introduced the definition $\lambda_{\alpha\beta} = \varepsilon_{\alpha\beta\gamma}\Lambda_\gamma$, while the transition magnetic moments are assumed to be complex parameters and they can be cast in the form

$$\Lambda_\alpha = |\Lambda_\alpha|e^{i\zeta_\alpha}, \quad \Lambda_i = |\Lambda_i|e^{i\zeta_i}, \quad (6.39)$$

where three complex phases ζ_1 , ζ_2 and ζ_3 enter the transition magnetic moment matrix.

The effective neutrino magnetic moment is expressed in terms of the components of the neutrino magnetic moment matrix in Eq.(6.38) as follows [168]

$$(\mu_\nu^{\text{flavour}})^2 = a_-^\dagger \lambda^\dagger \lambda a_- + a_+^\dagger \lambda \lambda^\dagger a_+, \quad (6.40)$$

and thus

$$\begin{aligned} (\mu_\nu^{\text{flavour}})^2 &= |a_-^1 \Lambda_\mu - a_-^2 \Lambda_e|^2 + |a_-^1 \Lambda_\tau - a_-^3 \Lambda_e|^2 \\ &\quad + |a_-^2 \Lambda_\tau - a_-^3 \Lambda_\mu|^2 + |a_+^1 \Lambda_\mu - a_+^2 \Lambda_e|^2 \\ &\quad + |a_+^1 \Lambda_\tau - a_+^3 \Lambda_e|^2 + |a_+^2 \Lambda_\tau - a_+^3 \Lambda_\mu|^2, \end{aligned} \quad (6.41)$$

where a_\pm^i denotes the i -th component of the a_\pm vector. The latter expression can be translated into the mass basis through a rotation, by using the leptonic mixing matrix. Introducing the transformations

$$\tilde{a}_- = U^\dagger a_-, \quad \tilde{a}_+ = U^\top a_+, \quad \tilde{\lambda} = U^\top \lambda U, \quad (6.42)$$

the effective neutrino magnetic moment can be written in the mass basis

$$(\mu_\nu^{\text{mass}})^2 = \tilde{a}_-^\dagger \tilde{\lambda}^\dagger \tilde{\lambda} \tilde{a}_- + \tilde{a}_+^\dagger \tilde{\lambda} \tilde{\lambda}^\dagger \tilde{a}_+, \quad (6.43)$$

leading to

$$\begin{aligned} (\mu_\nu^{\text{mass}})^2 &= |\tilde{a}_-^1 \Lambda_2 - \tilde{a}_-^2 \Lambda_1|^2 + |\tilde{a}_-^1 \Lambda_3 - \tilde{a}_-^3 \Lambda_1|^2 \\ &\quad + |\tilde{a}_-^2 \Lambda_3 - \tilde{a}_-^3 \Lambda_2|^2 + |\tilde{a}_+^1 \Lambda_2 - \tilde{a}_+^2 \Lambda_1|^2 \\ &\quad + |\tilde{a}_+^1 \Lambda_3 - \tilde{a}_+^3 \Lambda_1|^2 + |\tilde{a}_+^2 \Lambda_3 - \tilde{a}_+^3 \Lambda_2|^2. \end{aligned} \quad (6.44)$$

Therefore, one can see that the limits on the effective neutrino magnetic moment obtained from neutrino experiments are in reality a restriction on a combination of physical observables.

Focusing on reactor antineutrinos, e.g. the only non-zero parameter entering Eq.(6.41) is a_+^1 . In this case we have an initial electron antineutrino flux, so that the only non-zero entry in the flavour basis will be a_+^1 . Therefore, from Eq.(6.41), the effective Majorana transition magnetic moment strength parameter describing reactor neutrino experiments can deduced as

$$(\mu_\nu^{\text{flavour}})^2 = |\Lambda_\mu|^2 + |\Lambda_\tau|^2. \quad (6.45)$$

The above expression, in the mass basis becomes [169]

$$\begin{aligned} (\mu_\nu^{\text{mass}})^2 = & |\mathbf{\Lambda}|^2 - s_{12}^2 c_{13}^2 |\Lambda_2|^2 - c_{12}^2 c_{13}^2 |\Lambda_1|^2 - s_{13}^2 |\Lambda_3|^2 \\ & - 2s_{12} c_{12} c_{13}^2 |\Lambda_1| |\Lambda_2| \cos \delta_{12} \\ & - 2c_{12} c_{13} s_{13} |\Lambda_1| |\Lambda_3| \cos \delta_{13} \\ & - 2s_{12} c_{13} s_{13} |\Lambda_2| |\Lambda_3| \cos \delta_{23}, \end{aligned} \quad (6.46)$$

where the usual abbreviations have been used $c_{ij} = \cos \theta_{ij}$, $s_{ij} = \sin \theta_{ij}$ and $\delta_{12} = \xi_3$, $\delta_{23} = \xi_2 - \delta$ and $\delta_{13} = \delta_{12} - \delta_{23}$. Here, δ is the Dirac CP phase of the leptonic mixing matrix and the difference between the transition magnetic moment phases is defined as $\xi_1 = \zeta_3 - \zeta_2$, $\xi_2 = \zeta_3 - \zeta_2$ and $\xi_3 = \zeta_2 - \zeta_1$ ⁵.

Focusing on the neutrino signal produced from stopped pion-muon beams, we express the relevant neutrino magnetic moment accordingly. By assuming the same proportion of ν_e , ν_μ and $\bar{\nu}_\mu$ (e.g., $a_-^1 = 1$, $a_-^2 = 1$ and $a_+^2 = 1$), the effective magnetic moment strength parameter in the flavour basis is written in terms of the relevant phase between the transition magnetic moments $|\Lambda_e|$ and $|\Lambda_\mu|$, as [169]

$$(\mu_\nu^{\text{flavour}})^2 = |\mathbf{\Lambda}|^2 + |\Lambda_e|^2 + 2|\Lambda_\mu|^2 - 2|\Lambda_\mu| |\Lambda_e| \cos(\zeta_e - \zeta_\mu), \quad (6.47)$$

where $|\mathbf{\Lambda}|^2 = |\Lambda_e|^2 + |\Lambda_\mu|^2 + |\Lambda_\tau|^2$. For the corresponding expression in the mass basis, see Ref [169]. Specifically, concentrating on the muon neutrino signal and considering the muon neutrino as having a Majorana nature, we have, in the flavour basis [170]

$$(\mu_\nu^{\text{flavour}})^2 = |\Lambda_e|^2 + |\Lambda_\tau|^2, \quad (6.48)$$

with $|\Lambda_e|$ and $|\Lambda_\tau|$ being the elements of the neutrino transition magnetic moment matrix λ describing the corresponding transitions from the muon neutrino to the tau and electron antineutrino states, respectively. A full description of this formalism can be found in Refs. [168, 169].

⁵Two of them are independent.

6.3 Tensorial non-standard neutrino interactions

The investigation of neutrino electromagnetic (EM) properties started long ago [171, 172], mainly after the introduction of the minimally extended standard model with right-handed neutrinos [67, 68]. In this context, at the one loop level the magnetic moment, μ_ν , of a massive neutrino is in general non-zero and its magnitude is proportional to the neutrino mass, m_ν [173]. Actually, the theoretical and experimental study of neutrino EM phenomena [70], is widely considered as one of the most powerful tools to probe possible interactions involving neutrinos beyond the Standard Model (SM) [25]. Furthermore, in an astrophysical environment with extreme conditions (huge magnetic fields, currents, etc.), important non-standard effects may occur due to non-trivial EM properties of neutrinos [164, 174], which may lead to significant alterations of existing scenarios for massive star evolution [118].

Exotic neutrino properties arise in neutrino-nucleus processes, occurring due to non-standard neutrino interactions (NSI) of the form [25]

$$\nu_\alpha(\bar{\nu}_\alpha) + (A, Z) \rightarrow \nu_\beta(\bar{\nu}_\beta) + (A, Z), \quad (6.49)$$

providing us with model independent constraints of various NSI parameters [22]. In the current literature, even though only vector terms are mainly considered in the relevant Lagrangian [111], tensorial NSI terms have attracted the interest of studying the aforementioned processes, while robust constraints to the corresponding couplings have been extracted from neutrino-nucleus coherent scattering [175]. In addition, because tensor interaction does not obey the chirality constraint imposed by vector-type couplings, it allows a large class of interactions to be investigated [115]. More specifically from a particle physics point of view, tensor NSI terms are possible to be generated via Fierz reordering of the effective low-energy operators appearing in models with scalar leptoquarks [176] as well as in R-parity-violating supersymmetry [177].

In general, the non-zero neutrino mass, is experimentally confirmed from neutrino oscillation in propagation data [100–102] and implies that the neutrino is the only particle that exhibits non-standard properties [165], which are directly connected to the fundamental interactions of particle physics. As a concrete example, neutrino EM properties are useful to distinguish Dirac and Majorana neutrinos and also to probe phenomena of new physics beyond the SM [178]. In fact, recent studies, based on model-independent analyses of the contributions to neutrino magnetic moment (NMM), have shown that, if a NMM of the order of $\mu_\nu \geq 10^{-15} \mu_B$ were experimentally observed, it would confirm the Majorana nature of neutrinos [179, 180].

In this Chapter, we mainly focus on contributions to the neutrino-nucleus reactions of Eq.(6.49), due to tensorial terms of the NSI Lagrangian, paying special

attention on the nuclear physics aspects of these exotic processes. The cross sections, that arise from the effective four-fermion contact interaction Lagrangian, are expressed in terms of the nuclear proton and neutron form factors. Subsequently, the sensitivity on the tensor NSI parameters is obtained from a χ^2 analysis of the expected data from the COHERENT experiment [73–75] recently proposed to operate at the Spallation Neutron Source (SNS) at Oak Ridge [86, 87] by using promising nuclear detectors as ^{20}Ne , ^{40}Ar , ^{76}Ge and ^{132}Xe . Constraints of this type translate into relevant sensitivities on the upper limits of NMM predicted within the context of the tensor components entering the NSI Lagrangian. The latter can be compared with existing limits derived from $\bar{\nu}_e - e$ scattering data [181, 182] coming out of reactor neutrino experiments, such as the TEXONO [183] and GEMMA [184] experiments, as well as with other astrophysical observations [185].

On the basis of our nuclear calculations (performed with QRPA) [40, 55, 85, 124] for the dominant coherent process [32, 135], we evaluate the number of events due to vector and tensor NSI parts of the neutrino-nucleus cross section, and estimate the contribution due to the NMM [166, 167, 170, 186]. Our results for the number of events, refer to the ^{76}Ge isotope which is the current detector medium of the TEXONO and GEMMA experiments. It is worth mentioning that, even though within the SM, gauge invariance and anomaly cancellation constraints require neutrinos to be neutral particles, however non-vanishing electric milli-charge [187] is expected for massive neutrinos which may induce additional neutrino-photon interactions [188–190]. Furthermore, by taking advantage of the present sensitivity on the transition NMM, we come out with potential stringent constraints (by one order of magnitude more severe than existing limits) on the neutrino milli-charge q_ν .

6.4 Description of the formalism

In general the search for potential existence of phenomena beyond the SM involving NSI at the four-fermion approximation, becomes accessible through phenomenological low-energy effective Lagrangians as

$$\mathcal{L}_{\text{NSI}} = -2\sqrt{2}G_F \sum_X \sum_{\substack{f=q,\ell \\ \alpha,\beta=e,\mu,\tau}} \epsilon_{\alpha\beta}^{fX} [\bar{\nu}_\alpha \Gamma_X \nu_\beta] [\bar{f} \Gamma_X f], \quad (6.50)$$

where $X = \{V, A, S, P, T\}$, $\Gamma_X = \{\gamma_\mu, \gamma_\mu \gamma_5, 1, \gamma_5, \sigma_{\mu\nu}\}$ and $\sigma_{\mu\nu} = i[\gamma_\mu, \gamma_\nu]/2$. The magnitude of the NSI couplings $\epsilon_{\alpha\beta}^{fX}$, is taken with respect to the Fermi coupling constant G_F [70, 111], ν_α denotes three light Majorana neutrinos and f is a quark q , or a charged lepton ℓ . In this Chapter, we focus on the tensorial

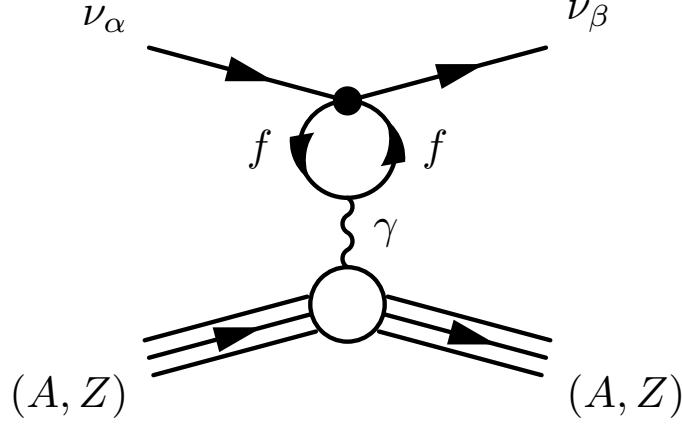


Figure 6.2: Nuclear level effective Feynman diagram for magnetic moment of a neutrino induced by tensorial NSI. The non-standard physics enters in the complicated vertex denoted by the large dot \bullet .

neutrino-nucleus NSI described by the Lagrangian [175]

$$\mathcal{L}_{\text{NSI}}^T = -2\sqrt{2}G_F \sum_{\substack{f=u,d \\ \alpha,\beta=e,\mu,\tau}} \epsilon_{\alpha\beta}^{fT} [\bar{\nu}_\alpha \sigma^{\mu\nu} \nu_\beta] [\bar{f} \sigma_{\mu\nu} f] . \quad (6.51)$$

The extraction of the latter Lagrangian is illustrated in Fig. 6.2, where the nuclear-level Feynman loop-diagram represents the photon exchange between a fermion and a quark generating a neutrino magnetic moment. The non-standard physics enters through the complicated leptonic vertex (see also Ref. [25]).

6.4.1 Non-standard neutrino-nucleus reaction cross sections

For neutral-current processes, the vector NSI part of the effective Lagrangian (6.50), is parametrised in terms of non-universal (NU) $\epsilon_{\alpha\alpha}^{fV}$ and flavour-changing (FC) vector couplings $\epsilon_{\alpha\beta}^{fV}$ ($\alpha \neq \beta$) [22]. For coherent scattering, a nucleus of mass M recoils (no intrinsic excitation occurs) with energy which, in the approximation $T_N \ll E_\nu$ (low-energy limit), is maximised as, $T_N^{\text{max}} = 2E_\nu^2/(M + 2E_\nu)$. Then, to a good approximation, the square of the three momentum transfer is equal to $Q^2 = 2MT_N$, and the coherent vector NSI differential cross section with respect to T_N is given by Eq.(5.13) and the corresponding nuclear matrix element can be found in Eq.(5.11) (see Chapt. 5 for details).

For NSI scattering, the differential cross section with respect to the recoil

energy T_N due to tensor interactions (at nuclear level) reads

$$\frac{d\sigma_{\text{NSI},\nu\alpha}^T}{dT_N} = \frac{4G_F^2 M}{\pi} \left[\left(1 - \frac{T_N}{2E_\nu}\right)^2 - \frac{MT_N}{4E_\nu^2} \right] |\langle g.s. || G_{T,\nu\alpha}^{\text{NSI}}(Q) || g.s. \rangle|^2. \quad (6.52)$$

The corresponding tensorial NSI matrix element arising from the Lagrangian (6.51) takes the form

$$\begin{aligned} |\mathcal{M}_{T,\nu\alpha}^{\text{NSI}}|^2 &\equiv |\langle g.s. || G_{T,\nu\alpha}^{\text{NSI}}(Q) || g.s. \rangle|^2 = \\ &[(2\epsilon_{\alpha\beta}^{uT} + \epsilon_{\alpha\beta}^{dT}) ZF_Z(Q^2) + (\epsilon_{\alpha\beta}^{uT} + 2\epsilon_{\alpha\beta}^{dT}) NF_N(Q^2)]^2, \end{aligned} \quad (6.53)$$

(there is no interference between the tensorial NSI and the SM amplitude [175]) where $F_{Z(N)}(Q^2)$ denote the nuclear (electromagnetic) form factors for protons and neutrons.

6.4.2 NSI neutrino transition magnetic moments

In flavour space $\alpha, \beta = e, \mu, \tau$, neutrino magnetic moments $\mu_{\alpha\beta}$ are generated by the tensorial part of the Hermitian magnetic form factor $f_{\alpha\beta}^M(0) = \mu_{\alpha\beta}$ in the effective neutrino EM current [174]

$$-f_{\alpha\beta}^M(q^2) \bar{\nu}_\beta i\sigma_{\mu\nu} \nu_\alpha, \quad (6.54)$$

(for the relation of the NMM between the flavour basis $\mu_{\alpha\beta}$ and the mass basis μ_{ij} with $i, j = 1, 2, 3$, see Eq.(6.37)). It is worth mentioning that, within the minimally extended SM, in order to include neutrino masses, diagonal NMMs $\mu_{\alpha\alpha}$ are possible only for Dirac neutrinos. However, transition NMMs $\mu_{\alpha\beta}$ can be obtained for both Dirac and Majorana neutrinos [174].

As it is known, the SM predicts extremely small values for the NMMs (of the order of $\mu_\nu \leq 10^{-19} \mu_B (m_\nu/1\text{eV})$ [171], where μ_B is the Bohr magneton). Presently, the best upper limit on μ_ν has been set from astrophysical observations as [185]

$$\mu_\nu \leq 3 \times 10^{-12} \mu_B. \quad (6.55)$$

Other constraints are available through reactor $\bar{\nu}_e - e$ scattering data of the TEXONO experiment [183]

$$\mu_{\bar{\nu}_e} < 7.4 \times 10^{-11} \mu_B \quad (90\% \text{ C.L.}), \quad (6.56)$$

and of the GEMMA experiment [184]

$$\mu_{\bar{\nu}_e} < 2.9 \times 10^{-11} \mu_B \quad (90\% \text{ C.L.}). \quad (6.57)$$

In our convention the leading order contribution to the NMM for neutrino-quark ($\nu_\alpha - q$) NSI is expressed as

$$\mu_{\alpha\beta} = \sum_q 2\sqrt{2}G_F \epsilon_{\alpha\beta}^{qT} \frac{N_c Q_q}{\pi^2} m_e m_q \ln\left(2\sqrt{2}G_F m_q^2\right) \mu_B, \quad (6.58)$$

where m_q and Q_q are the quark mass and charge respectively, while N_c is the number of quark colours (see also Ref. [115]). Analogously, the NMM for neutrino-lepton ($\nu_\alpha - \ell$) NSI takes the form

$$\mu_{\alpha\beta} = - \sum_{\ell} 2\sqrt{2}G_F \epsilon_{\alpha\beta}^{\ell T} \frac{m_e m_\ell}{\pi^2} \ln \left(2\sqrt{2}G_F m_\ell^2 \right) \mu_B, \quad (6.59)$$

with m_ℓ being the mass of the charged leptons.

In Ref. [166], it has been suggested that the presence of a NMM yields an additional contribution to the weak interaction cross section. Thus, the differential EM cross section $d\sigma/dT_N$ due to a tensor NSI (transition) magnetic moment is written in terms of the fine structure constant, a_{em} , as

$$\frac{d\sigma_{\text{magn}}}{dT_N} = \frac{\pi a_{em}^2 \mu_{\alpha\beta}^2 Z^2}{m_e^2} \left(\frac{1 - T_N/E_\nu}{T_N} \right) F_Z^2(Q^2), \quad (6.60)$$

which contains the proton nuclear form factor (see also Ref. [186]). From the Lagrangian (6.50) the total cross section reads

$$\frac{d\sigma_{\text{tot}}}{dT_N} = \frac{d\sigma_{\text{SM}}}{dT_N} + \frac{d\sigma_{\text{NSI}}^V}{dT_N} + \frac{d\sigma_{\text{NSI}}^T}{dT_N} + \frac{d\sigma_{\text{magn}}}{dT_N}, \quad (6.61)$$

(the flavour indices have been suppressed).

6.5 Results and discussion

At first, the nuclear structure details that reflect the dependence of the coherent differential cross section on the recoil energy, T_N , through Eq.(6.61), are studied. This involves realistic calculations of $d\sigma_{\nu_\alpha}/dT_N$, for both vector and tensor operators for a set of currently interesting nuclear detectors. For each nuclear system, the required pairing residual interaction was obtained from a Bonn C-D two-body potential (strong two-nucleon forces) which was slightly renormalised with two pairing parameters, $g_{\text{pair}}^{p(n)}$, for proton (neutron) pairs [26]. The nuclear form factors for protons and neutrons are obtained as in Ref. [55], by solving iteratively the BCS equations [32, 40, 85, 135].

6.5.1 Tensorial NSI couplings from SNS experiments

The COHERENT experiment [73–75] proposed to operate at the SNS (Oak Ridge) has excellent capabilities not only to measure, for the first time, coherent neutral-current neutrino-nucleus events, but also to search for new physics beyond the SM [70]. In general, any deviation from the SM predictions is interesting, therefore in the present study we explore the role of the sensitivity of the above experiment in putting stringent bounds on the tensor NSI, by taking advantage

of our realistic nuclear structure calculations. We determine potential limits for the exotic parameters $\epsilon_{\alpha\beta}^{fT}$ and compare them with available constraints reported in similar studies [115, 175].

To this aim, we first evaluate the expected number of events, on various detector materials of the COHERENT experiment, through the integral [26, 70]

$$N = K \int_{E_{\nu\min}}^{E_{\nu\max}} \eta^{\text{SNS}}(E_{\nu}) dE_{\nu} \int_{T_N^{\text{thres}}}^{T_{N\max}} \frac{d\sigma}{dT_N}(E_{\nu}, T_N) dT_N, \quad (6.62)$$

where $K = N_{\text{targ}} \Phi^{\text{SNS}} t_{\text{tot}}$, with N_{targ} being the number of atoms of the studied target nucleus, and t_{tot} the total time of exposure. The relevant neutrino energy-distribution $\eta^{\text{SNS}}(E_{\nu})$ and the neutrino fluxes Φ^{SNS} (strongly depended on the detector distances from the SNS source), are taken from Refs. [86, 87].

To estimate the sensitivity on the tensorial parameters we adopt the futuristic statistical method for the χ^2 defined as [111]

$$\chi^2 = \left(\frac{N_{\text{events}}^{\text{SM}} - N_{\text{events}}^{\text{NSI}}}{\delta N_{\text{events}}} \right)^2. \quad (6.63)$$

Since the experiment is not running yet, the calculations are performed without binning the sample relying on statistical errors only (systematic errors are discussed in Ref. [70]). Calculations which take into consideration possible background errors are addressed in Ref. [170]. In Eq.(6.63) $N_{\text{events}}^{\text{SM}}$ ($N_{\text{events}}^{\text{NSI}}$) denotes the exact number of SM (tensorial NSI) events expected to be recorded by a COHERENT detector and the parameters $\epsilon_{\alpha\beta}^{qT}$ are varied so as to fit the hypothetical data. In our calculations we consider the promising target nuclei, ^{20}Ne , ^{40}Ar , ^{76}Ge , (^{132}Xe) at 20 m (40 m) from the SNS source, assuming an energy threshold of 1 keV and a detector mass of one ton. The considered time window of data taking is fixed to one year assuming perfect detection efficiency. For the sake of convenience, from the SNS delayed-beam we take into account only the ν_e component. This allows us also to compare our predictions with those of Ref. [175]. For the various target nuclei, the present results are illustrated in Fig. 6.3, from where we conclude that higher prospects are expected for ^{76}Ge . In principle, more severe constraints are expected for heavier target nuclei, however, the detector distance from the spallation target plays crucial role, and thus, a light ^{20}Ne detector located at 20 m performs better than a heavy ^{132}Xe detector at 40 m. The corresponding sensitivity at 90% C.L. on the NSI couplings, coming out of the ν_e and the $\bar{\nu}_{\mu} + \nu_{\mu}$ beams, are listed in Table 6.1. Furthermore, focusing on the neutrino-quark ($q = u, d$) tensor NSI involved in the Lagrangian (6.51), we exploit the constraints of Table 6.1 and utilise Eq.(6.58), in order to extract the sensitivity on the NMM (see Table 6.1). At this point, we consider useful to make a comparison between the results obtained through our nuclear calculations and those obtained by assuming zero momentum transfer (where $F_{N,Z}(0) = 1$) i.e

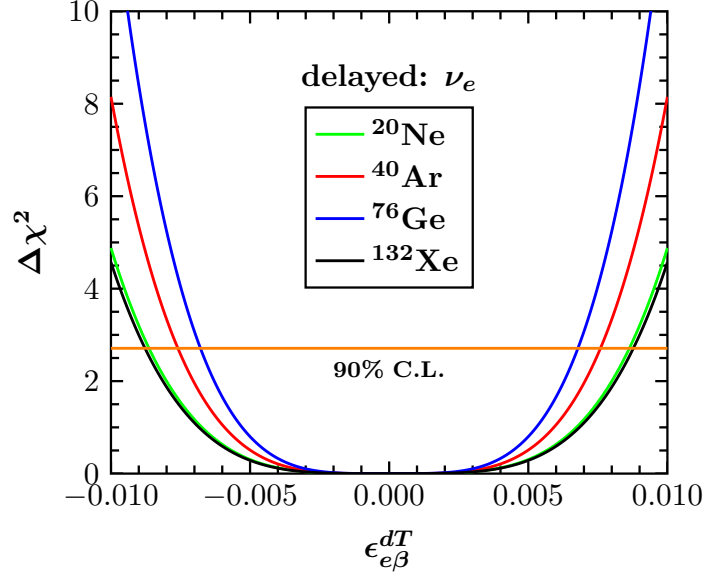


Figure 6.3: $\Delta\chi^2$ profiles as function of the $\epsilon_{e\beta}^{dT}$ NSI parameters, for potential nuclear detectors of the COHERENT experiment (for statistical errors only).

when neglecting the nuclear physics details. This leads to the conclusion that, in the majority of the cases the obtained results differ by about 20%.

In recent years, it has been shown that, in order to constrain more than one parameters simultaneously, two detectors consisting of target material with maximally different ratio $k = (A + N)/(A + Z)$ are required [70, 111]. To this purpose, we exploit the advantageous multi-target approach of the COHERENT experiment and in Fig. 6.4 we illustrate the allowed regions in the $\epsilon_{e\beta}^{dT}-\epsilon_{e\beta}^{uT}$ and $\epsilon_{\mu\beta}^{dT}-\epsilon_{\mu\beta}^{uT}$ plane at 68%, 90% and 99% C.L., obtained by varying both tensorial NSI parameters. As expected, the most restricted area corresponds to the delayed beam for which the number of events is larger.

6.5.2 NSI neutrino-nucleus events at the TEXONO experiment

One of the most important connections of the present work with ongoing and future reactor neutrino experiments is related to the detection of $\bar{\nu}_e$ -nucleus processes. Towards this aim, for our convenience at first we exploit the available experimental data on the reactor $\bar{\nu}_e$ beams [181, 182], in order to fit analytic expressions describing their energy-distribution by using numerical optimisation techniques. Then, the obtained expressions are applied to predict the number of events expected to be measured in the currently interesting ^{76}Ge detector material of the TEXONO [183] and GEMMA [184] experiments. In Fig. 6.5 we compare

parameter	^{20}Ne	^{40}Ar	^{76}Ge	^{132}Xe
$ \epsilon_{e\beta}^{dT} \times 10^{-3}$	8.6	7.6	6.8	8.8
$ \epsilon_{e\beta}^{uT} \times 10^{-3}$	8.6	8.1	7.5	9.8
$\mu_{e\beta} \times 10^{-12} \mu_B$	3.0	2.7	2.5	3.2
$ \epsilon_{\mu\beta}^{dT} \times 10^{-3}$	7.1	6.3	5.6	7.2
$ \epsilon_{\mu\beta}^{uT} \times 10^{-3}$	7.1	6.7	6.2	8.1
$\mu_{\mu\beta} \times 10^{-12} \mu_B$	2.5	2.3	2.1	2.7

Table 6.1: Sensitivity to tensor NSI parameters $\epsilon_{\alpha\beta}^{fT}$ at 90% C.L. for various potential detector materials of the COHERENT experiment. The sensitivity on transition NMM is also shown at 90% C.L.

lepton	quark $Q_q = -1/3$	quark $Q_q = 2/3$
$ \epsilon_{e\beta}^{eT} $	3.3	$ \epsilon_{e\beta}^{dT} $ 0.43
$ \epsilon_{e\beta}^{\mu T} $	2.8×10^{-2}	$ \epsilon_{e\beta}^{sT} $ 2.8×10^{-2}
$ \epsilon_{e\beta}^{\tau T} $	2.7×10^{-3}	$ \epsilon_{e\beta}^{bT} $ 1.4×10^{-3}
		$ \epsilon_{e\beta}^{cT} $ 1.7×10^{-3}
		$ \epsilon_{e\beta}^{tT} $ 9.8×10^{-3}

Table 6.2: Sensitivity to NSI parameters $\epsilon_{e\beta}^{fT}$, from Eq.(6.58) taking into consideration the results of the TEXONO experiment.

the differential cross sections $d\sigma/dT_N$ for the SM, tensor NSI and electromagnetic components.

From existing measurements of the TEXONO experiment and by employing Eqs.(6.58) and (6.59), we find the upper bounds on NMM, listed in Table 6.2. Even though some of the derived constraints are less stringent to those given in Table 6.1, it is possible to put limits on more parameters apart from the $\epsilon_{\alpha\beta}^{u(d)T}$.

Since the TEXONO experiment is not running up to now, precise knowledge on the fuel composition is presently not available. For this reason, we focus on the dominant ^{235}U component of the reactor neutrino distribution covering the energy range $E_{\bar{\nu}_e} < 2$ MeV, for which there are only theoretical estimations for the $\bar{\nu}_e$ -spectrum [182]. For energies above 2 MeV, we take the existing experimental data from Ref. [181]. In our analysis the normalised spectrum is fitted by the expression

$$\eta_{\bar{\nu}_e}^{\text{react}}(E_\nu) = a (E_\nu)^b \exp \left[c (E_\nu)^d \right], \quad (6.64)$$

(it resembles the Maxwell-Boltzmann distribution) with the fitted values of parameters: $\alpha = 11.36$, $b = 1.32$, $c = -3.33$ and $d = 0.56$ (see Fig. 6.6).

In Fig. 6.7, we present the estimated number of events expected to be measured at the TEXONO experiment, as a function of the nuclear energy threshold, originating from the various components of the vector NSI. As detector medium,

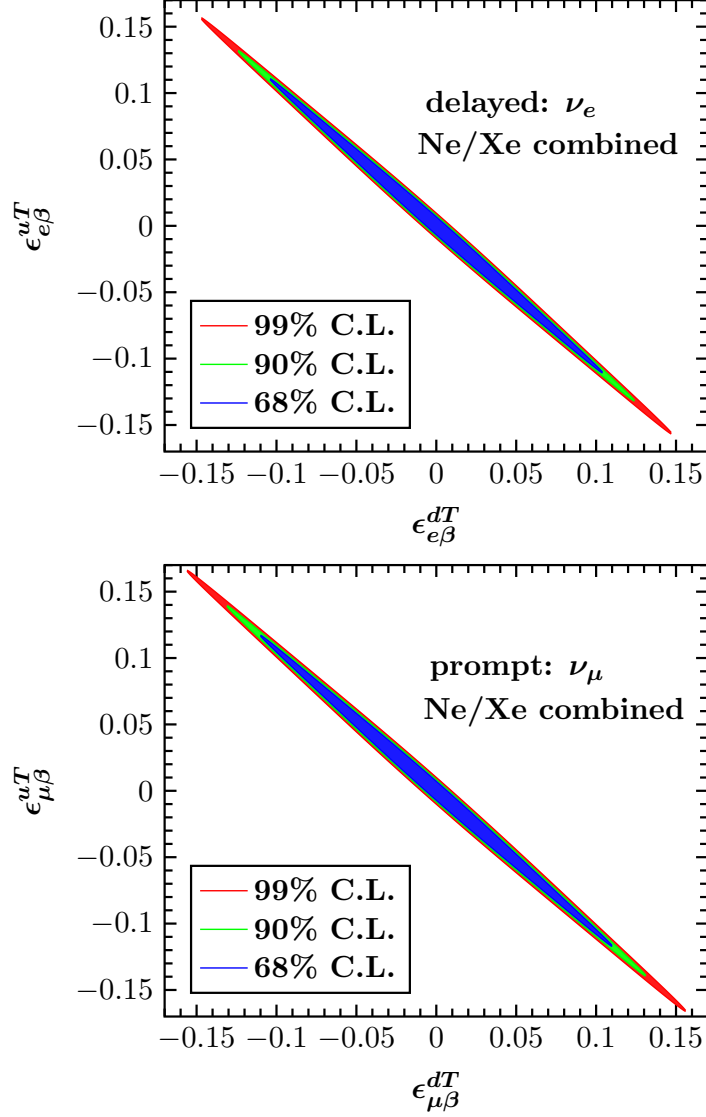


Figure 6.4: Allowed regions in the $\epsilon_{e\beta}^{dT}$ - $\epsilon_{e\beta}^{uT}$ (upper panel) and $\epsilon_{\mu\beta}^{dT}$ - $\epsilon_{\mu\beta}^{uT}$ (lower panel) tensor NSI parameter space. Only statistical errors are taken into consideration.

we consider either 1 kg of ^{76}Ge or 1 kg of ^{28}Si , operating with 100% efficiency for 1 year total exposure, located at 28 m from the reactor core (a typical flux of $\Phi^{\text{react}} = 10^{13} \nu s^{-1} \text{cm}^{-2}$ is assumed). Specifically, for the dominant SM reaction channel, assuming a minimum threshold of $T_N^{\text{thres}} = 400 \text{eV}$, we find a number of 4280 (2835) scattering events for ^{76}Ge (^{28}Si) which are in good agreement with previous results [183]. Similarly, in Fig. 6.8, we show the total number of counts over threshold due to tensor NSI and NMM, for the same detector composition, by employing the constraints of Table 6.1. Then, for a ^{76}Ge detector

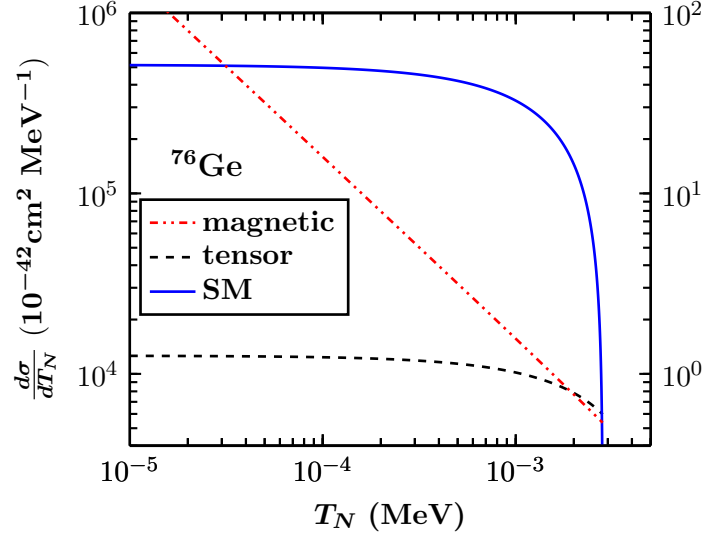


Figure 6.5: Differential cross sections $d\sigma/dT_N$ versus the nuclear recoil energy T_N , for the SM weak interaction, tensorial NSI and electromagnetic individual parts, assuming ingoing neutrinos with energy 10 MeV. The scale of the EM differential cross section is on the right axis. The utilised parameters for the tensor NSI and the NMM are taken from Table 6.1.

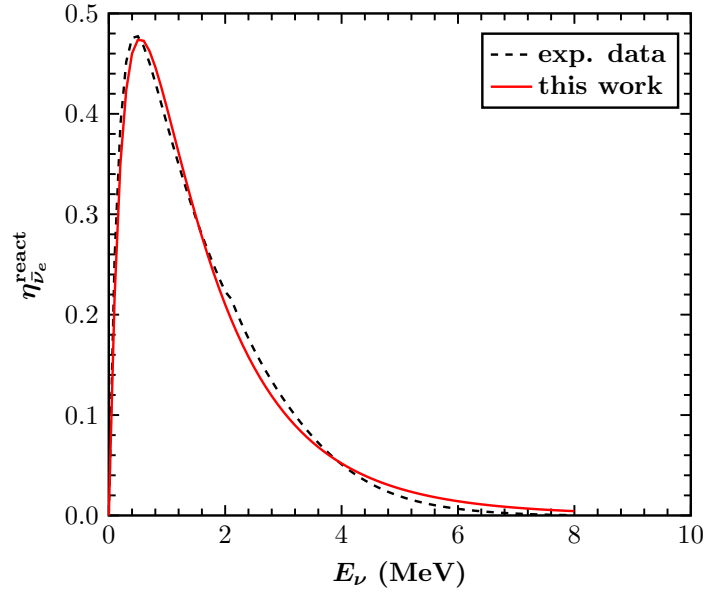


Figure 6.6: Experimental and fitted, reactor neutrino spectra, $\eta_{\nu_e}^{\text{react}}$, assuming the dominant ^{235}U component only (see the text).

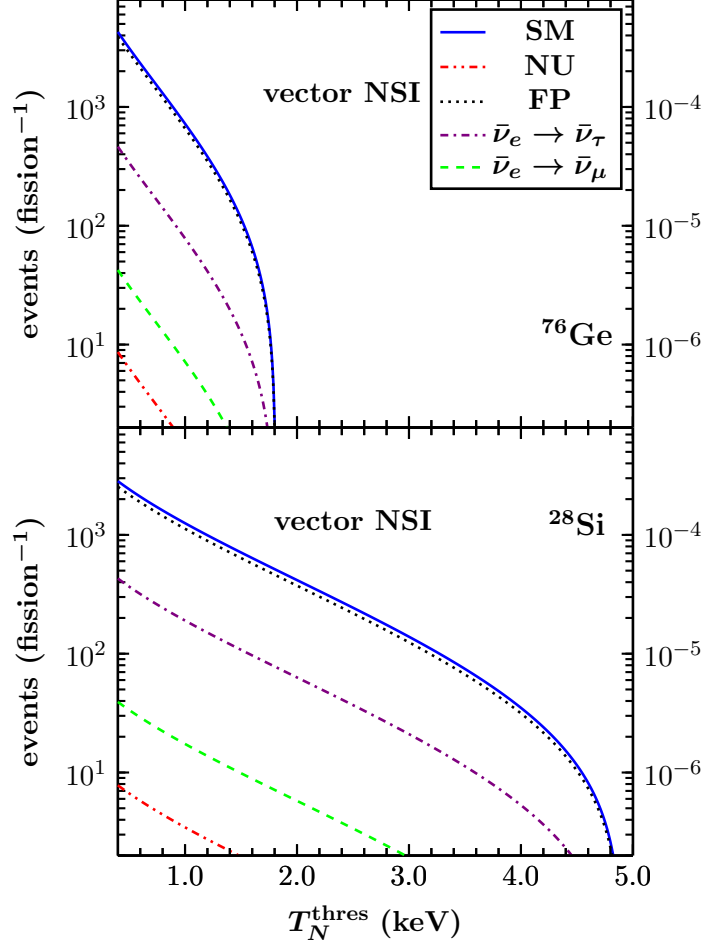


Figure 6.7: Number of events over nuclear recoil threshold due to vectorial NSI, for 1 kg of ^{76}Ge and 1 kg of ^{28}Si . The vectorial NSI parameters used, are taken from Refs. [25] and [22]. Notice, that the number of counts for the case of the $\nu_e \rightarrow \nu_\mu$ reaction channel is plotted with respect to the right axis.

and a $T_N^{\text{thres}} = 400 \text{ eV}$ threshold, our calculations indicate measurable rates, yielding 218 events for processes occurring due to tensor NSI. For interactions due to the presence of a NMM, we obtain < 1 events, in comparison to the 55 events expected by incorporating the current TEXONO limit.

6.5.3 Neutrino milli-charge

Before closing, we find it interesting to examine the impact of tensorial NSI on other electric properties of the neutrino, that are attributed to the neutrino mass [166]. Within this framework, milli-charged neutrinos [189, 190], appear with enhanced NMM by acquiring an additional contribution to that which is

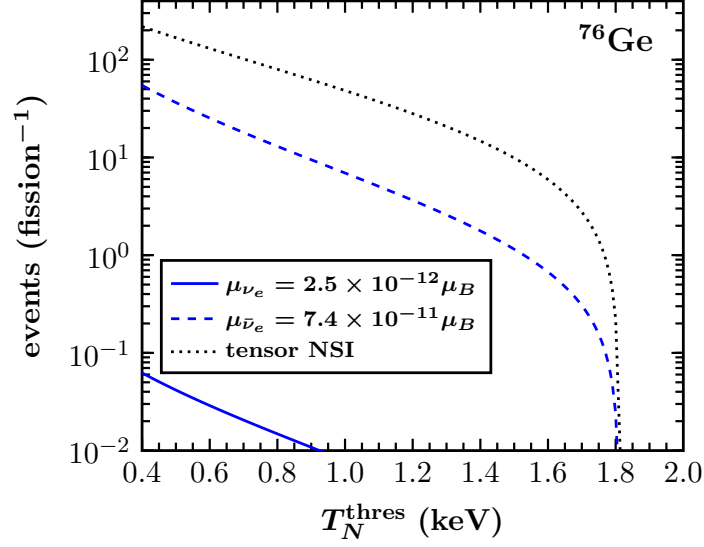


Figure 6.8: Number of events over nuclear recoil threshold due to tensor NSI and NMM for 1 kg of ^{76}Ge . Constraints for the tensor NSI and NMM parameters are taken from Table 6.1. For comparison, the number of counts due to the NMM using existing limits of the TEXONO experiment, is also illustrated.

generated via loop diagrams in theories beyond the SM [171, 173].

The differential cross section with respect to the nuclear recoil energy due to an effective neutrino milli-charge, \mathbf{q}_ν , is [187]

$$\left(\frac{d\sigma}{dT_e}\right)_{\mathbf{q}_\nu} \approx 2\pi a_{em} \frac{1}{m_e T_e^2} \mathbf{q}_\nu^2. \quad (6.65)$$

This has to be compared with the magnetic cross section contribution [167]

$$\left(\frac{d\sigma}{dT_e}\right)_{\mu_\nu} \approx \pi a_{em}^2 \frac{1}{m_e^2 T_e} \left(\frac{\mu_\nu}{\mu_B}\right)^2. \quad (6.66)$$

In Ref. [174], it has been suggested that in order to obtain a limit on the neutrino charge \mathbf{q}_ν , the ratio $R = \left(\frac{d\sigma}{dT_e}\right)_{\mathbf{q}_\nu} / \left(\frac{d\sigma}{dT_e}\right)_{\mu_\nu}$ should become smaller than unity, i.e. $R < 1$. Such constraints could be reached irrespectively of whether any deviation from the SM cross section of the $\nu - e^-$ process were observed or not [188]. After writing the upper limit on the neutrino milli-charge in the form

$$|\mathbf{q}_\nu| \lesssim 3 \times 10^{-2} \left(\frac{T_e}{1\text{keV}}\right)^{1/2} \left(\frac{\mu_\nu}{\mu_B}\right) e_0, \quad (6.67)$$

and employing the sensitivity on the NMM for the case of ^{76}Ge (see Table 6.1), for a typical threshold of the order $T_e = 400$ eV we obtain

$$|\mathbf{q}_\nu| \lesssim 4.7 \times 10^{-14} e_0. \quad (6.68)$$

The latter, is by one order of magnitude better than that of previous studies (see Ref. [174]).

6.6 Conclusions

In this Chapter, through the use of realistic nuclear structure calculations, we address various exotic channels of the neutral-current neutrino-nucleus scattering processes. More specifically, we have concentrated on sizeable contributions due to the presence of tensor NSI terms of relevant beyond the SM Lagrangians. Within this framework, possible neutrino EM phenomena, that are naturally generated from the tensor operators, such as neutrino transition magnetic moments and neutrino milli-charges, are investigated.

Using our reliable cross sections for SM and NSI neutrino processes, we have computed the number of neutrino scattering events expected to be measured at the Spallation Neutron Source experiments. To this purpose, we have chosen as target nuclei the ^{20}Ne , ^{40}Ar , ^{76}Ge and ^{132}Xe isotopes, that constitute the main detector materials of the planned COHERENT experiment. Through a χ^2 -type analysis, we have estimated the sensitivity of the latter experiment on the tensor NSI parameters. We remark that, especially for the case of the $\epsilon_{\mu\beta}^{qT}$ ($q = u, d$) couplings, such bounds are presented here for the first time. Moreover, by exploiting these potential constraints, the resulted sensitivities on the transition neutrino magnetic moments lead to contributions which are of the same order of magnitude with existing limits coming from astrophysical observations. Furthermore, due to their large size, they are accessible by current experimental setups and, therefore, they may be testable with future experiments searching for coherent neutrino-nucleus scattering. We have also devoted special effort in obtaining precise predictions for the number of neutrino-nucleus events expected to be recorded by the promising TEXONO and GEMMA reactor- $\bar{\nu}_e$ experiments.

Chapter 7

Sensitivities to electromagnetic neutrino parameters

7.1 Introduction

In the present Chapter, Majorana neutrino electromagnetic properties are studied through neutral-current coherent elastic neutrino-nucleus scattering (CENNS). We focus on the potential of the recently planned COHERENT experiment at the Spallation Neutron Source to probe muon-neutrino magnetic moments. The resulting sensitivities are determined on the basis of a χ^2 analysis employing realistic nuclear structure calculations performed in the context of the QRPA. We find that they can improve existing limits by about half an order of magnitude. In addition, we show that these experimental facilities allow for Standard Model precision tests in the low energy regime, with a competitive determination of the weak mixing angle. Finally, they also offer the capability to probe other electromagnetic neutrino properties, such as the neutrino charge-radius. We illustrate our results for various choices of the experimental setup and the target material.

The possibility of measuring neutral-current CENNS at the TEXONO experiment has opened high expectations towards probing exotic neutrino properties. Focusing on low threshold Germanium-based targets with kg-scale mass, we find a remarkable efficiency not only for detecting CENNS events due to the weak interaction, but also for probing novel electromagnetic neutrino interactions. Specifically, we demonstrate that such experiments are complementary in performing precision Standard Model tests as well as in shedding light on sub-leading effects due to neutrino magnetic moment and neutrino charge-radius. This work, apart from realistic nuclear structure calculations takes into consideration the crucial quenching effect corrections. Such a treatment, in conjunction with a simple statistical analysis, shows that the attainable sensitivities are improved by one order of magnitude as compared to those of previous studies.

7.2 The role of effective neutrino electromagnetic parameters

The robust confirmation of the existence of neutrino masses and mixing [67, 68], thanks to the milestone discovery of neutrino oscillations in propagation from solar, atmospheric, accelerator and reactor neutrino sources has opened a window to probe new physics beyond the Standard Model (SM) (for the relevant experimental references see e.g. [191, 192]). While the ultimate origin of neutrino mass remains a mystery [5], oscillation results have motivated a plethora of SM extensions to generate small neutrino masses [193]. A generic feature of such models is the existence of non-trivial neutrino EM properties [157, 164, 165, 167, 174, 194]. Although the three-neutrino oscillation paradigm seems to be in rather solid grounds [103, 104], non-trivial neutrino electromagnetic properties may still play an important sub-leading role in precision neutrino studies [195].

The lowest-order contribution of neutrino EM interactions involves neutrino magnetic moments (NMM) [167, 196, 197], as well as the neutrino charge-radius [163, 198, 199] arising from loop-level radiative corrections [159, 161]. Note that a direct neutrino magnetic moment measurement could provide a key insight in the understanding of the electroweak interactions, and the Majorana nature of neutrinos [168, 200]. Indeed, in contrast to the case of Majorana neutrinos, only massive Dirac neutrinos can have non-vanishing diagonal magnetic moments [157, 164, 174, 194]. In the general Majorana case, only off-diagonal transition magnetic moments exist, they form an anti-symmetric matrix, calculable from first principles, given the underlying gauge theory.

Within the minimally extended SM model with Dirac neutrino masses, one expects tiny NMM, of the order of $\mu_\nu \leq 10^{-19} \mu_B \left(\frac{m_\nu}{\text{eV}}\right)$, expressed in Bohr magnetons μ_B [162, 166]. However, appreciably larger Majorana neutrino transition magnetic moments are expected in many theoretical models, such as those involved with left-right symmetry [201], scalar leptoquarks [176], R-parity-violating supersymmetry [177], and large extra dimensions [202]. Currently, the most stringent upper limits, $\mu_\nu \leq \text{few} \times 10^{-12} \mu_B$, come from astrophysics [185, 196, 197, 203]. In addition, there are bounds from measurements by various terrestrial neutrino scattering experiments. The present status of such constraints is summarised in Table 7.1 where one can see that the direct constraints on μ_{ν_μ} and μ_{ν_e} are still rather poor. It should be mentioned, however, that currently operating reactor neutrino experiments such as TEXONO and GEMMA have set robust constraints on $\mu_{\bar{\nu}_e}$.

The possibility of probing neutrino EM parameters, such as the NMM and the neutrino charge-radius, through coherent elastic neutrino-nucleus scattering (CENNS) [61, 63] can be explored on the basis of a sensitivity χ^2 -type analysis [21, 70, 111, 131, 132, 206, 207]. To this end here we perform realistic nuclear structure calculations [55, 123] in order to compute accurately the relevant cross sections

Experiment	reaction	observable	constraint ($10^{-10}\mu_B$)
LSND [204]	$\nu_\mu e^- \rightarrow \nu_\mu e^-$	μ_{ν_μ}	6.8
LAMPF [205]	$\nu_e e^- \rightarrow \nu_e e^-$	μ_{ν_e}	10.8
TEXONO [183]	$\bar{\nu}_e e^- \rightarrow \bar{\nu}_e e^-$	$\mu_{\bar{\nu}_e}$	0.74
GEMMA [184]	$\bar{\nu}_e e^- \rightarrow \bar{\nu}_e e^-$	$\mu_{\bar{\nu}_e}$	0.29

Table 7.1: Summary of the current 90% C.L. constraints on neutrino magnetic moments from various experiments.

[25, 26, 120]. The required proton and neutron nuclear form factors are reliably obtained within the context of the QRPA method by considering realistic strong nuclear forces [40, 84, 85, 135, 137]. Concentrating on ongoing and planned neutrino experiments, we have devoted special effort in estimating the expected number of CENNS events with high significance. Specifically, our study is focused on the proposed detector materials of the COHERENT experiment [73–75] at the Spallation Neutron Source (SNS) [69]. Even though a CENNS event has never been experimentally measured, we however remark that the highly intense neutrino beams [86, 87] provided at the SNS indicate very encouraging prospects towards the detection of this reaction for the first time [78, 79], by using low energy detectors [208]. Furthermore, neutrinos from stopped pion-muon beams [71, 72] at the SNS [76, 117, 209] or elsewhere [77] have motivated many studies searching for physics beyond the SM model too [26, 27, 116, 132].

In the present Chapter we quantify the prospects, not only of detecting CENNS events at the SNS, but also of performing precision electroweak measurements and probing neutrino properties beyond the SM. We conclude that the extracted sensitivities on the effective NMM improve with respect to previous results of studies of this type. We obtain for the first time robust upper limits on μ_{ν_μ} . Moreover, we obtain a sensitivity for the neutrino charge-radius, which is competitive with those of previous studies. Furthermore, we explore the sensitivity of these experiments for Standard Model precision measurements of the weak mixing angle in the energy regime of few MeV.

The detection of neutral-current CENNS processes by measuring the nuclear recoil spectrum of the scattered nucleus has by now become feasible [70]. As a concrete example, the newly formed COHERENT Collaboration at the SNS has excellent prospects [73–75], motivating also theoretical effort [26, 170]. In this work, we consider the possibility of revealing signs of new physics through a detailed study of CENNS at the TEXONO experiment [19, 183, 209]. We demonstrate that the use of sub-keV Germanium-based kg-scale detectors [190, 210, 211], provides a favourable experimental set up with good prospects for performing precision SM tests, as well as probing EM neutrino properties [166], such as the neutrino magnetic moment [168, 196, 197, 200] and the neutrino charge-radius [159, 161, 163, 198, 199]. In addition, this work highlights that

the present calculations become more realistic by considering quenching effect corrections [97, 212, 213]. The sensitivity is evaluated by assuming that a given experiment searching for CENNS events will measure exactly the SM expectation. Thus, any deviation [21, 111, 131] is understood as a signature of new physics [24, 25, 132, 206, 207].

Apart from the possibility of the first ever detection of CENNS events, our present results emphasise the potentiality of discovering neutrino interactions beyond the SM expectations [214]. In our estimates we perform nuclear structure calculations within the context of the QRPA that uses realistic nuclear forces [40, 55, 85, 123, 135, 148], and employ a χ^2 -type statistical analysis. We find that the prospects for improving current bounds on μ_{ν_e} are rather promising and complementary to future sensitivities on the muon neutrino magnetic moment, μ_{ν_μ} [170].

7.2.1 Standard model prediction

Within the context of SM, for low energies ($E_\nu \ll M_W$) accessible to neutrino experiments, the weak neutral-current CENNS can be naturally studied by considering the $V \pm A$ interaction of four-fermion $\nu\nu ff$ type operators. The scattering amplitude \mathcal{M}_{SM} can be compactly written as

$$\mathcal{M}_{\text{SM}} = \frac{G_F}{\sqrt{2}} j_\mu \left(g_V \mathcal{J}^\mu - g_A \mathcal{J}_{(5)}^\mu \right), \quad (7.1)$$

where the neutrino weak current is given as usual by

$$j_\mu = \bar{\nu}(k_f) \gamma_\mu (1 - \gamma_5) \nu(k_i), \quad (7.2)$$

and the hadronic (axial) vector current, $\mathcal{J}_{(5)}^\mu$, has been computed in Chapt. 4. The vector and axial vector couplings for protons and neutrons (g_V and g_A) are defined in Eq.(4.70), while for the quark couplings we have

$$\begin{aligned} g_{\alpha\alpha}^{u,L} &= \rho_{\nu N}^{NC} \left(\frac{1}{2} - \frac{2}{3} \hat{\kappa}_{\nu N} \hat{s}_Z^2 \right) + \lambda^{u,L}, \\ g_{\alpha\alpha}^{d,L} &= \rho_{\nu N}^{NC} \left(-\frac{1}{2} + \frac{1}{3} \hat{\kappa}_{\nu N} \hat{s}_Z^2 \right) + \lambda^{d,L}, \\ g_{\alpha\alpha}^{u,R} &= \rho_{\nu N}^{NC} \left(-\frac{2}{3} \hat{\kappa}_{\nu N} \hat{s}_Z^2 \right) + \lambda^{u,R}, \\ g_{\alpha\alpha}^{d,R} &= \rho_{\nu N}^{NC} \left(\frac{1}{3} \hat{\kappa}_{\nu N} \hat{s}_Z^2 \right) + \lambda^{d,R}. \end{aligned} \quad (7.3)$$

In the latter expressions, after including the relevant radiative corrections, we have $\hat{s}_Z^2 = \sin^2 \theta_W = 0.23120$, $\rho_{\nu N}^{NC} = 1.0086$, $\hat{\kappa}_{\nu N} = 0.9978$, $\lambda^{u,L} = -0.0031$,

$\lambda^{d,L} = -0.0025$ and $\lambda^{d,R} = 2\lambda^{u,R} = 7.5 \times 10^{-5}$ [195]. From the scattering amplitude in Eq.(7.1), the differential cross section with respect to the nuclear recoil energy, T_N , for the case of a CENNS off a spherical spin-zero nucleus of mass M , reads

$$\left(\frac{d\sigma}{dT_N}\right)_{\text{SM}} = \frac{G_F^2 M}{2\pi} \left[1 - \frac{MT_N}{E_\nu^2} + \left(1 - \frac{T_N}{E_\nu}\right)^2\right] \left|\langle g.s. || \hat{\mathcal{M}}_{00}(Q) || g.s. \rangle\right|^2. \quad (7.4)$$

Note, that additional corrections are incorporated in Eq.(7.4) compared to Eq.(4.68).

For $g.s. \rightarrow g.s.$ transitions, the corresponding coherent nuclear matrix element takes the form [25, 26]

$$\begin{aligned} \langle g.s. || \hat{\mathcal{M}}_{00}(Q) || g.s. \rangle &= [2(g_{\alpha\alpha}^{u,L} + g_{\alpha\alpha}^{u,R}) + (g_{\alpha\alpha}^{d,L} + g_{\alpha\alpha}^{d,R})] ZF_Z(Q^2) \\ &+ [(g_{\alpha\alpha}^{u,L} + g_{\alpha\alpha}^{u,R}) + 2(g_{\alpha\alpha}^{d,L} + g_{\alpha\alpha}^{d,R})] NF_N(Q^2). \end{aligned} \quad (7.5)$$

The latter Coulomb matrix element, is therefore the radiatively corrected version of Eq.(4.69) given in Chapt. 4. Note that, due to the smallness of the coupling of protons with the Z -boson, the main contribution to the CENNS cross section essentially scales with the square of the neutron number N of the target nucleus (see e.g. [25]). We stress that the differential cross section is evaluated with high significance by weighting the nuclear matrix element with corrections provided by the proton (neutron) nuclear form factors $F_{Z(N)}(Q^2)$. This way the finite nuclear size is taken into account with respect to the typical momentum transfer, $Q \simeq \sqrt{2MT_N}$. Furthermore, the N^2 enhancement of the CENNS cross section makes the relevant experiments favourable facilities to probe the neutron form factor of the target nucleus at low energies [70, 73–75].

From a nuclear theory point of view, the reliability of the present CENNS cross sections calculations is maximised in terms of accuracy by performing nuclear structure calculations in the context of QRPA [123, 135]. Motivated by its successful application on similar calculations for various semi-leptonic nuclear processes [40, 85, 148], in this work we construct explicitly the nuclear ground state, $|g.s.\rangle \equiv |0^+\rangle$, of the relevant even-even isotope through the solution of the BCS equations (for a detailed description see Ref. [26]).

7.2.2 Electromagnetic neutrino-nucleus cross sections

The existence of neutrino masses is well-established thanks to the current neutrino oscillation data, implying that they could have exotic properties, such as non-zero neutrino magnetic moments. The non-zero EM moments of a neutrino generate additional contributions to the SM weak neutrino-nucleus scattering process which can be described from the EM amplitude

$$\mathcal{M}_{\text{EM}} = \frac{4\pi a_{em}}{q^2} j_\mu^{(\nu)} \mathcal{J}^\mu, \quad (7.6)$$

where $j_\mu^{(\nu)}$ is the effective EM current given in Eq.(6.5). In this framework, potential neutrino-nucleus interactions of EM nature have been considered [157, 164, 165, 167, 174, 194], resulting in corrections to the weak CENNS cross section of the form [166]

$$\left(\frac{d\sigma}{dT_N}\right)_{\text{tot}} = \left(\frac{d\sigma}{dT_N}\right)_{\text{SM}} + \left(\frac{d\sigma}{dT_N}\right)_{\text{EM}}. \quad (7.7)$$

Here, the helicity-violating EM contribution to the neutrino-nucleus cross section can be parametrised in terms of the proton nuclear form factor, the fine structure constant a_{em} and the electron mass m_e as [27]

$$\left(\frac{d\sigma}{dT_N}\right)_{\text{EM}} = \frac{\pi a_{em}^2 \mu_{eff}^2 Z^2}{m_e^2} \left(\frac{1 - T_N/E_\nu}{T_N} + \frac{T_N}{4E_\nu^2}\right) F_Z^2(Q^2). \quad (7.8)$$

We stress, however (as for the SM differential cross section) the electromagnetic cross section given in Eq.(7.8) more advanced in comparison with Eq.(6.60). The details regarding the interpretation of the parameter, μ_{eff} , describing the effective neutrino magnetic moment are given in Subsect. 6.2.1.

If the neutrino is of Dirac-type as in the SM, then the magnetic moment is undetectably small due to its proportionality to the neutrino mass. Even though from oscillation data the latter is well-known to be small, one cannot rule out the possibility of sizeable neutrino magnetic moments. Indeed, in general scenarios where neutrinos are Majorana fermions, as expected on general grounds, larger transition magnetic moments are possible. For example, relatively sizeable contributions may be predicted in models involving NSI [27]. From the experimental physics perspective, a potential signal will be detected as a distortion of the nuclear recoil spectrum at very low energies where the EM cross section dominates due to its $\sim 1/T_N$ dependence. For this reason, such challenging technological constraints require innovative experimental advances towards reducing the threshold to the sub-keV region.

Apart from the neutrino magnetic moment, the neutrino charge-radius is another interesting electromagnetic property to be considered. Despite having vanishing electric charge, the first derivative in the expansion of the neutrino electric form factor entering the decomposition of the leptonic matrix element (see Subsect. 6.1.2) may provide non-trivial information concerning other neutrino electric properties [174]. The corresponding matrix element takes the current-current form

$$\mathcal{M}^{(\langle r_\nu^2 \rangle + \mathbf{a}_\nu)} = 4\pi a_{em} \left[\bar{\nu} \gamma_\mu \left(\frac{1}{6} \langle r_\nu^2 \rangle + \mathbf{a}_\nu \gamma_5 \right) \nu \right] \mathcal{J}^\mu, \quad (7.9)$$

evidenced by the $1/q^2$ photon propagator being cancelled by the q^2 factor in the associated neutrino current and the identities

$$\bar{\nu}_L \gamma_\mu \nu_L = -\bar{\nu}_L \gamma_\mu \gamma_5 \nu_L, \quad \bar{\nu}_R \sigma_{\mu\nu} \nu_L = -\bar{\nu}_R \sigma_{\mu\nu} \gamma_5 \nu_L. \quad (7.10)$$

Therefore, it is deduced that the neutrino charge-radius, $\langle r_\nu^2 \rangle$, and the neutrino anapole moment, \mathbf{a}_ν , cannot be distinguished in ultrarelativistic neutrino scattering and should effectively appear as one moment, i.e. the effective neutrino charge radius squared, defined as

$$\langle r_\nu^2 \rangle^{(eff)} = \langle r_\nu^2 \rangle - 6\mathbf{a}_\nu. \quad (7.11)$$

From now on, we will always denote $\langle r_\nu^2 \rangle^{(eff)} = \langle r_\nu^2 \rangle$. We remind that, the gauge invariant definition of the neutrino effective charge-radius $\langle r_{\nu_\alpha}^2 \rangle$, $\alpha = \{e, \mu, \tau\}$, was proposed long ago [159, 161], as a physical observable related to the vector and axial vector form factors involving the EM interaction of a Dirac neutrino [165, 166]. In this framework, at the one-loop approximation a correction of few percent to the weak mixing angle has been obtained [163, 198, 199]

$$\sin^2 \theta_W \rightarrow \sin^2 \overline{\theta}_W + \frac{\sqrt{2}\pi a_{em}}{3G_F} \langle r_{\nu_\alpha}^2 \rangle. \quad (7.12)$$

7.3 Neutrinos from the spallation sources

There are several experimental proposals that plan to detect for the first time a CENNS [76, 77, 117, 209] signal. In this Section, we describe the ongoing COHERENT experiment [73–75], proposed to operate at the Spallation Neutron Source (SNS) at Oak Ridge National Lab [69]. This facility provides excellent prospects for measuring CENNS events for the first time. In general, any potential deviation from the SM expectations can be directly interpreted as signature of new physics and, thus, has prompted many theoretical studies searching for physics within [78, 79] and beyond the SM [26, 70, 111, 116, 132].

Currently, the SNS constitutes the leading facility for neutron physics searches, producing neutrons by firing a pulsed proton beam at a liquid mercury target [117]. In addition to neutrons, the mercury target generates pions, which decay producing neutrino beams as a free by-product. These beams are exceptionally intense, of the order of $\Phi = 2.5 \times 10^7 \nu \text{ s}^{-1} \text{ cm}^{-2}$ ($\Phi = 6.3 \times 10^6 \nu \text{ s}^{-1} \text{ cm}^{-2}$) per flavour at 20 m (40 m) from the spallation target [86]. The corresponding spectra are given in Eq.(4.76).

In this work we will distinguish two cases, the optimistic and the realistic ones. The first case is convenient for exploring the nuclear responses of different nuclear detector isotopes, in order to get a first idea of the relevant neutrino parameters within and beyond the SM. The second case is useful in quantifying the sensitivities attainable with various individual technologies of each experimental setup. In our calculations, we assume a time window of 1 year for the optimistic and 2.4×10^7 s for the realistic case [76]. Detailed information on the different detector setups considered here is summarised in Table 7.2. For a comprehensive description of the relevant nuclear isotopes including the experimental criteria and advantages of adopting each of them, the reader is referred to Refs. [26, 70].

		COHERENT experiment			
		^{20}Ne [73]	^{40}Ar [73]	^{76}Ge [116]	^{132}Xe [73, 208]
realistic	mass	391 kg	456 kg	100 kg	100 kg
	distance	46 m	46 m	20 m	40 m
	efficiency	50%	50%	67%	50%
	recoil window	30-160 keV	20-120 keV	10-78 keV	8-46 keV
optimistic	mass	1 ton	1 ton	1 ton	1 ton
	distance	20 m	20 m	20 m	20 m
	efficiency	100%	100%	100%	100%
	recoil window	1keV – T_{max}	1keV – T_{max}	1keV – T_{max}	1keV – T_{max}

Table 7.2: Summary of the detector concepts assumed in this work. We consider four possible nuclei as targets and two possible experimental setups for each nucleus, a realistic one, for different detector masses, distances, recoil energy windows, and efficiencies, and the optimistic case where all the variables are allowed to have their “best” value.

7.3.1 Numerical results

Assuming negligible neutrino oscillation effects in short-distance propagation, for each interaction channel, $x = \text{SM, EM, tot}$, the total number of counts above a certain threshold, T_N^{thres} , is given through the expression

$$N_x^{\text{events}} = K \int_{E_{\nu\text{min}}}^{E_{\nu\text{max}}} \eta^{\text{SNS}}(E_{\nu}) dE_{\nu} \int_{T_N^{\text{thres}}}^{T_{N\text{max}}} \left(\frac{d\sigma}{dT_N}(E_{\nu}, T_N) \right)_x dT_N, \quad (7.13)$$

where $K = N_{\text{targ}} t_{\text{tot}} \Phi$, with N_{targ} the total number of atomic targets in the detector, t_{tot} the time window of data taking, and Φ the total neutrino flux. In the present calculations, the various experimental concepts are taken into account by fixing the corresponding input parameters as discussed previously.

7.3.2 Standard Model precision tests at SNS

We first examine the sensitivity of the COHERENT experiment to the weak mixing angle $\sin^2 \theta_W$ of the SM in the low energy regime of the SNS operation. In order to quantify this sensitivity, assuming that the experimental proposal will measure exactly the SM prediction, we perform a statistical analysis based on a χ^2 with statistical errors only

$$\chi^2 = \left(\frac{N_{SM}^{\text{events}} - N_{\text{SNS}}^{\text{events}}(\sin^2 \theta_W)}{\delta N_{SM}^{\text{events}}} \right)^2, \quad (7.14)$$

where the number of SM events, N_{SM}^{events} , depends on the Coulomb nuclear matrix element entering the coherent rate. As central value for the SM weak mixing angle prediction we adopt the PDG value $\hat{s}_Z^2 = 0.23120$. We then compute the

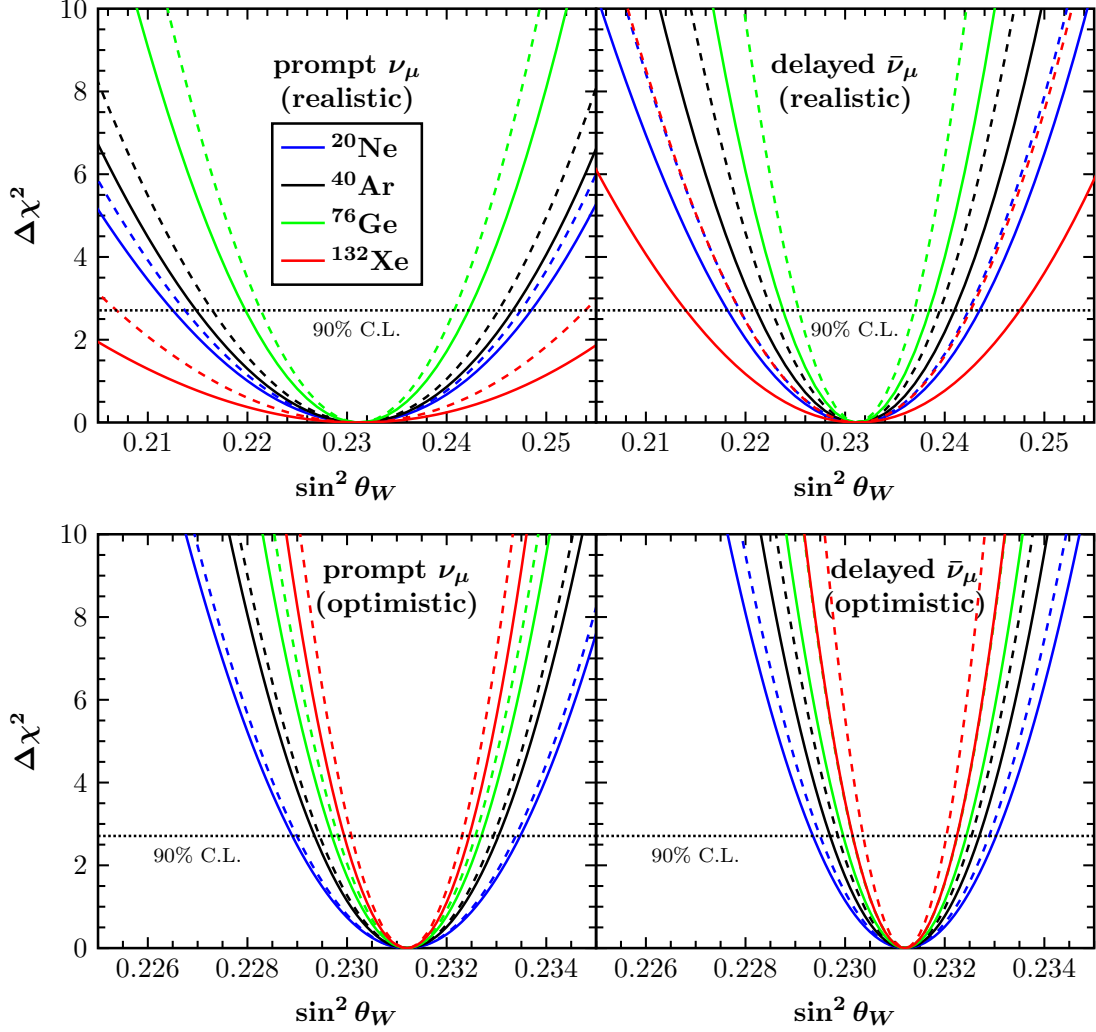


Figure 7.1: $\Delta\chi^2$ profiles in terms of the weak mixing angle $\sin^2\theta_W$ showing the sensitivity of the COHERENT experiment to SM precision tests. The PDG value $\hat{s}_Z^2 = 0.23120$, is used as the central value. Left (right) panels illustrate the results obtained by considering the prompt (delayed) flux, while upper (lower) panels account for the realistic (optimistic) case. Here, the solid (dashed) lines refer to the nuclear BCS method (zero momentum transfer).

χ^2 function depending on the expected number of events for a given value of the mixing angle, $N_{\text{SNS}}^{\text{events}}(\sin^2\theta_W)$. The corresponding results for the various detector materials of the COHERENT experiment are shown in Fig. 7.1. In Table 7.3, we illustrate the band, $\delta\sin^2\theta_W \equiv \delta s_W^2$, at 1σ error, evaluated as $\delta s_W^2 = (s_{Wmax}^2 - s_{Wmin}^2)/2$ and the corresponding the uncertainty $\delta s_W^2/\hat{s}_Z^2$, with s_{Wmax}^2 and s_{Wmin}^2 being the upper and lower bounds respectively. At the optimistic level, our results indicate that better sensitivities are expected for heavier target nuclei,

Nucleus	$\delta s_W^2(\nu_\mu)$	Uncer. (%)	$\delta s_W^2(\bar{\nu}_\mu)$	Uncer. (%)	$\delta s_W^2(\nu_e)$	Uncer. (%)
^{20}Ne	0.0110 [0.0014]	4.74 [0.61]	0.0077 [0.0011]	3.33 [0.48]	0.0091 [0.0013]	3.94 [0.56]
^{40}Ar	0.0097 [0.0011]	4.17 [0.48]	0.0061 [0.0009]	2.64 [0.39]	0.0074 [0.0010]	3.20 [0.43]
^{76}Ge	0.0068 [0.0009]	2.94 [0.39]	0.0045 [0.0008]	1.92 [0.35]	0.0055 [0.0009]	2.36 [0.37]
^{132}Xe	0.0181 [0.0008]	7.83 [0.35]	0.0102 [0.0006]	4.39 [0.26]	0.0127 [0.0007]	5.47 [0.30]

Table 7.3: Expected sensitivities to the weak mixing angle $\sin^2 \theta_W(\nu_\alpha) \equiv s_W^2(\nu_\alpha)$, assuming the various channels ($\nu_\mu, \bar{\nu}_\mu, \nu_e$) of the SNS beam for a set of possible detectors at the COHERENT experiment. For the realistic [optimistic] case, the band $\delta s_W^2(\nu_\alpha)$ and the corresponding uncertainty are evaluated within 1σ error.

Nucleus	^{20}Ne	^{40}Ar	^{76}Ge	^{132}Xe
$\delta s_W^2(\nu_\mu)$	0.0052 [0.0007]	0.0042 [0.0006]	0.0031 [0.0005]	0.0073 [0.0004]
Uncer. (%)	2.23 [0.30]	1.82 [0.26]	1.34 [0.22]	3.14 [0.17]

Table 7.4: Expected sensitivities to the weak mixing angle $\sin^2 \theta_W(\nu_\mu) \equiv s_W^2(\nu_\mu)$, through a combined analysis of the prompt and delayed beams ($\nu_\mu + \bar{\nu}_\mu$). Same conventions as in Table 7.3 are used.

such as ^{132}Xe . This is understood as a direct consequence of the significantly larger number of expected events provided by heavier nuclear isotopes [26]. However, once we consider the realistic case, the expectations change drastically so that, for the case of a ^{76}Ge detector we find a better sensitivity, due to a closer location to the SNS source (20 m in comparison with the 40 m for the ^{132}Xe case) and a higher efficiency in recoil acceptance (see Table 7.2). Furthermore, in Fig. 7.2 and Table 7.4, we show that the expected sensitivities improve through a combined measurement of the prompt and delayed beams ($\nu_\mu + \bar{\nu}_\mu$).

7.3.3 EM neutrino interactions at SNS

One of the main goals of our present work, is to examine the sensitivity of the COHERENT experiment to the possible detection of CENNS events due to neutrino EM effects, associated to various effective transition neutrino magnetic moment parameters (NMM) such as $\mu_{\nu_\mu}, \mu_{\bar{\nu}_\mu}$ and μ_{ν_e} . The total number of events expected in an experiment searching for CENNS depends strongly on the nuclear

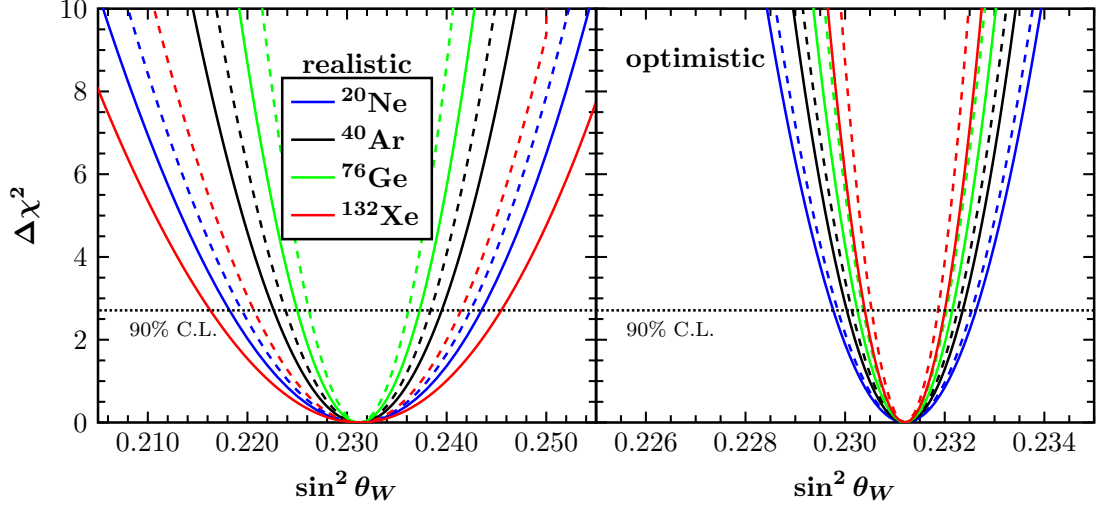


Figure 7.2: $\Delta\chi^2$ profiles in terms of the weak mixing angle $\sin^2\theta_W$ from the combined measurement of the prompt and delayed beams ($\nu_\mu + \bar{\nu}_\mu$). Same conventions as in Fig. 7.1 are used.

energy threshold T_N^{thres} , as well as the total mass of the detector [26, 170]. For low energy thresholds and more massive detectors, the total number of events expected is significantly larger and, therefore, the attainable sensitivities are higher. We remind that, for a possible NMM detection, a very low energy threshold is required, since the EM cross section dominates at low energies.

The sensitivity is evaluated by assuming that a given experiment searching for CENNS events, will measure exactly the SM expectation, thus any deviation is understood as a signature of new physics. Following [200] we define the χ^2 function as

$$\chi^2 = \left(\frac{N_{SM}^{\text{events}} - N_{\text{tot}}^{\text{events}}(\mu_{\nu_\alpha})}{\delta N_{SM}^{\text{events}}} \right)^2. \quad (7.15)$$

By employing the aforementioned method, we find that the COHERENT experiment could provide useful complementary limits on μ_{ν_μ} . On the other hand, the sensitivity to μ_{ν_e} , is not expected to be as good as that of reactor experiments [27, 183, 184] (see Subsect. 7.4.2). However, a combined analysis of the prompt and delayed muon neutrino beams ($\nu_\mu + \bar{\nu}_\mu$), could help to further improve the sensitivity to a neutrino magnetic moment. The same applies to the combination of different detectors using the same neutrino source. For different nuclear targets, the present results are shown in Figs. 7.3 and 7.4 and the sensitivities on neutrino magnetic moments at 90% C.L. are summarised in Table 7.5.

The sensitivity to neutrino magnetic moments has been also computed for the case of a combined measurement with different target nuclei. In this framework, we take advantage of the multi-target strategy of the COHERENT exper-

Nucleus	^{20}Ne	^{40}Ar	^{76}Ge	^{132}Xe
μ_{ν_μ}	9.09 [2.31]	9.30 [2.47]	8.37 [2.54]	12.94 [2.54]
$\mu_{\bar{\nu}_\mu}$	10.28 [2.53]	10.46 [2.69]	9.39 [2.75]	14.96 [2.74]
μ_{ν_e}	10.22 [2.44]	10.55 [2.60]	9.46 [2.68]	15.20 [2.68]
$\mu_{\nu_\mu}^{\text{comb}}$	8.07 [2.02]	8.24 [2.16]	7.41 [2.22]	11.58 [2.21]

Table 7.5: Upper limits on the neutrino magnetic moment (in units of $10^{-10}\mu_B$) at 90% C.L. expected at the COHERENT experiment for the realistic [optimistic] case. The results indicated with $(^{\text{comb}})$ are obtained from a combined measurement of the prompt and delayed beams.

iment [73–75] and define the χ^2 as

$$\chi^2 = \sum_{\text{nuclei}} \left(\frac{N_{SM}^{\text{events}} - N_{\text{tot}}^{\text{events}}(\mu_{\nu_\alpha})}{\delta N_{SM}^{\text{events}}} \right)^2. \quad (7.16)$$

Assuming two nuclear targets at a time and taking into consideration the experimental technologies discussed previously, we have found that among all possible combinations the most stringent sensitivity corresponds to a combined measurement of $^{20}\text{Ne}+^{76}\text{Ge}$, that for the realistic (optimistic) case reads

$$\mu_{\nu_\mu} = 6.48 (1.77) \times 10^{-10} \mu_B \quad 90\% \text{ C.L.} \quad (7.17)$$

The above sensitivity is better than the case with only one detector. Notice also that the optimistic sensitivity shown here gives an idea to the potential constraint that could be achieved by improving the experimental setup. Moreover, a combined measurement of all possible target nuclei would lead to somewhat better expected sensitivities, i.e.,

$$\mu_{\nu_\mu} = 5.87 (1.52) \times 10^{-10} \mu_B \quad 90\% \text{ C.L.} \quad (7.18)$$

Eventually, we explore the possibility to vary more than one parameter at the same time. To this aim, a χ^2 analysis is performed, but in this case the fitted parameters were simultaneously varied. Within this context, the contours of the $(\sin^2 \theta_W - \mu_\nu)$ parameter space at 90% C.L. are illustrated in Fig. 7.5. Figure 7.6 and Fig. 7.7 are similar to left and right panels of Fig. 7.5 respectively, but they present additional information for the 68% and 99% C.L. sensitivities. Finally, in Fig. 7.8 the allowed regions of the parameter space in the $(\mu_{\bar{\nu}_\mu} - \mu_{\nu_e})$ plane are shown, where the corresponding results have been evaluated at 90% C.L.

7.3.4 Sensitivity to the neutrino charge-radius

Through CENNS, we estimate for the first time the sensitivity of a low energy SNS experiment to constrain the neutrino charge-radius. The obtained bounds,

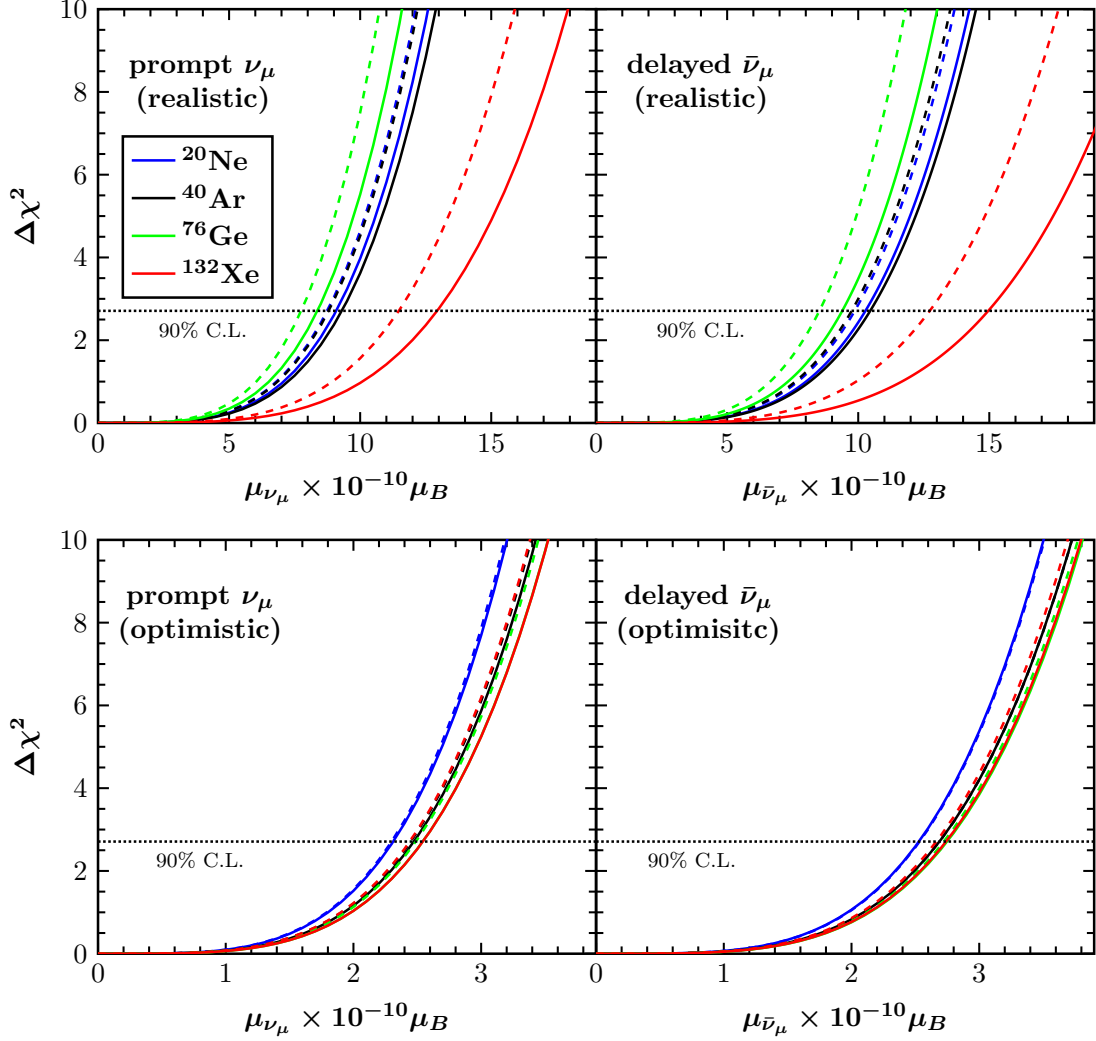


Figure 7.3: $\Delta\chi^2$ profiles for a neutrino magnetic moment, μ_{ν_μ} in units of $10^{-10}\mu_B$, of the COHERENT experiment, assuming various nuclear detectors. Same conventions as in Fig. 7.1 are used.

are derived in the context of a χ^2 analysis in the same spirit of the discussion made above and they are presented in Figs. 7.9 and 7.10 and listed in Table 7.6. As expected, the results behave similarly to the case of the weak mixing angle, thus we conclude that for the realistic (optimistic) case a 100 kg ^{76}Ge (heavy ^{132}Xe) detector at 20 m is required to constrain more significantly the neutrino charge-radius. Furthermore, through a combined measurement of the prompt and delayed beams ($\nu_\mu + \bar{\nu}_\mu$) an appreciably improved sensitivity can be reached for $\langle r_{\nu_\mu}^2 \rangle$ in comparison to $\langle r_{\nu_e}^2 \rangle$. These sensitivities are better than current ones (see Ref. [174] and references therein) and depending on the detector setup may improve by one order of magnitude.

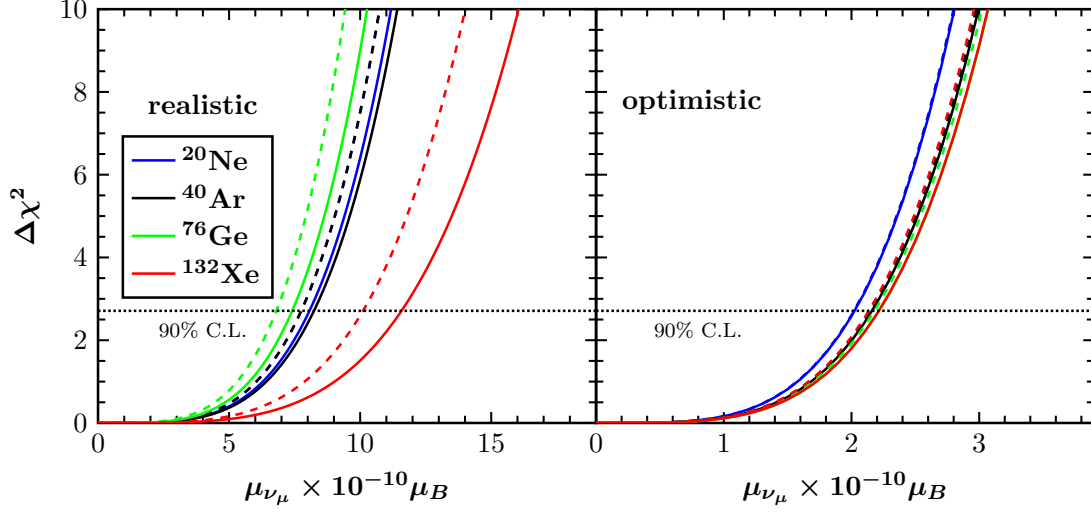


Figure 7.4: $\Delta\chi^2$ profiles for a neutrino magnetic moment, $\mu_{\nu\mu}$, in units of $10^{-10}\mu_B$, from the combined measurement of the prompt and delayed beams ($\nu_\mu + \bar{\nu}_\mu$). Same conventions as in Fig. 7.1 are used.

7.4 Neutrinos from reactors

We now turn our attention towards exploring how well one can probe neutrino EM phenomena with the TEXONO experiment [19, 183, 209] through low-energy CENNS measurements near the Kuo-Sheng Nuclear Power Station. Towards this purpose, the TEXONO Collaboration has pursued a research program aiming at detecting neutrino-nucleus events by using high purity Germanium-based detectors HPGe with sub-keV threshold [190, 210, 211]. According to the proposal, we consider a 1 kg ^{76}Ge -detector operating with a threshold as low as $T_{thres} = 100 \text{ eV}_{ee}$. Due to the absence of precise information regarding the fuel composition of the reactor core, we only include the dominant ^{235}U component of the antineutrino spectrum. In this respect, for the present study we assume a typical neutrino flux of $\Phi_{\bar{\nu}_e} = 10^{13} \nu \text{ s}^{-1} \text{ cm}^{-2}$ for a detector location at 28 m from the reactor core. In order to estimate the reactor antineutrino energy-distribution $\eta_{\bar{\nu}_e}(E_\nu)$ for energies above 2 MeV, existing experimental data from Ref. [215] are employed. We stress that the main part of reactor antineutrinos is released with energies $E_{\bar{\nu}_e} < 2 \text{ MeV}$, thus their contribution is crucial and must be taken into account. For their description we adopt the theoretical estimates given in Ref. [182]. This will bring about improved sensitivities on the neutrino magnetic moment.

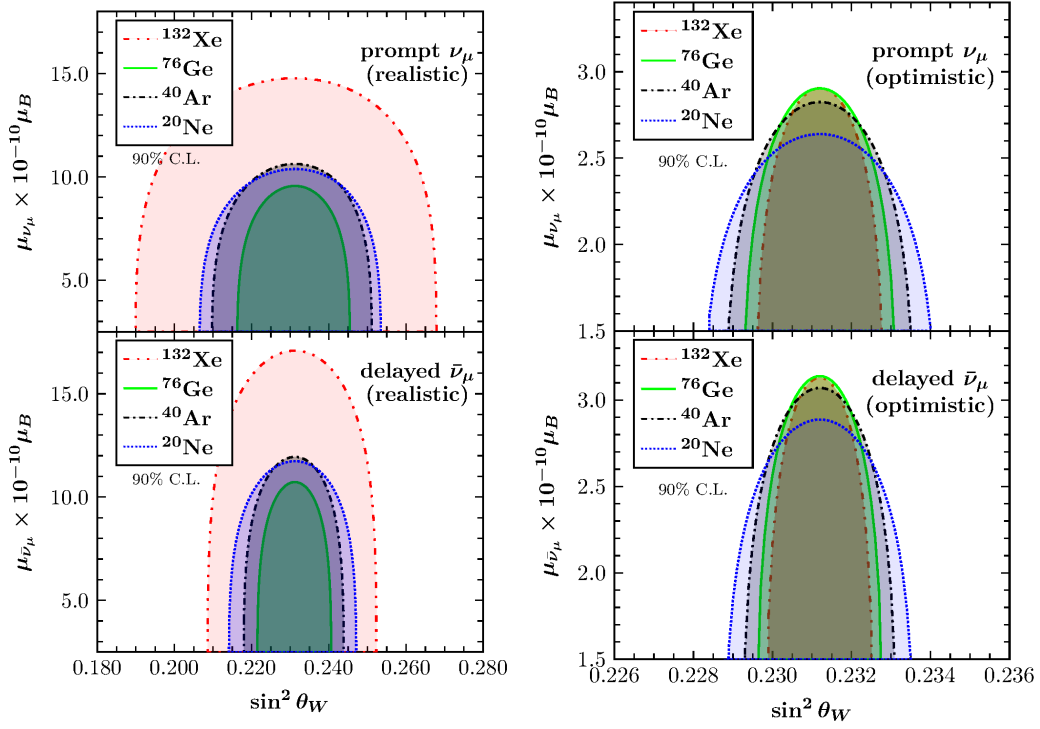


Figure 7.5: The $\mu_{\nu_\mu}(\mu_{\bar{\nu}_\mu})$ - $\sin^2 \theta_W$ contours obtained from a two parameter χ^2 analysis. Allowed regions are shown for 90% C.L. Left (right) panels account for the realistic (optimistic) case, while the upper (lower) panels refer to the prompt (delayed) flux.

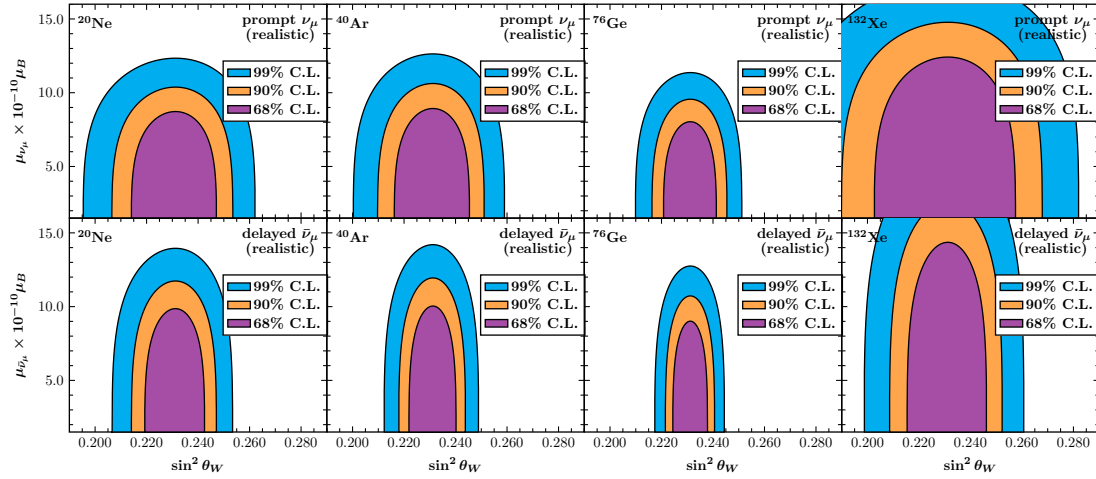


Figure 7.6: Same as left panel of Fig. 7.5. In addition to 90%, allowed regions to 68% and 99% C.L. are also presented.

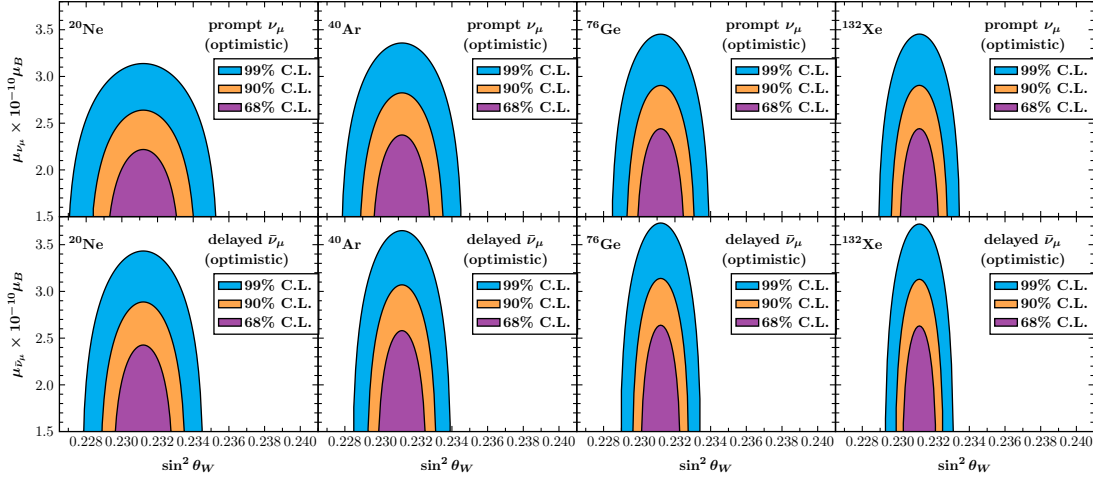


Figure 7.7: Same as right panel of Fig. 7.5. In addition to 90%, allowed regions to 68% and 99% C.L. are also presented.

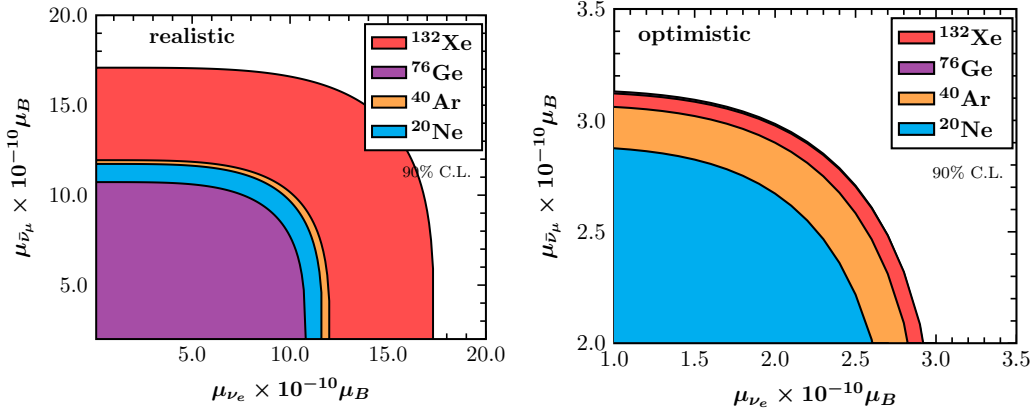


Figure 7.8: The $\mu_{\bar{\nu}_\mu} - \mu_{\nu_e}$ contours obtained from a two parameter χ^2 analysis. Allowed regions are shown for 90% C.L. Left (right) panel accounts for the realistic (optimistic) case.

7.4.1 Signal cross sections

At first, we present and discuss the individual weak and electromagnetic differential and total CENNS cross sections [see Eq.(7.7)] weighted over experimental reactor antineutrino spectra [182, 215]. These convoluted cross sections determine the neutrino signals expected to be recorded at a nuclear detector (e.g. the ^{76}Ge of the TEXONO experiment). For each interaction channel x , [$x = \text{SM}, \text{EM}, \text{tot}$] the energy-integrated differential cross section, $\langle d\sigma/dT \rangle_x$, is defined as

$$\left\langle \frac{d\sigma}{dT_N} \right\rangle_x = \int dE_\nu \left(\frac{d\sigma}{dT_N}(E_\nu, T_N) \right)_x \eta_{\bar{\nu}_e}(E_\nu), \quad (7.19)$$

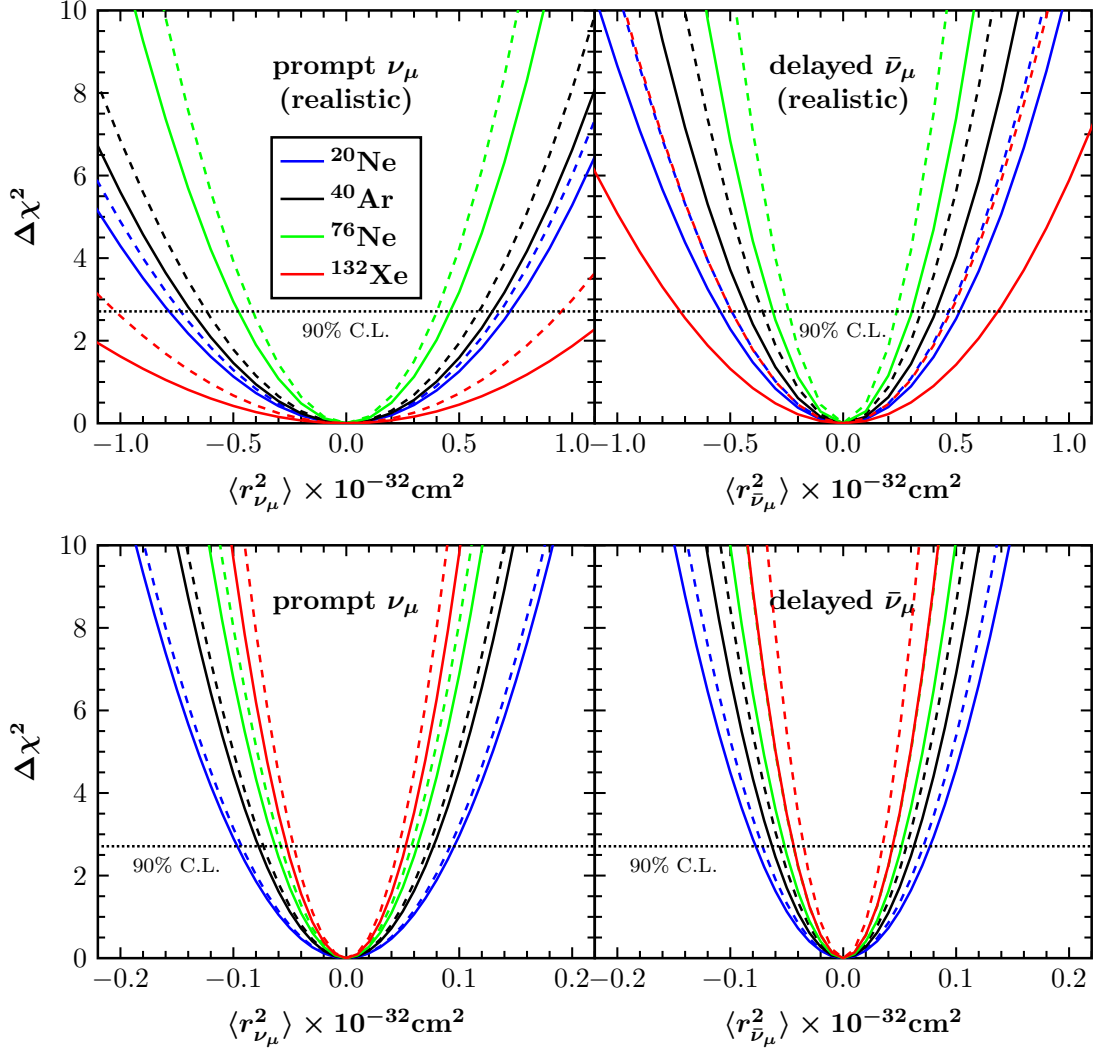


Figure 7.9: $\Delta\chi^2$ profiles for a neutrino charge-radius, $\langle r_{\nu\mu}^2 \rangle$ in units of 10^{-32}cm^2 , of the COHERENT experiment, assuming various nuclear detectors. Same conventions as in Fig. 7.1 are used.

where $\eta_{\bar{\nu}_e}(E_\nu)$ denotes the normalised neutrino energy-distribution. The corresponding signal cross section σ_x^{sign} reads

$$\sigma_x^{\text{sign}}(E_\nu) = \int dT_N \left(\frac{d\sigma}{dT_N}(E_\nu, T_N) \right)_x \eta_{\bar{\nu}_e}(E_\nu). \quad (7.20)$$

For the ^{76}Ge detector, assuming the experimental constraints placed recently by TEXONO ($\mu_{\bar{\nu}_e} = 7.4 \times 10^{-11} \mu_B$ [183] and $\langle r_{\bar{\nu}_e}^2 \rangle = 6.6 \times 10^{-32}\text{cm}^2$ [19]), the computed results are illustrated in Fig. 7.11. One sees that in the case of σ^{sign} , the curve involving neutrino magnetic moment contribution exceeds that of the pure SM weak rate at low neutrino energies, E_ν . The curve containing neutrino

Nucleus	^{20}Ne	^{40}Ar	^{76}Ge	^{132}Xe
$\langle r_{\bar{\nu}_\mu}^2 \rangle$	-0.55 – 0.52 [-0.08 – 0.08]	-0.43 – 0.41 [-0.06 – 0.06]	-0.31 – 0.30 [-0.05 – 0.05]	-0.72 – 0.69 [-0.04 – 0.04]
$\langle r_{\nu_\mu}^2 \rangle$	-0.79 – 0.73 [-0.10 – 0.10]	-0.69 – 0.65 [-0.08 – 0.08]	-0.48 – 0.46 [-0.06 – 0.06]	-1.31 – 1.20 [-0.05 – 0.05]
$\langle r_{\nu_e}^2 \rangle$	-0.65 – 0.61 [-0.09 – 0.09]	-0.53 – 0.50 [-0.07 – 0.07]	-0.38 – 0.37 [-0.06 – 0.06]	-0.90 – 0.85 [-0.05 – 0.05]
$\langle r_{\nu_\mu}^2 \rangle^{\text{comb}}$	-0.44 – 0.42 [-0.06 – 0.06]	-0.36 – 0.35 [-0.05 – 0.05]	-0.26 – 0.26 [-0.04 – 0.04]	-0.63 – 0.60 [-0.03 – 0.03]

Table 7.6: Expected sensitivities on the neutrino charge-radius (in units of 10^{-32}cm^2) from the analysis of the COHERENT experiment. The limits are presented at 90% C.L. for the realistic [optimistic] case. The results indicated with $(^{\text{comb}})$ are obtained from a combined measurement of the prompt and delayed beams.

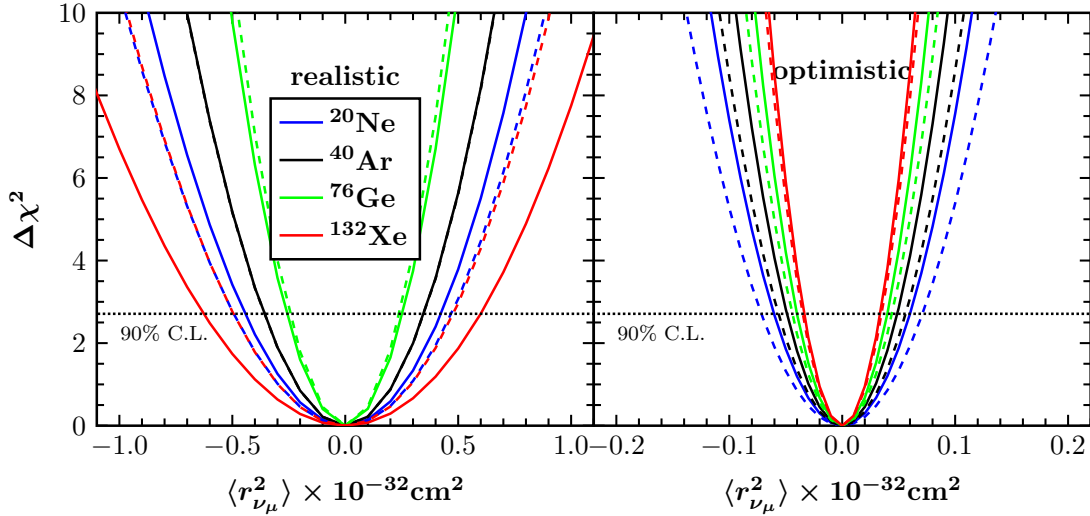


Figure 7.10: $\Delta\chi^2$ profiles for the neutrino charge-radius, $\langle r_{\nu_\mu}^2 \rangle$ in units of 10^{-32}cm^2 , from the combined measurement of the prompt and delayed beams ($\nu_\mu + \bar{\nu}_\mu$). Same conventions as in Fig. 7.1 are used.

charge-radius contributions through Eq.(7.12) is showing a similar behaviour as the pure SM (the photon propagator cancellation leads to four-fermion contact interaction [190, 214]).

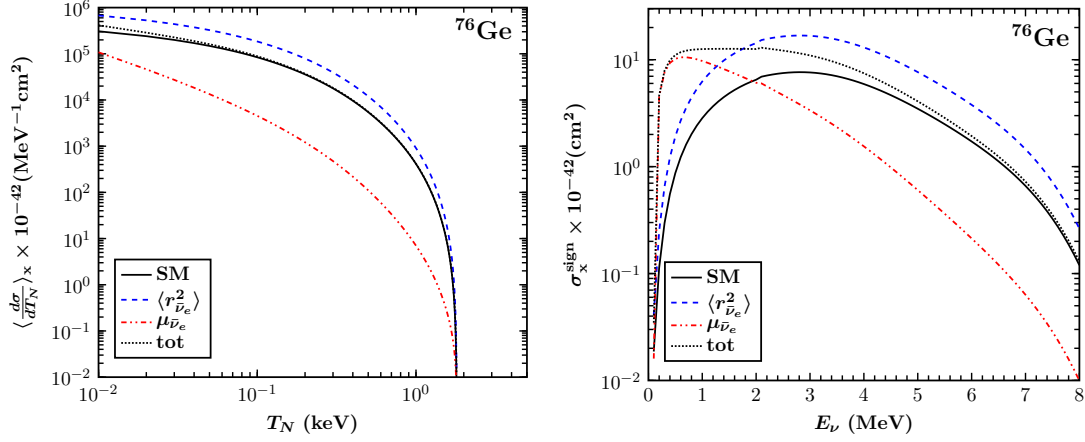


Figure 7.11: Weak and electromagnetic differential (*left panel*) and total (*right panel*) cross sections convoluted with reactor $\bar{\nu}_e$ -spectra.

(Target, Threshold)	COHERENT (100 kg ^{76}Ge , 10 keV $_{ee}$)		TEXONO (1 kg ^{76}Ge , 100 eV $_{ee}$)				
	67%	100%	100%	50%	50%	50%	
Efficiency	67%						
Quenching	$\mathcal{Q}_f = 1$	$\mathcal{Q}_f = 1$	$\mathcal{Q}_f = 0.20$	$\mathcal{Q}_f = 0.25$	$\mathcal{Q}_f = 1$	$\mathcal{Q}_f = 0.20$	$\mathcal{Q}_f = 0.25$
$\delta s_W^2(\bar{\nu}_e)$	0.0055	0.0010	0.0033	0.0025	0.0014	0.0046	0.0035
Uncer. (100%)	2.36	0.43	1.41	1.08	0.61	1.97	1.51
$\mu_{\bar{\nu}_e} \times 10^{-10} \mu_B$	9.46	0.40	0.98	0.83	0.47	1.17	0.99
$\langle r_{\bar{\nu}_e}^2 \rangle \times 10^{-32} \text{cm}^2$	-0.38 - 0.37	-0.07 - 0.07	-0.22 - 0.22	-0.17 - 0.17	-0.10 - 0.10	-0.32 - 0.31	-0.24 - 0.24

Table 7.7: Summary of the sensitivities obtained for $\sin^2 \theta_W$ (1σ) and for the EM neutrino parameters (90% C.L.) at the TEXONO experiment. The results refer to various sensitivities and quenching factors. Comparing with Ref. [170] one sees that a substantial improvement in the sensitivity for the weak mixing angle $\sin^2 \theta_W$, the magnetic moment $\mu_{\bar{\nu}_e}$ parameter and the neutrino charge-radius $\langle r_{\bar{\nu}_e}^2 \rangle$ w.r.t. the COHERENT proposal.

7.4.2 Statistical analysis

Our present analysis is strongly based on the estimation of the number of CENNS events. Therefore, we first provide a brief description of the conventions and approximations we use in our calculations. For each interaction channel x , the number of CENNS events above a minimum nuclear recoil energy, $T_{N_{\min}}$, reads [111]

$$N_x = K \int_{E_{\nu_{\min}}}^{E_{\nu_{\max}}} \eta_{\bar{\nu}_e}(E_{\nu}) dE_{\nu} \int_{T_{N_{\min}}}^{T_{N_{\max}}} \left(\frac{d\sigma}{dT_N}(E_{\nu}, T_N) \right)_x dT_N. \quad (7.21)$$

In the above expression, $K = N_{\text{targ}} t_{\text{tot}} \Phi_{\bar{\nu}_e}$, with N_{targ} being the total number of atoms in the detector and t_{tot} the relevant irradiation period. Note that potential effects due to neutrino oscillation in propagation are neglected, since this is well satisfied for the short-baselines considered here. The numerical results throughout

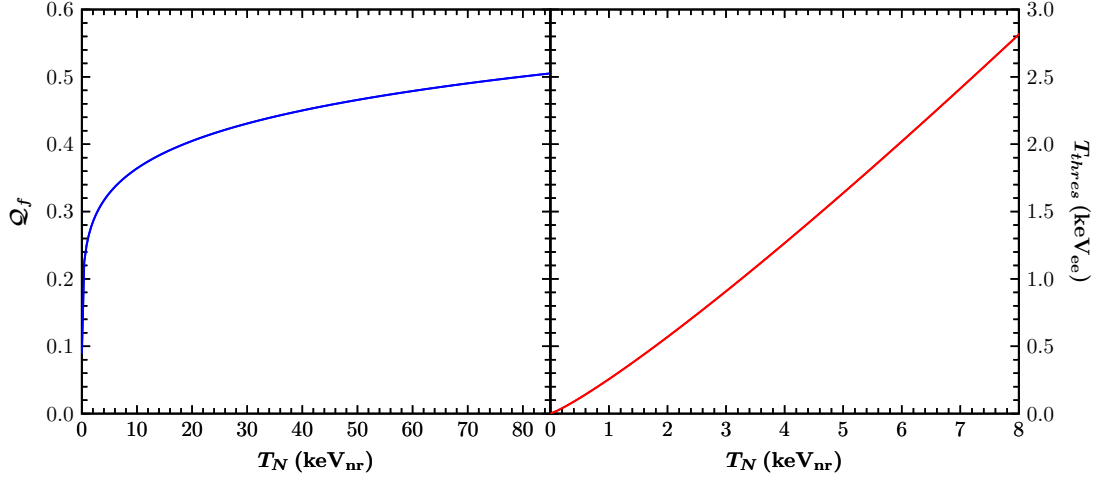


Figure 7.12: (*Left panel*): The quenching factor, Q_f , as a function of the nuclear recoil energy, T_N , for ^{76}Ge and (*Right panel*): the equivalent electron energy as a function of the nuclear recoil energy, T_N .

this work refer to a 1 kg ^{76}Ge -detector, one year of data taking and a detector threshold of 100 eV_{ee}. In addition, we consider two different detector efficiencies including an optimistic approach of a perfectly efficient detection capability and the more realistic scenario assuming a recoil acceptance of 50%.

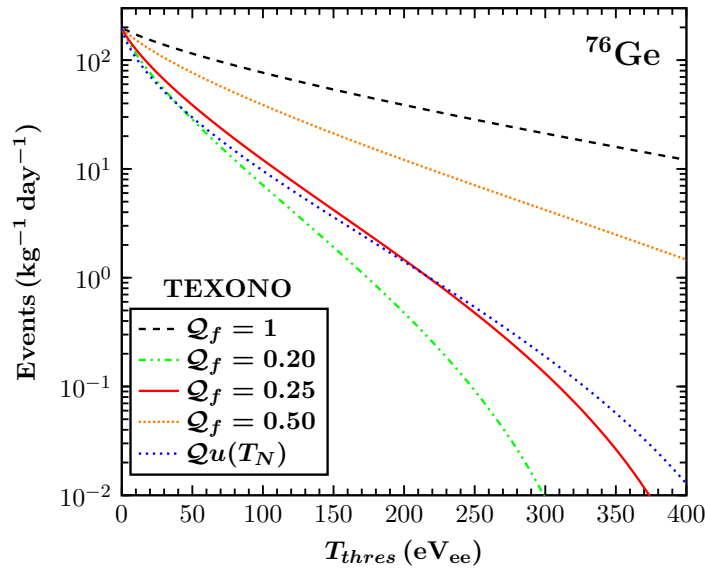


Figure 7.13: CENNS events as a function of the detector threshold assuming different quenching factors and a 1kg-day ^{76}Ge target. A notable agreement is verified between the results obtained for the case of constant $Q_f = 0.25$ and the empirical quenching factor of Eq.(7.22).

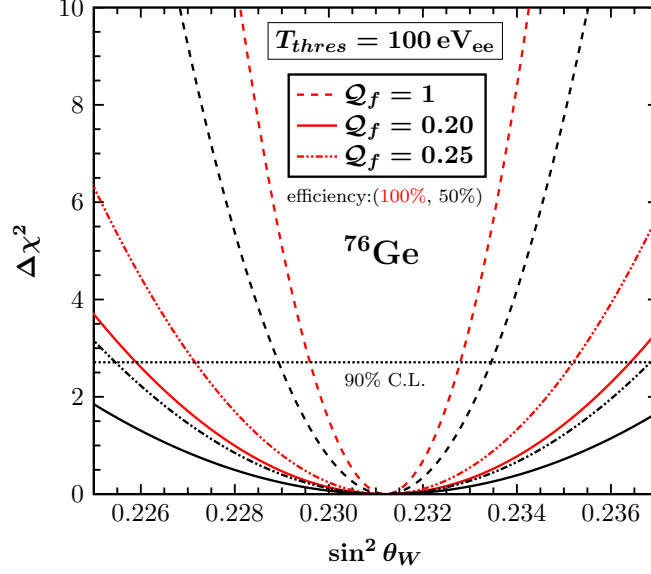


Figure 7.14: $\Delta\chi^2$ sensitivity profiles as a function of the weak mixing angle θ_W at TEXONO. The results are presented for two detector efficiencies 100% (50%) shown with red (black) colour and three values of the quenching factors $\mathcal{Q}_f = (1, 0.20, 0.25)$ indicated with (dashed, solid, dashdotted) lines.

The present calculations take into consideration the fact that the nuclear recoil events are quenched [212] (in Ref. [170], where for each target the calculation is referred to the nuclear recoil energy window [73, 75], such a treatment is not necessary). Corrections of this type are crucial since for a given ionisation detector the observed energy (equivalent to an electron energy) is lower than the total nuclear recoil energy, i.e. much energy is converted to heat (phonons) which is not measured, especially at low energies [97]. To convert from nuclear recoil energy (eV_{nr}) to electron equivalent energy (eV_{ee}), we multiply the energy scale by a quenching factor, \mathcal{Q}_f (see right panel of Fig. 7.12. In principle \mathcal{Q}_f varies with the nuclear recoil energy [213] and has to be determined experimentally. Usually, for its estimation the following empirical form is considered [212]

$$\mathcal{Q}_f(T_N) = r_1 \left[\frac{T_N}{1\text{keV}} \right]^{r_2}, \quad r_1 \simeq 0.256, \quad r_2 \simeq 0.153 \quad (7.22)$$

(see left panel of Fig. 7.12). We note, however, that for the sub-keV Germanium-based targets considered here it can be well-approximated as constant with typical values in the range 0.20-0.25 [210]. Thus, the TEXONO threshold $T_{\text{thres}} = 100 \text{ eV}_{\text{ee}}$ corresponds to nuclear recoil energy $T_{N_{\text{min}}} = 500 \text{ eV}_{\text{nr}}$ for $\mathcal{Q}_f = 0.20$ and $T_{N_{\text{min}}} = 400 \text{ eV}_{\text{nr}}$ for $\mathcal{Q}_f = 0.25$, correspondingly the maximum nuclear recoil energy $T_{N_{\text{max}}} = 1.81 \text{ keV}_{\text{nr}}$, is restricted to a maximum observable energy of 362 and 452 eV_{ee} . Figure 7.13, presents a graphical illustration of the

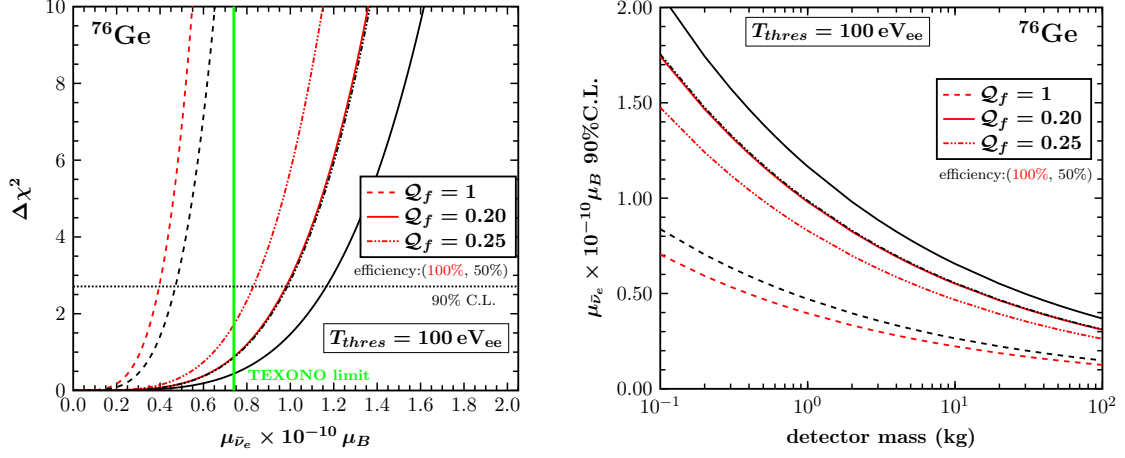


Figure 7.15: (*Left panel*) $\Delta\chi^2$ profiles in terms of the neutrino magnetic moment parameter $\mu_{\bar{\nu}_e}$ in units of $10^{-10}\mu_B$ at TEXONO. (*Right panel*) Sensitivity to $\mu_{\bar{\nu}_e}$ at 90% C.L. as a function of the detector mass. Same conventions as in Fig. 7.14 are used.

variation of the expected CENNS event rates at different threshold and quenching factor.

The sensitivity of the TEXONO experiment to the SM weak mixing angle $\sin^2\theta_W$ is quantitatively determined on the basis of a χ^2 -type analysis relying on statistical errors only [170]

$$\chi^2 = \left(\frac{N_{SM} - N_{SM}(\sin^2\theta_W)}{\delta N_{SM}} \right)^2. \quad (7.23)$$

In our calculational procedure we have assumed that the TEXONO experiment will detect the precise number of SM events, N_{SM} , by fixing the electroweak mixing parameter to the PDG value i.e. $\hat{s}_Z^2 = 0.23120$ [195]. We estimate the expected events $N_{SM} = (27962, 2586, 4415)$ assuming $\mathcal{Q}_f = (1, 0.20, 0.25)$ and a detection threshold 100 eV_{ee} , in good agreement with Ref. [211]. The χ^2 function is then minimised with respect to $\sin^2\theta_W$, by varying this parameter around its central value, taken as the value reported by the PDG.

We have explicitly verified that there are good prospects for making precision tests of the SM by using low-energy ^{76}Ge detectors. Our results for the TEXONO sensitivity to the weak mixing angle are presented in Fig. 7.14. Furthermore, we have also evaluated the 1σ error band on $\sin^2\theta_W$ defined as $\delta\sin^2\theta_W \equiv \delta s_W^2 = (s_{Wmax}^2 - s_{Wmin}^2)/2$ as well as the corresponding uncertainty $\delta s_W^2/\hat{s}_Z^2$, with s_{Wmax}^2 (s_{Wmin}^2) being the respective upper (lower) bound. The resulting sensitivities are shown in Table 7.7. Specifically, neglecting the quenching corrections ($\mathcal{Q}_f = 1$), the improvement upon previous results [170] is up to 82% (74% when realistic efficiencies are taken into account). Furthermore, the effect for $\mathcal{Q}_f = 0.20$ (0.25)

leads to reduction of $\delta \sin^2 \theta_W$ sensitivity by a factor of 3.3 (2.5) for both detection efficiencies.

Prompted by the upcoming generation of low-threshold nuclear detectors, we have made an effort to identify possible deviations from the SM neutrino-quark interaction cross section originated by non-standard neutrino EM properties. In particular, analysing their sensitivity to electromagnetic CENNS events we have found that important deviations may be induced by the presence of a non-zero transition neutrino magnetic moment $\mu_{eff} \equiv \mu_{\bar{\nu}_e}$. In order to determine this sensitivity we use a χ^2 function of the form [200]

$$\chi^2 = \left(\frac{N_{\text{SM}} - N_{\text{tot}}(\mu_{\bar{\nu}_e})}{\delta N_{\text{SM}}} \right)^2. \quad (7.24)$$

In Eq.(7.24), we substitute the SM cross section by the one given in Eq.(7.7) in order to account for possible events, N_{tot} , originating from the corrections associated to the non-trivial structure of the neutrino EM current, as discussed previously. The corresponding results obtained by varying the effective transition neutrino magnetic moment, $\mu_{\bar{\nu}_e}$, are presented in Fig. 7.15 (left panel). The experimental TEXONO limit from $\bar{\nu}_e - e$ scattering, $\mu_{\bar{\nu}_e} = 7.4 \times 10^{-11} \mu_B$ [183], is also shown for comparison (the most stringent bound on the neutrino magnetic moment comes from the reactor experiment GEMMA as $\mu_{\bar{\nu}_e} = 2.9 \times 10^{-11} \mu_B$ at 90% C.L. [216]). One sees that the prospects are very promising. Indeed, from Table 7.7, we find that the attainable sensitivities are improved by about one order of magnitude compared to the corresponding expectations at a SNS facility, considered recently in [170]. Note however, that experiments at the SNS are not optimised to measure electron-neutrino properties.

Moreover, it is worth mentioning that for the case of a 100 eV_{ee} threshold and $\mathcal{Q}_f = 1$, the resulting sensitivity is by 46% (36% for the case of realistic efficiency) better than the existing limits derived from $\bar{\nu}_e - e$ scattering TEXONO data [183]. However, assuming $\mathcal{Q}_f = 0.20$ (0.25) the above sensitivity reduces by a factor of 2.5 (2.1) for both recoil acceptances. From our calculations we have also found that neglecting quenching corrections the sensitivity to $\mu_{\bar{\nu}_e}$ of a given detector with mass m is roughly equivalent to that of a detector with ten times bigger mass for the case of $\mathcal{Q}_f = 0.25$. The results concerning this point are shown in Fig. 7.15 (right panel).

It is however, interesting to explore the case of a binned χ^2 analysis

$$\chi^2(\mu_{\bar{\nu}_e}) = \sum_{i=1}^N \chi_i = \sum_{i=1}^N \left[\frac{N_{\text{SM}}(i) - N_{\mu_{\bar{\nu}_e}}(i)}{\delta N_{\text{SM}}(i)} \right]^2, \quad (7.25)$$

where (i) denotes the corresponding bin associated to the corresponding i -th recoil energy window. The corresponding results are shown in Table 7.8 and indicate that a binned sample is not needed when we deal with future data. A

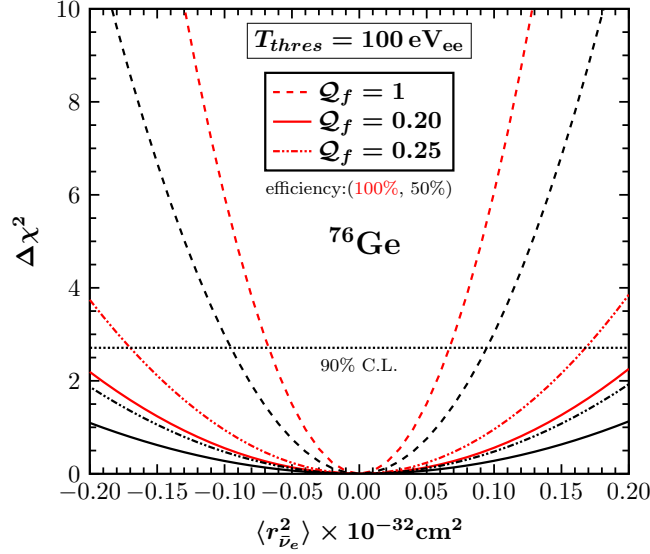


Figure 7.16: $\Delta\chi^2$ sensitivity profiles as a function of the neutrino charge radius $\langle r_{\bar{\nu}_e}^2 \rangle$ at TEXONO. Same conventions as in Fig. 7.11 are used.

bin width	# bins	$\Delta\chi^2/\mu_{\bar{\nu}_e}$	$\mu_{\bar{\nu}_e}/10^{-10} \mu_B$	difference
-	no	110	0.3960	-
50 eV	28	120	0.3879	2.0%
100 eV	14	118	0.3889	1.8%
200 eV	7	116	0.3909	1.3%

Table 7.8: Sensitivities of TEXONO experiment to neutrino magnetic moment. A comparison is made for binned and no-binned sample.

global analysis including the above sensitivity and the sensitivity expected at the COHERENT experiment has no impact to the present result, i.e.

$$\mu_{\bar{\nu}_e}^{\text{comb}} = 0.3959 (0.4709) \times 10^{-10} \mu_B, \quad (7.26)$$

for the optimistic (realistic) case [see Table 7.7 for comparison].

In view of our previous discussion, the TEXONO sensitivity to $\langle r_{\bar{\nu}_e}^2 \rangle$ -related searches is estimated through the definition of the χ^2 given in Eq.(7.23) by replacing $\sin^2 \theta_W$ with that of Eq.(7.12) and fixing $\sin^2 \bar{\theta}_W$ to the PDG value. After the χ^2 minimisation we find that the TEXONO experiment is expected to be very sensitive to EM contributions of this type. The estimated 90% C.L. sensitivities are presented in Table 7.7 and in Fig. 7.16. In the particular case of $Q_f = 0.25$ we see that thanks to the observation of CENNS events, TEXONO can reach an improvement of the order of 35% or more, with respect to similar calculations [170]. Again, this sensitivity reduces by a factor of 3.2 (2.4) when

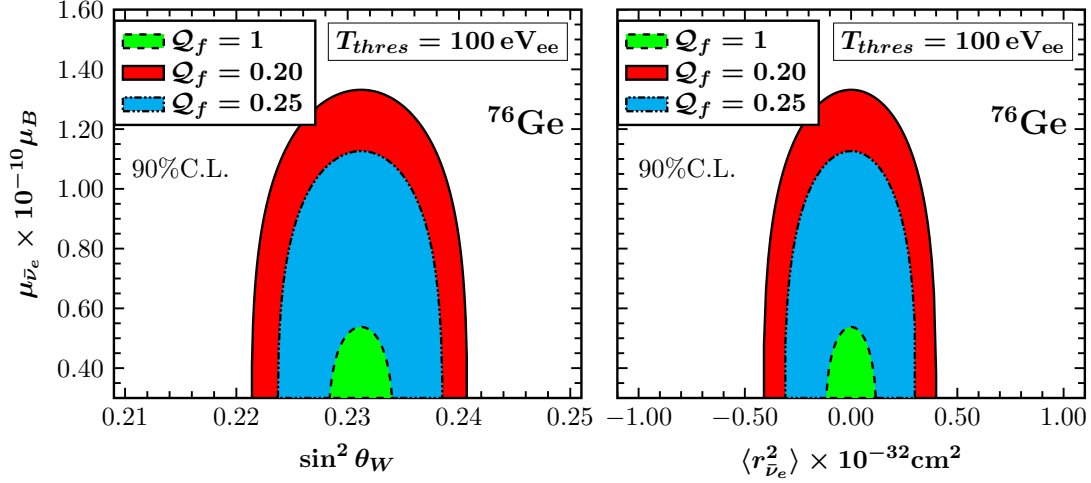


Figure 7.17: 90% C.L. allowed regions in the $(\sin^2 \theta_W - \mu_{\bar{\nu}_e})$ plane (*left panel*) and the $(\langle r_{\bar{\nu}_e}^2 \rangle - \mu_{\bar{\nu}_e})$ plane (*right panel*) from a two parameter combined analysis. See the text for more details.

quenching corrections $\mathcal{Q}_f = 0.20$ (0.25) are taken into account. Moreover, it is worth noting that the latter sensitivities are by one order of magnitude better than the current TEXONO constraint obtained from $\bar{\nu}_e - e$ scattering [19].

Finally, it is also interesting to show the combined sensitivities obtained by varying two of the above parameters ($\sin^2 \theta_W$, $\mu_{\bar{\nu}_e}$ and $\langle r_{\bar{\nu}_e}^2 \rangle$) simultaneously. The 90% C.L. allowed regions in the $(\sin^2 \theta_W - \mu_{\bar{\nu}_e})$ and $(\langle r_{\bar{\nu}_e}^2 \rangle - \mu_{\bar{\nu}_e})$ plane are shown in the left and right panel of Fig. 7.17, respectively for different quenching factors. One notices that the resulting parameter space is substantially reduced with respect to the corresponding sensitivity regions for muon neutrinos at a SNS experiment (see e.g. Ref. [170]). The latter is a direct consequence of the low-threshold TEXONO detectors adopted in the present study.

7.5 Conclusions

In this Chapter, at first, we have studied the sensitivities on Majorana neutrino magnetic moments, attainable through neutral-current coherent neutrino-nucleus scattering cross section calculations, at the Spallation Neutron Source facilities. The limits on the effective neutrino magnetic moment, μ_{eff} , obtained from neutrino experiments are in reality a restriction on a combination of physical observables. In this sense, an improvement in the muon effective neutrino magnetic moment will contribute towards improving the constraints on the physical observables through a combined analysis of neutrino data. The sensitivities we have extracted are obtained by means of a simple χ^2 analysis employing realistic nuclear structure calculations within the quasi-particle random phase approxi-

ation (QRPA), for the evaluation of the coherent cross section. We find that, current limits on the muon neutrino magnetic moment, μ_{ν_μ} , can be improved by about a factor of five. In addition, we show that the SNS allows for a competitive determination of the electroweak mixing angle θ_W . Moreover, the COHERENT proposal may provide an excellent probe for investigating other electromagnetic neutrino properties, such as the neutrino charge-radius.

In the next part of this Chapter, we have explored the possibility of performing Standard Model precision studies and probing for new physics through low energy neutral-current coherent elastic neutrino-nucleus scattering (CENNS) at the TEXONO experiment. Moreover, we have presented a comprehensive analysis for the case of potential sub-leading neutrino EM interactions. The calculated convoluted cross sections, clearly indicate the need for novel detector technologies with sub-keV sensitivities. Furthermore, from a nuclear physics point of view, the reactor neutrino beam induces transitions in the bound nuclear spectrum while the SNS beam may in addition excite much higher transitions of the nuclear detector. We conclude that, apart from providing the first ever detection of CENNS events, low threshold Germanium-based kg-scale detectors, e.g. TEXONO, will bring substantial improvements on precision SM tests as well as sensitivities on neutrino EM properties, such as the neutrino magnetic moment and the neutrino charge-radius. We show explicitly that, the sensitivities improve by up to one order of magnitude with respect to previous estimates. In this Chapter, apart from realistic nuclear structure calculations within the context of the QRPA, we have also taken into account quenching effects. We have, furthermore, checked that our sensitivities are determined mainly by the number of events: a binned sample would result in differences less than 3%. For the case of the electron antineutrino magnetic moment, $\mu_{\bar{\nu}_e}$, it is also worth mentioning that, a global fit including an experiment at the SNS added to the TEXONO experiment will not essentially improve these results, since SNS provides the best sensitivities for μ_{ν_μ} in the case of muonic neutrinos.

In view of the operation of the proposed sensitive neutrino experiments our results, presented for various choices of experimental setups and target materials, may contribute towards a deeper understanding of the so-far hidden neutrino properties.

Chapter 8

Sterile neutrinos from neutrino-nucleus scattering

8.1 Introduction

In this Chapter, at first, we review the basic features of the theory regarding neutrino oscillations in vacuum, and derive the well-known three-neutrino oscillation formulas. In this context the neutrino is required to be a massive particle. Contrary to the case of charged leptons where their mass eigenstates are simultaneous eigenstates of the Hamiltonian, the weak eigenstates of neutrinos do not coincide with their mass eigenstates. For this reason, the flavour states of neutrinos are not conserved with time evolution, leading to the phenomenon of neutrino oscillations. The discovery of neutrino oscillations in propagation constitutes a solid proof of physics beyond the SM emphasising that the neutrino is the only particle that exhibits exotic properties.

In the next stage, we consider the existence of an additional sterile neutrino state in the theory. To this purpose, the sub-leading impact of a fourth neutrino generation is investigated at reactor and Spallation Neutron Source (SNS) neutrino experiments. Specifically, the sensitivity of the TEXONO and COHERENT experiments to sterile neutrinos is explored through coherent elastic neutrino-nucleus scattering (CENNS). The present study involves realistic nuclear structure calculations within the framework of the QRPA for the high purity Germanium detectors (HPGe) which operate with sub-keV thresholds in conjunction with a sensitivity analysis.

8.2 Neutrino oscillations in vacuum

Neutrino oscillations are a quantum mechanical phenomenon where a neutrino of a specific flavour can be later detected to have a different flavour. It is of great experimental and theoretical interest, since neutrino oscillations require massive

neutrinos which means that new physics beyond the Standard Model is required. They occur because of the mixing in the charged weak current

$$|\nu_\alpha\rangle = \sum_i U_{\alpha i}^* |\nu_i\rangle, \quad (8.1)$$

where the weak neutrino eigenstates or flavour states $|\nu_\alpha\rangle$, $\alpha = e, \mu, \tau$ are superposition of the mass neutrino eigenstates $|\nu_i\rangle$, $i = 1, 2, 3$ and U is a $n \times n$ unitary (mixing) matrix. Both flavour and mass neutrino eigenstates have the property of being orthonormal

$$\begin{aligned} \langle \nu_\alpha | \nu_\beta \rangle &= \delta_{\alpha\beta}, \\ \langle \nu_i | \nu_j \rangle &= \delta_{ij}. \end{aligned} \quad (8.2)$$

Eq.(8.1) can alternatively be written in matrix form

$$\begin{pmatrix} \nu_e \\ \nu_\mu \\ \nu_\tau \end{pmatrix} = \begin{pmatrix} U_{e1} & U_{e2} & U_{e3} \\ U_{\mu1} & U_{\mu2} & U_{\mu3} \\ U_{\tau1} & U_{\tau2} & U_{\tau3} \end{pmatrix} \begin{pmatrix} \nu_1 \\ \nu_2 \\ \nu_3 \end{pmatrix}. \quad (8.3)$$

The unitary matrix $U_{\alpha i}$ can immediately be parametrised as follows

$$\begin{aligned} U_{\text{PMNS}} &= \\ &= \begin{pmatrix} 1 & 0 & 0 \\ 0 & c_{23} & s_{23} \\ 0 & -s_{23} & c_{23} \end{pmatrix} \begin{pmatrix} c_{13} & 0 & s_{13}e^{-i\delta} \\ 0 & 1 & 0 \\ -s_{13}e^{i\delta} & 0 & c_{13} \end{pmatrix} \begin{pmatrix} c_{12} & s_{12} & 0 \\ -s_{12} & c_{12} & 0 \\ 0 & 0 & 1 \end{pmatrix} \\ &\quad \times \begin{pmatrix} e^{i\alpha_1/2} & & \\ & e^{i\alpha_2/2} & \\ & & 1 \end{pmatrix} \\ &= \begin{pmatrix} c_{12}c_{13} & s_{12}c_{13} & s_{13}e^{-i\delta} \\ -s_{12}c_{23} - c_{12}s_{23}s_{13}e^{i\delta} & c_{12}c_{23} - s_{12}s_{23}s_{13}e^{i\delta} & s_{23}c_{13} \\ s_{12}s_{23} - c_{12}c_{23}s_{13}e^{i\delta} & -c_{12}s_{23} - s_{12}c_{23}s_{13}e^{i\delta} & c_{23}c_{13} \end{pmatrix} \\ &\quad \times \begin{pmatrix} e^{i\alpha_1/2} & & \\ & e^{i\alpha_2/2} & \\ & & 1 \end{pmatrix}, \end{aligned} \quad (8.4)$$

with $s_{ij} = \sin \theta_{ij}$ and $c_{ij} = \cos \theta_{ij}$.

This matrix namely, Pontecorvo-Maki-Nakagawa-Sakata (PMNS) or lepton or neutrino mixing matrix, is a complex 3×3 rotation matrix which is element of $SU(3)$ and therefore has 8 parameters, 3 angles and 5 phases plus a diagonal Majorana matrix. Due to field redefinitions we can eliminate four out of five phases and then we are left with only three angles and one phase, the so-called δ CP violating phase.

The first of the previous four matrices corresponds to the atmospheric neutrinos and the third to the solar neutrinos, both of them being well measured by the

experiments. The second one, contains the δ phase, which is not well measured yet, while the diagonal Majorana matrix does not contribute to rotations since it is diagonal. The δ phase requires all angles to be zero, but since we know from experiments that θ_{12} and θ_{23} are not zero, we believe that if this phase indeed exists, it is associated with θ_{13} . In addition, the Majorana α_1 and α_2 CP violating phases are physically meaningful, only if neutrinos are Majorana particles.

From Eq.(8.1), it becomes obvious that the weak eigenstates $|\nu_\alpha\rangle$ are identical to the mass eigenstates $|\nu_i\rangle$, if only the PMNS matrix is the identity matrix, but from experiments we know this is not the case. Moreover, a non-unitary PMNS matrix immediately implies the existence of sterile neutrinos or physics beyond the Standard Model.

8.2.1 Two neutrino flavour oscillation probabilities

A useful simplification is to compute the two neutrino oscillation probability introducing the rotation matrix in two dimensions

$$\begin{pmatrix} \nu_e \\ \nu_\mu \end{pmatrix} = \begin{pmatrix} \cos \theta & \sin \theta \\ -\sin \theta & \cos \theta \end{pmatrix} \begin{pmatrix} \nu_1 \\ \nu_2 \end{pmatrix}. \quad (8.5)$$

while the muon neutrino eigenstate in terms of the two mass eigenstates reads

$$|\nu_\mu\rangle = -\sin \theta |\nu_1\rangle + \cos \theta |\nu_2\rangle. \quad (8.6)$$

By using the Schrödinger equation we evolve the neutrino state in time

$$i \frac{d}{dt} |\nu_i(t)\rangle = H |\nu_i(t)\rangle, \quad (8.7)$$

which implies the plane wave solution

$$|\nu_i(t)\rangle = e^{-iE_i t} |\nu_i(0)\rangle. \quad (8.8)$$

Using the fact that neutrinos are generally ultra-relativistic ($m < 1\text{eV}$, $E > 100\text{keV}$), and hence $E \approx p \gg m$ (“equal-momentum approximation”), we can write

$$E_i = \sqrt{p^2 + m_i^2} = p \sqrt{1 + \frac{m_i^2}{p^2}} \approx p + \frac{m_i^2}{2p} \approx E + \frac{m_i^2}{2E}. \quad (8.9)$$

Combining this gives

$$\begin{aligned} |\nu_\mu(t)\rangle &= -\sin \theta |\nu_1\rangle e^{-i(E+m_1^2/2E)t} + \cos \theta |\nu_2\rangle e^{-i(E+m_2^2/2E)t} \\ &= e^{-i(E+m_1^2/2E)t} \left(-\sin \theta |\nu_1\rangle + \cos \theta |\nu_2\rangle e^{+i\frac{m_1^2-m_2^2}{2E}t} \right). \end{aligned} \quad (8.10)$$

By making the following substitutions

$$\Delta m_{12}^2 = m_1^2 - m_2^2, \quad (8.11)$$

$$z = E + m_1^2/2E, \quad (8.12)$$

$$t = L/c = L, \quad (8.13)$$

(the last relation holds true since we work in natural units) one gets

$$|\nu_\mu(t)\rangle = e^{-iz} \left(-\sin\theta |\nu_1\rangle + \cos\theta |\nu_2\rangle e^{+i\frac{\Delta m_{12}^2}{2E}L} \right). \quad (8.14)$$

The probability to detect ν_e can be found by the transition of amplitudes

$$P_{\nu_\mu \rightarrow \nu_e} = |\langle \nu_e | \nu_\mu \rangle|^2, \quad (8.15)$$

and using the orthogonality relation of the states given in Eq.(8.2), one has

$$\begin{aligned} P_{\nu_\mu \rightarrow \nu_e} &= |\langle \nu_e | \nu_\mu \rangle|^2 \\ &= e^{-iz} e^{iz} \sin^2\theta \cos^2\theta \left(-1 + e^{+i\frac{\Delta m_{12}^2}{2E}L} \right) \left(-1 + e^{-i\frac{\Delta m_{12}^2}{2E}L} \right), \end{aligned} \quad (8.16)$$

which finally gives

$$\begin{aligned} P_{\nu_\mu \rightarrow \nu_e} &= \frac{1}{2} \sin^2 2\theta \left[1 - \cos \left(\frac{\Delta m_{12}^2}{2E} L \right) \right], \\ &= \sin^2 2\theta \sin^2 \left(\frac{\Delta m_{12}^2 L}{4E} \right). \end{aligned} \quad (8.17)$$

By restoring the natural units the disappearance probability takes the form

$$P_{\nu_\mu \rightarrow \nu_e}(L, E) = \sin^2 2\theta \sin^2 \left(1.267 \Delta m_{12}^2 [\text{eV}^2] \frac{L [\text{km}]}{E [\text{GeV}]} \right). \quad (8.18)$$

Then, the survival probability of ν_μ is trivially obtained as

$$P_{\nu_\mu \rightarrow \nu_\mu}(L, E) = 1 - \sin^2 2\theta \sin^2 \left(1.267 \Delta m_{12}^2 [\text{eV}^2] \frac{L [\text{km}]}{E [\text{GeV}]} \right), \quad (8.19)$$

while CP invariance implies that for the antineutrino case it also holds

$$P_{\bar{\nu}_\mu \rightarrow \bar{\nu}_\mu} = P_{\nu_\mu \rightarrow \nu_\mu}(L, E). \quad (8.20)$$

8.2.2 Three neutrino flavour oscillation probabilities

The Schrödinger equation implies the time propagation of neutrinos, thus in natural units one writes

$$|\nu_i(t)\rangle = e^{-iE_it} |\nu_i(0)\rangle, \quad (8.21)$$

while the transition probabilities can be found from squaring the amplitudes

$$P_{\nu_\alpha \rightarrow \nu_\beta}(t) = |A_{\nu_\alpha \rightarrow \nu_\beta}(t)|^2 = \left| \left(\sum_j U_{\alpha j} e^{iE_j t} U_{\beta j}^* \right) \left(\sum_i U_{\alpha i}^* e^{-iE_i t} U_{\beta i} \right) \right|. \quad (8.22)$$

Assuming that all neutrinos have equal momenta and propagate with the speed of light one finds

$$P_{\nu_\alpha \rightarrow \nu_\beta}(L, E) = \sum_{i,j} U_{\alpha i}^* U_{\beta i} U_{\alpha j} U_{\beta j}^* \exp\left(-i \frac{\Delta m_{ij}^2 L}{2E}\right). \quad (8.23)$$

The last equation can be written in the form

$$P_{\nu_\alpha \rightarrow \nu_\beta}(L, E) = \sum_i |U_{\alpha i}|^2 |U_{\beta i}|^2 + 2 \sum_{i>j} \Re \left[U_{\alpha i}^* U_{\beta i} U_{\alpha j} U_{\beta j}^* \exp\left(-i \frac{\Delta m_{ij}^2 L}{2E}\right) \right]. \quad (8.24)$$

By using the unitary relation

$$\begin{aligned} U^\dagger U &= 1, \\ \sum_i U_{\alpha i} U_{\beta i}^* &= \delta_{\alpha\beta}, \end{aligned} \quad (8.25)$$

we have

$$\sum_{ij} U_{\alpha i}^* U_{\beta i} U_{\alpha j} U_{\beta j}^* = \sum_i U_{\alpha i}^* U_{\beta i} \sum_j U_{\alpha j} U_{\beta j}^* = (\delta_{\alpha\beta})^2 = \delta_{\alpha\beta}. \quad (8.26)$$

In addition, we evaluate the summation

$$\begin{aligned} \sum_{ij} U_{\alpha i}^* U_{\beta i} U_{\alpha j} U_{\beta j}^* &= \sum_{i=j} U_{\alpha i}^* U_{\beta i} U_{\alpha j} U_{\beta j}^* + \sum_{i>j} U_{\alpha i}^* U_{\beta i} U_{\alpha j} U_{\beta j}^* + \sum_{i<j} U_{\alpha i}^* U_{\beta i} U_{\alpha j} U_{\beta j}^* \\ &= \sum_i |U_{\alpha i}|^2 |U_{\beta i}|^2 + 2 \sum_{i>j} \Re [U_{\alpha i}^* U_{\beta i} U_{\alpha j} U_{\beta j}^*], \end{aligned} \quad (8.27)$$

and we therefore arrive at the relation

$$\delta_{\alpha\beta} - 2 \sum_{i>j} \Re [U_{\alpha i}^* U_{\beta i} U_{\alpha j} U_{\beta j}^*] = \sum_i |U_{\alpha i}|^2 |U_{\beta i}|^2. \quad (8.28)$$

Thus, Eq.(8.24) is written as

$$\begin{aligned}
P_{\nu_\alpha \rightarrow \nu_\beta}(L, E) &= \delta_{\alpha\beta} - 2 \sum_{i>j} \Re e \left\{ U_{ai}^* U_{\beta i} U_{\alpha j} U_{\beta j}^* \left[1 - \exp \left(-i \frac{\Delta m_{ij}^2 L}{2E} \right) \right] \right\}, \\
&= \delta_{\alpha\beta} - 4 \sum_{i>j} \sin \left(\frac{\Delta m_{ij}^2 L}{4E} \right) \Im m \left\{ U_{ai}^* U_{\beta i} U_{\alpha j} U_{\beta j}^* \exp \left(-i \frac{\Delta m_{ij}^2 L}{4E} \right) \right\}.
\end{aligned} \tag{8.29}$$

Eventually, by using the property

$$\begin{aligned}
U_{ai}^* U_{\beta i} U_{\alpha j} U_{\beta j}^* \exp \left(-i \frac{\Delta m_{ij}^2 L}{4E} \right) &= (\Re e [U_{ai}^* U_{\beta i} U_{\alpha j} U_{\beta j}^*] + i \Im m [U_{ai}^* U_{\beta i} U_{\alpha j} U_{\beta j}^*]) \\
&\quad \times \left[\cos \left(\frac{\Delta m_{ij}^2 L}{4E} \right) - i \sin \left(\frac{\Delta m_{ij}^2 L}{4E} \right) \right],
\end{aligned} \tag{8.30}$$

we recover the usual form of the three flavour neutrino oscillation probability

$$\begin{aligned}
P_{\nu_\alpha \rightarrow \nu_\beta}(L, E) &= \delta_{\alpha\beta} - 4 \sum_{i>j} \Re e [U_{ai}^* U_{\beta i} U_{\alpha j} U_{\beta j}^*] \sin^2 \left(\frac{\Delta m_{ij}^2 L}{4E} \right) \\
&\quad + 2 \sum_{i>j} \Im m [U_{ai}^* U_{\beta i} U_{\alpha j} U_{\beta j}^*] \sin \left(\frac{\Delta m_{ij}^2 L}{2E} \right).
\end{aligned} \tag{8.31}$$

As a concrete example, we find the ν_e oscillation probability. By direct substitution we get

$$\begin{aligned}
P_{\nu_e \rightarrow \nu_e} &= 1 - 4 |U_{e3}|^2 |U_{e1}|^2 \sin^2 \left(\Delta m_{13}^2 \frac{L}{4E} \right) \\
&\quad - 4 |U_{e3}|^2 |U_{e2}|^2 \sin^2 \left(\Delta m_{23}^2 \frac{L}{4E} \right) \\
&\quad - 4 |U_{e2}|^2 |U_{e1}|^2 \sin^2 \left(\Delta m_{12}^2 \frac{L}{4E} \right).
\end{aligned} \tag{8.32}$$

Using the fact that $\Delta m_{31}^2 \approx \Delta m_{32}^2$, we recall the unitarity relation of Eq.(8.25) and by restoring the natural units we get

$$\begin{aligned}
P_{\nu_e \rightarrow \nu_e} &= 1 - \cos^4 \theta_{13} \sin^2 2\theta_{12} \sin^2 \left(1.267 \Delta m_{12}^2 \frac{L}{E} \right) \\
&\quad - \sin^2 2\theta_{13} \sin^2 \left(1.267 \Delta m_{23}^2 \frac{L}{E} \right).
\end{aligned} \tag{8.33}$$

The survival probability, is simply

$$P_{\nu_\alpha \rightarrow \nu_\alpha} = 1 - P_{\nu_\alpha \rightarrow \nu_\beta}. \tag{8.34}$$

For the antineutrino case, Eq.(8.31) becomes

$$P_{\bar{\nu}_\alpha \rightarrow \bar{\nu}_\beta}(L, E) = \delta_{\alpha\beta} - 4 \sum_{i>j} \Re e [U_{ai}^* U_{\beta i} U_{\alpha j} U_{\beta j}^*] \sin^2 \left(\frac{\Delta m_{ij}^2 L}{4E} \right) - 2 \sum_{i>j} \Im m [U_{ai}^* U_{\beta i} U_{\alpha j} U_{\beta j}^*] \sin \left(\frac{\Delta m_{ij}^2 L}{2E} \right). \quad (8.35)$$

Moreover, under CPT invariance, it follows that $P_{\nu_e \rightarrow \nu_e} = P_{\bar{\nu}_e \rightarrow \bar{\nu}_e}$.

8.3 Impact of a light sterile neutrino to neutrino-nucleus scattering

We employ a minimal extension of the standard model by considering a fourth light sterile neutrino state added to the three active neutrinos. In this parametrisation, the weak flavour states of neutrinos ν_α , $\alpha = \{e, \mu, \tau, \dots\}$ are related to the mass eigenstates ν_i , $i = \{1, 2, 3, 4, \dots\}$ through the unitary transformation as $\nu_\alpha = \sum_i U_{\alpha i} \nu_i$. In the (3+1) scheme, the generated reactor antineutrinos $\bar{\nu}_e$ of energy E_ν are expected to travel the propagation distance L with the survival probability

$$P_{\bar{\nu}_e \rightarrow \bar{\nu}_e} = 1 - 4 \sum_{i=1}^3 \sum_{j>i}^4 |U_{ei}|^2 |U_{ej}|^2 \sin^2 (\Delta_{ij}), \quad (8.36)$$

where $\Delta_{ij} = \Delta m_{ij}^2 L / 4E_\nu$, with the mass splittings denoted as $\Delta m_{ij}^2 = m_i^2 - m_j^2$. The matrix elements entering Eq.(8.36) take the form [217]

$$U_{e1} = \cos \theta_{14} \cos \theta_{13} \cos \theta_{12}, \quad (8.37)$$

$$U_{e2} = \cos \theta_{14} \cos \theta_{13} \sin \theta_{12}, \quad (8.38)$$

$$U_{e3} = \cos \theta_{14} \sin \theta_{13}, \quad (8.39)$$

$$U_{e4} = \sin \theta_{14}. \quad (8.40)$$

In this framework, the hypothesis of a fourth neutrino generation yields the approximate disappearance probability [218]

$$P_{\bar{\nu}_e \rightarrow \bar{\nu}_e} = 1 - \cos^4 \theta_{14} \sin^2 2\theta_{13} \sin^2 \left(\frac{\Delta m_{13}^2 L}{4E_\nu} \right) - \sin^2 2\theta_{14} \sin^2 \left(\frac{\Delta m_{14}^2 L}{4E_\nu} \right). \quad (8.41)$$

Note, that for vanishing θ_{14} the latter expression reduces to the well-known oscillation probability for short-baselines and also that possible atmospheric driven oscillations are neglected since they are significant for $L > 100$ m. Due to the smallness of the recently measured θ_{13} neutrino angle at Daya Bay [219], for simplicity in our calculations we set $\sin^2 2\theta_{13} = 0$. Moreover, we use the fact that

within the framework of the (3+1) scheme it holds that [220]

$$\sin^2 2\theta_{\alpha\alpha} = 4|U_{\alpha 4}|^2 (1 - |U_{\alpha 4}|^2), \quad (8.42)$$

$$\sin^2 2\theta_{\alpha\beta} = 4|U_{\alpha 4}|^2 |U_{\beta 4}|^2, \quad (8.43)$$

where $\alpha, \beta = e, \mu, \tau, s$. Focusing on the relevant short-baseline (SBL) experiments, the above expressions enter the respective effective survival and transition probabilities (they have the same form for neutrinos and antineutrinos)

$$P_{\nu_\alpha \rightarrow \nu_\alpha} = 1 - \sin^2 2\theta_{\alpha\alpha} \sin^2 \left(\frac{\Delta m_{41}^2 L}{4E} \right), \quad (8.44)$$

$$P_{\nu_\alpha \rightarrow \nu_\beta} = \sin^2 2\theta_{\alpha\beta} \sin^2 \left(\frac{\Delta m_{41}^2 L}{4E} \right), \quad \alpha \neq \beta. \quad (8.45)$$

We furthermore note, the equivalence of Eq.(8.36) with Eq.(8.44) in the limit of vanishing θ_{13} .

8.4 Numerical results

Reactor neutrino experiments are sensitive to $|U_{e4}|^2$ through the measurement of $\sin^2 2\theta_{ee}$. In the presence of sterile neutrinos, the number of events over a given nuclear recoil threshold, T_N^{thres} , reads

$$N_{\text{sterile}}^{\text{events}} = K \int_{E_{\nu_{\text{min}}}}^{E_{\nu_{\text{max}}}} dE_\nu d \cos \theta P_{\bar{\nu}_e \rightarrow \bar{\nu}_e} \frac{d\phi_{\bar{\nu}_e}}{dE_\nu} \frac{d\sigma_{\bar{\nu}_e}}{d \cos \theta} \times \delta \left(T_N - \frac{Q^2}{2M} \right), \quad (8.46)$$

where $K = N_{\text{targ}} t_{\text{tot}}$, with N_{targ} the total number of atomic targets in the detector, t_{tot} the time window of exposure and Q^2 the momentum transfer (θ is the scattering angle), defined as

$$Q^2 = 4E_\nu^2 \sin^2(\theta/2). \quad (8.47)$$

Note, that contrary to our recent studies [170, 221] in the above expression potential neutrino oscillation in propagation effects are now taken into account. The numerical results throughout this work, assume 1 kg of ^{76}Ge target mass, one year of data taking and a detector threshold of 100 eV_{ee}. To maximise the reliability of our estimation on the expected event rate, corrections due to quenching effects are also considered, by assuming a quenching factor of $\mathcal{Q}_f = 0.25$ [221]. In order to get an idea of how the presence of sterile neutrinos affects the expected number of events at a given detector, we define the ratio

$$R = \frac{N_{\text{sterile}}^{\text{events}}}{N_{\text{SM}}^{\text{events}}}. \quad (8.48)$$

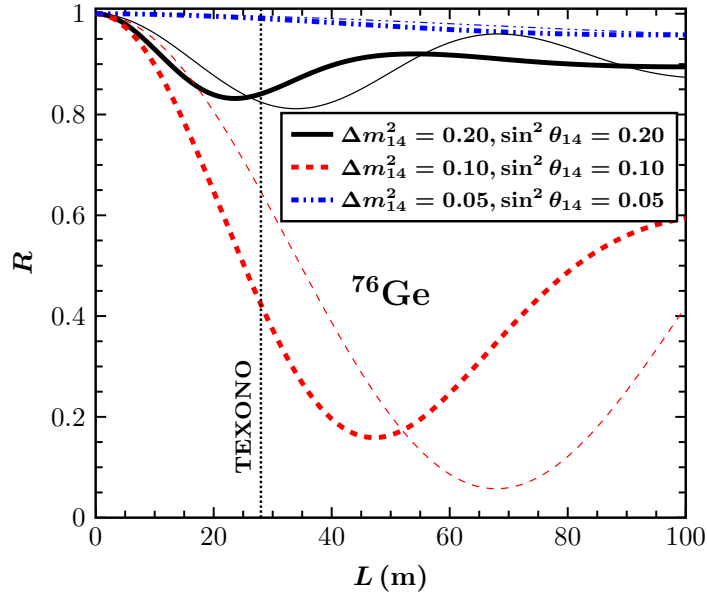


Figure 8.1: The ratio R in terms of a given baseline L . The thick (thin) lines correspond to $\mathcal{Q}_f = 1$ ($\mathcal{Q}_f = 0.25$). The TEXONO baseline is indicated with the vertical dotted line.

We mention that R is independent of detector mass and flux uncertainties. Apparently, the equality $R = \langle \sigma \rangle_{\text{sterile}} / \langle \sigma \rangle_{\text{SM}}$ holds true, where by $\langle \sigma \rangle$ we denote the averaged cross section over the neutrino distribution. Figure 8.1 illustrates graphically the corresponding numerical result for various choices of the sterile neutrino parameters, while Fig. 8.2 visualises the impact of sterile neutrino parameters on the expected number of events at the TEXONO experiment.

In our effort towards quantifying the sensitivity of the TEXONO experiment to sterile neutrinos, we define the χ^2 as

$$\chi^2 = \left(\frac{N_{\text{SM}}^{\text{events}} - N_{\text{sterile}}^{\text{events}}}{\delta N_{\text{SM}}^{\text{events}}} \right)^2. \quad (8.49)$$

Our present results indicate clearly that a dedicated experiment searching for CENNS has also satisfactory capabilities in probing sterile neutrinos. In Fig. 8.3 we illustrate the allowed 90% C.L. contours in the $(|U_{e4}|^2, \Delta m_{14}^2)$ plane obtained from a two-parameter χ^2 analysis as described above. For the case of TEXONO experiment, the lack of $\bar{\nu}_e$ disappearance is depicted in Fig. 8.4 and large values of $\sin^2 2\theta_{ee}$ are constrained by the exclusion curves, in agreement with the results of Refs. [220, 222]. In addition, as stated in Ref. [223], the requirement of large $|U_{e1}|^2 + |U_{e2}|^2$ for solar neutrino oscillations, implies that values with $|U_{e4}|^2$ close to unity are excluded. Therefore, for small $\sin^2 2\theta_{ee}$ one has

$$\sin^2 2\theta_{ee} \simeq 4|U_{e4}|^2. \quad (8.50)$$

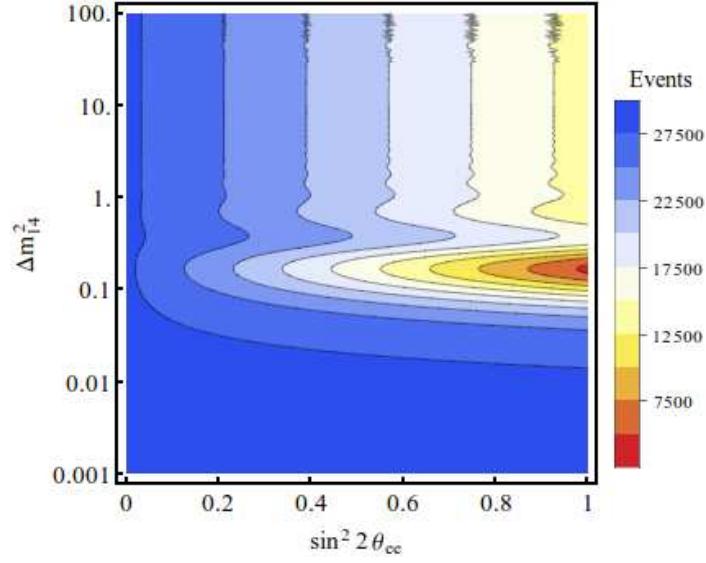


Figure 8.2: Contour plot of the number of events at TEXONO obtained through a raster scan of the sterile neutrino parameters.

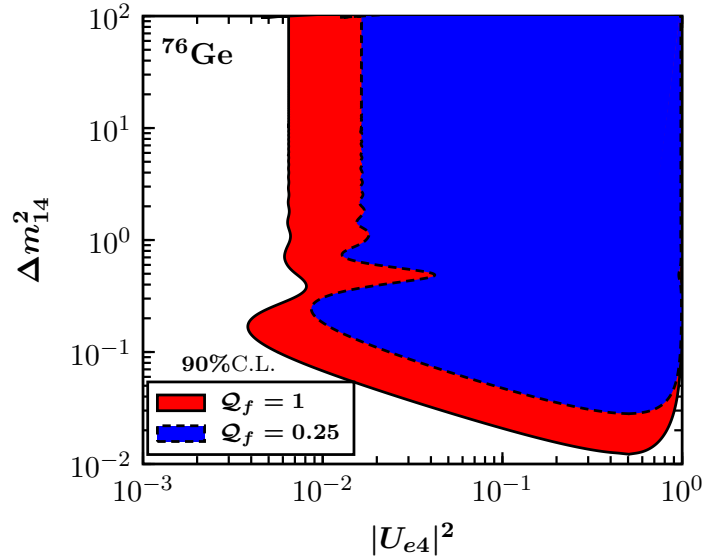


Figure 8.3: Allowed region at 90% C.L. in the $(|U_{e4}|^2, \Delta m_{14}^2)$ plane assuming a light sterile neutrino in the $(3+1)$ scheme, at the TEXONO experiment. The calculations consider one year of total exposure, 1 kg ^{76}Ge detector and two possible quenching factors.

The latter expression satisfies the general expectation that the fourth generation massive neutrino is mostly sterile. Focusing on the muon neutrinos produced at the SNS, the resulted constraints on $\sin^2 2\theta_{\mu\mu}$ extracted from the analysis of the

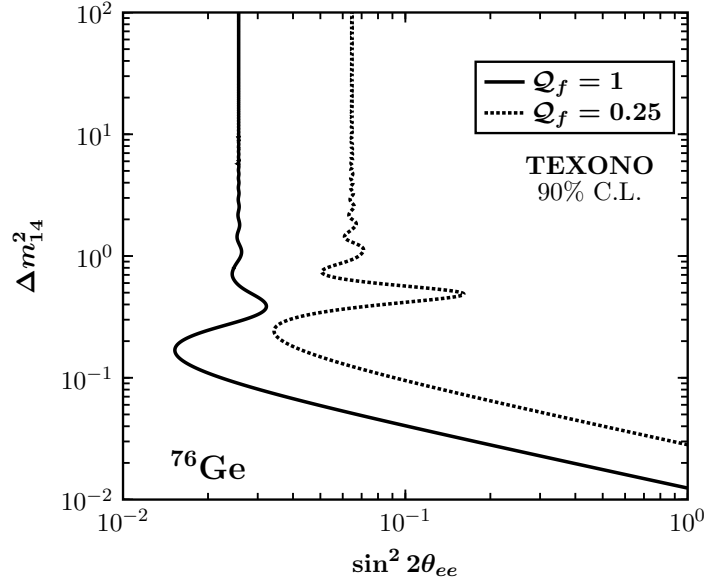


Figure 8.4: Excluded region at 90% C.L. in the $(\sin^2 2\theta_{ee}, \Delta m_{14}^2)$ plane assuming a light sterile neutrino in the (3+1) scheme, at the TEXONO experiment. For the details see Fig. 8.3.

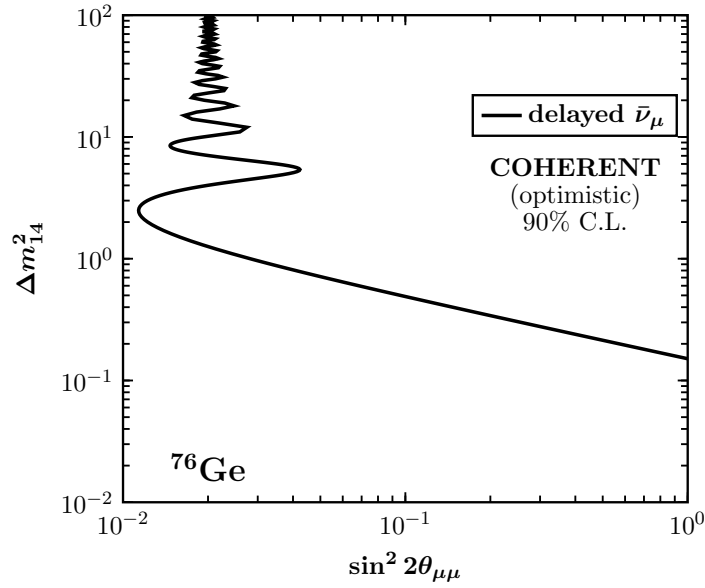


Figure 8.5: Excluded region at 90% C.L. in the $(\sin^2 2\theta_{\mu\mu}, \Delta m_{14}^2)$ plane assuming a light sterile neutrino in the (3+1) scheme, at the COHERENT experiment. Only the delayed $\bar{\nu}_\mu$ beam is taken into account.

COHERENT experiment [75, 116] (see Fig. 8.5), in conjunction with the large values of $|U_{\mu 1}|^2 + |U_{\mu 2}|^2 + |U_{\mu 3}|^2$ indicated by atmospheric neutrino data [224],

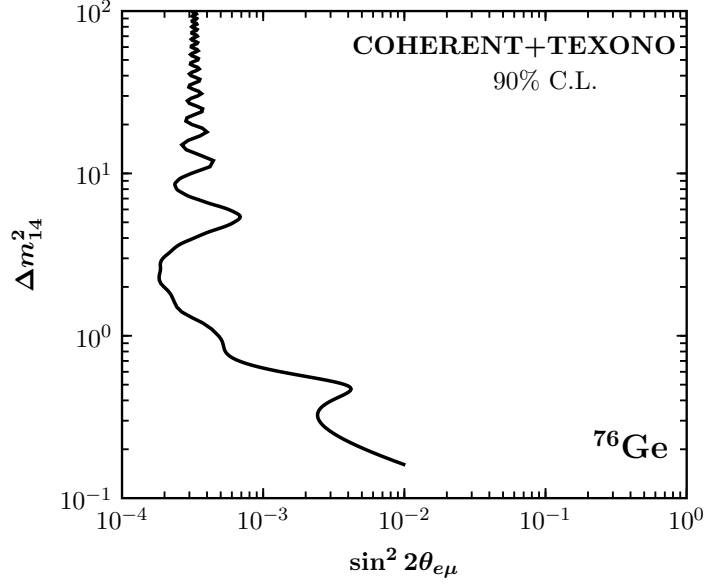


Figure 8.6: Excluded region at 90% C.L. in the $(\sin^2 2\theta_{e\mu}, \Delta m_{14}^2)$ plane from a combined analysis of futuristic COHERENT and TEXONO data in the (3+1) scheme.

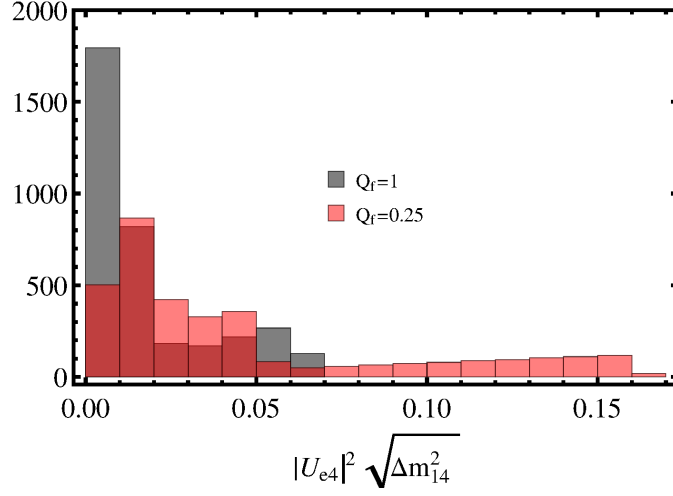
imply small values for $|U_{\mu 4}|^2$. Then, analogously to reactor neutrino experiments, one writes

$$\sin^2 2\theta_{\mu\mu} \simeq 4|U_{\mu 4}|^2. \quad (8.51)$$

A combination of Eq.(8.43) with Eqs.(8.50) and (8.51) yields the appearance-disappearance constraint [225]

$$\sin^2 2\theta_{e\mu} = \frac{1}{4} \sin^2 2\theta_{ee} \sin^2 2\theta_{\mu\mu}. \quad (8.52)$$

Therefore, $\sin^2 2\theta_{e\mu}$ is quadratically suppressed for small values of $\sin^2 2\theta_{ee}$ and $\sin^2 2\theta_{\mu\mu}$. From the corresponding exclusion curve in Fig. 8.6 we see that the combined constraint of Eq.(8.52) has the potential to provide a high sensitivity to sterile neutrino searches. Confronting the present results to existing constraints extracted from the LSND [226] and MiniBooNE [227] data, we conclude that the projected sensitivities from CENNS are generically more severe. The obtained results are also competitive to recent constraints extracted from global analyses of SBL neutrino oscillation searches [220, 228].

Figure 8.7: Contribution to $m_{2\beta}$ due to a sterile neutrino.

8.4.1 Impact of sterile neutrinos on beta-decay and on neutrinoless double beta-decay

Motivated by the result of Fig. 8.6, at this point we consider a heavy sterile neutrino, i.e.

$$m_1, m_2, m_3 \ll m_4. \quad (8.53)$$

with $\Delta m_{14}^2 > 0.1$ (eV²). Specifically, we consider the normal scheme only, since the inverted hierarchy is ruled out from cosmology [229, 230].

We now turn our attention to neutrinoless double- β decay which is predicted to occur in the presence of massive Majorana neutrinos. In this case, the decay rate is proportional to the effective Majorana mass [231]

$$m_{2\beta} = \left| \sum_k U_{ek}^2 m_k \right|. \quad (8.54)$$

In the context of the (3+1) scheme, the presence of the additional sterile neutrino generates an additional phase, α_4 , which enters the definition of the effective Majorana mass, as follows

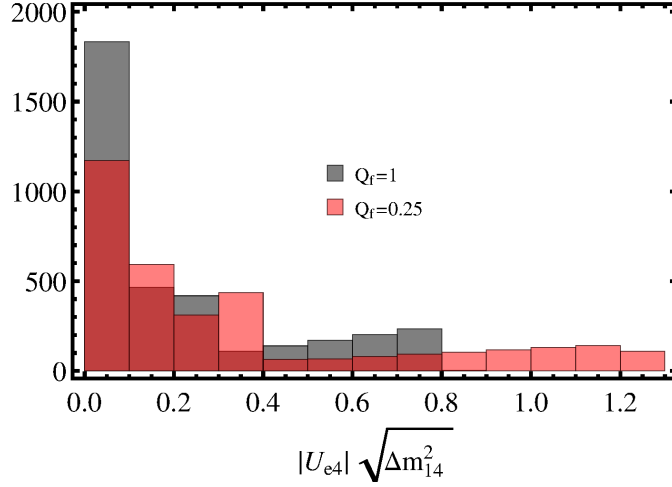
$$|m_{2\beta}| = \left| |U_{e1}|m_1 + |U_{e2}|e^{i\alpha_2}m_2 + |U_{e3}|e^{i\alpha_3}m_3 + |U_{e4}|e^{i\alpha_4}m_4 \right|. \quad (8.55)$$

In the particular case of a heavy sterile neutrino, as illustrated in Eq.(8.53), the relevant contribution to $m_{2\beta}$ reads [232]

$$|U_{e4}|^2 \sqrt{\Delta m_{14}^2}. \quad (8.56)$$

For the case of beta-decay the effective electron mass, m_β , takes the form

$$m_\beta^2 = \sum_i |U_{ei}|^2 m_i^2. \quad (8.57)$$

Figure 8.8: Contribution to m_β due to a sterile neutrino.

Therefore, assuming a heavy sterile neutrino the relevant term contributing to m_β is

$$|U_{e4}| \sqrt{\Delta m_{14}^2}. \quad (8.58)$$

From the χ^2 analysis of the TEXONO experiment (assuming different quenching factors), the relevant contributions to $m_{2\beta}$ and m_β [see Eqs.(8.56),(8.58)] are shown in the histograms of Figs 8.7 and 8.8 respectively. In both cases, one sees that for $Q_f = 1$, very small values are favoured, while for $Q_f = 0.25$ larger values are also possible. Furthermore, the results indicate that the contribution of a fourth generation sterile neutrino to m_β is about one order of magnitude larger as compared to that for $m_{2\beta}$.

8.5 Conclusions

In this Chapter, we explored the possibility of detecting physical observables related to the potential effects of sterile neutrinos to short-baseline CENNS experiments. Focusing on the normal (3+1) scheme, we found that the recently planned neutral current neutrino-nucleus experiments such as the TEXONO and COHERENT, have good prospects of detecting the existence of sterile neutrinos. From our present results we extract the conclusion that, on the basis of dedicated low-energy experiments looking for CENNS events, the analysis of neutrino oscillations might be complementary to charged-current appearance and disappearance searches. We verified that, by employing high-purity Germanium detectors with sub-keV sensitivities, more severe constraints can be provided on the sterile mixing parameters. Such measurements are crucial towards understanding better the neutrino interactions at all energy scales and will provide a clear evidence for new physics.

Chapter 9

Summary of Thesis and outlook

9.1 Summary and conclusions

The present Thesis addresses interesting open questions of the current neutrino physics into the overlap field of nuclear astrophysics, astroparticle physics, theoretical nuclear physics and fundamental electroweak interactions. In particular, the subject of exotic lepton flavour violating processes in the field of nuclei which is a concrete example of the coexistence of particle physics, nuclear physics, astrophysics and cosmology is extensively studied.

We focused on both conventional and exotic channels of neutral-current neutrino-nucleus scattering and performed calculations in the context of the Donnelly-Walecka method, paying special attention on the nuclear physics aspects of the process. Specifically, in our study the contributions to new physics that arise from the non-standard interaction (NSI) parameters entering the corresponding beyond the Standard Model Lagrangians, are comprehensively evaluated. These parameters are distinguished in flavour-conserving and flavour-violating terms and the corresponding nuclear matrix elements have been formulated and computed. For the case of elastic channel, realistic nuclear structure calculations have been performed through the advanced Bardeen-Cooper-Schrieffer (BCS) nuclear method, while the inelastic channels have been studied by employing the state-of-the-art quasi-particle random phase approximation (pp-nn QRPA).

The developed codes (in FORTRAN and Mathematica) provide a refined version of the BCS method for the successful simulation of SM, NSI and EM coherent neutrino-nucleus scattering events. The latter is appropriate to construct explicitly the nuclear ground state of complex even-even nuclei. To this purpose, realistic strong two-nucleon pairing forces are taken into consideration through the Bonn C-D (meson-exchange) potential for the residual interaction, while for the nuclear field we use a coulomb corrected Woods-Saxon potential with additional spin-orbit corrections. In order to obtain the nuclear form factors with high reliability, we solved iteratively the BCS equations and determined the single

quasi-particle energies and occupation amplitudes for each $(n, l)j$ level of the chosen model space, separately for protons and neutrons. The renormalisation of the residual interaction was obtained through the appropriate adjustment of the pairing interaction strength parameters, $g_{\text{pair}}^{p(n)}$, in order to reproduce the empirical energy gaps, $\Delta_{p(n)}$, with high accuracy.

Realistic calculations have been carried out for a set of interesting nuclei covering the entire periodic table (from light to heavy nuclides) and we mainly focused on the ^{20}Ne , ^{40}Ar , ^{76}Ge and ^{132}Xe isotopes. Such nuclear systems are of particular interest for ongoing and recently planned multipurpose experiments (for Supernova, Spallation Source, reactor and Cold Dark Matter studies) that aim to detect coherent neutrino-nucleus scattering events for the first time. The obtained results indicate that measurable rates are expected even for kg-scale detectors at the COHERENT and TEXONO experiments. We have shown that the involved nuclear physics aspects are of primary importance and lead to differences of up to 30% or larger in comparison with previous studies.

We have verified explicitly that the aforementioned facilities, by employing low-threshold detectors, are expected to be extremely sensitive to new physics that arises from the inclusion of NSI. In addition, it is demonstrated that neutrino vectorial NSI is largely connected to charged lepton flavour violating processes, and for this reason, we have evaluated the expected upper bounds on NSI coming out of the sensitivity of muon-to-electron conversion experiments. From a statistical analysis of the tensorial NSI terms, we extracted stringent upper limits to the NSI neutrino transition magnetic moments and neutrino milli-charges. Moreover, focusing on reactor neutrino experiments, we arrived at the conclusion that within the current limits, more events are expected due to tensor NSI as compared to those induced by a neutrino magnetic moment.

Our present results indicate that, through neutrino-nucleus scattering, the attainable sensitivities on EM neutrino parameters are improved by up to one order of magnitude compared to previous studies. We have, furthermore, shown that the aforementioned experiments have a high potential to put severe constraints on the neutrino charge-radius. We also concluded that they offer the capability to perform Standard Model precision tests in the low energy regime, with a competitive determination of the weak mixing angle. From experimental physics perspectives, quenching factors have been also taken into consideration.

In addition to the above, we have demonstrated that, experiments searching for neutrino-nucleus scattering have excellent capabilities to probe sterile neutrinos. The corresponding results, derived through a statistical analysis, indicate that reactor neutrino experiments operating with high purity Germanium detectors have excellent prospects to constrain the mixing parameters characterising light sterile neutrino states.

In summary, the outcomes of this Thesis may contribute usefully towards analysing the event-signal recorded in neutrino detectors, and in conjunction with data expected to be measured in current and future neutrino experiments, they

may furthermore provide additional information to understand deeper the fundamental electroweak interactions in the neutral- and charged-lepton sector, both for conventional and exotic processes.

9.2 Future perspectives

The reliability of the developed method and its successful application to conventional and exotic neutral-current neutrino-nucleus processes, has highly motivated us to extend the present research and study a broad class of interesting electroweak phenomena.

A generalisation of the method in order to explore charged-current NSI neutrino-nucleus processes is of significant importance. Moreover, special effort may be devoted to examine the impact of various SM extensions as well as Supersymmetric models that may provide additional corrections to the weak SM neutrino-nucleus scattering.

Through appropriate, but relatively simple modifications, the high efficiency and flexibility of the constructed codes, offer the possibility to study neutral-current flavour violating processes in the charged lepton sector, such as the exotic muon-to-electron (or high energy electron-to-muon) conversion in nuclei. The relevant experiments Mu2e and COMET are expected to operate soon and have prompted a great rush to produce adequate SM extensions and further study regarding the nuclear physics aspects of the process in order to analyse and interpret the future data.

In a future step we are intended to explore in detail neutral-current and charged-current non-standard neutrino-nucleon processes. Such processes are of great importance and could be the origin of the unexplained observed excess of electronlike events in the MiniBooNE detector as well as to provide more direct clues regarding the LSND anomaly.

We are also intended to conduct a comprehensive research study related to WIMP-nucleus and WIMP-nucleon interactions by paying special attention to the spin-dependent component of the process through a refined version of the odd-A QRPA method. From experimental physics perspectives, the comprehensive study of this channel is of key interest, since the inelastic signal will be recorded beyond the detector threshold energy, while the elastic signal is mostly cut-off by the detector threshold.

Appendix A

A.1 Notation and conventions

We adopt the standard Bjorken and Drell convention, i.e. we use natural units $\hbar = c = k_B = 1$ and the $(+ - - -)$ signature

$$g^{\mu\nu} = \begin{pmatrix} 1 & 0 & 0 & 0 \\ 0 & -1 & 0 & 0 \\ 0 & 0 & -1 & 0 \\ 0 & 0 & 0 & -1 \end{pmatrix}. \quad (\text{A.1})$$

The Dirac gamma matrices, form a Clifford algebra, and are defined by the anti-commutation relations

$$\{\gamma^\mu, \gamma^\nu\} = \gamma^\mu\gamma^\nu + \gamma^\nu\gamma^\mu = 2g^{\mu\nu}, \quad (\text{A.2})$$

so that $\gamma^\mu\gamma_\mu = 4$ and $\gamma^0\gamma^{\mu\dagger}\gamma^0 = \gamma^\mu$.

The conventions for γ^5 and $\epsilon_{\mu\nu\rho\sigma}$ are

$$\gamma^5 \equiv \gamma_5 = i\gamma^0\gamma^1\gamma^2\gamma^3 = \frac{i}{4!}\epsilon_{\mu\nu\rho\sigma}\gamma^\mu\gamma^\nu\gamma^\rho\gamma^\sigma, \quad \epsilon_{0123} = 1. \quad (\text{A.3})$$

In the chiral or Weyl basis the Dirac matrices are

$$\gamma^0 = \begin{bmatrix} 0 & 1 \\ 1 & 0 \end{bmatrix}, \quad \gamma^i = \begin{bmatrix} 0 & \sigma^i \\ -\sigma^i & 0 \end{bmatrix}, \quad \gamma^5 = \begin{bmatrix} -1 & 0 \\ 0 & 1 \end{bmatrix}, \quad (\text{A.4})$$

with σ_i denoting the Pauli matrices

$$\sigma_1 = \begin{bmatrix} 0 & 1 \\ 1 & 0 \end{bmatrix}, \quad \sigma_2 = \begin{bmatrix} 0 & -i \\ i & 0 \end{bmatrix}, \quad \sigma_3 = \begin{bmatrix} 1 & 0 \\ 0 & -1 \end{bmatrix}. \quad (\text{A.5})$$

The spin tensor satisfies the relations

$$\sigma^{\mu\nu} = \frac{i}{2}[\gamma^\mu, \gamma^\nu], \quad \sigma_i\sigma_j = \delta_{ij} + i \sum_k \epsilon_{ijk}\sigma_k. \quad (\text{A.6})$$

By defining the projection operators

$$P_R \equiv \begin{bmatrix} 0 & 0 \\ 0 & 1 \end{bmatrix} = \frac{1 + \gamma^5}{2}, \quad P_L \equiv \begin{bmatrix} 1 & 0 \\ 0 & 0 \end{bmatrix} = \frac{1 - \gamma^5}{2}, \quad (\text{A.7})$$

in the Weyl basis the spinor component fields take the following simple form

$$\psi_R = \frac{1 + \gamma^5}{2} \psi_D, \quad \psi_L = \frac{1 - \gamma^5}{2} \psi_D. \quad (\text{A.8})$$

The projection operators satisfy the properties

$$\begin{aligned} P_R + P_L &= 1, \\ (P_R)^2 &= P_R, \\ (P_L)^2 &= P_L. \end{aligned} \quad (\text{A.9})$$

The very important relations also hold true

$$\begin{aligned} \psi_R &= P_L \psi, & \psi_L &= P_R \psi, \\ P_R P_L &= 0, & P_L P_R &= 0. \end{aligned} \quad (\text{A.10})$$

A.2 Trace identities

The Gamma matrices obey the following trace identities

1. The trace of the product of an odd number of γ is 0,
2. $\text{tr}(\gamma^\mu \gamma^\nu) = 4g^{\mu\nu}$,
3. $\text{tr}(\gamma^\mu \gamma^\nu \gamma^\rho \gamma^\sigma) = 4(g^{\mu\nu} g^{\rho\sigma} - g^{\mu\rho} g^{\nu\sigma} + g^{\mu\sigma} g^{\nu\rho})$,
4. $\text{tr}(\gamma^5) = \text{tr}(\gamma^\mu \gamma^\nu \gamma^5) = 0$,
5. $\text{tr}(\gamma^\mu \gamma^\nu \gamma^\rho \gamma^\sigma \gamma^5) = -4i\epsilon^{\mu\nu\rho\sigma}$.

By introducing the Feynman slash notation $\not{a} \equiv \gamma^\mu a_\mu$, one has the properties

$$\not{a} \not{a} = a^\mu a_\mu = a^2, \quad (\text{A.11})$$

$$\not{a} \not{b} + \not{b} \not{a} = 2a \cdot b, \quad (\text{A.12})$$

$$\gamma_\mu \not{a} \gamma^\mu = -2\not{a}, \quad (\text{A.13})$$

$$\gamma_\mu \not{a} \not{b} \gamma^\mu = 4a \cdot b, \quad (\text{A.14})$$

$$\gamma_\mu \not{a} \not{b} \not{c} \gamma^\mu = -2\not{a} \not{b} \not{c}. \quad (\text{A.15})$$

The corresponding trace identities read

$$\text{tr}(\not{a}\not{b}) = 4a \cdot c, \quad (\text{A.16})$$

$$\text{tr}(\gamma_5 \not{a}\not{b}) = 0, \quad (\text{A.17})$$

$$\text{tr}(\not{a}\not{b}\not{c}\not{d}) = 4[(a \cdot b)(c \cdot d) - (a \cdot c)(b \cdot d) + (a \cdot d)(b \cdot c)], \quad (\text{A.18})$$

$$\text{tr}(\gamma_5 \not{a}\not{b}\not{c}\not{d}) = 4i\epsilon_{\mu\nu\rho\sigma}a^\mu b^\nu c^\rho d^\sigma. \quad (\text{A.19})$$

$$(\text{A.20})$$

$$\text{tr}[\gamma^\mu \not{p}_1 \gamma^\nu \not{p}_2] = 4[p_1^\mu p_2^\nu + p_1^\nu p_2^\mu - (p_1 \cdot p_2)g^{\mu\nu}], \quad (\text{A.21})$$

$$\text{tr}[\gamma^\mu(1 - \gamma_5)\not{p}_1 \gamma^\nu(1 - \gamma_5)\not{p}_2] = 2\text{tr}[\gamma^\mu \not{p}_1 \gamma^\nu \not{p}_2] - 8i\epsilon^{\mu\nu\rho\sigma}p_{1\rho}p_{2\sigma}. \quad (\text{A.22})$$

$$\text{tr}[\gamma^\mu \not{p}_1 \gamma^\nu \not{p}_2] \text{tr}[\gamma_\mu \not{p}_3 \gamma_\nu \not{p}_4] = 32[(p_1 \cdot p_3)(p_2 \cdot p_4) + (p_1 \cdot p_4)(p_2 \cdot p_3)], \quad (\text{A.23})$$

$$\text{tr}[\gamma^\mu \not{p}_1 \gamma^\nu \gamma_5 \not{p}_2] \text{tr}[\gamma_\mu \not{p}_3 \gamma_\nu \gamma_5 \not{p}_4] = 32[(p_1 \cdot p_3)(p_2 \cdot p_4) - (p_1 \cdot p_4)(p_2 \cdot p_3)]. \quad (\text{A.24})$$

$$\begin{aligned} \text{tr}[\gamma^\mu(1 - \gamma_5)\not{p}_1 \gamma^\nu(1 - \gamma_5)\not{p}_2] \text{tr}[\gamma_\mu(1 - \gamma_5)\not{p}_3 \gamma_\nu(1 - \gamma_5)\not{p}_4] = \\ 256(p_1 \cdot p_3)(p_2 \cdot p_4). \end{aligned} \quad (\text{A.25})$$

A.3 Mandelstam variables

Assuming the incoming and outgoing neutrinos to have four-momentum $k_i = (E_\nu, \mathbf{k}_i)$ and $k_f = (E'_\nu, \mathbf{k}_f)$ respectively and the incoming and out coming nucleus $p_i = (E_N, \mathbf{p}_i)$ and $p_f = (E'_N, \mathbf{p}_f)$, the Mandelstam variables read

$$\begin{aligned} s &= (k_i + p_i)^2 = M^2 + 2ME_\nu, \\ u &= (p_i - k_f)^2 = M^2 - 2ME'_\nu, \\ t &= (k_i - k_f)^2 = q^2 = -Q^2 = 2M(E'_\nu - E_\nu). \end{aligned} \quad (\text{A.26})$$

Appendix B

B.1 Nuclear matrix elements of the hadronic current

In previous comprehensive $\mu^- \rightarrow e^-$ conversion studies, it has been claimed that the reformulation of the quark-level effective Lagrangian yields the effective nucleon-level Lagrangian written in terms of the nucleon isospin operators as [123, 126, 133, 134, 233]

$$\begin{aligned} \mathcal{L}_{eff}^N = G_\alpha \left[\sum_{A,B} j_\mu^A \left(\alpha_{A,B}^{(0)} J_{(0)}^{B\mu} + \alpha_{A,B}^{(3)} J_{(3)}^{B\mu} \right) + \sum_{C,D} j^C \left(\alpha_{C,D}^{(0)} J_{(0)}^D + \alpha_{C,D}^{(3)} J_{(3)}^D \right) \right. \\ \left. + j_{\mu\nu} \left(\alpha_T^{(0)} J_{(0)}^{\mu\nu} + \alpha_T^{(3)} J_{(3)}^{\mu\nu} \right) \right], \quad \alpha = \text{ph, nph}. \end{aligned} \quad (\text{B.1})$$

Here, the index α refers to the photonic ($\alpha = \text{ph}$) and non-photonic ($\alpha = \text{nph}$) contribution [126]. The components of the isoscalar, $J_{(0)}$, and isovector, $J_{(3)}$, nucleon currents are defined as

$$J_{(k)}^{V\mu} = \bar{N} \gamma^\mu \tau_k N, \quad (\text{B.2})$$

$$J_{(k)}^{A\mu} = \bar{N} \gamma^\mu \gamma_5 \tau_k N, \quad (\text{B.3})$$

$$J_{(k)}^S = \bar{N} \tau_k N, \quad (\text{B.4})$$

$$J_{(k)}^P = \bar{N} \gamma_5 \tau_k N, \quad (\text{B.5})$$

$$J_{(k)}^{\mu\nu} = \bar{N} \sigma^{\mu\nu} \tau_k N, \quad (\text{B.6})$$

with $k = 0, 3$. Each component is separately treated, however not all of them should be taken into account. In fact, the pseudoscalar and tensor nucleon components are negligible. Therefore, at nuclear-level the effective interaction Hamiltonian \hat{H}_{eff} , takes the well-known current-current form [123, 126].

At low and intermediate energies, considered in the present study, any semileptonic process is described by an effective interaction Hamiltonian, written in terms of the leptonic \hat{j}_μ^{lept} and hadronic $\hat{\mathcal{J}}^\mu$ currents as

$$\hat{H}_{eff} = \frac{G}{\sqrt{2}} \int d^3\mathbf{x} \hat{j}_\mu^{lept}(\mathbf{x}) \hat{J}^\mu(\mathbf{x}), \quad (\text{B.7})$$

where $G = G_F$ for neutral-current processes and $G = G_c$ for charged-current processes.

By assuming that the nuclear states $|J^\pi, T\rangle$ are characterised by well-defined energy, momentum, spin J , parity π , and isospin T (J-projected method). In first-quantisation, for the case of free motion of nucleons within the nucleus, the operator of the hadronic current density is defined as

$$\mathcal{J}_\mu(\mathbf{x}) = \sum_{i=1}^A \mathcal{J}_\mu(\mathbf{x}_i) \delta^{(3)}(\mathbf{x} - \mathbf{x}_i) = \sum_{i=1}^A [J_\mu(\mathbf{x}_i) + J_{\mu 5} \mathbf{x}_i] \delta^{(3)}(\mathbf{x} - \mathbf{x}_i), \quad (\text{B.8})$$

where the nuclear matrix elements for J_μ for polar-vector and $J_{\mu 5}$ for axial vector currents respectively, take the form

$$\langle p_f | \hat{J}_\mu^\pm(0) | p_i \rangle = \bar{u}(p_f) [F_1^V \gamma_\mu + F_2^V \sigma_{\mu\nu} q_\nu] \tau_\pm u(p_i), \quad (\text{B.9})$$

$$\langle p_f | \hat{J}_{\mu 5}^\pm(0) | p_i \rangle = \bar{u}(p_f) [F_1^A \gamma_5 \gamma_\mu - i F_P \gamma_5 q_\mu] \tau_\pm u(p_i). \quad (\text{B.10})$$

In the non-relativistic limit (valid for low-momentum transfer), the corresponding single-nucleon matrix elements in the momentum space become

$$J_{0\alpha}^V(\mathbf{q}) = F_1^\alpha \tau_\alpha, \quad (\text{B.11})$$

$$\mathbf{J}_\alpha^V(\mathbf{q}) = \left(\frac{F_1^\alpha}{2M} (2\mathbf{p} + \mathbf{q}) + \frac{F_1^\alpha + F_2^\alpha}{2M} i\boldsymbol{\sigma} \times \mathbf{q} \right) \tau_\alpha, \quad (\text{B.12})$$

$$J_{0\alpha}^A(\mathbf{q}) = \left(\frac{F_A^\alpha}{2M} \boldsymbol{\sigma} \cdot (2\mathbf{p} + \mathbf{q}) - \frac{\omega}{2M} F_P^\alpha \boldsymbol{\sigma} \cdot \mathbf{q} \right) \tau_\alpha, \quad (\text{B.13})$$

$$\mathbf{J}_\alpha^A(\mathbf{q}) = F_A^\alpha \boldsymbol{\sigma} \tau_\alpha. \quad (\text{B.14})$$

Incorporating the previous lines, the latter expressions in position space read

$$J_{0\alpha}^V(\mathbf{r}) = F_1^\alpha \tau_\alpha, \quad (\text{B.15})$$

$$\mathbf{J}_\alpha^V(\mathbf{r}) = \left(-i \frac{F_1^\alpha}{2M} (\vec{\nabla} - \overleftarrow{\nabla}) - \frac{F_1^\alpha + F_2^\alpha}{2M} \boldsymbol{\sigma} \times \vec{\nabla} \right) \tau_\alpha, \quad (\text{B.16})$$

$$J_{0\alpha}^A(\mathbf{r}) = \left(-i \frac{F_A^\alpha}{2M} \boldsymbol{\sigma} \cdot (\vec{\nabla} - \overleftarrow{\nabla}) - i \frac{\omega}{2M} F_P^\alpha \boldsymbol{\sigma} \cdot \vec{\nabla} \right) \tau_\alpha, \quad (\text{B.17})$$

$$\mathbf{J}_\alpha^A(\mathbf{r}) = F_A^\alpha \boldsymbol{\sigma} \tau_\alpha, \quad (\text{B.18})$$

where the isospin index $\alpha = \pm, 0$ denotes the respective transition nature.

The matrix element of the leptonic current, between an initial $|\ell_i\rangle$ and a final state $|\ell_f\rangle$ takes the form

$$\langle \ell_f | \hat{j}_\mu^{\text{lept}} | \ell_i \rangle = \ell_\mu e^{-i\mathbf{q}\cdot\mathbf{x}}. \quad (\text{B.19})$$

For neutrino-nucleus processes, the leptonic matrix elements ℓ^μ can be cast in the form

$$\ell_\mu = \bar{u}(k_f) \gamma_\mu (1 - \gamma_5) u(k_i), \quad (\text{B.20})$$

and the momentum transfer is equal to $q = k_i - k_f = p_f - p_i$.

We proceed by defining a complete orthonormal set of spatial unit vectors. Any vector can be expanded in this set as follows

$$\mathbf{1} = \sum_{\lambda=0,\pm 1} l_\lambda \mathbf{e}_\lambda^\dagger. \quad (\text{B.21})$$

It is convenient to first go from plane polarisation to circular polarisation with the transformation

$$\begin{aligned} \mathbf{e}_{\pm 1} &\equiv \mp \frac{1}{\sqrt{2}} (\mathbf{e}_{\mathbf{q}1} \pm i \mathbf{e}_{\mathbf{q}2}), & \mathbf{e}_0 &\equiv \mathbf{e}_{\mathbf{q}0} \equiv \frac{\mathbf{q}}{|\mathbf{q}|} \equiv \frac{\vec{q}}{\kappa}, \\ \mathbf{e}_\lambda^\dagger \cdot \mathbf{e}_{\lambda'} &\equiv \delta_{\lambda\lambda'}, & \mathbf{e}_\lambda^\dagger &= (-1)^\lambda \mathbf{e}_{-\lambda}. \end{aligned} \quad (\text{B.22})$$

Hence, $l_\lambda = \mathbf{e}_\lambda \cdot \mathbf{1}$ and, $l_{\lambda=0} \equiv \mathbf{e}_0 \cdot \mathbf{1} \equiv l_3$

$$l_{\pm 1} = \mp \frac{1}{\sqrt{2}} (l_1 \pm i l_2), \quad l_0 \equiv l_3. \quad (\text{B.23})$$

In this case the plane wave can be expanded as

$$e^{i\mathbf{q}\cdot\mathbf{x}} = \sum_l i^l \sqrt{4\pi(2l+1)} j_l(\rho) Y_{l0}(\Omega_x), \quad (\text{B.24})$$

with $\rho = \kappa|\mathbf{x}|$ and $\kappa = |\mathbf{q}|$. The vector Spherical Harmonics are defined by the relations [51]

$$\mathbf{Y}_{Jl1}^M \equiv \sum_{m\lambda} \langle lm1\lambda | l1JM \rangle Y_{lm}(\Omega_x) \mathbf{e}_\lambda, \quad \lambda = \pm 1, 0, \quad (\text{B.25})$$

and can be inverted by using the orthogonality properties of the Clebsch-Gordan coefficients

$$Y_{lm} \mathbf{e}_\lambda = \sum_{JM} \langle lm1\lambda | l1JM \rangle \mathbf{Y}_{Jl1}^M. \quad (\text{B.26})$$

The vector Spherical Harmonics project an irreducible tensor operator (ITO) of rank J from any vector density operator in the nuclear Hilbert space. A Combination of Eq.(B.24) with Eq.(B.26) and using of the properties of the Clebsch-Gordan coefficients yields

$$\mathbf{e}_{\mathbf{q}\lambda} e^{i\mathbf{q}\cdot\mathbf{x}} = \sum_l \sum_J i^l \sqrt{4\pi(2l+1)} j_l(\rho) \langle l01\lambda | l1J\lambda \rangle \mathbf{Y}_{Jl1}^\lambda(\Omega_x). \quad (\text{B.27})$$

Therefore, the Clebsch-Gordan coefficient limits the sum on l to three terms, $l = J$ and $J \pm 1$. Evaluating for $\lambda = \pm 1$, one finds

$$\mathbf{e}_{\mathbf{q}\lambda} e^{i\mathbf{q}\cdot\mathbf{x}} = - \sum_{J \geq 1}^{\infty} \sqrt{2\pi(2J+1)} i^J \left\{ \lambda j_J(\rho) \mathbf{Y}_{JJ1}^\lambda + \frac{1}{\kappa} \nabla \times [j_J(\rho) \mathbf{Y}_{JJ1}^\lambda] \right\}, \quad (\text{B.28})$$

and for $\lambda = 0$

$$\mathbf{e}_{\mathbf{q}0} e^{i\mathbf{q}\cdot\mathbf{x}} = \frac{-i}{\kappa} \sum_{J \geq 0}^{\infty} \sqrt{4\pi(2J+1)} i^J \nabla [j_J(\rho) Y_{J0}]. \quad (\text{B.29})$$

Thus, by substituting the latter results to

$$\begin{aligned} \langle f | \hat{H}_{eff} | i \rangle &= \frac{G}{\sqrt{2}} \ell^\mu \int d^3\mathbf{x} e^{-i\mathbf{q}\cdot\mathbf{x}} \langle f | \hat{\mathcal{J}}_\mu(\mathbf{x}) | i \rangle, \\ &= \frac{G}{\sqrt{2}} \int d^3\mathbf{x} e^{-i\mathbf{q}\cdot\mathbf{x}} [l_0 \mathcal{J}_0(\mathbf{x})_{fi} - \mathbf{1} \cdot \mathcal{J}(\mathbf{x})_{fi}] \end{aligned} \quad (\text{B.30})$$

one finds Eq.(4.4)

$$\begin{aligned} \langle f | \hat{H}_{eff} | i \rangle &= -\frac{G}{\sqrt{2}} \langle f | \left\{ \sum_{J \geq 0} \sqrt{4\pi(2J+1)} (-i)^J \left(l_3 \hat{\mathcal{L}}_{J0}(\kappa) - l_0 \hat{\mathcal{M}}_{J0}(\kappa) \right) \right. \\ &\quad \left. + \sum_{\lambda=\pm 1} \sum_{J \geq 1} \sqrt{2\pi(2J+1)} (-i)^J l_\lambda \left(\lambda \hat{\mathcal{T}}_{J-\lambda}^{mag}(\kappa) + \hat{\mathcal{T}}_{J-\lambda}^{el}(\kappa) \right) \right\} | i \rangle. \end{aligned} \quad (\text{B.31})$$

B.2 Compact expressions of the reduced transition matrix elements

The single-particle transition matrix elements $\langle j_1 || T_i^J || j_2 \rangle$ of the operators given in Eqs.(4.29)–(4.35) are compactly written as [135]

$$\langle j_1 || T^J || j_2 \rangle = e^{-y} y^{\beta/2} \sum_{\mu=0}^{n_{max}} \mathcal{P}_\mu^J y^\mu, \quad y = (\kappa b/2)^2 \quad (\text{B.32})$$

where $n_{max} = (N_1 + N_2 - \beta)/2$ and $N_i = 2n_i + l_i$ indicates the Harmonic Oscillator quanta of the i -th level.

As a first step of our calculational procedure, we have constructed an efficient modern Mathematica code to compute the reduced ME for all basic operators T_i^J and for any configuration $(j_1, j_2)J$, using the analytical expressions of Eq.(4.28).

As expected, the coefficients obtained in Ref. [135, 234], coincide with those of the present work. As an example, the coefficients $\mathcal{P}_\mu^{6,J}$ for the reduced ME of the operator $T_6^J \equiv \Delta_M^J$ are tabulated in Table B.1. We mention however, that in Ref. [234], only configurations for which $N_1 - N_2 \leq 3$ are included, while in our code there is not any similar restriction. We conclude that all geometrical coefficients \mathcal{P}_μ^J are simple rational numbers for the diagonal elements (not shown here), or square roots of rational numbers for the non-diagonal elements. The double differential cross sections of Eq.(4.37) from which the nuclear calculations start, includes reduced ME of the form $|\langle j_1 || T_i^J || j_2 \rangle|^2$, hence their evaluation is crucial. We currently perform realistic nuclear structure calculations for coherent cross sections that depend on the nuclear form factors for protons and neutrons. The appropriate code, provides improved results, by a refined version of the fractional occupation probabilities method of Ref. [57].

$(n_1 l_1)_{j_1} - (n_2 l_2)_{j_2}$	J	$\mu = 0$	$\mu = 1$	$\mu = 2$	$\mu = 3$	$\mu = 4$
$0p_{1/2} - 0s_{1/2}$	1	$\sqrt{\frac{1}{6}}$				
$0p_{3/2} - 0s_{1/2}$	1	$-\sqrt{\frac{1}{3}}$	0			
$0d_{5/2} - 0s_{1/2}$	2	$-\sqrt{\frac{3}{5}}$	0			
$0f_{5/2} - 0p_{1/2}$	2	$-\sqrt{\frac{7}{5}}$	$\sqrt{\frac{20}{63}}$	0		
$0d_{7/2} - 0p_{1/2}$	4	$\sqrt{\frac{8}{63}}$	0			
$1p_{3/2} - 1s_{1/2}$	1	$-\sqrt{\frac{5}{9}}$	$\sqrt{\frac{4}{45}}$	$-\sqrt{\frac{4}{45}}$	0	
$0d_{3/2} - 0f_{7/2}$	3	$-\sqrt{\frac{16}{175}}$	$\sqrt{\frac{4}{45}}$	$-\sqrt{\frac{16}{1575}}$	0	
$1f_{5/2} - 2p_{3/2}$	2	0	$\sqrt{\frac{8}{7}}$	$-\sqrt{\frac{288}{343}}$	$\sqrt{\frac{2888}{27783}}$	$-\sqrt{\frac{32}{27783}}$

Table B.1: The coefficients $\mathcal{P}_\mu^{6,J}$ for the the $\langle j_1 || \Delta_M^J || j_2 \rangle$.

B.3 Nucleon form factors

The free nucleon form factors $F_X(Q^2)$, $X=1, A, P$ and $\mu^V(Q^2)$ entering Eqs.(4.16)–(4.23) are written as functions of the four momentum transfer Q^2 , as

$$F_1^V(Q^2) = 1.000 \left[1 + \left(\frac{Q}{840 \text{ MeV}} \right)^2 \right]^{-2} \quad (\text{B.33})$$

$$\mu^V(Q^2) = 4.706 \left[1 + \left(\frac{Q}{840 \text{ MeV}} \right)^2 \right]^{-2} \quad (\text{B.34})$$

$$F_A(Q^2) = g_A \left[1 + \left(\frac{Q}{1032 \text{ MeV}} \right)^2 \right]^{-2} \quad (\text{B.35})$$

$$F_P(Q^2) = \frac{2 m_N F_A(Q^2)}{Q^2 + m_\pi^2} \quad (\text{B.36})$$

where m_N is the nucleon mass and g_A is the free nucleon coupling constant.

Appendix C

C.1 Clebsch-Gordan coefficients

Let us consider two commuting angular momenta \mathbf{J}_1 and \mathbf{J}_2 , where $\mathbf{J}_1 + \mathbf{J}_2 = \mathbf{J}$ with the corresponding quantum numbers j_1, j_2, j and projections m_1, m_2, m . For the total angular momentum, the product eigenstates

$$|j_1 m_1 j_2 m_2\rangle = |j_1 m_1\rangle |j_2 m_2\rangle, \quad (\text{C.1})$$

form an orthonormal set if each state $|j_i m_i\rangle$ forms separately an orthonormal set in the i -th subspace. This forms complete set of states, namely the uncoupled basis. In the case of coupled angular momentum, the complete set of states forms the coupled basis denoted by

$$|j_1 j_2 j m\rangle. \quad (\text{C.2})$$

Thus the two basis are related through the relation

$$\begin{aligned} |j_1 j_2 j m\rangle &= \sum_{m_1, m_2} |j_1 m_1 j_2 m_2\rangle \langle j_1 m_1 j_2 m_2 | j_1 j_2 j m\rangle \\ &\equiv \sum_{m_1, m_2} (j_1 m_1 j_2 m_2 | j m) |j_1 j_2 j m\rangle. \end{aligned} \quad (\text{C.3})$$

The quantity $(j_1 m_1 j_2 m_2 | j m)$ is referred to as the Clebsch-Gordan coefficient and obeys the addition law

$$(j_1 m_1 j_2 m_2 | j m) = 0 \quad \text{unless} \quad m_1 + m_2 = m, \quad (\text{C.4})$$

and the triangular condition

$$|j_1 - j_2| \leq j \leq j_1 + j_2 \equiv \Delta(j_1 j_2; j). \quad (\text{C.5})$$

The Clebsch-Gordan coefficients $(j_1 m_1 j_2 m_2 | j m)$ are real

$$(j_1 j_1 j_2 j_2 | j_1 + j_2 j_1 + j_2) = 1, \quad (j_1 m_1 j_2 - j_2 | j m) \geq 0. \quad (\text{C.6})$$

and fulfil the constraint $j_1 + j_2 + j = \text{integer}$. These conditions fix the phases of all Clebsch-Gordan coefficients.

The orthogonality of the Clebsch-Gordan coefficients is expressed as

$$\sum_{m_1 m_2} (j_1 m_1 j_2 m_2 | j m) (j_1 m_1 j_2 m_2 | j' m') = \delta_{j j'} \delta_{m m'}, \quad (\text{C.7})$$

while starting from the completeness of the coupled basis

$$\sum_{j m} |j_1 j_2 j m\rangle \langle j_1 j_2 j m| = 1, \quad (\text{C.8})$$

one derives the completeness property of the Clebsch-Gordan coefficients

$$\sum_{j m} (j_1 m_1 j_2 m_2 | j m) (j_1 m'_1 j_2 m'_2 | j m) = \delta_{m_1 m'_1} \delta_{m_2 m'_2}. \quad (\text{C.9})$$

C.2 3-j symbols

The 3-j symbols [35] entering the Wigner-Eckart theorem (see Sect. C.6) and employed for the coupling of two angular momenta j_1 and j_2 with $j_3 = j_1 + j_2$, are related to the Clebsch-Gordan coefficients as

$$\begin{pmatrix} j_1 & j_2 & j_3 \\ m_1 & m_2 & m_3 \end{pmatrix} = \begin{cases} (-1)^{j_1 - j_2 - m_3} [\hat{j}_3]^{-1} (j_1 m_1 j_2 m_2 | j_3 - m_3), \\ 0 \quad (\text{if } m_1 + m_2 + m_3 \neq 0 \text{ and } j_1 + j_2 \neq j_3). \end{cases} \quad (\text{C.10})$$

The inverse relation can be found by noting that $j_1 - j_2 - m_3$ is an integer and making the substitution $m_3 \rightarrow -m_3$, we find

$$(j_1 m_1 j_2 m_2 | j_3 m_3) = (-1)^{j_1 - j_2 + m_3} \hat{j}_3 \begin{pmatrix} j_1 & j_2 & j_3 \\ m_1 & m_2 & -m_3 \end{pmatrix}, \quad (\text{C.11})$$

with the usual hat notation, $\hat{j} = \sqrt{2j+1}$.

C.3 6-j symbols

For three angular momenta coupling j_1, j_2, j_3 two couplings are required. For example, from the coupling of $j_1 + j_2$ one gets j_{12} which couples to j_3 giving j (one would arrive at the same result if the coupling $j_2 + j_3$ giving j_{23} which couples to j_1 to give j). This coupling is expressed in terms of the 6-j symbols as [35]

$$\begin{aligned} |j_1, j_2 j_3(j_{23}); j m\rangle &= \sum_{j_{12}} |j_1 j_2(j_{12}) j_3; j m\rangle \\ &\quad \times \langle j_1 j_2(j_{12}) j_3; j m | j_1, j_2 j_3(j_{23}); j m\rangle \\ &\equiv \sum_{j_{12}} (-1)^{j_1 + j_2 + j_3 + j} \hat{j}_{12} \hat{j}_{23} \begin{Bmatrix} j_1 & j_2 & j_{12} \\ j_3 & j & j_{23} \end{Bmatrix} |j_1 j_2(j_{12}) j_3; j m\rangle. \end{aligned} \quad (\text{C.12})$$

The 6-j symbols satisfy the triangular inequalities

$$\left\{ \begin{array}{ccc} j_1 & j_2 & j_{12} \\ j_3 & j & j_{23} \end{array} \right\} = 0 \quad \text{unless} \quad \begin{cases} \Delta(j_1 j_2; j_{12}), \Delta(j_3 j; j_{23}), \\ \Delta(j_3 j_2; j_{23}), \Delta(j_1 j; j_{23}). \end{cases} \quad (\text{C.13})$$

C.4 9-j symbols

For the case of four angular momenta coupling j_1, j_2, j_3, j_4 the following couplings hold true

- $j_1 + j_3 = j_{13}, j_2 + j_4 = j_{24}, j_{13} + j_{24} = j$,
- $j_1 + j_2 = j_{12}, j_3 + j_4 = j_{34}, j_{12} + j_{34} = j$.

This coupling is expressed in terms of the 9-j symbols as [35]

$$\begin{aligned} |j_1, j_3(j_{13})j_2j_4(j_{24}); jm\rangle &= \sum_{j_{12}j_{34}} |j_1j_2(j_{12})j_3j_4(j_{34}); jm\rangle \\ &\quad \times \langle j_1j_2(j_{12})j_3j_4(j_{34}); jm | j_1j_3(j_{13})j_2j_4(j_{24}); jm\rangle \\ &\equiv \sum_{j_{12}j_{34}} \hat{j}_{12}\hat{j}_{34}\hat{j}_{13}\hat{j}_{24} \left\{ \begin{array}{ccc} j_1 & j_2 & j_{12} \\ j_3 & j_4 & j_{34} \\ j_{13} & j_{24} & j \end{array} \right\} |j_1j_2(j_{12})j_3j_4(j_{34}); jm\rangle. \end{aligned} \quad (\text{C.14})$$

The 9-j symbols satisfy the triangular inequalities

$$\left\{ \begin{array}{ccc} j_1 & j_2 & j_{12} \\ j_3 & j_4 & j_{34} \\ j_{13} & j_{24} & j \end{array} \right\} = 0 \quad \text{unless} \quad \begin{cases} \Delta(j_1 j_2; j_{12}), \Delta(j_3 j_4; j_{34}), \Delta(j_{13} j_{24}; j), \\ \Delta(j_1 j_3; j_{13}), \Delta(j_2 j_4; j_{24}), \Delta(j_{12} j_{34}; j). \end{cases} \quad (\text{C.15})$$

C.5 Racah W-coefficients

The Racah coefficients differ from the 6-j symbols by a phase factor

$$\left\{ \begin{array}{ccc} j_1 & j_2 & j_{12} \\ j_3 & j & j_{23} \end{array} \right\} = (-1)^{j_1+j_{12}+j_3+j_{23}} W(j_1 j_2 j j_3; j_{12} j_{23}). \quad (\text{C.16})$$

The Racah coefficients are combined to the recoupling coefficients through the following relations

$$W(j_1 j_2 j j_3; j_{12} j_{23}) \equiv \left[\hat{j}_{12} \right]^{-1} \left[\hat{j}_{23} \right]^{-1} \langle (j_1, (j_2 j_3) j_{23}) j | ((j_1 j_2) j_{12}, j_3) j \rangle. \quad (\text{C.17})$$

C.6 The Wigner-Eckart theorem

The matrix elements of irreducible tensor operators are expressed in terms of the 3-j symbols as

$$\langle j'm'|\hat{\mathcal{T}}_{JM}|jm\rangle = (-1)^{j'-m'} \begin{pmatrix} j' & J & j \\ -m' & M & m \end{pmatrix} \langle j'|\|\hat{\mathcal{T}}_J\|j\rangle, \quad (\text{C.18})$$

where the quantity $\langle j'|\|\hat{\mathcal{T}}_J\|j\rangle$ is the so-called reduced matrix element. The following selection rules apply

$$\langle j'm'|\hat{\mathcal{T}}_{JM}|jm\rangle = 0 \begin{cases} \Delta(jJ; j), \\ m + M = m'. \end{cases} \quad (\text{C.19})$$

C.7 Products of coupled tensor operators

Consider the spherical operators, \mathbf{T}_{J_1} of rank J_1 and \mathbf{T}_{J_2} of rank J_2 . In this case we define the spherical tensor \mathbf{T}_J as their tensor product or rank J if the following condition is fulfilled

$$T_{JM} = \sum_{M_1 M_2} (J_1 M_1 J_2 M_2 | JM) T_{J_1 M_1} T_{J_2 M_2} \equiv [\mathbf{T}_{J_1} \mathbf{T}_{J_2}]_{JM}. \quad (\text{C.20})$$

Then, the scalar product of two spherical tensors reads

$$\mathbf{T}_J \cdot \mathbf{S}_J = (-1)^J \hat{J} [\mathbf{T}_J \mathbf{S}_J]_{00} = \sum_M (-1)^M T_{JM} S_{J,-M}, \quad (\text{C.21})$$

and the corresponding cross product takes form

$$(\mathbf{T} \times \mathbf{S})_M = -i\sqrt{2} [\mathbf{T}_1 \mathbf{S}_1]_{1M}. \quad (\text{C.22})$$

Appendix D

D.1 Woods-Saxon wavefunctions

The angular momentum eigenstates of the operators \mathbf{l}^2 and $\mathbf{l} \cdot \mathbf{s}$ are the states $|l\frac{1}{2}jm\rangle$. The respective eigenvalues are

$$\begin{aligned}
 \mathbf{l}^2|l\frac{1}{2}jm\rangle &= l(l+1)\hbar^2|l\frac{1}{2}jm\rangle, \\
 \mathbf{s}^2|l\frac{1}{2}jm\rangle &= \frac{3}{4}\hbar^2|l\frac{1}{2}jm\rangle, \\
 \mathbf{j}^2|l\frac{1}{2}jm\rangle &= j(j+1)\hbar^2|l\frac{1}{2}jm\rangle, \\
 j_Z|l\frac{1}{2}jm\rangle &= m\hbar|l\frac{1}{2}jm\rangle.
 \end{aligned} \tag{D.1}$$

Using the fact that $\mathbf{j}^2 = (\mathbf{l} + \mathbf{s})^2 = \mathbf{l}^2 + 2\mathbf{l} \cdot \mathbf{s} + \mathbf{s}^2$, the above expressions, lead to

$$\mathbf{l} \cdot \mathbf{s}|l\frac{1}{2}jm\rangle = \frac{1}{2}[j(j+1) - l(l+1) - \frac{3}{4}]\hbar^2|l\frac{1}{2}jm\rangle. \tag{D.2}$$

Then, the Schrödinger equation for the Woods-Saxon Hamiltonian

$$h = \frac{-\hbar^2}{2m_N}(\nabla_r^2 - \frac{\mathbf{l}^2/\hbar^2}{r^2}) + V_{\text{WS}}(r) + V_c(r) + V_{ls}(r)\mathbf{l} \cdot \mathbf{s} \tag{D.3}$$

becomes

$$\begin{aligned}
 h|nl\frac{1}{2}jm\rangle &= \left\{ \frac{-\hbar^2}{2m_N} \left[\nabla_r^2 - \frac{l(l+1)}{r^2} \right] + V_{\text{WS}}(r) + V_c(r) \right. \\
 &\quad \left. + \frac{1}{2} \left[j(j+1) - l(l+1) - \frac{3}{4} \right] \hbar^2 V_{ls}(r) \right\} |nl\frac{1}{2}jm\rangle, \\
 &\equiv h_{lj}(r)|nl\frac{1}{2}jm\rangle, \\
 &= \varepsilon_{nlj}|nl\frac{1}{2}jm\rangle,
 \end{aligned} \tag{D.4}$$

where $\nabla_r^2 = \frac{1}{r^2} \frac{d}{dr} (r^2 \frac{d}{dr})$. In the above expression with $h_{lj}(r)$ it is indicated that the quantum numbers l and j are parameters of the radial Hamiltonian. In the single-nucleon coordinate space the radial wavefunction $f_{nlj}(r)$ is written as ¹

$$h_{lj}(r)f_{nlj}(r) = \varepsilon_{nlj}f_{nlj}(r). \quad (\text{D.5})$$

The above differential equation is solved for the eigenvalues ε_{nlj} and the eigenfunctions $f_{nlj}(r)$ (orthogonal with respect to n), whereas the orthogonality with respect to l, j is satisfied as follows

$$\int_0^\infty r^2 f_{nlj}(r) f_{n'lj}(r) = \delta_{nn'}. \quad (\text{D.6})$$

D.2 Harmonic Oscillator wavefunctions

Apart from direct numerical methods, the radial differential equation (D.5) may be solved by writing the wavefunctions $f_{nlj}(r)$ in terms of linear combinations of the Harmonic Oscillator wavefunctions, $g_{\nu l}(r)$ in the form

$$f_{nlj}(r) = \sum_{\nu} A_{\nu}^{(nlj)} g_{\nu l}(r), \quad (\text{D.7})$$

up to a normalisation condition $A_{\nu}^{(nlj)}$ satisfying

$$\sum_{\nu} [A_{\nu}^{(nlj)}]^2 = 1. \quad (\text{D.8})$$

The solution is found through the diagonalisation

$$\langle \nu' | h_{lj}(r) | \nu \rangle = \int_0^\infty dr r^2 g_{\nu' l}(r) h_{lj}(r) g_{\nu l}(r), \quad (\text{D.9})$$

and therefore transforming the Hamiltonian to the Harmonic Oscillator basis.

The three dimensional Harmonic Oscillator potential is defined as (see also Sect. 3.3)

$$V_{\text{HO}}(r) = -V_1 + kr^2 = -V_1 + \frac{1}{2}m_N\omega^2 r^2, \quad (\text{D.10})$$

where V_1 and k are fitting parameters. For this potential, the Harmonic Oscillator wavefunctions, $g_{nl}(r)$, are solutions of the radial Schrödinger equation

$$\frac{-\hbar^2}{2m_N} \left[\nabla_r^2 - \frac{l(l+1)}{r^2} \right] g_{nl}(r) - V_1 + \frac{1}{2}m_N\omega^2 r^2 g_{nl}(r) = \varepsilon_{nl} g_{nl}(r), \quad (\text{D.11})$$

with the energy eigenvalues

$$\varepsilon_{nl} = -V_1 + (N + \frac{3}{2})\hbar\omega = -V_1 + (2n + l + \frac{3}{2})\hbar\omega. \quad (\text{D.12})$$

¹Note that, $|nl\frac{1}{2}jm\rangle = f_{nlj}(r)|l\frac{1}{2}jm\rangle$

We employ the usual convention for the definition Major Harmonic Oscillator quantum number, N , as

$$N = 2n + l, \quad n = 0, 1, 2, 3, \dots, \quad (\text{D.13})$$

and then, the wavefunction $g_{nl}(r)$ is written explicitly in terms of the Laguerre polynomials, $L_n^{(l+\frac{1}{2})}(x)$, and the Gamma function $\Gamma(x)$ according to the relation

$$g_{nl}(r) = \sqrt{\frac{2n!}{b^3 \Gamma(n + l + \frac{3}{2})}} \left(\frac{r}{b}\right)^l e^{-r^2/2b^2} L_n^{(l+\frac{1}{2})}(r^2/b^2). \quad (\text{D.14})$$

The associated Laguerre polynomials are more conveniently written as

$$L_n^{l+1/2}(x) = \sum_{m=0}^n \frac{(-)^m}{m!} \binom{n+l+1/2}{n-m} x^m = \sum_{m=0}^n \Lambda_m(nl) x^m, \quad (\text{D.15})$$

with

$$\Lambda_m(nl) = \frac{(-)^m}{m!} \binom{n+l+1/2}{n-m}. \quad (\text{D.16})$$

[see also Eq.(3.136)]. The parameter b , namely the oscillator length, which characterises the width of the Oscillator potential reads

$$b = \sqrt{\frac{\hbar}{m_N \omega}}. \quad (\text{D.17})$$

In our calculations we use $\hbar\omega = 41 A^{-1/3}$ MeV and $b = 1.005 A^{-1/6}$ fm. Further corrections, imposed due to center-of-mass motion and the finite nucleon size are addressed in Ref. [57]. The oscillator functions obey the orthogonality relation

$$\int_0^\infty dr r^2 g_{nl}(r) g_{n'l}(r) = \delta_{nn'}. \quad (\text{D.18})$$

Furthermore, it is possible to extract numerical values for $g_{nl}(r)$ by introducing the auxiliary functions $v_{nl}(r)$ as

$$g_{nl}(r) = \sqrt{\frac{2^{l+2-n} (2n+2l+1)!!}{b^3 \sqrt{\pi} n! [(2l+1)!!]^2}} \left(\frac{r}{b}\right)^l e^{-r^2/2b^2} v_{nl}(r^2/b^2), \quad (\text{D.19})$$

as well as the recursion relations

$$\begin{aligned} v_{n,l-1}(x) &= v_{n-1,l-1}(x) - 2x v_{n-1,l}(x) / (2l+1), \\ v_{n,l}(x) &= [(2l+1)v_{n,l-1}(x) + 2n v_{n-1,l}(x)] / (2n+2l+1). \end{aligned} \quad (\text{D.20})$$

D.3 Quasi-boson approximation (QBA)

The QRPA states $|\omega\rangle$ must be orthonormal. Thus, recalling the QRPA-phonon creation operator, Q_ω^\dagger , given in Eq.(3.107)

$$Q_\omega^\dagger = \sum_{a \leq b} \left[X_{ab}^\omega A_{ab}^\dagger(JM) - Y_{ab}^\omega \tilde{A}_{ab}(JM) \right], \quad (\text{D.21})$$

we have

$$\begin{aligned} \delta_{\omega\omega'} &= \langle \omega | \omega' \rangle = \langle QRPA | Q_\omega Q_{\omega'}^\dagger | QRPA \rangle = \langle QRPA | \left[Q_\omega Q_{\omega'}^\dagger \right] | QRPA \rangle \\ &= \sum_{\substack{a \leq b \\ c \leq d}} \left\{ X_{ab}^{\omega*} X_{cd}^{\omega'} \langle QRPA | \left[A_{ab}(JM), A_{cd}^\dagger(J'M') \right] | QRPA \rangle \right. \\ &\quad \left. + Y_{ab}^{\omega*} X_{cd}^{\omega'} \langle QRPA | \left[\tilde{A}_{ab}^\dagger(JM), \tilde{A}_{cd}(J'M') \right] | QRPA \rangle \right\}. \quad (\text{D.22}) \end{aligned}$$

According to the QBA the correlated QRPA vacuum, $|QRPA\rangle$, is approximated with the $|BCS\rangle$ vacuum. Thus, using

$$\begin{aligned} \langle BCS | \left[A_{ab}(JM), A_{cd}^\dagger(J'M') \right] | BCS \rangle &= \delta_{ac} \delta_{bd} \delta_{JJ'} \delta_{MM'}, \\ \langle BCS | \left[\tilde{A}_{ab}^\dagger(JM), \tilde{A}_{cd}(J'M') \right] | BCS \rangle &= \delta_{ac} \delta_{bd} \delta_{JJ'} \delta_{MM'}, \end{aligned} \quad (\text{D.23})$$

we arrive at the relations

$$\begin{aligned} \langle QRPA | \left[A_{ab}(JM), A_{cd}^\dagger(J'M') \right] | QRPA \rangle \\ \approx^{\text{QBA}} \langle BCS | \left[A_{ab}(JM), A_{cd}^\dagger(J'M') \right] | BCS \rangle \\ = \delta_{ac} \delta_{bd} \delta_{JJ'} \delta_{MM'} \quad (a \leq b, c \leq d), \end{aligned} \quad (\text{D.24})$$

$$\begin{aligned} \langle QRPA | \left[\tilde{A}_{ab}^\dagger(JM), \tilde{A}_{cd}(J'M') \right] | QRPA \rangle \\ \approx^{\text{QBA}} \langle BCS | \left[\tilde{A}_{ab}^\dagger(JM), \tilde{A}_{cd}(J'M') \right] | BCS \rangle \\ = -\delta_{ac} \delta_{bd} \delta_{JJ'} \delta_{MM'} \quad (a \leq b, c \leq d). \end{aligned} \quad (\text{D.25})$$

In this approximation, Eq.(D.22) becomes

$$\delta_{\omega\omega'} = \delta_{nn'} \delta_{JJ'} \delta_{MM'} \delta_{\pi\pi'} = \delta_{JJ'} \delta_{MM'} \delta_{\pi\pi'} \sum_{a \leq b} (X_{ab}^{\omega*} X_{ab}^{\omega'} - Y_{ab}^{\omega*} Y_{ab}^{\omega'}). \quad (\text{D.26})$$

Thus, we obtain Eq.(3.116), i.e. the orthogonality relation of the QRPA

$$\sum_{a \leq b} \left(X_{ab}^{nJ^\pi*} X_{ab}^{n'J^\pi} - Y_{ab}^{nJ^\pi*} Y_{ab}^{n'J^\pi} \right) = \delta_{nn'}. \quad (\text{D.27})$$

The completeness relations are derived as follows. The QBA result in Eq.(D.24) gives

$$\begin{aligned}\delta_{ac}\delta_{bd} &= \langle QRPA | \left[A_{ab}(JM), A_{cd}^\dagger(JM) \right] | QRPA \rangle \\ &= \langle QRPA | A_{ab}(JM), A_{cd}^\dagger(JM) | QRPA \rangle \\ &\quad - \langle QRPA | \left[A_{cd}^\dagger(JM), A_{ab}(JM) \right] | QRPA \rangle,\end{aligned}\tag{D.28}$$

with the restrictions $a \leq b, c \leq d$. For the QRPA states

$$\begin{aligned}|\omega\rangle &\equiv |nJ^\pi M\rangle = Q_\omega^\dagger |QRPA\rangle, \\ |\tilde{\omega}\rangle &\equiv (-1)^{J+M} |nJ^\pi - M\rangle \equiv \tilde{Q}_\omega^\dagger |QRPA\rangle.\end{aligned}\tag{D.29}$$

with fixed values for J^π and M , the completeness relations read

$$\begin{aligned}\sum_n |\omega\rangle \langle \omega| &= \sum_n |nJ^\pi M\rangle \langle nJ^\pi M| = 1, \\ \sum_n |\tilde{\omega}\rangle \langle \tilde{\omega}| &= \sum_n |nJ^\pi - M\rangle \langle nJ^\pi - M| = 1.\end{aligned}\tag{D.30}$$

The two latter expressions together with Eq.(D.28) give

$$\begin{aligned}\delta_{ac}\delta_{bd} &= \sum_n \langle QRPA | A_{ab}(JM) Q_\omega^\dagger | QRPA \rangle \langle QRPA | Q_\omega A_{cd}^\dagger(JM) | QRPA \rangle \\ &\quad - \sum_n \langle QRPA | A_{cd}^\dagger(JM) \tilde{Q}_\omega^\dagger | QRPA \rangle \langle QRPA | \tilde{Q}_\omega A_{ab}(JM) | QRPA \rangle, \\ &= \sum_n \langle QRPA | \left[A_{ab}(JM), Q_\omega^\dagger \right] | QRPA \rangle \langle QRPA | \left[Q_\omega, A_{cd}^\dagger(JM) \right] | QRPA \rangle \\ &\quad - \sum_n \langle QRPA | \left[A_{cd}^\dagger(JM), \tilde{Q}_\omega^\dagger \right] | QRPA \rangle \langle QRPA | \left[\tilde{Q}_\omega, A_{ab}(JM) \right] | QRPA \rangle.\end{aligned}\tag{D.31}$$

Since the scattering amplitudes X and Y are independent of M , the insertion the expanded phonon operators together with Eq.(D.23) and the application of the

QBA to the commutators, yields

$$\begin{aligned}
\delta_{ac}\delta_{bd} &\stackrel{\text{QBA}}{\approx} \sum_n \sum_{\substack{a' \leq b' \\ c' \leq d'}} X_{a'b'}^\omega X_{c'd'}^{\omega*} \langle BCS | \left[A_{ab}(JM), A_{a'b'}^\dagger(JM) \right] | BCS \rangle \\
&\quad \times \langle BCS | \left[A_{c'd'}(JM), A_{cd}^\dagger(JM) \right] | BCS \rangle \\
&\quad - \sum_n \sum_{\substack{a' \leq b' \\ c' \leq d'}} (-Y_{c'd'}^\omega) (-Y_{a'b'}^{\omega*}) \langle BCS | \left[A_{cd}^\dagger(JM), A_{c'd'}(JM) \right] | BCS \rangle \\
&\quad \times \langle BCS | \left[A_{a'b'}^\dagger(JM), A_{ab}(JM) \right] | BCS \rangle \\
&= \sum_n (X_{ab}^\omega X_{cd}^{\omega*} - Y_{ab}^{\omega*} Y_{cd}^\omega) \\
&= \sum_n (X_{ab}^{nJ^\pi} X_{cd}^{nJ^{\pi*}} - Y_{ab}^{nJ^{\pi*}} Y_{cd}^{nJ^\pi}) .
\end{aligned} \tag{D.32}$$

The last result coincides with the first QRPA completeness relation that is given in Eq.(3.117). For the second completeness relation, working in a similar manner we have

$$\begin{aligned}
0 &= \langle QRPA | \left[A_{ab}(JM), \tilde{A}_{cd}(JM) \right] | QRPA \rangle \\
&= \sum_n \langle QRPA | A_{ab}(JM) Q_\omega^\dagger | QRPA \rangle \langle QRPA | Q_\omega \tilde{A}_{cd}(JM) | QRPA \rangle \\
&\quad - \sum_n \langle QRPA | \tilde{A}_{cd}(JM) \tilde{Q}_\omega^\dagger | QRPA \rangle \langle QRPA | \tilde{Q}_\omega A_{ab}(JM) | QRPA \rangle .
\end{aligned} \tag{D.33}$$

As in the previous case, expanding the phonon operator and employing the QBA, we get

$$\begin{aligned}
0 &\stackrel{\text{QBA}}{\approx} \sum_n \sum_{\substack{a' \leq b' \\ c' \leq d'}} X_{a'b'}^\omega (-Y_{c'd'}^{\omega*}) \langle BCS | \left[A_{ab}(JM), A_{a'b'}^\dagger(JM) \right] | BCS \rangle \\
&\quad \times \langle BCS | \left[\tilde{A}_{c'd'}^\dagger(JM), \tilde{A}_{cd}(JM) \right] | BCS \rangle \\
&\quad - \sum_n \sum_{\substack{a' \leq b' \\ c' \leq d'}} X_{c'd'}^\omega (-Y_{a'b'}^{\omega*}) \langle BCS | \left[\tilde{A}_{cd}(JM), \tilde{A}_{c'd'}^\dagger(JM) \right] | BCS \rangle \\
&\quad \times \langle BCS | \left[A_{a'b'}^\dagger(JM), A_{ab}(JM) \right] | BCS \rangle \\
&= \sum_n (X_{ab}^\omega Y_{cd}^{\omega*} - Y_{ab}^{\omega*} X_{cd}^\omega) \\
&= \sum_n (X_{ab}^{nJ^\pi} Y_{cd}^{nJ^{\pi*}} - Y_{ab}^{nJ^{\pi*}} X_{cd}^{nJ^\pi}) ,
\end{aligned} \tag{D.34}$$

which nothing else but the second completeness relation of the QRPA given in Eq.(3.118).

D.4 Coefficients entering the quasi-particle representation of pp - nn QRPA

The residual two-body interaction with respect to the BCS vacuum is given by Eq.(3.61)

$$V_{\text{res}} = \frac{1}{4} \sum_{\alpha\beta\gamma\delta} \bar{v}_{\alpha\beta\gamma\delta} \mathcal{N} \left[c_{\alpha}^{\dagger} c_{\beta}^{\dagger} c_{\delta} c_{\gamma} \right]_{BCS} . \quad (\text{D.35})$$

By substitution of the Bogoliubov-Valatin (BV) transformation of Eq.(3.21) into the latter, we get

$$V_{\text{res}} = \frac{1}{4} \sum_{\alpha\beta\gamma\delta} \bar{v}_{\alpha\beta\gamma\delta} \mathcal{N} \left[(u_a a_{\alpha}^{\dagger} - v_a \tilde{a}_{\alpha}) (u_b a_{\beta}^{\dagger} - v_b \tilde{a}_{\beta}) \right. \\ \left. \times (u_d a_{\delta} - v_d \tilde{a}_{\delta}^{\dagger}) (u_c a_{\gamma} - v_c \tilde{a}_{\gamma}^{\dagger}) \right]_{BCS} . \quad (\text{D.36})$$

Then, by changing the summation indices and using the symmetry properties of Eq.(3.30), we arrive at the result

$$V_{\text{res}} = \frac{1}{4} \bar{v}_{\alpha\beta\gamma\delta} \left[u_a u_b v_c v_d a_{\alpha}^{\dagger} a_{\beta}^{\dagger} \tilde{a}_{\delta}^{\dagger} \tilde{a}_{\gamma}^{\dagger} - 2u_a u_b u_c v_d a_{\alpha}^{\dagger} a_{\beta}^{\dagger} \tilde{a}_{\delta}^{\dagger} a_{\gamma} \right. \\ + u_a u_b u_c u_d a_{\alpha}^{\dagger} a_{\beta}^{\dagger} a_{\delta} a_{\gamma} - 2u_a v_b v_c v_d a_{\alpha}^{\dagger} \tilde{a}_{\delta}^{\dagger} \tilde{a}_{\gamma}^{\dagger} \tilde{a}_{\beta} - 4u_a v_b u_c v_d a_{\alpha}^{\dagger} \tilde{a}_{\delta}^{\dagger} \tilde{a}_{\beta} a_{\gamma} \\ - 2u_a v_b u_c u_d a_{\alpha}^{\dagger} \tilde{a}_{\beta} a_{\delta} a_{\gamma} + v_a v_b v_c v_d \tilde{a}_{\delta}^{\dagger} \tilde{a}_{\gamma}^{\dagger} \tilde{a}_{\alpha} \tilde{a}_{\beta} - 2v_a v_b u_c v_d \tilde{a}_{\delta}^{\dagger} \tilde{a}_{\alpha} \tilde{a}_{\beta} a_{\gamma} \\ \left. + v_a v_b u_c u_d \tilde{a}_{\alpha} \tilde{a}_{\beta} a_{\delta} a_{\gamma} \right] . \quad (\text{D.37})$$

Changing the summation indices the latter becomes

$$V_{\text{res}} = \sum_{\alpha\beta\gamma\delta} \bar{v}_{\alpha\beta\gamma\delta} \left[\frac{1}{4} u_a u_b v_c v_d (a_{\alpha}^{\dagger} a_{\beta}^{\dagger} \tilde{a}_{\delta}^{\dagger} \tilde{a}_{\gamma}^{\dagger} + \text{h.c.}) \right. \\ - \frac{1}{2} (u_a u_b u_c v_d - v_a v_b v_c u_d) (a_{\alpha}^{\dagger} a_{\beta}^{\dagger} \tilde{a}_{\delta}^{\dagger} a_{\gamma} + \text{h.c.}) \\ \left. + \frac{1}{4} (u_a u_b u_c u_d + v_a v_b v_c v_d) a_{\alpha}^{\dagger} a_{\beta}^{\dagger} a_{\delta} a_{\gamma} - u_a v_b u_c v_d a_{\alpha}^{\dagger} \tilde{a}_{\delta}^{\dagger} \tilde{a}_{\beta} a_{\gamma} \right] \\ \equiv H_{40} + H_{31} + H_{22} , \quad (\text{D.38})$$

where the definitions of H_{40} , H_{31} and H_{22} correspond to the tree lines of the above equation.

In angular-momentum-coupled form, the terms entering the definition of the residual interaction can be cast as

$$H_{40} = \frac{1}{2} \sum_{abcd} (-1)^J V_{abcd}^{(40)}(J) \left([a_a^\dagger a_b^\dagger]_J \cdot [a_c^\dagger a_d^\dagger]_J + \text{h.c.} \right), \quad (\text{D.39})$$

$$H_{31} = \sum_{abcd} (-1)^J V_{abcd}^{(31)}(J) \left([a_a^\dagger a_b^\dagger]_J \cdot [a_c^\dagger \tilde{a}_d]_J + \text{h.c.} \right), \quad (\text{D.40})$$

$$H_{22} = \frac{1}{2} \sum_{abcd} (-1)^J V_{abcd}^{(22)}(J) [a_a^\dagger a_b^\dagger]_J \cdot [\tilde{a}_c \tilde{a}_d]_J. \quad (\text{D.41})$$

D.5 The correlation matrix

The QRPA matrix \mathcal{B} has elements

$$B_{ab,cd}(J) = \langle BCS | A_{ab}(JM) \tilde{A}_{cd}(JM) \mathcal{H} | BCS \rangle. \quad (\text{D.42})$$

Expanding the angular momentum couplings in A_{ab} and \tilde{A}_{cd} and using the uncoupled expression for H_{40} ², we find

$$\begin{aligned} & B_{ab,cd}(J) \\ &= \frac{1}{4} (-1)^{J+M} \mathcal{N}_{ab}(J) \mathcal{N}_{cd}(J) \sum_{\substack{m_\alpha m_\beta \\ m_\gamma m_\delta}} (j_a m_\alpha j_b m_\beta | JM) (j_c m_\gamma j_d m_\delta | J - M) \\ & \quad \times \sum_{\alpha' \beta' \gamma' \delta'} u_{\alpha'} u_{\beta'} u_{\gamma'} u_{\delta'} (-1)^{j_{c'} - m_{\gamma'} + j_{d'} - m_{\delta'}} \bar{v}_{\alpha' \beta', -\gamma', -\delta'} \\ & \quad \times \langle BCS | a_\beta a_\alpha a_\delta a_\gamma a_{\alpha'}^\dagger a_{\beta'}^\dagger a_{\gamma'}^\dagger a_{\delta'}^\dagger | BCS \rangle \\ & \equiv \sum_{i=1}^{24} B_i. \end{aligned} \quad (\text{D.43})$$

²This is the only contributing term of the residual interaction

The 24 B_i terms arise from all possible contractions in the BCS vacuum expectation value

$$\begin{aligned}
& \langle BCS | a_\beta a_\alpha a_\delta a_\gamma a_\alpha^\dagger a_\beta^\dagger a_\delta^\dagger a_\gamma^\dagger | BCS \rangle \\
&= -\delta_{\alpha\alpha'} \delta_{\beta\beta'} \delta_{\gamma\gamma'} \delta_{\delta\delta'} + \delta_{\alpha\alpha'} \delta_{\beta\beta'} \delta_{\gamma\delta'} \delta_{\delta\gamma'} + \delta_{\alpha\alpha'} \delta_{\beta\delta'} \delta_{\delta\beta'} \delta_{\gamma\gamma'} \\
&\quad - \delta_{\alpha\alpha'} \delta_{\beta\delta'} \delta_{\delta\gamma'} \delta_{\gamma\beta'} - \delta_{\alpha\alpha'} \delta_{\beta\gamma'} \delta_{\delta\beta'} \delta_{\gamma\delta'} + \delta_{\alpha\alpha'} \delta_{\beta\gamma'} \delta_{\delta\delta'} \delta_{\gamma\beta'} \\
&\quad - \delta_{\alpha\beta'} \delta_{\beta\alpha'} \delta_{\delta\gamma'} \delta_{\gamma\delta'} + \delta_{\alpha\beta'} \delta_{\beta\alpha'} \delta_{\delta\delta'} \delta_{\gamma\gamma'} - \delta_{\alpha\beta'} \delta_{\beta\delta'} \delta_{\delta\alpha'} \delta_{\gamma\gamma'} \\
&\quad + \delta_{\alpha\beta'} \delta_{\beta\delta'} \delta_{\delta\gamma'} \delta_{\gamma\alpha'} - \delta_{\alpha\beta'} \delta_{\beta\gamma'} \delta_{\delta\delta'} \delta_{\gamma\alpha'} + \delta_{\alpha\beta'} \delta_{\beta\gamma'} \delta_{\delta\alpha'} \delta_{\gamma\delta'} \\
&\quad - \delta_{\alpha\delta'} \delta_{\beta\alpha'} \delta_{\delta\beta'} \delta_{\gamma\gamma'} + \delta_{\alpha\delta'} \delta_{\beta\alpha'} \delta_{\delta\gamma'} \delta_{\gamma\beta'} + \delta_{\alpha\delta'} \delta_{\beta\beta'} \delta_{\delta\alpha'} \delta_{\gamma\gamma'} \\
&\quad - \delta_{\alpha\delta'} \delta_{\beta\beta'} \delta_{\delta\gamma'} \delta_{\gamma\alpha'} + \delta_{\alpha\delta'} \delta_{\beta\gamma'} \delta_{\delta\beta'} \delta_{\gamma\alpha'} - \delta_{\alpha\delta'} \delta_{\beta\gamma'} \delta_{\delta\alpha'} \delta_{\gamma\beta'} \\
&\quad - \delta_{\alpha\gamma'} \delta_{\beta\alpha'} \delta_{\delta\delta'} \delta_{\gamma\beta'} + \delta_{\alpha\gamma'} \delta_{\beta\alpha'} \delta_{\delta\beta'} \delta_{\gamma\delta'} - \delta_{\alpha\gamma'} \delta_{\beta\beta'} \delta_{\delta\alpha'} \delta_{\gamma\delta'} \\
&\quad + \delta_{\alpha\gamma'} \delta_{\beta\beta'} \delta_{\delta\delta'} \delta_{\gamma\alpha'} - \delta_{\alpha\gamma'} \delta_{\beta\delta'} \delta_{\delta\beta'} \delta_{\gamma\alpha'} + \delta_{\alpha\gamma'} \delta_{\beta\delta'} \delta_{\delta\alpha'} \delta_{\gamma\beta'} .
\end{aligned} \tag{D.44}$$

The contributions in the above expression for $B_{ab,cd}$, form six groups each having four equal terms according to

$$\begin{aligned}
B_1 = B_2 = B_7 = B_8, \quad B_3 = B_5 = B_9 = B_{12}, \\
B_4 = B_6 = B_{10} = B_{11}, \quad B_{13} = B_{15} = B_{20} = B_{21}, \\
B_{14} = B_{16} = B_{19} = B_{22}, \quad B_{17} = B_{18} = B_{23} = B_{24},
\end{aligned} \tag{D.45}$$

thus, one needs to compute

$$B_{ab,cd}(J) = 4 (B_1 + B_3 + B_4 + B_{13} + B_{14} + B_{17}) . \tag{D.46}$$

For B_1 we have

$$\begin{aligned}
B_1 &= \frac{1}{4} (-1)^{J+M+1} \mathcal{N}_{ab}(J) \mathcal{N}_{cd}(J) u_a u_b v_c v_d \\
&\quad \times \sum_{\substack{m_\alpha m_\beta \\ m_\gamma m_\delta}} (j_a m_\alpha j_b m_\beta | JM) (j_c m_\gamma j_d m_\delta | J - M) (-1)^{j_c - m_\gamma + j_d - m_\delta} \bar{v}_{\alpha\beta, -\gamma, -\delta} .
\end{aligned} \tag{D.47}$$

Inverting the two-body matrix element to coupled form using the equalities above we obtain

$$\begin{aligned}
B_1 &= \frac{1}{4} (-1)^{J+M+1} \mathcal{N}_{ab}(J) \mathcal{N}_{cd}(J) u_a u_b v_c v_d \\
&\quad \times \sum_{\substack{m_\alpha m_\beta \\ m_\gamma m_\delta}} (j_a m_\alpha j_b m_\beta | JM) (j_c m_\gamma j_d m_\delta | J - M) (-1)^{j_c - m_\gamma + j_d - m_\delta} \\
&\quad \times \sum_{J'M'} [\mathcal{N}_{ab}(J') \mathcal{N}_{cd}(J')]^{-1} (j_a m_\alpha j_b m_\beta | J'M') (j_c - m_\gamma j_d - m_\delta | J'M') \\
&\quad \quad \times \langle ab; J' | V | cd; J' \rangle ,
\end{aligned} \tag{D.48}$$

which by employing the Clebsch-Gordan properties becomes

$$B_1 = -\frac{1}{4}u_a u_b v_c v_d \langle ab; J|V|cd; J \rangle. \quad (\text{D.49})$$

Analogously to the case of B_1 , the term B_3 takes the form

$$\begin{aligned} B_3 &= \frac{1}{4}(-1)^{J+M} \mathcal{N}_{ab}(J) \mathcal{N}_{cd}(J) u_a u_d v_b v_c \\ &\quad \times \sum_{\substack{m_\alpha m_\beta \\ m_\gamma m_\delta}} (j_a m_\alpha j_b m_\beta | JM) (j_c m_\gamma j_d m_\delta | J - M) (-1)^{j_c - m_\gamma + j_b - m_\beta} \\ &\quad \times \sum_{J'M'} [\mathcal{N}_{ad}(J') \mathcal{N}_{cb}(J')]^{-1} (j_a m_\alpha j_d m_\delta | J'M') (j_c - m_\gamma j_b - m_\beta | J'M') \\ &\quad \times \langle ad; J'|V|cb; J' \rangle. \end{aligned} \quad (\text{D.50})$$

The four Clebsch-Gordan coefficients with the phase factors sum into $6j$ symbol, thus B_3 becomes

$$\begin{aligned} B_3 &= -\frac{1}{4} \mathcal{N}_{ab}(J) \mathcal{N}_{cd}(J) u_a u_d v_b v_c \sum_{J'} [\mathcal{N}_{ad}(J') \mathcal{N}_{cb}(J')]^{-1} \\ &\quad \times \hat{J}'^2 \left\{ \begin{array}{ccc} j_a & j_b & J \\ j_c & j_d & J' \end{array} \right\} \langle ad; J'|V|cb; J' \rangle \\ &= \frac{1}{4} \mathcal{N}_{ab}(J) \mathcal{N}_{cd}(J) u_a u_d v_b v_c \langle ab^{-1}; J|V_{res}|cd^{-1}; J \rangle. \end{aligned} \quad (\text{D.51})$$

The term B_4 is treated as B_3 . The result is

$$\begin{aligned} B_4 &= (-1)^{j_c + j_d + J + 1} B_3(c \leftrightarrow d) \\ &= \frac{1}{4} (-1)^{j_c + j_d + J + 1} \mathcal{N}_{ab}(J) \mathcal{N}_{cd}(J) u_a u_c v_b v_d \langle ab^{-1}; J|V_{res}|dc^{-1}; J \rangle. \end{aligned} \quad (\text{D.52})$$

The terms B_{13} and B_{14} are deduced from B_4 , while B_{17} is obtained from B_1 . The results read

$$\begin{aligned} B_{13} &= \frac{1}{4} (-1)^{j_c + j_d + J + 1} \mathcal{N}_{ab}(J) \mathcal{N}_{cd}(J) u_b u_d v_a v_c \langle ab^{-1}; J|V_{res}|dc^{-1}; J \rangle, \\ B_{14} &= \frac{1}{4} \mathcal{N}_{ab}(J) \mathcal{N}_{cd}(J) u_b u_c v_a v_d \langle ab^{-1}; J|V_{res}|cd^{-1}; J \rangle, \\ B_{17} &= -\frac{1}{4} u_c u_d v_a v_b \langle ab; J|V_{res}|cd; J \rangle. \end{aligned} \quad (\text{D.53})$$

Then, the correlation matrix can be cast in the form

$$\begin{aligned} B_{ab,cd}(J) &= - (u_a u_b v_c v_d + v_a v_b u_c u_d) \langle ab; J|V|cd; J \rangle \\ &\quad + \mathcal{N}_{ab}(J) \mathcal{N}_{cd}(J) \left[(u_a v_b v_c u_d + v_a u_b u_c v_d) \langle ab^{-1}; J|V_{res}|cd^{-1}; J \rangle \right. \\ &\quad \left. - (-1)^{j_c + j_d + J} (u_a v_b u_c v_d + v_a u_b v_c u_d) \langle ab^{-1}; J|V_{res}|dc^{-1}; J \rangle \right]. \end{aligned} \quad (\text{D.54})$$

This expression can be compactly written in terms of the Baranger matrix elements

$$\begin{aligned}
G(abcdJ) &= -\frac{1}{2}[\mathcal{N}_{ab}(J)\mathcal{N}_{cd}(J)]^{-1}\langle ab; J|V|cd; J\rangle \\
&= -\frac{1}{2}\sqrt{1+\delta_{ab}(-1)^J}\sqrt{1+\delta_{cd}(-1)^J}\langle ab; J|V|cd; J\rangle, \\
F(abcdJ) &= -\frac{1}{2}\langle ab^{-1}; J|V_{res}|cd^{-1}; J\rangle,
\end{aligned} \tag{D.55}$$

in the form

$$\begin{aligned}
B_{ab,cd}(J) &= 2\mathcal{N}_{ab}(J)\mathcal{N}_{cd}(J)\left[(u_a u_b v_c v_d + v_a v_b u_c u_d)G(abcdJ) \right. \\
&\quad - (u_a v_b v_c u_d + v_a u_b u_c v_d)F(abcdJ) \\
&\quad \left. + (-1)^{j_c+j_d+J}(u_a v_b u_c v_d + v_a u_b v_c u_d)F(abdcJ)\right].
\end{aligned} \tag{D.56}$$

Appendix E

E.1 Supernova distributions

In Chapt. 4 and Chapt. 5, the calculations concerning Supernova neutrino scattering assume the Maxwell-Boltzmann neutrino energy spectra, $\eta_{\nu_\alpha}^{\text{SN}}(E_\nu) \equiv \eta_{\nu_\alpha}^{\text{MB}}(E_\nu)$, given in Eq.(4.74). Here we review two alternative SN neutrino energy-distributions that have been widely used in the literature, namely the Fermi-Dirac (FD) and the power-law (PL) ones. For the case of FD, here we provide for the first time analytical expressions regarding the normalisation constant and the mean energy.

E.1.1 Fermi-Dirac distribution

For each flavour $\alpha = \{e, \mu, \tau\}$, the emitted neutrino spectrum of a core collapse Supernova is assumed to resemble a FD energy-distribution

$$\eta_{\nu_\alpha}^{\text{FD}}(E_\nu) = N_2(\eta_{dg}) \frac{1}{T_{\nu_\alpha}^3} \frac{E_\nu^2}{1 + \exp(\frac{E_\nu}{T_{\nu_\alpha}} - \eta_{dg})}, \quad (\text{E.1})$$

where $\eta_{dg} = \mu/T_{\nu_\alpha}$ is the degeneracy parameter that depends on the inserted chemical potential, μ , and the temperature T_{ν_α} . The normalisation factor, $N_2(\eta_{dg})$, is defined as

$$\frac{1}{N_n(\eta_{dg})} = \int_0^\infty \frac{x^n}{1 + \exp(x - \eta_{dg})} dx, \quad x = E_\nu/T_{\nu_\alpha}. \quad (\text{E.2})$$

We find that the latter integral can be solved explicitly in terms of known functions¹, as

$$\int_0^\infty \frac{x^n}{1 + \exp(x - \eta_{dg})} dx = -\Gamma(n + 1) Li_{n+1}(-e^{\eta_{dg}}), \quad (\text{E.3})$$

¹With $\Re(n) > -1$.

where $\Gamma(x)$ is the known gamma-function and $Li_n(z)$ the polylogarithm function

$$Li_n(z) = \sum_{k=1}^{\infty} \frac{z^k}{k^n}. \quad (\text{E.4})$$

Therefore, for $n = 2$, the normalisation factor of the FD distribution reads

$$\begin{aligned} N_2(\eta_{dg}) &= \frac{1}{-\Gamma(2+1)Li_{2+1}(-e^{\eta_{dg}})}, \\ &= -\frac{1}{2Li_3(-e^{\eta_{dg}})}, \end{aligned} \quad (\text{E.5})$$

and thus, the FD distribution given in Eq.(E.1) takes the final form

$$\eta_{\nu\alpha}^{\text{FD}}(E_\nu) = -\frac{1}{2Li_3(-e^{\eta_{dg}})} \frac{1}{T_{\nu\alpha}^3} \frac{E_\nu^2}{1 + \exp(\frac{E_\nu}{T_{\nu\alpha}} - \eta_{dg})}. \quad (\text{E.6})$$

From the definition of the mean energy, we have

$$\begin{aligned} \langle E_{\nu\alpha} \rangle &= \int_0^\infty E_\nu \eta_{\nu\alpha}^{\text{FD}}(E_\nu) dE_\nu, \\ &= N_2(\eta_{dg}) \int_0^\infty \frac{E_\nu^3}{T_{\nu\alpha}^3} \frac{1}{1 + \exp(\frac{E_\nu}{T_{\nu\alpha}} - \eta_{dg})}. \end{aligned} \quad (\text{E.7})$$

By changing variables, we write

$$\begin{aligned} \langle E_{\nu\alpha} \rangle &= N_2(\eta_{dg}) T_{\nu\alpha} \int_0^\infty \frac{x^3}{1 + \exp(x - \eta_{dg})}, \\ &= N_2(\eta_{dg}) \frac{T}{N_3(\eta_{dg})}, \\ &= -\frac{1}{2Li_3(-e^{\eta_{dg}})} T_{\nu\alpha} [-\Gamma(3+1)Li_{3+1}(-e^{\eta_{dg}})], \\ \Rightarrow \langle E_{\nu\alpha} \rangle &= 3 \frac{Li_4(-e^{\eta_{dg}})}{Li_3(-e^{\eta_{dg}})} T_{\nu\alpha}. \end{aligned} \quad (\text{E.8})$$

By expanding the exact result given in Eq.(E.8), up to $\sim \eta_{dg}^3$ terms, it yields

$$\begin{aligned} \langle E_{\nu\alpha} \rangle &= T_{\nu\alpha} \left\{ \frac{7\pi^4}{180\zeta(3)} + \eta_{dg} \left(3 - \frac{7\pi^6}{1620\zeta(3)^2} \right) \right. \\ &\quad + \frac{\eta_{dg}^2 (-2430\pi^2\zeta(3)^2 - 378\pi^4\zeta(3)\ln(2) + 7\pi^8)}{14580\zeta(3)^3} \\ &\quad \left. + \frac{\eta_{dg}^3 (1863\pi^4\zeta(3)^2 + 756\pi^6\zeta(3)\ln(2) - 174960\zeta(3)^3\ln(2) - 7\pi^{10})}{131220\zeta(3)^4} \right\}, \end{aligned} \quad (\text{E.9})$$

where $\zeta(s) = \sum_{n=1}^{\infty} \frac{1}{n^s}$ is the Riemann zeta function with $\zeta(3) = 1.20206$. However, for numerical calculations, it is more convenient to write

$$\langle E_{\nu\alpha} \rangle = (3.15137 + 0.125037\eta_{dg} + 0.0429024\eta_{dg}^2 + 0.00592166\eta_{dg}^3) T_{\nu\alpha}. \quad (\text{E.10})$$

Equivalence with Maxwell-Boltzmann

It is not difficult to show that for $\eta_{dg} \rightarrow -\infty$, the Fermi-Dirac distribution reduces to the Maxwell-Boltzmann distribution. Starting from FD, one has

$$\begin{aligned}
\eta_{\nu_\alpha}^{\text{FD}}(E_\nu) &= \left[\int_0^\infty \frac{x^2}{1 + e^{(x-\eta_{dg})}} dx \right]^{-1} \frac{1}{T_{\nu_\alpha}^3} \frac{E_\nu^2}{1 + e^{(\frac{E_\nu}{T_{\nu_\alpha}} - \eta_{dg})}}, \\
&= \left[\int_0^\infty \frac{x^2 e^{\eta_{dg}}}{e^{\eta_{dg}} + e^x} dx \right]^{-1} \frac{1}{T_{\nu_\alpha}^3} \frac{E_\nu^2 e^{\eta_{dg}}}{e^{\eta_{dg}} + e^{E_\nu/T_{\nu_\alpha}}}, \\
&= \left[\int_0^\infty \frac{x^2}{e^{\eta_{dg}} + e^x} dx \right]^{-1} \frac{1}{T_{\nu_\alpha}^3} \frac{E_\nu^2}{e^{\eta_{dg}} + e^{E_\nu/T_{\nu_\alpha}}}, \\
&\stackrel{\eta_{dg} \rightarrow -\infty}{=} \frac{1}{\int_0^\infty x^2 e^{-x} dx} \frac{E_\nu^2 / T_{\nu_\alpha}^3}{e^{E_\nu/T_{\nu_\alpha}}}, \\
&= \frac{1}{\Gamma(2+1)} \frac{E_\nu^2 / T_{\nu_\alpha}^3}{e^{E_\nu/T_{\nu_\alpha}}}, \\
&= \frac{E_\nu^2}{2T_{\nu_\alpha}^3} e^{-E_\nu/T_{\nu_\alpha}}, \\
&\equiv \eta_{\nu_\alpha}^{\text{MB}}(E_\nu).
\end{aligned} \tag{E.11}$$

E.1.2 Power-law distribution

Often times, the emitted energy spectrum of Supernova neutrinos is described by the power law distribution

$$\eta_{\nu_\alpha}^{\text{PL}} = N(a) \left(\frac{E_\nu}{\langle E_{\nu_\alpha} \rangle} \right)^a e^{-(a+1)E_\nu/\langle E_{\nu_\alpha} \rangle}, \tag{E.12}$$

where the flavour dependence is based on the mean energy, $\langle E_{\nu_\alpha} \rangle$, while the normalisation factor reads

$$N(a) = \frac{(a+1)^{a+1}}{\Gamma(a+1)\langle E_{\nu_\alpha} \rangle}. \tag{E.13}$$

Appendix F

F.1 Nuclear charge density distribution

The nuclear charge density distribution, $\rho(r)$, is defined as the Fourier transform of the nuclear form factor $F(\mathbf{q}^2)$ and for a spherically symmetric nuclei in the plane wave Born approximation is written as

$$\rho(r) = \frac{1}{2\pi^2} \int F(\mathbf{q}^2) j_0(|\mathbf{q}|r) \mathbf{q}^2 d|\mathbf{q}|, \quad (\text{F.1})$$

where $j_0(x)$ is the zero-order Spherical Bessel function and $|\mathbf{q}|$ denotes the magnitude of the three-momentum transfer ¹. Experimentally it can be studied with high accuracy from electron scattering data available into a finite momentum range. In particular the amplitudes of Fourier components of the nuclear charge density with wavelengths are restricted between $2\pi/|\mathbf{q}|_{\min}$ and $2\pi/|\mathbf{q}|_{\max}$. In the literature, several model-independent analyses have been adopted, the most common definitions and normalisations of which are presented below.

F.1.1 Fourier-Bessel analysis

The Fourier-Bessel analysis is defined as [235]

$$\rho(r) = \begin{cases} \sum_{v=1}^N a_v j_0(v\pi r/R) & \text{for } r \leq R, \\ 0 & \text{for } r > R, \end{cases} \quad (\text{F.2})$$

where R is the cutoff radius and $N = R|\mathbf{q}|_{\max}/\pi$. In this model, the first N coefficients of the series are determined directly by the experimental data. It is worth mentioning that uncertainties in the nuclear charge distribution due to experimental errors and from the lack of knowledge regarding the large $|\mathbf{q}|$

¹Note that, in Chapt. 4 we have also introduced the definition $\kappa = |\mathbf{q}|$ [see Eq. (4.42)].

behaviour can be determined separately [56]. The chosen normalisation is such that the integral over the nuclear charge density reads

$$\frac{4\pi}{Z} \int \rho(r)r^2 dr = 1, \quad (\text{F.3})$$

where Z denotes the atomic number of the nucleus.

F.1.2 Other models describing the charge distribution

Fermi models

The two-parameter Fermi model is defined as

$$\rho(r) = \rho_0 / (1 + e^{(r-c)/z}), \quad (\text{F.4})$$

and the three-parameter Fermi model is written as

$$\rho(r) = \rho_0(1 + wr^2/c^2) / (1 + e^{(r-c)/z}), \quad (\text{F.5})$$

where the parameters c, z, w are determined experimentally.

Gaussian models

The uniform Gaussian model reads

$$\rho(r) = \rho_0 \int e^{-(r-x)^2/g^2} x^2 dx, \quad (\text{F.6})$$

while the three-parameter Gaussian model is defined in a similar form to the three-parameter Fermi model given in Eq.(F.5), as

$$\rho(r) = \rho_0(1 + wr^2/c^2) / (1 + e^{(r^2-c^2)/z^2}). \quad (\text{F.7})$$

Another useful parametrisation is the so-called sum of Gaussians model [236]

$$\rho(r) = \sum_i A_i \left[e^{-(r-R_i)^2/\gamma^2} + e^{-(r+R_i)^2/\gamma^2} \right], \quad (\text{F.8})$$

where the parameters, A_i , are expressed in terms of the width of the Gaussian, γ , and the fraction, Q_i , of the charge contained in the i -th Gaussian, as follows

$$A_i = \frac{ZQ_i}{2\pi^{3/2}\gamma^3(1 + 2R_i^2/\gamma^2)}. \quad (\text{F.9})$$

The positions, R_i , and the values of Q_i (obeying the normalisation $\sum_i Q_i = 1$), are fitted to the data.

Harmonic Oscillator model

The Harmonic Oscillator model is defined through the simple expression

$$\rho(r) = \rho_0 [1 + \alpha(r/a)^2] e^{-(r/a)^2}, \quad (\text{F.10})$$

with the parameters

$$\alpha = \alpha_0 a_0^2 \left[a^2 + \frac{3}{2} \alpha_0 (a^2 - a_0^2) \right], \quad (\text{F.11})$$

$$a_0^2 = (a^2 - a_p^2) A / (A - 1), \quad (\text{F.12})$$

$$\alpha_0 = (Z - 2) / 3, \quad (\text{F.13})$$

$$a_p^2 = \frac{2}{3} \langle r^2 \rangle_{\text{proton}}, \quad (\text{F.14})$$

and $\langle r^2 \rangle_{\text{proton}}$ denoting the mean square radius of the proton charge distribution.

Bibliography

- [1] S. Weinberg, *A Model of Leptons*, *Phys. Rev. Lett.* **19** (1967) 1264–1266.
- [2] S. L. Glashow, *Partial Symmetries of Weak Interactions*, *Nucl. Phys.* **22** (1961) 579–588.
- [3] A. Salam, *Weak and Electromagnetic Interactions*, *Conf. Proc.* **C680519** (1968) 367–377.
- [4] C. Giunti and C. W. Kim, *Fundamentals of Neutrino Physics and Astrophysics*. Oxford University Press, Oxford, UK, 2007. ISBN: 978-0-19-850871-7.
- [5] J. W. Valle and J. C. Romao, *Neutrinos in high energy and astroparticle physics*. Wiley-VCH, Berlin, 1st edition ed., 2015.
- [6] F. Englert and R. Brout, *Broken Symmetry and the Mass of Gauge Vector Mesons*, *Phys. Rev. Lett.* **13** (1964) 321–323.
- [7] P. W. Higgs, *Broken Symmetries and the Masses of Gauge Bosons*, *Phys. Rev. Lett.* **13** (1964) 508–509.
- [8] G. S. Guralnik, C. R. Hagen, and T. W. B. Kibble, *Global Conservation Laws and Massless Particles*, *Phys. Rev. Lett.* **13** (1964) 585–587.
- [9] P. W. Anderson, *Plasmons, Gauge Invariance, and Mass*, *Phys. Rev.* **130** (1963) 439–442.
- [10] J. Goldstone, *Field Theories with Superconductor Solutions*, *Nuovo Cim.* **19** (1961) 154–164.
- [11] J. Goldstone, A. Salam, and S. Weinberg, *Broken Symmetries*, *Phys. Rev.* **127** (1962) 965–970.

- [12] N. Cabibbo, *Unitary Symmetry and Leptonic Decays*, *Phys. Rev. Lett.* **10** (1963) 531–533. [[648\(1963\)](#)].
- [13] M. Kobayashi and T. Maskawa, *CP Violation in the Renormalizable Theory of Weak Interaction*, *Prog. Theor. Phys.* **49** (1973) 652–657.
- [14] S. L. Glashow, J. Iliopoulos, and L. Maiani, *Weak Interactions with Lepton-Hadron Symmetry*, *Phys. Rev.* **D2** (1970) 1285–1292.
- [15] J. D. Bjorken and S. D. Drell, *Relativistic Quantum Fields*. McGraw-Hill College, first edition ed., 6, 1965. ISBN: 9780070054943.
- [16] M. E. Peskin and D. V. Schroeder, *An Introduction To Quantum Field Theory (Frontiers in Physics)*. Westview Press, first edition ed., 10, 1995. ISBN: 9780201503975.
- [17] F. J. Hasert et al., *Search for Elastic ν_μ Electron Scattering*, *Phys. Lett.* **B46** (1973) 121–124.
- [18] **TEXONO** Collaboration, H. B. Li et al., *Limit on the electron neutrino magnetic moment from the Kuo-Sheng reactor neutrino experiment*, *Phys. Rev. Lett.* **90** (2003) 131802, [[hep-ex/0212003](#)].
- [19] **TEXONO collaboration** Collaboration, M. Deniz et al., *Measurement of Neutrino-Electron Scattering Cross-Section with a CsI(Tl) Scintillating Crystal Array at the Kuo-Sheng Nuclear Power Reactor*, *Phys. Rev.* **D81** (2010) 072001, [[arXiv:0911.1597](#)].
- [20] Z. Berezhiani and A. Rossi, *Limits on the nonstandard interactions of neutrinos from $e^+ e^-$ colliders*, *Phys. Lett.* **B535** (2002) 207–218, [[hep-ph/0111137](#)].
- [21] J. Barranco, O. G. Miranda, C. A. Moura, and J. W. F. Valle, *Constraining non-standard interactions in $\nu(e) e$ or anti- $\nu(e) e$ scattering*, *Phys. Rev.* **D73** (2006) 113001, [[hep-ph/0512195](#)].
- [22] S. Davidson, C. Pena-Garay, N. Rius, and A. Santamaria, *Present and future bounds on nonstandard neutrino interactions*, *JHEP* **03** (2003) 011, [[hep-ph/0302093](#)].
- [23] T. Ohlsson, *Status of non-standard neutrino interactions*, *Rept. Prog. Phys.* **76** (2013) 044201, [[arXiv:1209.2710](#)].
- [24] O. G. Miranda and H. Nunokawa, *Non standard neutrino interactions: current status and future prospects*, *New J. Phys.* **17** (2015), no. 9 095002, [[arXiv:1505.06254](#)].

- [25] D. Papoulias and T. Kosmas, *Nuclear aspects of neutral current non-standard ν -nucleus reactions and the role of the exotic $\mu^- \rightarrow e^-$ transitions experimental limits*, *Phys.Lett.* **B728** (2014) 482–488, [[arXiv:1312.2460](#)].
- [26] D. Papoulias and T. Kosmas, *Standard and non-standard neutrino-nucleus reactions cross sections and event rates to neutrino detection experiments*, *Adv.High Energy Phys.* **2015** (2015) 763648, [[arXiv:1502.02928](#)].
- [27] D. K. Papoulias and T. S. Kosmas, *Neutrino transition magnetic moments within the non-standard neutrino-nucleus interactions*, *Phys. Lett.* **B747** (2015) 454–459, [[arXiv:1506.05406](#)].
- [28] C. H. Llewellyn Smith, *Neutrino Reactions at Accelerator Energies*, *Phys. Rept.* **3** (1972) 261–379.
- [29] G. T. Garvey, W. C. Louis, and D. H. White, *Determination of proton strange form-factors from neutrino p elastic scattering*, *Phys. Rev.* **C48** (1993) 761–765.
- [30] W. M. Alberico, S. M. Bilenky, and C. Maieron, *Strangeness in the nucleon: Neutrino - nucleon and polarized electron - nucleon scattering*, *Phys. Rept.* **358** (2002) 227–308, [[hep-ph/0102269](#)].
- [31] W. M. Alberico, S. M. Bilenky, C. Giunti, and K. M. Graczyk, *Electromagnetic form factors of the nucleon: New Fit and analysis of uncertainties*, *Phys. Rev.* **C79** (2009) 065204, [[arXiv:0812.3539](#)].
- [32] K. G. Balasi, E. Ydrefors, and T. S. Kosmas, *Theoretical study of neutrino scattering off the stable even Mo isotopes at low and intermediate energies*, *Nucl. Phys.* **A868-869** (2011) 82–98.
- [33] **MiniBooNE** Collaboration, A. A. Aguilar-Arevalo et al., *Measurement of the Neutrino Neutral-Current Elastic Differential Cross Section on Mineral Oil at $E_\nu \sim 1$ GeV*, *Phys. Rev.* **D82** (2010) 092005, [[arXiv:1007.4730](#)].
- [34] D. J. Rowe, *Nuclear Collective Motion. Models and Theory*. Methuen & Co., 1st ed., 9, 1970. ISBN: 9780416449600.
- [35] A. de Shalit and H. Feshbach, *Theoretical Nuclear Physics: Nuclear structure*. John Wiley & Sons Inc, New York, USA, 1974. ISBN 10: 0471203858.
- [36] P. Ring and P. Schuck, *The Nuclear Many-body Problem*. Springer, Heidelberg, Germany, 1980. ISBN: 978-3-540-21206-5.

- [37] J. D. Walecka, *Theoretical Nuclear And Subnuclear Physics*. World Scientific Pub Co Inc, 2 ed., 9, 2004. ISBN: 9789812388988.
- [38] J. Suhonen, *From Nucleons to Nucleus: Concepts of Microscopic Nuclear Theory*. Springer, Berlin, Germany, 2007. ISBN: 9783540488613, 9783540488590.
- [39] M. G. Mayer and J. H. D. Jensen, *Elementary Theory Of Nuclear Shell Structure*. Literary Licensing, LLC, 2, 2013. ISBN: 9781258591205.
- [40] P. G. Giannaka and T. S. Kosmas, *Detailed description of exclusive muon capture rates using realistic two-body forces*, *Phys. Rev.* **C92** (2015), no. 1 014606, [[arXiv:1506.05400](https://arxiv.org/abs/1506.05400)].
- [41] A. Bohr and B. Mottelson, *Nuclear Structure: Single Particle Motion v. 1*. Addison Wesley Publishing Company, 12, 1969. ISBN: 9780805310153.
- [42] H. Esbensen and G. Bertsch, *Interference effects in the Coulomb dissociation of 8B* , *Phys. Lett.* **B359** (1995), no. 1-2 13 – 16.
- [43] Y. Tanaka, Y. Oda, F. Petrovich, and R. Sheline, *Effect of the spin-orbit potential on the single particle levels in the superheavy region*, *Phys. Lett.* **B83** (1979), no. 3-4 279 – 283.
- [44] M. G. Mayer, *Nuclear configurations in the spin-orbit coupling model. i. empirical evidence*, *Phys. Rev.* **78** (Apr, 1950) 16–21.
- [45] J. Bardeen, L. N. Cooper, and J. R. Schrieffer, *Theory of superconductivity*, *Phys. Rev.* **108** (Dec, 1957) 1175–1204.
- [46] A. Bohr, B. R. Mottelson, and D. Pines, *Possible analogy between the excitation spectra of nuclei and those of the superconducting metallic state*, *Phys. Rev.* **110** (1958) 936–938.
- [47] S. T. Belyaev *Mat. Fys. Medd. Dan. Vid. Selsk.* **31** (1959) 1.
- [48] M. Baranger, *Extension of the shell model for heavy spherical nuclei*, *Phys. Rev.* **120** (Nov, 1960) 957–968.
- [49] N. N. Bogoliubov *Sov. Phys. JETP* **7** (1958) 41.
- [50] J. G. Valatin, *Generalized hartree-fock method*, *Phys. Rev.* **122** (1961) 1012–1020.
- [51] A. R. Edmonds, *Angular Momentum in Quantum Mechanics*. Princeton University Press, reissue ed., 1, 1996. ISBN: 9780691025896.

- [52] R. Machleidt, K. Holinde, and C. Elster, *The Bonn Meson Exchange Model for the Nucleon Nucleon Interaction*, *Phys. Rept.* **149** (1987) 1–89.
- [53] V. G. J. Stoks, R. A. M. Klomp, C. P. F. Terheggen, and J. J. de Swart, *Construction of high quality NN potential models*, *Phys. Rev.* **C49** (1994) 2950–2962, [[nucl-th/9406039](#)].
- [54] R. Machleidt, *The High precision, charge dependent Bonn nucleon-nucleon potential (CD-Bonn)*, *Phys. Rev.* **C63** (2001) 024001, [[nucl-th/0006014](#)].
- [55] T. S. Kosmas, J. D. Vergados, O. Civitarese, and A. Faessler, *Study of the muon number violating (μ^- , e^-) conversion in a nucleus by using quasiparticle RPA*, *Nucl. Phys.* **A570** (1994) 637–656.
- [56] H. De Vries, C. W. De Jager, and C. De Vries, *Nuclear charge and magnetization density distribution parameters from elastic electron scattering*, *Atom. Data Nucl. Data Tabl.* **36** (1987) 495–536.
- [57] T. Kosmas and J. Vergados, *Nuclear densities with fractional occupation probabilities of the states*, *Nucl. Phys.* **A536** (1992), no. 1 72 – 86.
- [58] T. S. Kosmas and J. D. Vergados, *Nuclear Matrix Elements for the Coherent $\mu - e$ Conversion Process*, *Phys. Lett.* **B215** (1988) 460–464.
- [59] T. S. Kosmas and J. D. Vergados, *Study of the flavor violating (μ^- , e^-) conversion in nuclei*, *Nucl. Phys.* **A510** (1990) 641–670.
- [60] J. Engel, *Nuclear form-factors for the scattering of weakly interacting massive particles*, *Phys. Lett.* **B264** (1991) 114–119.
- [61] D. Z. Freedman, *Coherent neutrino nucleus scattering as a probe of the weak neutral current*, *Phys. Rev.* **D9** (1974) 1389–1392.
- [62] D. L. Tubbs and D. N. Schramm, *Neutrino Opacities at High Temperatures and Densities*, *Astrophys. J.* **201** (1975) 467–488.
- [63] A. Drukier and L. Stodolsky, *Principles and Applications of a Neutral Current Detector for Neutrino Physics and Astronomy*, *Phys. Rev.* **D30** (1984) 2295.
- [64] K. Langanke, *Weak interaction, nuclear physics and supernovae*, *Acta Phys. Polon.* **B39** (2008) 265–282.
- [65] H. Ejiri, *Nuclear spin isospin responses for low-energy neutrinos*, *Phys. Rept.* **338** (2000) 265–351.
- [66] T. S. Kosmas and E. Oset, *Charged current neutrino nucleus reaction cross-sections at intermediate-energies*, *Phys. Rev.* **C53** (1996) 1409–1415.

- [67] J. Schechter and J. W. F. Valle, *Neutrino Masses in $SU(2) \times U(1)$ Theories*, *Phys. Rev.* **D22** (1980) 2227.
- [68] J. Schechter and J. W. F. Valle, *Neutrino Decay and Spontaneous Violation of Lepton Number*, *Phys. Rev.* **D25** (1982) 774.
- [69] <http://www.phy.ornl.gov/nusns>.
- [70] K. Scholberg, *Prospects for measuring coherent neutrino-nucleus elastic scattering at a stopped-pion neutrino source*, *Phys. Rev.* **D73** (2006) 033005, [[hep-ex/0511042](http://arxiv.org/abs/hep-ex/0511042)].
- [71] **MiniBooNE** Collaboration, A. A. Aguilar-Arevalo et al., *The Neutrino Flux prediction at MiniBooNE*, *Phys. Rev.* **D79** (2009) 072002, [[arXiv:0806.1449](http://arxiv.org/abs/0806.1449)].
- [72] W. C. Louis, *Searches for muon-to-electron (anti) neutrino flavor change*, *Prog. Part. Nucl. Phys.* **63** (2009) 51–73.
- [73] A. Bolozdynya, F. Cavanna, Y. Efremenko, G. Garvey, V. Gudkov, et al., *Opportunities for Neutrino Physics at the Spallation Neutron Source: A White Paper*, [arXiv:1211.5199](http://arxiv.org/abs/1211.5199).
- [74] **CSI** Collaboration, D. Akimov et al., *Coherent Scattering Investigations at the Spallation Neutron Source: a Snowmass White Paper*, [arXiv:1310.0125](http://arxiv.org/abs/1310.0125).
- [75] **COHERENT** Collaboration, D. Akimov et al., *The COHERENT Experiment at the Spallation Neutron Source*, [arXiv:1509.08702](http://arxiv.org/abs/1509.08702).
- [76] K. Scholberg, T. Wongjirad, E. Hungerford, A. Empl, D. Markoff, P. Mueller, Y. Efremenko, D. McKinsey, and J. Nikkel, *The CLEAR Experiment*, in *Particles and fields. Proceedings, Meeting of the Division of the American Physical Society, DPF 2009, Detroit, USA, July 26-31, 2009*, 2009. [arXiv:0910.1989](http://arxiv.org/abs/0910.1989).
- [77] J. Yoo, “Measuring coherent-NC ν As at Fermilab.” <http://if-neutrino.fnal.gov/neutrino1-pagers.pdf>, 2011.
- [78] S. Brice, R. Cooper, F. DeJongh, A. Empl, L. Garrison, et al., *A method for measuring coherent elastic neutrino-nucleus scattering at a far off-axis high-energy neutrino beam target*, *Phys.Rev.* **D89** (2014), no. 7 072004, [[arXiv:1311.5958](http://arxiv.org/abs/1311.5958)].
- [79] J. I. Collar, N. E. Fields, M. Hai, T. W. Hossbach, J. L. Orrell, C. T. Overman, G. Perumpilly, and B. Scholz, *Coherent neutrino-nucleus scattering detection with a CsI[Na] scintillator at the SNS spallation source*, *Nucl. Instrum. Meth.* **A773** (2014) 56, [[arXiv:1407.7524](http://arxiv.org/abs/1407.7524)].

- [80] **Kamiokande-II** Collaboration, K. Hirata et al., *Observation of a Neutrino Burst from the Supernova SN 1987a*, *Phys. Rev. Lett.* **58** (1987) 1490–1493.
- [81] R. M. Bionta et al., *Observation of a Neutrino Burst in Coincidence with Supernova SN 1987a in the Large Magellanic Cloud*, *Phys. Rev. Lett.* **58** (1987) 1494.
- [82] M. T. Keil, G. G. Raffelt, and H.-T. Janka, *Monte Carlo study of supernova neutrino spectra formation*, *Astrophys. J.* **590** (2003) 971–991, [[astro-ph/0208035](#)].
- [83] W. C. Haxton, *RADIOCHEMICAL NEUTRINO DETECTION VIA I-127 (electron-neutrino, e-) Xe-127*, *Phys. Rev. Lett.* **60** (1988) 768–771.
- [84] P. Giannaka and T. Kosmas, *Electron-capture and its role to explosive neutrino-nucleosynthesis*, *J.Phys.Conf.Ser.* **410** (2013) 012124.
- [85] P. Giannaka and T. Kosmas, *Electron capture cross sections for stellar nucleosynthesis*, *Advances in High Energy Physics* **2015** (2015) 398796, [[arXiv:1502.07225](#)].
- [86] F. Avignone and Y. Efremenko, *Neutrino nucleus cross-section measurements at intense, pulsed spallation sources*, *J.Phys.* **G29** (2003) 2615–2628.
- [87] Y. Efremenko and W. Hix, *Opportunities for Neutrino Physics at the Spallation Neutron Source (SNS)*, *J.Phys.Conf.Ser.* **173** (2009) 012006, [[arXiv:0807.2801](#)].
- [88] C. J. Horowitz, K. J. Coakley, and D. N. McKinsey, *Supernova observation via neutrino - nucleus elastic scattering in the CLEAN detector*, *Phys. Rev.* **D68** (2003) 023005, [[astro-ph/0302071](#)].
- [89] A. J. Anderson, J. M. Conrad, E. Figueroa-Feliciano, K. Scholberg, and J. Spitz, *Coherent Neutrino Scattering in Dark Matter Detectors*, *Phys. Rev.* **D84** (2011) 013008, [[arXiv:1103.4894](#)].
- [90] T. S. Kosmas and J. D. Vergados, *Cold dark matter in SUSY theories. The Role of nuclear form-factors and the folding with the LSP velocity*, *Phys. Rev.* **D55** (1997) 1752–1764, [[hep-ph/9701205](#)].
- [91] J. D. Vergados and T. S. Kosmas, *Searching for cold dark matter: A Case of coexistence of supersymmetry and nuclear physics*, *Phys. Atom. Nucl.* **61** (1998) 1066–1080, [[hep-ph/9802270](#)]. [*Yad. Fiz.*61,1166(1998)].

- [92] **CDMS-II** Collaboration, P. L. Brink et al., *Beyond the CDMS-II dark matter search: SuperCDMS*, *eConf C041213* (2004) 2529, [[astro-ph/0503583](#)].
- [93] **GERDA** Collaboration, G. Zuzel, *The GERDA experiment at Gran Sasso*, *Acta Phys. Polon.* **B41** (2010) 1469–1476.
- [94] D. N. McKinsey and K. J. Coakley, *Neutrino detection with CLEAN*, *Astropart. Phys.* **22** (2005) 355–368, [[astro-ph/0402007](#)].
- [95] **WARP** Collaboration, R. Brunetti et al., *Warp liquid argon detector for dark matter survey*, *New Astron. Rev.* **49** (2005) 265–269, [[astro-ph/0405342](#)].
- [96] **XENON100** Collaboration, E. Aprile et al., *The XENON100 Dark Matter Experiment*, *Astropart. Phys.* **35** (2012) 573–590, [[arXiv:1107.2155](#)].
- [97] Y. Giomataris and J. D. Vergados, *A Network of neutral current spherical TPC's for dedicated supernova detection*, *Phys. Lett.* **B634** (2006) 23–29, [[hep-ex/0503029](#)].
- [98] J. Monroe and P. Fisher, *Neutrino Backgrounds to Dark Matter Searches*, *Phys. Rev.* **D76** (2007) 033007, [[arXiv:0706.3019](#)].
- [99] M. Biassoni and C. Martinez, *Study of supernova ν -nucleus coherent scattering interactions*, *Astropart. Phys.* **36** (2012) 151–155, [[arXiv:1110.3536](#)].
- [100] **Super-Kamiokande** Collaboration, S. Fukuda et al., *Solar B-8 and hep neutrino measurements from 1258 days of Super-Kamiokande data*, *Phys. Rev. Lett.* **86** (2001) 5651–5655, [[hep-ex/0103032](#)].
- [101] **SNO** Collaboration, Q. R. Ahmad et al., *Measurement of day and night neutrino energy spectra at SNO and constraints on neutrino mixing parameters*, *Phys. Rev. Lett.* **89** (2002) 011302, [[nucl-ex/0204009](#)].
- [102] **KamLAND** Collaboration, K. Eguchi et al., *First results from KamLAND: Evidence for reactor anti-neutrino disappearance*, *Phys. Rev. Lett.* **90** (2003) 021802, [[hep-ex/0212021](#)].
- [103] D. V. Forero, M. Tortola, and J. W. F. Valle, *Global status of neutrino oscillation parameters after Neutrino-2012*, *Phys. Rev.* **D86** (2012) 073012, [[arXiv:1205.4018](#)].
- [104] D. V. Forero, M. Tortola, and J. W. F. Valle, *Neutrino oscillations refitted*, *Phys. Rev.* **D90** (2014), no. 9 093006, [[arXiv:1405.7540](#)].

- [105] J. W. F. Valle, *Understanding and Probing Neutrinos*, *Nucl. Phys. Proc. Suppl.* **229-232** (2012) 23–29.
- [106] **COMET** Collaboration, Y. G. Cui et al., *Conceptual design report for experimental search for lepton flavor violating $\mu^- \rightarrow e^-$ conversion at sensitivity of 10^{-16} with a slow-extracted bunched proton beam (COMET)*, report num.: *KEK-2009-10* (2009).
- [107] **COMET** Collaboration, A. Kurup, *The COherent Muon to Electron Transition (COMET) experiment*, *Nucl. Phys. Proc. Suppl.* **218** (2011) 38–43.
- [108] **Mu2e** Collaboration, R. J. Abrams et al., *Mu2e Conceptual Design Report*, [arXiv:1211.7019](https://arxiv.org/abs/1211.7019).
- [109] **Mu2e** Collaboration, F. Cervelli, *The Mu2e experiment at Fermilab*, *J. Phys. Conf. Ser.* **335** (2011) 012073.
- [110] Y. Kuno and Y. Okada, *Muon decay and physics beyond the standard model*, *Rev. Mod. Phys.* **73** (2001) 151–202, [[hep-ph/9909265](https://arxiv.org/abs/hep-ph/9909265)].
- [111] J. Barranco, O. G. Miranda, and T. I. Rashba, *Probing new physics with coherent neutrino scattering off nuclei*, *JHEP* **12** (2005) 021, [[hep-ph/0508299](https://arxiv.org/abs/hep-ph/0508299)].
- [112] A. Friedland, C. Lunardini, and M. Maltoni, *Atmospheric neutrinos as probes of neutrino-matter interactions*, *Phys. Rev.* **D70** (2004) 111301, [[hep-ph/0408264](https://arxiv.org/abs/hep-ph/0408264)].
- [113] A. Friedland, C. Lunardini, and C. Pena-Garay, *Solar neutrinos as probes of neutrino matter interactions*, *Phys. Lett.* **B594** (2004) 347, [[hep-ph/0402266](https://arxiv.org/abs/hep-ph/0402266)].
- [114] A. Friedland and C. Lunardini, *A Test of tau neutrino interactions with atmospheric neutrinos and K2K*, *Phys. Rev.* **D72** (2005) 053009, [[hep-ph/0506143](https://arxiv.org/abs/hep-ph/0506143)].
- [115] K. J. Healey, A. A. Petrov, and D. Zhuridov, *Nonstandard neutrino interactions and transition magnetic moments*, *Phys. Rev.* **D87** (2013), no. 11 117301, [[arXiv:1305.0584](https://arxiv.org/abs/1305.0584)]. [Erratum: *Phys. Rev.* **D89**, no. 5, 059904 (2014)].
- [116] A. Anderson, J. Conrad, E. Figueroa-Feliciano, C. Ignarra, G. Karagiorgi, et al., *Measuring Active-to-Sterile Neutrino Oscillations with Neutral Current Coherent Neutrino-Nucleus Scattering*, *Phys. Rev.* **D86** (2012) 013004, [[arXiv:1201.3805](https://arxiv.org/abs/1201.3805)].

- [117] P. S. Amanik and G. C. McLaughlin, *Nuclear neutron form factor from neutrino nucleus coherent elastic scattering*, *J. Phys.* **G36** (2009) 015105.
- [118] P. S. Amanik, G. M. Fuller, and B. Grinstein, *Flavor changing supersymmetry interactions in a supernova*, *Astropart. Phys.* **24** (2005) 160–182, [[hep-ph/0407130](#)].
- [119] A. Esteban-Pretel, R. Tomas, and J. W. F. Valle, *Interplay between collective effects and non-standard neutrino interactions of supernova neutrinos*, *Phys. Rev.* **D81** (2010) 063003, [[arXiv:0909.2196](#)].
- [120] D. Papoulias and T. Kosmas, *Exotic lepton flavour violating processes in the presence of nuclei*, *J.Phys.Conf.Ser.* **410** (2013) 012123.
- [121] H. C. Chiang, E. Oset, T. S. Kosmas, A. Faessler, and J. D. Vergados, *Coherent and incoherent (μ^- , e^-) conversion in nuclei*, *Nucl. Phys.* **A559** (1993) 526–542.
- [122] T. S. Kosmas and J. D. Vergados, *(μ^- , e^-) conversion: A Symbiosis of particle and nuclear physics*, *Phys. Rept.* **264** (1996) 251–266, [[nucl-th/9408011](#)].
- [123] T. S. Kosmas, *Exotic $\mu^- \rightarrow e^-$ conversion in nuclei: Energy moments of the transition strength and average energy of the outgoing e^-* , *Nucl. Phys.* **A683** (2001) 443–462.
- [124] T. S. Kosmas, *Current nuclear physics issues in studying the neutrinoless (μ^- , e^-) conversion in nuclei*, *Prog. Part. Nucl. Phys.* **48** (2002) 307–316. [,307(2002)].
- [125] T. S. Kosmas, G. K. Leontaris, and J. D. Vergados, *Lepton flavor nonconservation*, *Prog. Part. Nucl. Phys.* **33** (1994) 397–448, [[hep-ph/9312217](#)].
- [126] F. Deppisch, T. S. Kosmas, and J. W. F. Valle, *Enhanced $\mu^- \rightarrow e^-$ conversion in nuclei in the inverse seesaw model*, *Nucl. Phys.* **B752** (2006) 80–92, [[hep-ph/0512360](#)].
- [127] D. V. Forero, S. Morisi, M. Tortola, and J. W. F. Valle, *Lepton flavor violation and non-unitary lepton mixing in low-scale type-I seesaw*, *JHEP* **09** (2011) 142, [[arXiv:1107.6009](#)].
- [128] S. P. Das, F. F. Deppisch, O. Kittel, and J. W. F. Valle, *Heavy Neutrinos and Lepton Flavour Violation in Left-Right Symmetric Models at the LHC*, *Phys. Rev.* **D86** (2012) 055006, [[arXiv:1206.0256](#)].

- [129] A. A. Petrov and D. V. Zhuridov, *Lepton flavor-violating transitions in effective field theory and gluonic operators*, *Phys. Rev.* **D89** (2014), no. 3 033005, [[arXiv:1308.6561](#)].
- [130] P. S. Amanik and G. M. Fuller, *Stellar Collapse Dynamics With Neutrino Flavor Changing Neutral Currents*, *Phys. Rev.* **D75** (2007) 083008, [[astro-ph/0606607](#)].
- [131] O. G. Miranda, M. A. Tortola, and J. W. F. Valle, *Are solar neutrino oscillations robust?*, *JHEP* **10** (2006) 008, [[hep-ph/0406280](#)].
- [132] J. Barranco, O. G. Miranda, and T. I. Rashba, *Low energy neutrino experiments sensitivity to physics beyond the Standard Model*, *Phys. Rev.* **D76** (2007) 073008, [[hep-ph/0702175](#)].
- [133] T. S. Kosmas, S. Kovalenko, and I. Schmidt, *Nuclear $\mu^- \rightarrow e^-$ conversion in strange quark sea*, *Phys. Lett.* **B511** (2001) 203, [[hep-ph/0102101](#)].
- [134] T. S. Kosmas, S. Kovalenko, and I. Schmidt, *B quark mediated neutrinoless $\mu^- \rightarrow e^-$ conversion in presence of R parity violation*, *Phys. Lett.* **B519** (2001) 78–82, [[hep-ph/0107292](#)].
- [135] V. Chasioti and T. Kosmas, *A unified formalism for the basic nuclear matrix elements in semi-leptonic processes*, *Nucl. Phys.* **A829** (2009), no. 3-4 234 – 252.
- [136] V. Tsakstara and T. S. Kosmas, *Low-energy neutral-current neutrino scattering on Te-128, Te-130 isotopes*, *Phys. Rev.* **C83** (2011) 054612.
- [137] T. W. Donnelly and J. D. Walecka, *Semileptonic Weak and Electromagnetic Interactions with Nuclei: Isoelastic Processes*, *Nucl. Phys.* **A274** (1976) 368–412.
- [138] T. W. Donnelly and R. D. Peccei, *Neutral Current Effects in Nuclei*, *Phys. Rept.* **50** (1979) 1.
- [139] W. R. Molzon, *Improved tests of muon and electron flavor symmetry in muon processes*, *Springer Tracts Mod. Phys.* **163** (2000) 105–128.
- [140] R. H. Bernstein and P. S. Cooper, *Charged Lepton Flavor Violation: An Experimenter's Guide*, *Phys. Rept.* **532** (2013) 27–64, [[arXiv:1307.5787](#)].
- [141] H. Klapdor-Kleingrothaus and I. Krivosheina, eds., *Proceedings of the First International Symposium on Lepton and Baryon Number Violation*, p.534, (Bristol and Philadelphia), Institute of Physics Publishing, 1998. unpublished.

- [142] **SINDRUM II** Collaboration, C. Dohmen et al., *Test of lepton flavor conservation in $\mu \rightarrow e$ conversion on titanium*, *Phys. Lett.* **B317** (1993) 631–636.
- [143] **Mu2e** Collaboration, K. Knoepfel et al., *Feasibility Study for a Next-Generation Mu2e Experiment*, in *Community Summer Study 2013: Snowmass on the Mississippi (CSS2013) Minneapolis, MN, USA, July 29-August 6, 2013*, 2013. [arXiv:1307.1168](#).
- [144] R. J. Barlow, *The PRISM/PRIME project*, *Nucl. Phys. Proc. Suppl.* **218** (2011) 44–49.
- [145] Y. Kuno, *COMET and PRISM: Search for charged lepton flavor violation with muons*, *Nucl. Phys. Proc. Suppl.* **225-227** (2012) 228–231.
- [146] **MEG** Collaboration, J. Adam et al., *New constraint on the existence of the $\mu^+ \rightarrow e^+ \gamma$ decay*, *Phys. Rev. Lett.* **110** (2013) 201801, [[arXiv:1303.0754](#)].
- [147] **SINDRUM** Collaboration, U. Bellgardt et al., *Search for the Decay $\mu^+ \rightarrow e^+ e^+ e^-$* , *Nucl. Phys.* **B299** (1988) 1.
- [148] V. Tsakstara and T. S. Kosmas, *Analyzing astrophysical neutrino signals using realistic nuclear structure calculations and the convolution procedure*, *Phys. Rev.* **C84** (2011) 064620.
- [149] **ATLAS** Collaboration, G. Aad et al., *Observation of a new particle in the search for the Standard Model Higgs boson with the ATLAS detector at the LHC*, *Phys. Lett.* **B716** (2012) 1–29, [[arXiv:1207.7214](#)].
- [150] **CMS** Collaboration, S. Chatrchyan et al., *Observation of a new boson at a mass of 125 GeV with the CMS experiment at the LHC*, *Phys. Lett.* **B716** (2012) 30–61, [[arXiv:1207.7235](#)].
- [151] S. Weinberg, *Baryon and Lepton Nonconserving Processes*, *Phys. Rev. Lett.* **43** (1979) 1566–1570.
- [152] M. Blennow, S. Choubey, T. Ohlsson, and S. K. Raut, *Exploring Source and Detector Non-Standard Neutrino Interactions at ESS ν SB*, *JHEP* **09** (2015) 096, [[arXiv:1507.02868](#)].
- [153] L. Wolfenstein, *Neutrino Oscillations in Matter*, *Phys. Rev.* **D17** (1978) 2369–2374.
- [154] V. D. Barger, R. J. N. Phillips, and K. Whisnant, *Solar neutrino solutions with matter enhanced flavor changing neutral current scattering*, *Phys. Rev.* **D44** (1991) 1629–1643.

- [155] W. Greiner and J. Reinhardt, *Quantum Electrodynamics*. Springer-Verlag, New York, 2nd ed., 1, 1994. ISBN: 9780387580920.
- [156] C. Giunti and A. Studenikin, *Neutrino electromagnetic interactions: a window to new physics*, *Rev. Mod. Phys.* **87** (2015) 531, [[arXiv:1403.6344](https://arxiv.org/abs/1403.6344)].
- [157] B. Kayser, *Majorana Neutrinos and their Electromagnetic Properties*, *Phys.Rev.* **D26** (1982) 1662.
- [158] J. F. Nieves, *Baryon and lepton number nonconserving processes and intermediate mass scales*, *Nucl. Phys.* **B189** (1981) 182.
- [159] W. A. Bardeen, R. Gastmans, and B. Lautrup, *Static quantities in Weinberg's model of weak and electromagnetic interactions*, *Nucl.Phys.* **B46** (1972) 319–331.
- [160] M. Dvornikov and A. Studenikin, *Electric charge and magnetic moment of massive neutrino*, *Phys. Rev.* **D69** (2004) 073001, [[hep-ph/0305206](https://arxiv.org/abs/hep-ph/0305206)].
- [161] S. Lee, *Higher-order corrections to leptonic processes and the renormalization of weinberg's theory of weak interactions in the unitary gauge*, *Phys.Rev.* **D6** (1972) 1701–1717.
- [162] B. W. Lee and R. E. Shrock, *Natural Suppression of Symmetry Violation in Gauge Theories: Muon - Lepton and Electron Lepton Number Nonconservation*, *Phys. Rev.* **D16** (1977) 1444.
- [163] J. Bernabeu, L. Cabral-Rosetti, J. Papavassiliou, and J. Vidal, *On the charge radius of the neutrino*, *Phys.Rev.* **D62** (2000) 113012, [[hep-ph/0008114](https://arxiv.org/abs/hep-ph/0008114)].
- [164] J. Schechter and J. W. F. Valle, *Majorana Neutrinos and Magnetic Fields*, *Phys. Rev.* **D24** (1981) 1883–1889. [Erratum: *Phys. Rev.* **D25**,283(1982)].
- [165] R. E. Shrock, *Electromagnetic Properties and Decays of Dirac and Majorana Neutrinos in a General Class of Gauge Theories*, *Nucl. Phys.* **B206** (1982) 359.
- [166] P. Vogel and J. Engel, *Neutrino Electromagnetic Form-Factors*, *Phys. Rev.* **D39** (1989) 3378.
- [167] J. F. Beacom and P. Vogel, *Neutrino magnetic moments, flavor mixing, and the Super-Kamiokande solar data*, *Phys. Rev. Lett.* **83** (1999) 5222–5225, [[hep-ph/9907383](https://arxiv.org/abs/hep-ph/9907383)].

- [168] W. Grimus, M. Maltoni, T. Schwetz, M. A. Tortola, and J. W. F. Valle, *Constraining Majorana neutrino electromagnetic properties from the LMA-MSW solution of the solar neutrino problem*, *Nucl. Phys.* **B648** (2003) 376–396, [[hep-ph/0208132](#)].
- [169] B. C. Canas, O. G. Miranda, A. Parada, M. Tortola, and J. W. F. Valle, *Updating neutrino magnetic moment constraints*, *Phys. Lett.* **B753** (2016) 191–198, [[arXiv:1510.01684](#)].
- [170] T. S. Kosmas, O. G. Miranda, D. K. Papoulias, M. Tortola, and J. W. F. Valle, *Probing neutrino magnetic moments at the Spallation Neutron Source facility*, *Phys. Rev.* **D92** (2015), no. 1 013011, [[arXiv:1505.03202](#)].
- [171] W. J. Marciano and A. I. Sanda, *Exotic Decays of the Muon and Heavy Leptons in Gauge Theories*, *Phys. Lett.* **B67** (1977) 303–305.
- [172] K. Fujikawa and R. Shrock, *The Magnetic Moment of a Massive Neutrino and Neutrino Spin Rotation*, *Phys. Rev. Lett.* **45** (1980) 963.
- [173] S. M. Bilenky and S. T. Petcov, *Massive Neutrinos and Neutrino Oscillations*, *Rev. Mod. Phys.* **59** (1987) 671. [Erratum: *Rev. Mod. Phys.* 60,575(1988)].
- [174] C. Brogini, C. Giunti, and A. Studenikin, *Electromagnetic Properties of Neutrinos*, *Adv. High Energy Phys.* **2012** (2012) 459526, [[arXiv:1207.3980](#)].
- [175] J. Barranco, A. Bolanos, E. A. Garces, O. G. Miranda, and T. I. Rashba, *Tensorial NSI and Unparticle physics in neutrino scattering*, *Int. J. Mod. Phys.* **A27** (2012) 1250147, [[arXiv:1108.1220](#)].
- [176] A. V. Povarov, *Scalar-leptoquark contributions to the neutrino magnetic moment*, *Phys. Atom. Nucl.* **70** (2007) 871–878. [*Yad. Fiz.* 70,905(2007)].
- [177] M. Gozdz, *Constraining an R-parity violating supergravity model with the Higgs induced Majorana neutrino magnetic moments*, *Phys. Rev.* **D85** (2012) 055016, [[arXiv:1201.0873](#)].
- [178] N. F. Bell, V. Cirigliano, M. J. Ramsey-Musolf, P. Vogel, and M. B. Wise, *How magnetic is the Dirac neutrino?*, *Phys. Rev. Lett.* **95** (2005) 151802, [[hep-ph/0504134](#)].
- [179] N. F. Bell, M. Gorchtein, M. J. Ramsey-Musolf, P. Vogel, and P. Wang, *Model independent bounds on magnetic moments of Majorana neutrinos*, *Phys. Lett.* **B642** (2006) 377–383, [[hep-ph/0606248](#)].

- [180] N. F. Bell, *How Magnetic is the Neutrino?*, *Int. J. Mod. Phys. A* **22** (2007) 4891–4899, [[arXiv:0707.1556](#)].
- [181] K. Schreckenbach, G. Colvin, W. Gelletly, and F. Von Feilitzsch, *DETERMINATION OF THE ANTI-NEUTRINO SPECTRUM FROM U-235 THERMAL NEUTRON FISSION PRODUCTS UP TO 9.5-MEV*, *Phys. Lett.* **B160** (1985) 325–330.
- [182] V. I. Kopeikin, L. A. Mikaelyan, and V. V. Sinev, *Spectrum of electronic reactor anti-neutrinos*, *Phys. Atom. Nucl.* **60** (1997) 172–176. [*Yad. Fiz.*60,230(1997)].
- [183] **TEXONO** Collaboration, H. T. Wong et al., *A Search of Neutrino Magnetic Moments with a High-Purity Germanium Detector at the Kuo-Sheng Nuclear Power Station*, *Phys. Rev.* **D75** (2007) 012001, [[hep-ex/0605006](#)].
- [184] **GEMMA** Collaboration, A. Beda, V. Brudanin, V. Egorov, D. Medvedev, V. Pogosov, et al., *The results of search for the neutrino magnetic moment in GEMMA experiment*, *Adv.High Energy Phys.* **2012** (2012) 350150.
- [185] G. G. Raffelt, *Limits on neutrino electromagnetic properties: An update*, *Phys. Rept.* **320** (1999) 319–327.
- [186] A. C. Dodd, E. Papageorgiu, and S. Ranfone, *The Effect of a neutrino magnetic moment on nuclear excitation processes*, *Phys. Lett.* **B266** (1991) 434–438.
- [187] V. Berestetskii, E. Lifshitz, and L. Pitaevskii, *Relativistic quantum theory: Parts 1 and 2*. Oxford, U.K.: Pergamon Press, 1979.
- [188] A. Studenikin, *New bounds on neutrino electric millicharge from limits on neutrino magnetic moment*, *Europhys. Lett.* **107** (2014) 21001, [[arXiv:1302.1168](#)]. [Erratum: *Europhys. Lett.*107,39901(2014)].
- [189] S. N. Gninenko, N. V. Krasnikov, and A. Rubbia, *Search for millicharged particles in reactor neutrino experiments: A Probe of the PVLAS anomaly*, *Phys. Rev.* **D75** (2007) 075014, [[hep-ph/0612203](#)].
- [190] J.-W. Chen, H.-C. Chi, K.-N. Huang, H.-B. Li, C. P. Liu, L. Singh, H. T. Wong, C.-L. Wu, and C.-P. Wu, *Constraining neutrino electromagnetic properties by germanium detectors*, *Phys. Rev.* **D91** (2015), no. 1 013005, [[arXiv:1411.0574](#)].

- [191] M. Maltoni, T. Schwetz, M. Tortola, and J. W. F. Valle, *Status of global fits to neutrino oscillations*, *New J.Phys.* **6** (2004) 122, [[hep-ph/0405172](#)]. this review gives a comprehensive set of references.
- [192] H. Nunokawa, S. J. Parke, and J. W. Valle, *CP Violation and Neutrino Oscillations*, *Prog.Part.Nucl.Phys.* **60** (2008) 338–402, [[arXiv:0710.0554](#)].
- [193] S. M. Boucenna, S. Morisi, and J. W. Valle, *The low-scale approach to neutrino masses*, *Adv.High Energy Phys.* **2014** (2014) 831598, [[arXiv:1404.3751](#)].
- [194] J. F. Nieves, *Electromagnetic Properties of Majorana Neutrinos*, *Phys. Rev.* **D26** (1982) 3152.
- [195] **Particle Data Group** Collaboration, J. Beringer et al., *Review of Particle Physics (RPP)*, *Phys.Rev.* **D86** (2012) 010001.
- [196] O. G. Miranda and J. W. F. others, *Constraining the neutrino magnetic moment with anti- neutrinos from the sun*, *Phys. Rev. Lett.* **93** (2004) 051304, [[hep-ph/0311014](#)].
- [197] O. G. Miranda, T. I. Rashba, A. I. Rez, and J. W. F. Valle, *Enhanced solar anti-neutrino flux in random magnetic fields*, *Phys. Rev.* **D70** (2004) 113002, [[hep-ph/0406066](#)].
- [198] M. Hirsch, E. Nardi, and D. Restrepo, *Bounds on the tau and muon neutrino vector and axial vector charge radius*, *Phys. Rev.* **D67** (2003) 033005, [[hep-ph/0210137](#)].
- [199] J. Barranco, O. Miranda, and T. Rashba, *Improved limit on electron neutrino charge radius through a new evaluation of the weak mixing angle*, *Phys.Lett.* **B662** (2008) 431–435, [[arXiv:0707.4319](#)].
- [200] M. Tortola, *Constraining neutrino magnetic moment with solar and reactor neutrino data*, *PoS AHEP2003* (2003) 022, [[hep-ph/0401135](#)].
- [201] M. Czakon, J. Gluza, and M. Zralek, *Neutrino magnetic moments in left-right symmetric models*, *Phys.Rev.* **D59** (1999) 013010.
- [202] R. Mohapatra, S.-P. Ng, and H.-b. Yu, *Reactor searches for neutrino magnetic moment as a probe of extra dimensions*, *Phys.Rev.* **D70** (2004) 057301, [[hep-ph/0404274](#)].
- [203] N. Viaux, M. Catelan, P. B. Stetson, G. Raffelt, J. Redondo, A. A. R. Valcarce, and A. Weiss, *Neutrino and axion bounds from the globular cluster M5 (NGC 5904)*, *Phys. Rev. Lett.* **111** (2013) 231301, [[arXiv:1311.1669](#)].

- [204] **LSND collaboration** Collaboration, L. B. Auerbach et al., *Measurement of electron-neutrino electron elastic scattering*, *Phys. Rev.* **D63** (2001) 112001, [[hep-ex/0101039](#)].
- [205] R. Allen, H. Chen, P. Doe, R. Hausammann, W. Lee, et al., *Study of electron-neutrino electron elastic scattering at LAMPF*, *Phys.Rev.* **D47** (1993) 11–28.
- [206] F. J. Escrihuela, O. G. Miranda, M. A. Tortola, and J. W. F. Valle, *Constraining nonstandard neutrino-quark interactions with solar, reactor and accelerator data*, *Phys. Rev.* **D80** (2009) 105009, [[arXiv:0907.2630](#)].
- [207] F. J. Escrihuela, M. Tortola, J. W. F. Valle, and O. G. Miranda, *Global constraints on muon-neutrino non-standard interactions*, *Phys. Rev.* **D83** (2011) 093002, [[arXiv:1103.1366](#)].
- [208] V. Chepel and H. Araujo, *Liquid noble gas detectors for low energy particle physics*, *JINST* **8** (2013) R04001, [[arXiv:1207.2292](#)].
- [209] **TEXONO** Collaboration, A. Soma et al., *Extraction of Physics Signals Near Threshold with Germanium Detectors in Neutrino and Dark Matter Experiments*, [arXiv:1411.4802](#).
- [210] H. T. Wong, H.-B. Li, J. Li, Q. Yue, and Z.-Y. Zhou, *Research program towards observation of neutrino-nucleus coherent scattering*, *J.Phys.Conf.Ser.* **39** (2006) 266–268, [[hep-ex/0511001](#)].
- [211] H. T. Wong, *Neutrino-nucleus coherent scattering and dark matter searches with sub-keV germanium detector*, *Nucl.Phys.* **A844** (2010) 229C–233C.
- [212] E. Simon et al., *SICANE: A Detector array for the measurement of nuclear recoil quenching factors using a monoenergetic neutron beam*, *Nucl. Instrum. Meth.* **A507** (2003) 643–656, [[astro-ph/0212491](#)].
- [213] J. D. Vergados, F. T. Avignone, III, and I. Giomataris, *Coherent Neutral Current Neutrino-Nucleus Scattering at a Spallation Source: A Valuable Experimental Probe*, *Phys. Rev.* **D79** (2009) 113001, [[arXiv:0902.1055](#)].
- [214] C. Giunti, K. A. Kouzakov, Y.-F. Li, A. V. Lokhov, A. I. Studenikin, and S. Zhou, *Electromagnetic neutrinos in terrestrial experiments and astrophysics*, [arXiv:1506.05387](#).
- [215] T. A. Mueller et al., *Improved Predictions of Reactor Antineutrino Spectra*, *Phys. Rev.* **C83** (2011) 054615, [[arXiv:1101.2663](#)].

- [216] A. G. Beda, V. B. Brudanin, V. G. Egorov, D. V. Medvedev, V. S. Pogosov, E. A. Shevchik, M. V. Shirchenko, A. S. Starostin, and I. V. Zhitnikov, *Gemma experiment: The results of neutrino magnetic moment search*, *Phys. Part. Nucl. Lett.* **10** (2013) 139–143.
- [217] **Daya Bay** Collaboration, F. P. An et al., *Search for a Light Sterile Neutrino at Daya Bay*, *Phys. Rev. Lett.* **113** (2014) 141802, [[arXiv:1407.7259](#)].
- [218] A. de Gouvea and T. Wytock, *Light Sterile Neutrino Effects at θ_{13} -Sensitive Reactor Neutrino Experiments*, *Phys. Rev.* **D79** (2009) 073005, [[arXiv:0809.5076](#)].
- [219] **Daya Bay** Collaboration, F. P. An et al., *Spectral measurement of electron antineutrino oscillation amplitude and frequency at Daya Bay*, *Phys. Rev. Lett.* **112** (2014) 061801, [[arXiv:1310.6732](#)].
- [220] C. Giunti and M. Laveder, *3+1 and 3+2 Sterile Neutrino Fits*, *Phys. Rev.* **D84** (2011) 073008, [[arXiv:1107.1452](#)].
- [221] T. S. Kosmas, O. G. Miranda, D. K. Papoulias, M. Tortola, and J. W. F. Valle, *Sensitivities to neutrino electromagnetic properties at the TEXONO experiment*, *Phys. Lett.* **B750** (2015) 459–465, [[arXiv:1506.08377](#)].
- [222] G. Mention, M. Fechner, T. Lasserre, T. A. Mueller, D. Lhuillier, M. Cribier, and A. Letourneau, *The Reactor Antineutrino Anomaly*, *Phys. Rev.* **D83** (2011) 073006, [[arXiv:1101.2755](#)].
- [223] C. Giunti and E. M. Zavanin, *Appearance-disappearance relation in 3 + N_s short-baseline neutrino oscillations*, *Mod. Phys. Lett.* **A31** (2015), no. 01 1650003, [[arXiv:1508.03172](#)].
- [224] M. Maltoni and T. Schwetz, *Sterile neutrino oscillations after first MiniBooNE results*, *Phys. Rev.* **D76** (2007) 093005, [[arXiv:0705.0107](#)].
- [225] N. Okada and O. Yasuda, *A Sterile neutrino scenario constrained by experiments and cosmology*, *Int. J. Mod. Phys.* **A12** (1997) 3669–3694, [[hep-ph/9606411](#)].
- [226] **LSND** Collaboration, A. Aguilar-Arevalo et al., *Evidence for neutrino oscillations from the observation of anti-neutrino(electron) appearance in a anti-neutrino(muon) beam*, *Phys. Rev.* **D64** (2001) 112007, [[hep-ex/0104049](#)].
- [227] **MiniBooNE** Collaboration, A. A. Aguilar-Arevalo et al., *Event Excess in the MiniBooNE Search for $\bar{\nu}_\mu \rightarrow \bar{\nu}_e$ Oscillations*, *Phys. Rev. Lett.* **105** (2010) 181801, [[arXiv:1007.1150](#)].

- [228] J. Kopp, M. Maltoni, and T. Schwetz, *Are there sterile neutrinos at the eV scale?*, *Phys. Rev. Lett.* **107** (2011) 091801, [[arXiv:1103.4570](#)].
- [229] J. Hamann, S. Hannestad, G. G. Raffelt, I. Tamborra, and Y. Y. Y. Wong, *Cosmology seeking friendship with sterile neutrinos*, *Phys. Rev. Lett.* **105** (2010) 181301, [[arXiv:1006.5276](#)].
- [230] E. Giusarma, M. Corsi, M. Archidiacono, R. de Putter, A. Melchiorri, O. Mena, and S. Pandolfi, *Constraints on massive sterile neutrino species from current and future cosmological data*, *Phys. Rev.* **D83** (2011) 115023, [[arXiv:1102.4774](#)].
- [231] S. M. Bilenky, C. Giunti, J. A. Grifols, and E. Masso, *Absolute values of neutrino masses: Status and prospects*, *Phys. Rept.* **379** (2003) 69–148, [[hep-ph/0211462](#)].
- [232] C. Giunti and M. Laveder, *Short-Baseline Electron Neutrino Disappearance, Tritium Beta Decay and Neutrinoless Double-Beta Decay*, *Phys. Rev.* **D82** (2010) 053005, [[arXiv:1005.4599](#)].
- [233] A. Faessler, T. S. Kosmas, S. Kovalenko, and J. D. Vergados, *Exotic μe conversion in nuclei and R-parity violating supersymmetry*, *Nucl. Phys.* **B587** (2000) 25–44.
- [234] T. Donnelly and W. Haxton, *Multipole operators in semileptonic weak and electromagnetic interactions with nuclei: Harmonic oscillator single-particle matrix elements*, *Atomic Data and Nuclear Data Tables* **23** (1979), no. 2 103 – 176.
- [235] B. Dreher, J. Friedrich, K. Merle, H. Rothhaas, and G. Lührs, *The determination of the nuclear ground state and transition charge density from measured electron scattering data*, *Nucl. Phys.* **A 235** (1974), no. 1 219 – 248.
- [236] I. Sick, *Model-independent nuclear charge densities from elastic electron scattering*, *Nucl. Phys.* **A 218** (1974), no. 3 509 – 541.

